



ADVANCES IN CHEMICAL ENGINEERING

Volume 12

James Wei

ADVANCES IN CHEMICAL ENGINEERING

Volume 12

CONTRIBUTORS

COSTEL D. DENSON

B. GROSS

C. D. PRATER

ROBERT C. REID

JOHN H. SEINFELD

V. W. WEEKMAN, JR.

J. WEI

ADVANCES IN CHEMICAL ENGINEERING

Edited by

JAMES WEI

*Department of Chemical Engineering
Massachusetts Institute of Technology
Cambridge, Massachusetts*

Associate Editors

KENNETH B. BISCHOFF

*Department of Chemical Engineering
University of Delaware
Newark, Delaware*

THOMAS B. DREW

Peterborough, New Hampshire

JOHN H. SEINFELD

*Department of Chemical Engineering
California Institute of Technology
Pasadena, California*

**Volume 12
1983**



ACADEMIC PRESS

A Subsidiary of Harcourt Brace Jovanovich, Publishers

New York London

Paris San Diego San Francisco São Paulo Sydney Tokyo Toronto

**COPYRIGHT © 1983, BY ACADEMIC PRESS, INC.
ALL RIGHTS RESERVED.
NO PART OF THIS PUBLICATION MAY BE REPRODUCED OR
TRANSMITTED IN ANY FORM OR BY ANY MEANS, ELECTRONIC
OR MECHANICAL, INCLUDING PHOTOCOPY, RECORDING, OR ANY
INFORMATION STORAGE AND RETRIEVAL SYSTEM, WITHOUT
PERMISSION IN WRITING FROM THE PUBLISHER.**

**ACADEMIC PRESS, INC.
111 Fifth Avenue, New York, New York 10003**

United Kingdom Edition published by
**ACADEMIC PRESS, INC. (LONDON) LTD.
24/28 Oval Road, London NW1 7DX**

LIBRARY OF CONGRESS CATALOG CARD NUMBER: 56-6600

ISBN 0-12-008512-7

PRINTED IN THE UNITED STATES OF AMERICA

83 84 85 86 9 8 7 6 5 4 3 2 1

CONTENTS

CONTRIBUTORS	vii
PREFACE	ix

A Reaction Engineering Case History: Coke Burning in Thermofor Catalytic Cracking Regenerators

C. D. PRATER, J. WEI, V. W. WEEKMAN, JR., AND B. GROSS

I. Introduction	1
II. Single-Particle Kinetics.	3
III. Analytical Solution of the Kiln Equation for Slow Coke	13
IV. Extension of the Model for Fast and Slow Coke	26
V. Dynamic Response Model	31
VI. The Inclusion of the Kinetics of the Conversion of CO to CO ₂ in the Model	42
VII. Conclusion.	57
Nomenclature	57
References	59

Stripping Operations in Polymer Processing

COSTEL D. DENSON

I. Introduction	61
II. Nature of the Problem	64
III. Mass Transfer Rates in Wiped-Film Processors	67
IV. Bubble Entrainment and Enhanced Mass Transfer	87
V. The Length of a Transfer Unit.	99
Nomenclature	102
References	103

Rapid Phase Transitions from Liquid to Vapor

ROBERT C. REID

I. Summary	106
II. Introduction	112
III. Rapid Phase Transitions between Liquefied Natural Gas and Water.	113

IV. Smelt–Water Explosions	141
V. Molten Aluminum–Water Explosions	159
VI. Reactive Metal–Water Explosions	182
VII. Explosions with Liquid Refrigerants	186
VIII. Effects of Absolute Pressure on RPTs.	189
IX. Appendix: Superheated Liquids	198
Nomenclature	203
References	203

Atmospheric Diffusion Theory

JOHN H. SEINFELD

I. Introduction	210
II. Fundamental Equations of Turbulent Diffusion	212
III. Mean Concentration from an Instantaneous Source in Stationary, Homogeneous Turbulence	218
IV. Mean Concentration from Continuous Sources	224
V. Point Source Diffusion Formulas Based on a Gaussian Distribution.	233
VI. Validity of the Atmospheric Diffusion Equation.	250
VII. Meteorological Parameters Characterizing the Atmospheric Boundary Layer	253
VIII. Dispersion Parameters in Gaussian Models.	261
IX. Parameters in the Atmospheric Diffusion Equation	275
X. Monte Carlo Simulation of Turbulent Diffusion.	288
XI. Summary	294
References	295
INDEX	301
CONTENTS OF PREVIOUS VOLUMES.	311

CONTRIBUTORS

Numbers in parentheses indicate the pages on which the authors' contributions begin.

COSTEL D. DENSON (61), *Department of Chemical Engineering, University of Delaware, Newark, Delaware 19711*

B. GROSS (1), *Research Department, Mobil Research and Development Corporation, Paulsboro, New Jersey 08066*

C. D. PRATER (1), *Research Department, Mobil Research and Development Corporation, Paulsboro, New Jersey 08066*

ROBERT C. REID (105), *Department of Chemical Engineering, Massachusetts Institute of Technology, Cambridge, Massachusetts 02139*

JOHN H. SEINFELD (209), *Department of Chemical Engineering, California Institute of Technology, Pasadena, California 91125*

V. W. WEEKMAN, JR. (1), *Research Department, Mobil Research and Development Corporation, Paulsboro, New Jersey 08066*

J. WEI* (1), *Research Department, Mobil Research and Development Corporation, Paulsboro, New Jersey 08066*

*Present address: Department of Chemical Engineering, Massachusetts Institute of Technology, Cambridge, Massachusetts 02139.

This Page Intentionally Left Blank

PREFACE

This volume is the first effort of a new Board of Editors. We plan to provide timely and critical reviews of substantial developments in chemical engineering. We have a dual audience in mind: the generalists should learn where the major advances are in new knowledge and understanding, in new tools and equipment, in new processes and products, and in issues of general concern; the specialists should learn in some depth from critical evaluations of the literature of theoretical and experimental techniques and results and their future implications. These volumes will provide a forum for articles longer than a single research paper and shorter than a monograph or book. We believe that these reviews will prove valuable to the profession of chemical engineering.

James Wei
Kenneth B. Bischoff
Thomas B. Drew
John H. Seinfeld

This Page Intentionally Left Blank

A REACTION ENGINEERING CASE HISTORY: COKE BURNING IN THERMOFOR CATALYTIC CRACKING REGENERATORS

**C. D. Prater, J. Wei,¹
V. W. Weekman, Jr., and B. Gross**

**Research Department
Mobil Research and Development Corporation
Paulsboro, New Jersey**

I.	Introduction	1
II.	Single Particle Kinetics	3
	A. Intrinsic Kinetics from the Laboratory Experiments	3
	B. Diffusional Limited Burning.	9
III.	Analytical Solution of the Kiln Equation for Slow Coke	13
	A. Development of an Explicit Solution for the Kiln Equation for Slow Coke Burning	13
	B. Test and Use of the Explicit Solution	19
	C. Use of the Explicit Solution to Explore Kiln Performance	21
IV.	Extension of the Model for Fast and Slow Coke.	26
	A. The Effect of the Initial Temperature T_i on Residual Carbon	26
	B. The Inclusion of Fast Coke in the Model	27
V.	Dynamic Response Model.	31
VI.	The Inclusion of the Kinetics of the Conversion of CO to CO ₂ in the Model	42
	A. Kinetics of CO Formation and Conversion	45
	B. Diffusion Kinetics	47
VII.	Conclusion	57
	Nomenclature	57
	References	59

I. Introduction

The application of reaction kinetics to the design of chemical reactors has reached a level of maturity over the past 20 years. The discipline is

¹ Present address: Department of Chemical Engineering, Massachusetts Institute of Technology, Cambridge, Massachusetts 02139.

now comfortably established under its Reaction Engineering name and is already looking forward to its Seventh International Symposium. Publications in the field are increasing exponentially. Occasionally one finds a paper revealing some successful industrial applications, but these papers usually reveal only a small facet of the overall application. Because of the proprietary nature of most processes, the true reaction schemes or catalysts may be clouded in secrecy, the rate constants may not be given, and comparison with plant data may not be made available.

It is the purpose of this article to present in its entirety one of the early applications of reaction engineering, which was well under way in 1952 before the name Reaction Engineering was even coined. We will describe the laboratory kinetic experiments, the diffusional analysis, the integration of these phenomena into a mathematical process model, its field testing and validation, and subsequent use in process design, modification, control, and optimization.

The work took place over a >20-yr period and involved the talents of many people within the Mobil Research laboratories and the cooperation of many refinery personnel. At the first stage, the kinetics of single-particle burning was studied by P. B. Weisz and co-workers. At the second stage, the one-dimensional kiln equation was solved analytically by C. D. Prater, and the exploration of kiln performance was performed by J. Wei. At the third stage, extension of the model to both fast and slow coke by numerical techniques, and to dynamic responses was done by V. W. Weekman. Finally, the kinetics of CO conversion to CO₂ was included in the model by B. Gross. However, the complete development could not have been accomplished without help from a large supporting cast. The kinetics have been published (Weisz, 1966, Weisz and Goodwin, 1963, 1966) and some information about the model was given earlier (Prater *et al.*, 1963; Weekman *et al.*, 1967). However, much of the present material has not been published previously. It is hoped that the story in its entirety will give encouragement alike to those seeking to apply the scientific approach to industrial reactor design and to those engaged in fundamental research. In order to increase the value of this article as a reference and teaching tool, we have included detailed derivations of the final equations used in the reactor models.

The thermofor catalytic cracking (TCC) process was developed in the late 1930s and early 1940s, to break down heavy fuel oil into gasoline. During World War II, many units were built to meet the large aviation gasoline demand. It had been developed through the classic approach to scale up of building increasingly larger-scale components of the system. By the 1950s over 48 commercial units were in operation, as well as versions in the Soviet Union and the People's Republic of China; yet little

was understood about much of the operation of these units, particularly the regenerator (kiln) operation.

From Fig. 1, we see the general flow diagram of the air lift version of the unit. Bead catalyst² $\sim \frac{1}{8}$ inch (3.2×10^{-3} m) in diameter flows as a compact moving bed from the separator down through the reactor and into the kiln. In the earliest version of the units, the catalyst was returned to the top of the units by means of a bucket elevator. In the air lift version developed later, the catalyst beads flowing out of the kiln are blown by an air lift to the top of the separator, where they again pass down into the reactor. Oil is contacted with the catalyst in a concurrent fashion in the reactor. The reaction products are drawn off and separated in the fractionation section. Recycle from the fractionator returns and is mixed with the fresh gas oil and charged into the reactor. Carbonaceous material (coke) is laid down in the reaction section as a by-product of the cracking reactions. The coke acts to deactivate the catalyst, and the kiln functions to burn off the coke and to restore catalytic activity to its initial value. A typical kiln may be 35 ft (10.7 m) tall and 30 ft (9.1 m) in diameter.

Many variables under the control of the operator or designer affect the operation of the kiln. The flow patterns in the kiln are shown in Fig. 2, and some of the major process variables are listed. There are more than 14 major variables which influence the kiln design or operation. All variables strongly interact. Since it is exceedingly difficult to grasp the effect of even a few variables, different schools of thought had arisen about kiln operation. Each group had its own image based on the variables with which it was most familiar, much as the seven blind Hindus after feeling different parts of the elephant. Trying to change this situation, P. B. Weisz and co-workers in the early 1950s undertook a program to determine the kinetics of coke burning in the kiln.

II. Single Particle Kinetics

A. INTRINSIC KINETICS FROM THE LABORATORY EXPERIMENTS

Weisz and co-workers organized the kinetic experiments to study the key underlying phenomena of coke burning, independent of other complicating phenomena. Their first step in this direction was to recognize that

² The earliest catalyst was made from clay; later, synthetic beads from silica-alumina were introduced. In the early 1960s, catalysts were introduced that employed up to 10% X or Y zeolite in a silica-alumina matrix.

there were two kinds of coke on the catalyst (Weisz and Goodwin, 1966). One was designated "fast" coke, and consisted of chemisorbed material that became desorbed as the catalyst temperature rose. It burns mostly in the gas phase in the kiln. This coke could be removed by exposing the sample to an oxygen-free atmosphere at 1200°F (922 K) for approximately 15 min. The remaining coke, designated "slow" coke, was not desorbable and burned on the surface of the catalyst. This material constituted the

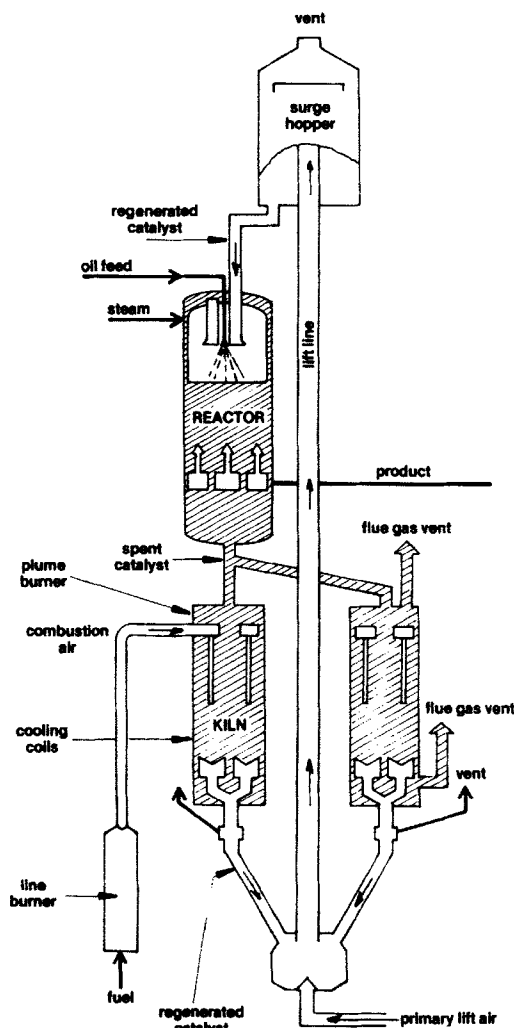


FIG. 1. Air lift TCC process.

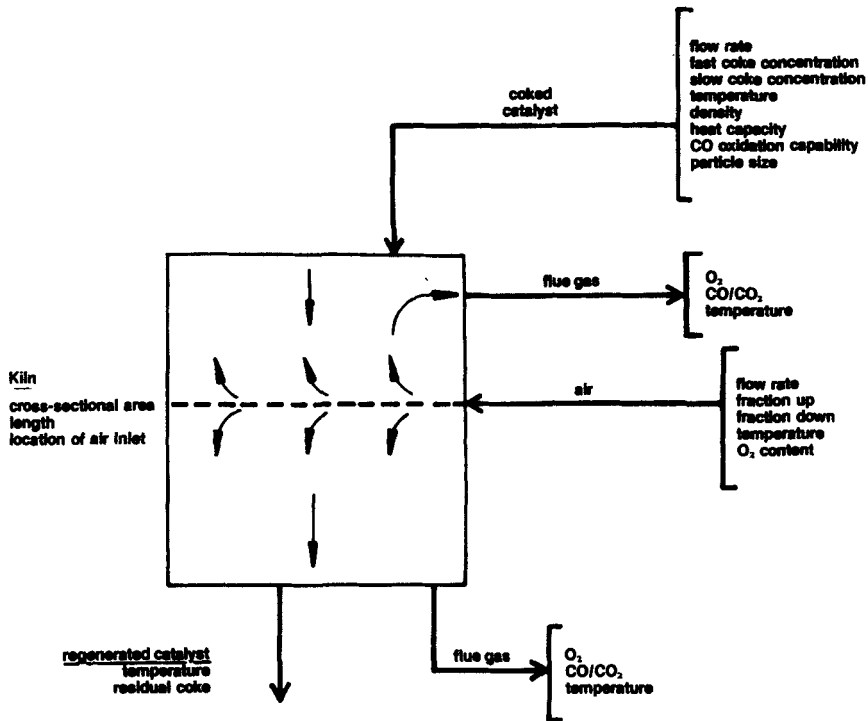


FIG. 2. Kiln flow and variables.

major portion of the coke. It is this coke to which they first directed their attention.

The rate at which carbon is burned from the catalyst in air was measured under differential reactor conditions by burning small samples of coked catalyst $(1.1-4.4) \times 10^{-3}$ lb $[(5-20) \times 10^{-5}$ kg] in a rapidly flowing airstream. By using high air rates, the oxygen concentration varied little during the experiments. Thus, oxygen dependence could be studied in an uncoupled manner. It was found that the rate of burning was sufficiently close to first order with respect to oxygen concentration (C_{Ox}) for most purposes.

The rate of oxygen utilization is related to the intrinsic rate of carbon burning by the ratio of CO to CO₂ produced in the burning reaction. This relation can be expressed in terms of a constant α that is defined as the moles of coke burned per mole of O₂ consumed, and varies between 1 and 2. The relation between the two rates is given by

$$d[C_c]/dt = \alpha(d[C_{Ox}]/dt) \quad (1)$$

It was found that, for intrinsic burning, the value of α was a function of the temperature only (Weisz, 1966).

At the higher temperatures, whole catalyst beads have greatly different rates of burning than beads pulverized to 200 mesh. This is caused by diffusional resistance in supplying oxygen to the coke burning sites within the whole beads. This diffusion effect can be seen in Fig. 3, where the oxygen consumption rate is plotted versus temperature for both powder and beads. The cracking catalyst bead is a porous and high-surface-area material in which the coke is deposited on the walls of the internal pores structure. This requires the transportation, by molecular diffusion, of oxygen to the place within the porous bead structure where the coke is

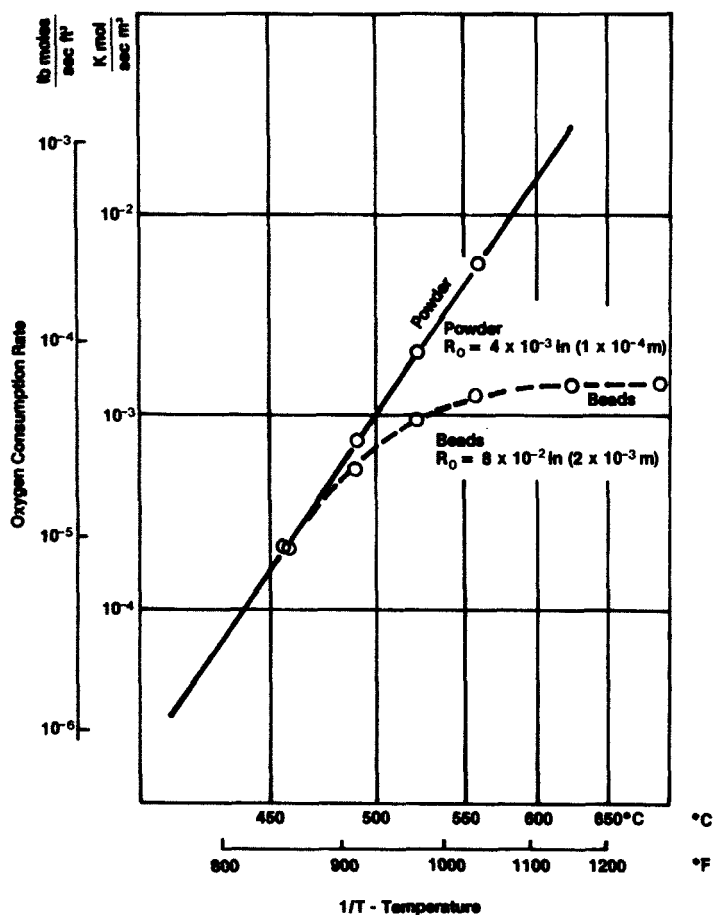


FIG. 3. Diffusional effects in single-bead experiments.

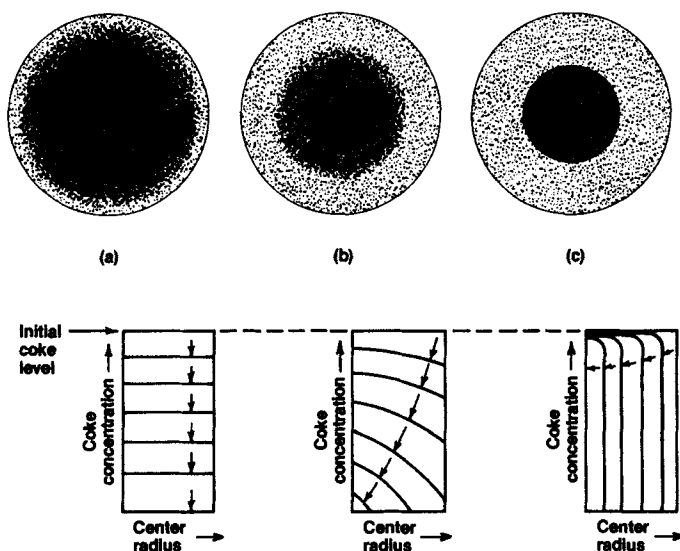


FIG. 4. "Fish eye" burning in cracking catalyst beads. Appearance after partial burn-off (top), and coke concentration versus radius in beads for successive stages of burn-off (bottom) for three temperature regions: (a) low, (b) intermediate, (c) high.

burned. The diameter of these pores is less than the mean free path of the oxygen molecules in the gas, so the diffusion will be in the Knudsen region. When the rate of intrinsic burning is very fast, a large concentration gradient of oxygen is required to supply the oxygen to the burning site within the bead, so the oxygen concentration at the burning site is less than that exterior to the bead. Since the intrinsic burning rate is proportional to the oxygen concentration, the overall rate of burning will be less than expected from the external oxygen concentration. If the intrinsic burning rate is fast enough, coke burning will advance through the bead as a sharply defined burning front. Hence, when beads that had been partially burned at sufficiently high temperatures are cracked open, an inner core of unburned carbon is found. Figure 4 shows this phenomenon for three silica-alumina beads which have been partially burned at three different temperature levels ranging from low to high (Weisz and Goodwin, 1963). The coke has been made visible by immersing the silica-alumina beads in carbon tetrachloride. Commercial operators had also noticed this phenomenon and called beads that exhibited these black cores "fish eye" beads.

From the physical evidence it is clear that, as expected, a sharp coke interface is formed at high temperatures between the burned and the

unburned portion of the bead. This sharp interface means that the burning rate at higher temperatures is completely limited by the rates of the diffusion of oxygen to the burning surface. At lower temperatures, there appears to be no sharp interface, thus the burning is only partly limited by the diffusion of oxygen and partly limited by the intrinsic rate of carbon burning. Hence, except at very low temperatures, the intrinsic kinetics of carbon burning could be determined only by using pulverized catalyst. Pulverizing the beads provided the means of uncoupling the intrinsic rate of burning from diffusional phenomena at higher temperature ranges.

Using the pulverized silica-alumina catalyst, it was found that slow coke burning is first order with respect to the fraction of carbon remaining on the catalyst (y) if the initial concentration of slow coke (C_c) is below 7–20% of the weight of the catalyst as shown in Fig. 5. The precise value of this ceiling on first-order behavior is determined by the surface area of the porous bead catalyst. Above this ceiling, the burning is not first order, as shown in Fig. 5. It was shown that this departure occurred when more coke is deposited on the catalyst than can be accommodated in a monolayer. These high coke levels were seldom encountered in commercial operations of the TCC unit using silica-alumina beads.

The temperature dependency of the rate constant k for the first-order

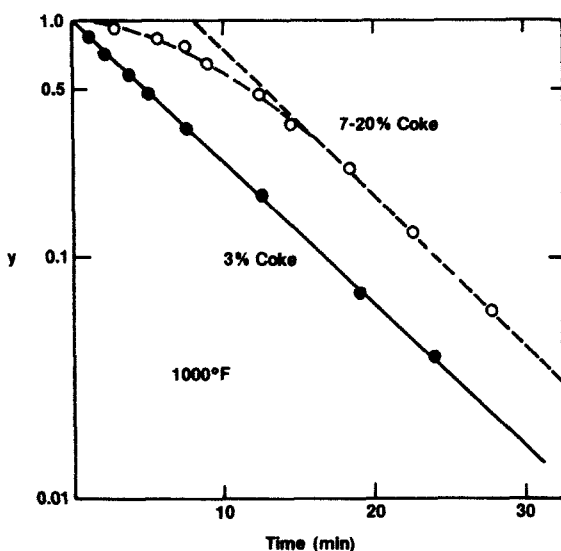


FIG. 5. Typical rate plots of carbon remaining versus burning time: (●) normal sample; (○) initial flattening due to carbon overload (partial inaccessibility). Redrawn from Weisz and Goodwin (1963).

coke burning was found to obey the Arrhenius relationship:

$$k = b \exp(-Q/RT) \quad (2)$$

Thus, for the monolayer region of coke concentration, the intrinsic rate of burning of slow coke is given by

$$(dy/dt)_I = byzC'_{ox} \exp(-Q/RT) \quad (3)$$

where C'_{ox} is the initial concentration of oxygen, $z = C_{ox}/C'_{ox}$ is the fraction of oxygen remaining, $y = C_c/C_c^0$ is the fraction of the original slow coke left on the catalyst.

The various gas oil charged to the TCC units differed greatly in composition. Thus, the possibility arose that the burning rate of coke could be a function of the composition of the charge stock from which it came. Weisz and Goodwin (1966) found that the slow coke burning rate is independent of the source of the charge stock and, within experimental error, is equal to that reported in the literature for graphite (Arthur, 1951). Figure 6 shows this independence. In this figure, the time required to burn 85% of the coke is plotted against the reciprocal of the absolute temperature. The 85% burning time is a convenient measure of the first-order rate constant:

$$t_{85} = -\ln 0.15/kC'_{ox} = 1.9/kC'_{ox} \quad (4)$$

$$\ln t_{85} = \ln(1.9/bC'_{ox}) + Q/RT \quad (5)$$

A variety of material could be used as the basis for cracking catalyst, including synthetic silica-alumina, natural clay, or silica-magnesia. If these materials did not contain significant amounts of metals such as chromium or platinum that catalyzed the burning of carbon, the burning rate of the coke is independent of the base as shown in Fig. 7.

B. DIFFUSIONAL LIMITED BURNING

The influence of diffusion on the burning rate is easy to calculate for the special limiting case in which the rate of supply of oxygen by diffusion determines the burning rate. As our previous discussion showed, a coked bead partially burned at a high temperature exhibits two sharply defined regions: an outer shell of cleanly burned bead surrounding a core of coke still at its initial concentration (C_c^0). At sufficiently high temperatures the concentration of coke can be considered to go from zero to initial value in a step function on passing between the two regions. Since there is no coke in the clean burned region, no oxygen is used in this region and the

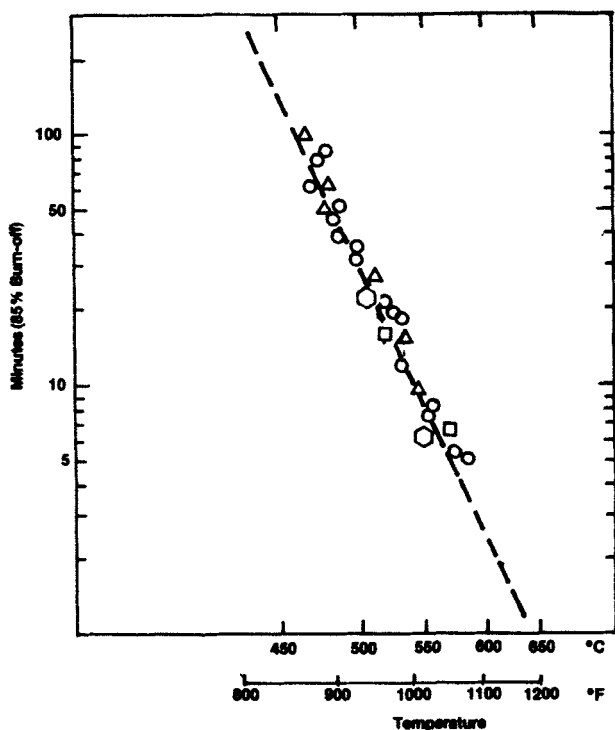


FIG. 6. Burning rate constant is independent of origin of coke. Five different modes of coking are represented by different symbols. From Weisz and Goodwin (1963).

concentration of oxygen at each point in this region must satisfy the following equation:

$$\nabla^2 C_{\text{ox}} = 0 \quad (6)$$

The oxygen concentration is zC'_{ox} at the outer surface of the bead, and is essentially zero at the burning front for this high-temperature burning. For a spherical bead of radius a with coke core of radius r_b , the solution of Eq. (6) is

$$C_{\text{ox}}(r) = zC'_{\text{ox}} \left(\frac{a}{a - r_b} \right) \left(\frac{r - r_b}{r} \right), \quad r_b \leq r \leq a \quad (7)$$

The rate of flow of oxygen (f) through the outer surface of the bead multiplied by α will be equal to the rate of burning of the coke in a single bead:

$$\alpha f = (4/3)\pi a^3 C_c^0 (dy/dt)_D \quad (8)$$

On the other hand, the rate of flow of oxygen through the outer surface of the bead can be obtained from Eq. (7) and is given by

$$f = 4\pi a^2 D (dC_{ox}/dr)_a \quad (9)$$

Furthermore,

$$y = (r_b/a)^3 \quad (10)$$

Hence, combining Eqs. (7)–(10) gives the diffusional limited rate of burning:

$$\left(\frac{dy}{dt}\right)_D = \frac{3D\alpha z C'_{ox}}{a^2 C_c^0} \frac{y^{1/3}}{1 - y^{1/3}} \quad (11)$$

There were great expectations that the quantification provided by Eqs. (3) and (11) for single beads would receive quick and productive application to kiln problems by the refinery engineers. To aid in this application,

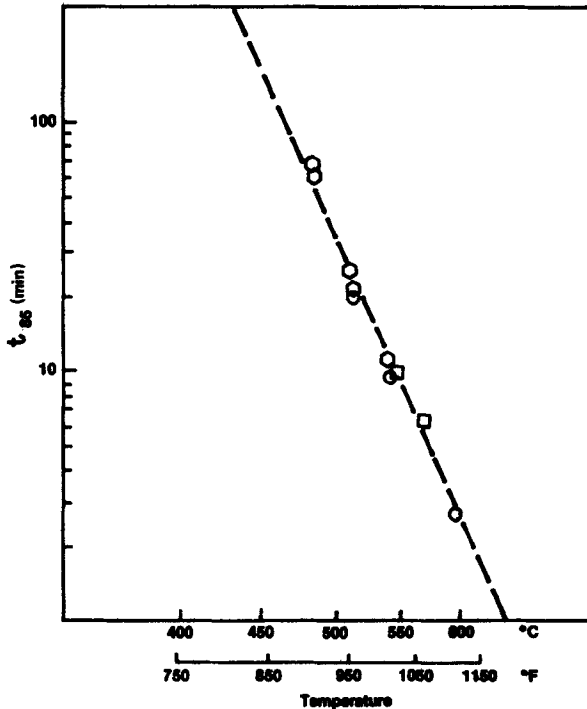


FIG. 7. Comparison of intrinsic combustion rate constant on various noncatalyzing oxide bases: (○) Filtrol 110; (□) silica-magnesia; (○) Fuller's earth. The dashed line denotes standard noncatalyzed kinetics.

a special "slide rule" (Fig. 8) was constructed to provide burning curves for any temperature, bead size and diffusivity, and coke concentration. In this slide rule, the transition region between intrinsic burning given by Eq. (3) and diffusion-controlled burning given by Eq. (11) was reproduced by means of a plastic template shown in Fig. 8. However, this excellent and penetrating study on single beads was very little used by the refinery engineers, and had almost no impact on kiln operation and design procedures. When reasons for this were sought, it became clear that the diffi-

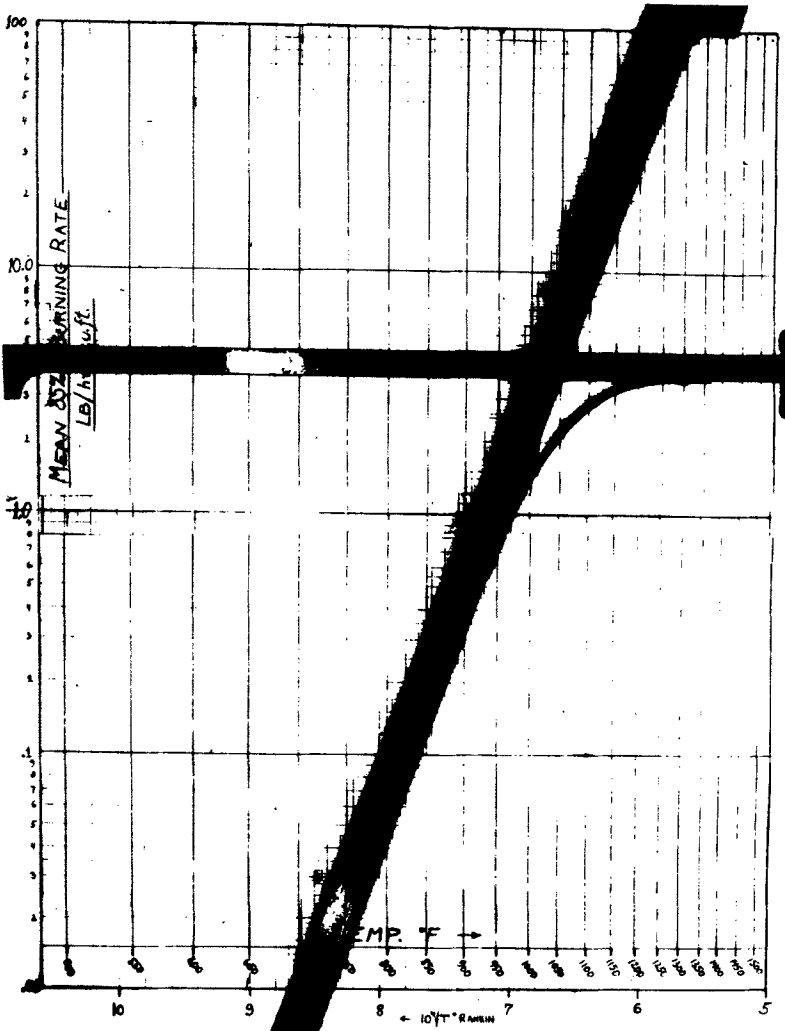


FIG. 8. Coke burning slide rule.

culty lay in the multiple dimensionality of the kiln problem. The user was unable to think clearly through the complex interactions in the operating kiln without the help of a comprehensive mathematical model, regardless of how good the quantification for a single bead. In the early 1950s when this work was completed, digital computers of sufficient capacity were not yet available, so that analytical solutions for the kiln equations were needed.

III. Analytical Solution of the Kiln Equation for Slow Coke

A. DEVELOPMENT OF AN EXPLICIT SOLUTION FOR THE KILN EQUATION FOR SLOW COKE BURNING

The first problem in setting up the kiln equation was to obtain an equation for the rate of burning in the transition region between the two limiting cases given by Eqs. (3) and (11). In the "slide rule," a piece of plastic was machined to fit the observed curve, and no explicit expression for this region was obtained. The dashed lines in the Arrhenius plot of Fig. 9 show the two limiting cases as a function of temperature. Instead of solving the equations for the transition region, which presents considerable mathematical difficulty, it was found that the integral burning rate to 85% completion could be empirically approximated in terms of the limiting cases by

$$(dy/dt)^{-1} = (dy/dt)_I^{-1} + (dy/dt)_D^{-1} \quad (12)$$

The points shown in Fig. 9 were calculated using Eq. (12) and show excellent agreement with the solid line which represents experimental data.

It should be noted here that since the original work done at Mobil was completed, there have been new developments published in the literature. Ishida and Wen (1968) analytically solved a special case for the transition region when the reaction rate does not depend on the local solids (coke) concentration. Wen (1968) has also numerically solved the more general problem for certain kinetic forms, and Amundson and co-workers have done much work on the diffusion and reaction in the boundary layer about a carbon particle (Caram and Amundson, 1977). We will not attempt to review the literature or compare the more accurate numerical solutions with our *ad hoc* approximation technique. However, we note that our technique was simple, fit the experimental and commercial data extremely well, and provided us with valuable insight and understanding

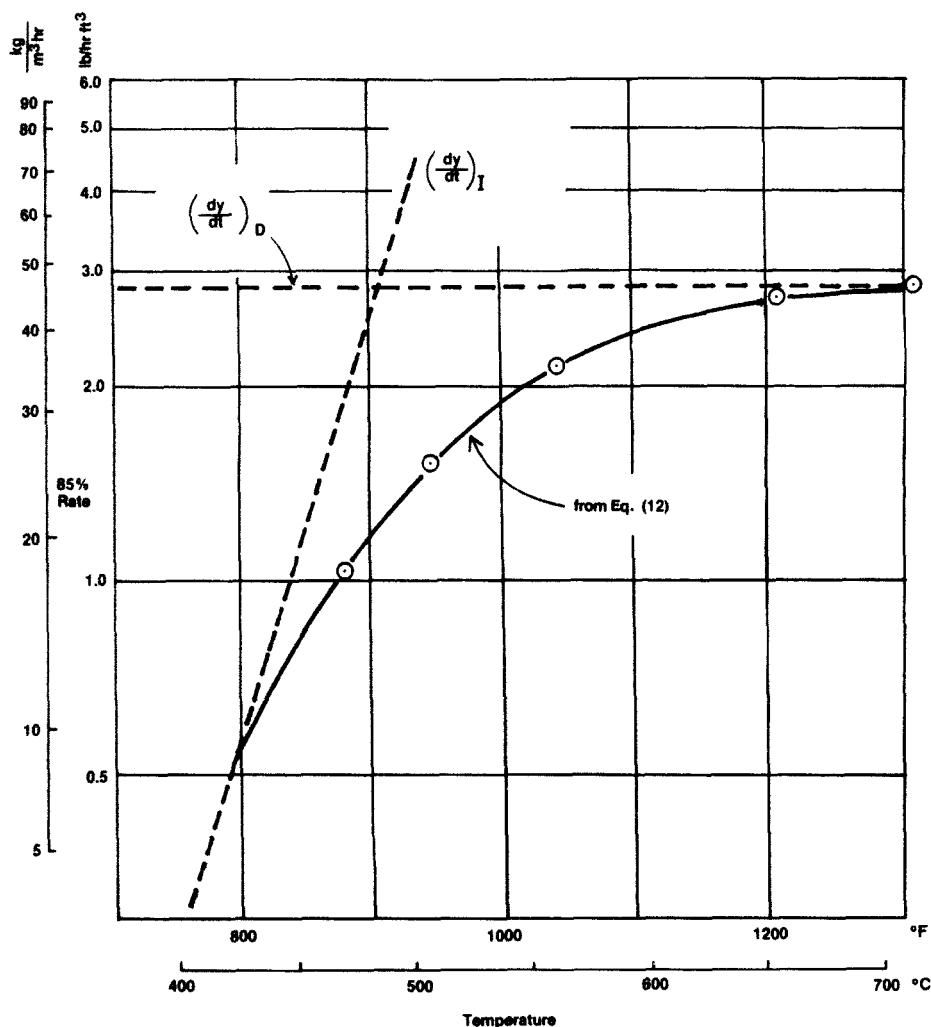


FIG. 9. A comparison of the results computed from Eq. (12) for transitional burning (indicated by \odot) with the observed burning rate behavior for silica-alumina catalyst (solid curve).

into the physical and chemical processes occurring in the kiln. Our philosophy has always been to use the simplest model possible to explain observed phenomena. Only when it fails is a more complex approach warranted.

The second problem was to obtain some quantification of the variation of the coefficient α which accounts for the relative production of CO and

CO_2 . For the operating conditions for kilns in the 1950s, an examination of the values of α observed led to the discovery that α was approximately a constant characteristic of each zone of the kiln. This phenomenon is illustrated in Fig. 10, in which the fraction of carbon remaining (y) is plotted against the fraction of oxygen remaining (z) along the length of the kiln. If α is a constant characteristic of each zone, then the points in each zone will be on straight lines. This is clearly the case in Fig. 10. Furthermore, for the operation modes in use at that time, the value for α for each zone varied little from kiln to kiln. Consequently, the value of α for each zone could be taken as a constant parameter characteristic of each zone, and its value could be determined from full-scale kiln data. Although this procedure left much to be desired, it made the search for an explicit solution much more likely to succeed.

A third problem was that of fast coke. This coke also exhibited first-order intrinsic burning, but with a rate constant 17 times that of slow coke at 950°F (783 K). Again a fortunate simplification was found so that the kiln equations would not have to be solved for two kinds of coke burning

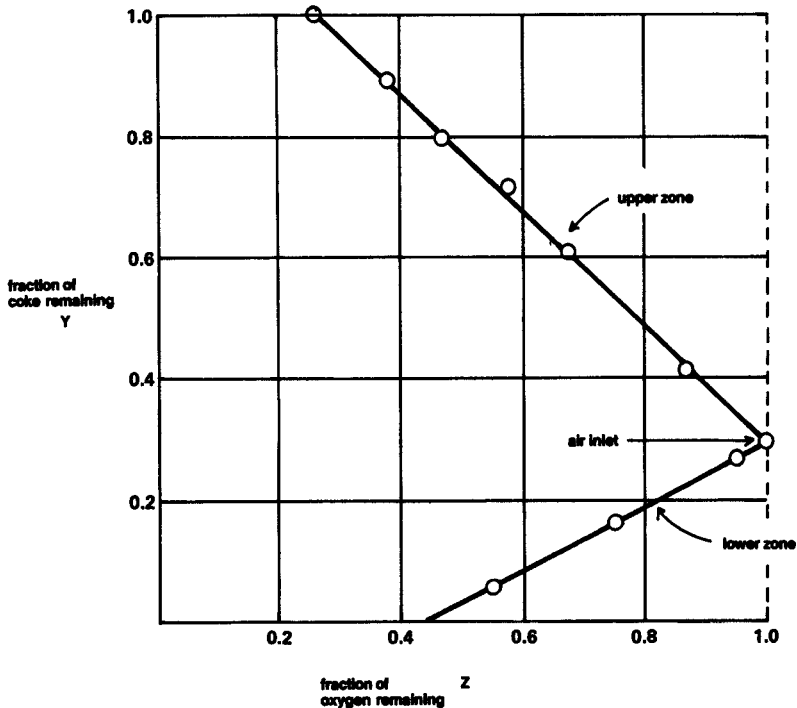


FIG. 10. Mass balance y versus z graph for kiln operating with conventional green silica-alumina catalyst.

simultaneously. With the design and mode of operation current at that time, essentially all of the fast coke had been burned at a point 1 or 2 ft (0.3 or 0.6 m) from the top of the upper zone. Thus, if the temperature and coke concentration at this point were taken as the initial values, the remainder of the kiln would be burning only slow coke according to Eqs. (3), (11), and (12).

Next we developed the one-dimensional kiln equations by assuming (1) piston flow for the solid and the gases, (2) negligible heat loss through the kiln walls, and (3) solid temperatures equal to gas temperatures over a horizontal section. These assumptions are justified since there is an intricate network of catalyst and air distributors to ensure uniform flow. The reactor diameter and height are several thousand times larger than the catalyst diameter, the kiln surface to volume ratio is quite small, and the solid heat capacity in the kiln is many hundred times greater than the gas heat capacity. The kiln equations were developed by the mass and heat balances in a differential section of the kiln, which related the temperature (T), the fraction of oxygen remaining (z), the fraction of coke remaining (y), in terms of the kiln vertical position (x). It was possible to simplify these equations by relating T and z in terms of y .

For each differential value, the carbon disappearance must equal α times the oxygen consumed. The molar carbon disappearance rate is given by $(W'_c F_c / M_c) dy$, where W'_c is the weight fraction of carbon on the catalyst as it enters the kiln, F_c is the flow of catalyst into the volume element, and M_c is the molecular weight of carbon. The molar oxygen consumption rate is given by $(F_a K_o) dz$, where F_a is the flow of air into the volume element, and K_o is the mole fraction of oxygen in air—normally 0.21:

$$\alpha F_a K_o dz = (W'_c F_c / M_c) dy \quad (13)$$

Integration of Eq. (13) from the inlet for constant α gives

$$y - y_i = \frac{\alpha K_o F_a M_c}{W'_c F_c} (z - z_i) = Y(z - z_i) \quad (14)$$

$$y = y_i - Yz_i + Yz = A + Yz$$

where y_i and z_i are inlet conditions and

$$Y = \alpha K_o F_a M_c / W'_c F_c, \quad A = y_i - Yz_i$$

Equation (14) is the equation for the straight lines in Fig. 10 used to demonstrate the approximate constancy of α over each zone of the kiln.

Similar consideration of the heat balance shows that

$$F_c W'_c \Delta H dy = -(F_c C_{pc} + F_a C_{pa} M_a) dT, \quad dT = -P dy \quad (15)$$

where C_{pc} and C_{pa} are the specific heats of catalyst and air, respectively, and M_a is the molecular weight of air. ΔH is the heat of combustion of coke to CO and CO₂. Integration of Eq. (15) for α constant gives

$$T = T_i + (y_i - y)P \quad (16)$$

where T_i and y_i are inlet conditions and

$$P = \frac{F_c W_c' \Delta H}{F_c C_{pc} + F_a M_a C_{pa}}$$

The velocity of flow of catalyst along the kiln is used to transform the time variable into a distance variable. The catalyst linear velocity is given by

$$dx/dt = -F_c/\sigma\rho_b \quad (17)$$

where σ is the cross-sectional area of the kiln and ρ_b is the bulk density of the catalyst (weight of catalyst per volume of kiln).

Combining Eqs. (3), (11), (12), (14), and (17) and forming the integral, we have

$$\begin{aligned} \int_{x_i}^x dx = \Psi \int_{y_i}^y \left\{ \exp\left(-\frac{Q}{RT}\right) [A - y]y \right\}^{-1} dy \\ - \Theta \int_{y_i}^y [(A - y)y^{1/3}]^{-1} [1 - y^{1/3}] dy \end{aligned} \quad (18)$$

where Ψ and Θ are given by,

$$\Psi = F_c Y / \sigma \rho_b b C'_{ox} \quad (19)$$

$$\Theta = -F_c a^2 C_c Y / \sigma \rho_b 3 D C'_{ox} \alpha \quad (20)$$

The two integrals on the right side of Eq. (15) will be treated separately. Consider the first integral on the right. Substitute the value of T in terms of y given by Eq. (16) and set $w = Q/RT$, $\mu = (RT_i/Q) = 1/w_i$, $\tau = RP/Q$, $\xi = 1/(A - y_i)\tau - \mu$, and $\zeta = -1/(y_i\tau + \mu)$; then the first integral on the right side of Eq. (16) becomes

$$\int_{y_i}^y \frac{dy}{e^{-Q/RT}(A - y)y} = - \int_{w_i}^w \frac{\tau \zeta \xi e^w dw}{(w + \xi)(w + \zeta)} \quad (21)$$

The right side of Eq. (21) can be decomposed by partial fraction and integrated to give

$$\int_{y_i}^y \frac{dy}{e^{-Q/RT}(A - y)y} = - \frac{1}{A} \left[\int_{w_i}^w \frac{e^w dw}{w + \xi} - \int_{w_i}^w \frac{e^w dw}{w + \zeta} \right] \quad (22)$$

$$= -\frac{1}{A} \left[e^{-\xi} \text{Ei}(w + \xi) - e^{-\zeta} \text{Ei}(w + \zeta) \right]_{w_i}^w \quad (23)$$

where $\text{Ei}(x)$ is the exponential integral defined by

$$\text{Ei}(x) = \int_{-\infty}^x \frac{e^t}{t} dt$$

The second integral on the right side of Eq. (18) gives

$$\begin{aligned} \int_{y_i}^y \frac{1 - y^{1/3}}{(A - y)y^{1/3}} dy = & -1/\delta[(1 - \delta) \ln(\delta - r_1) - (\delta + \frac{1}{2}) \ln(\delta^2 + \delta r_1 + r_1^2) \\ & + \sqrt{3} \tan^{-1}[(2r_1 + \delta)/\sqrt{3}\delta]]_{r_{1i}}^{r_1} \end{aligned} \quad (24)$$

where $r_1 = y^{1/3}$ and $\delta = A^{1/3}$. Hence,

$$\begin{aligned} x - x_i = & -\frac{\Psi}{A} [e^{-\xi} \text{Ei}(w + \xi) - e^{-\zeta} \text{Ei}(w + \zeta)]_{w_i}^w \\ & + (\Theta/\delta)[(1 - \delta) \ln(\delta - r_1) - (\delta + \frac{1}{2}) \ln(\delta^2 + \delta r_1 + r_1^2) \\ & + \sqrt{3} \tan^{-1}[(2r_1 + \delta)/\sqrt{3}\delta]]_{r_{1i}}^{r_1} \end{aligned} \quad (25)$$

There are 21 parameters in Eq. (25) (Table I). These provide the five dimensionless groups given in Table II. A 10-dimensional process variation space is needed to characterize the slow coke performance of the two-zone air lift TCC kilns, even when α is constant for each zone. It is not surprising that engineers and operators had problems in understanding the responses observed in the kiln.

Equation (25) expresses x as a function of w and r_1 , which in turn are functions of y . The parameter $A = y_i - Y_{z_i}$ contributes to ξ , δ , Ψ , and Θ . In the case of a concurrent zone, we have an initial-value integration; A is given by the boundary conditions at the top of the zone and is known. Thus, for a given y , the corresponding x can be calculated.

In the case of a countercurrent zone, we have a split boundary integration; $A = y_i - Y_{z_i}$ is given by the boundary conditions at the bottom of the zone and is unknown. However, if the upper limits of integration in Eq. (25) are made x_i , w_i , and r_{1i} , the left side of Eq. (25) becomes the length of the zone, L_i , and the right side becomes a function of y_i and can be solved for y_i by iteration. After y_i has been found, A can be calculated and then ξ , δ , Ψ , and Θ .

Equation (25) cannot be solved for x with an arbitrary value of y . First of all, y must be less than y_i , the inlet coke level into the zone. In addition, z must be positive at all times because burning ceases when there is no oxygen left. This means that a concurrent zone, $y > (y_i - Y)$ and, for a

TABLE I

PARAMETERS THAT DETERMINE THE PERFORMANCE OF THE MAIN SECTION OF THE KILN

*A. Fundamental Parameters**Burning*

Q	Activation energy	α	Moles carbon burned per mole oxygen consumed
R	Gas constant		
b	Frequency factor	ΔH	Heat of combustion

Catalyst

D	Catalyst diffusivity	ρ_b	Bulk density
a	Bead radius	ρ_t	Particle density
C_{pc}	Specific heat		

Air

C'_{ox}	Inlet concentration of oxygen	C_{pa}	Specific heat
-----------	-------------------------------	----------	---------------

*B. Kiln Parameters**Flow*

F_{ai}	Flow of air into the i th zone; negative for upflow, positive for downflow
F_c	Flow of catalyst
P_a	Pressure

Structural

σ	Cross-sectional area	L	Length of kiln
l	Air inlet location		

Boundary

T_i	Catalyst temperature at top of a zone
T_a	Temperature of air at air inlet
W'_c	Weight fraction of coke on catalyst

countercurrent zone, $y > (y_i + Y)$. Also according to Eq. (1), the intrinsic burning rate is first order with respect to both coke and oxygen, and x approaches infinity when $y = y_i - Y$ in the concurrent zone and $y = y_i + Y$ in the countercurrent zone, or when $y = 0$. In order to avoid obtaining a kiln of infinite length for all operating conditions, we consider a catalyst to be regenerated when y reaches some small value, say $y = 0.001$, instead of allowing it to go to $y = 0$.

B. TEST AND USE OF THE EXPLICIT SOLUTION

Since no suitable computer was then available, the first computations with the explicit solution were made "by hand," using mathematical

TABLE II
DIMENSIONLESS GROUPS

Group ^a	Related to:
$(RT_i)/Q = \mu$	The inlet intrinsic burning rate of end zone
$(R/Q)P = \tau$	Increase of burning rate in relation to coke consumption
$\left(\frac{\alpha F_a}{F_c}\right) \left(\frac{M_c C'_{ox}}{W'_c}\right) = Y$	Oxygen utilization
$\left(\frac{\alpha F_a}{\tau}\right) \left(\frac{C'_{ox} M_c}{W'_c}\right) \left(\frac{1}{b \rho_b}\right) = \frac{\Psi}{l}$	Dimensionless factor for intrinsic burning
$\frac{F_a}{l} \frac{a^2}{3D} \frac{\rho_t}{\rho_b} = \frac{\Theta}{l}$	A factor for diffusion burning

^a l is the location of the air inlet.

tables for the various functions prepared by the WPA during the 1930s depression. Not too long after the solutions were obtained, a Datatron computer became available and the explicit solution was programmed for computation on this computer.

Parameters in the model are listed in Table I. The flow, structural, and boundary conditions are known quantities. The frequency factor and activation energy for coke burning were the values determined by Weisz and Goodwin (1966) from the experiments discussed earlier, and the catalyst diffusivity D was measured directly in the laboratory. The value of α was determined from direct observations of the CO/CO₂ ratio in each zone of the operating kiln. The remaining parameters are known quantities. Thus, there are no adjustable parameters available to tune the fitting of predicted values to observed data, for the fraction of coke remaining and for the vertical temperature versus distance from the top of the kiln.

Figures 11–13 show three typical comparisons of commercial data (points) and computed (curves) fraction of coke remaining versus distance from the top of the kiln. The location of the air inlet is given by the arrow. The agreement is quite good for Figs. 11 and 12. The deviations in Fig. 13 are typical of the poorer agreements. These deviations arose from one of three causes: (1) changes in the kiln operating conditions during the several hours required to complete the sampling operations; (2) a spiraling flow of the catalyst in the donut-shaped kiln coupled with a nonuniform distribution of the initial values of the coke at the inlet of the kiln, which

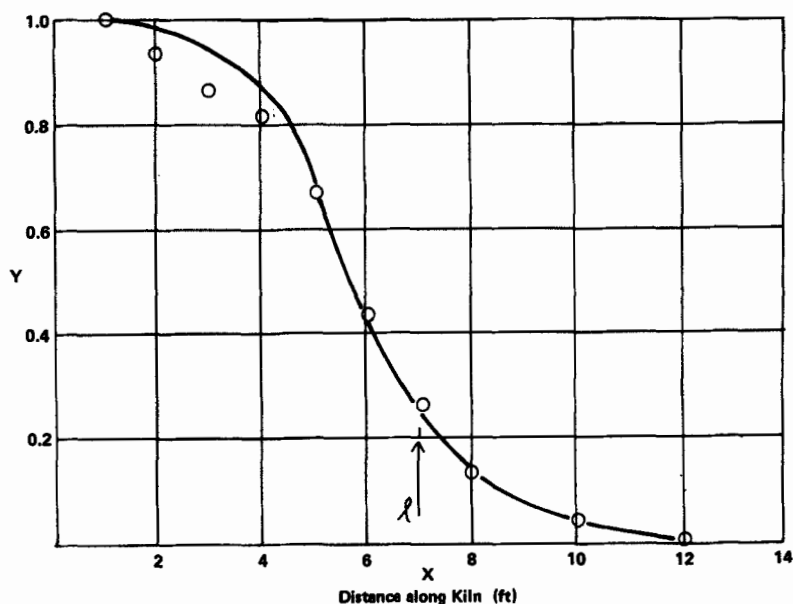


FIG. 11. Simulation of y versus x for the Beaumont T-2 kiln operating with conventional green silica-alumina catalyst. Computed results are given by the solid curve. The observed values, obtained from a vertical traverse, are given by the points. The operating conditions were as follows: flow of air up—23,500 scfm (665 scmm); flow of air down—13,600 scfm (385 scmm); air temperature at inlet—120°F (49°C); O_2 in air to kiln—21%; catalyst circulation rate—348 tons/hr (3.16×10^5 kg/hr); catalyst inlet temperature (1-ft level)—900°F (482°C); coke on catalyst (1-ft level)—1.5%.

caused samples with different boundary conditions to be obtained at various points on the vertical traverse; (3) poor data caused by the difficulties in operating the probes used in obtaining the samples. The temperature simulation was also good, as shown by the example in Table III.

C. USE OF THE EXPLICIT SOLUTION TO EXPLORE KILN PERFORMANCE

One good method of exploring the effects of variables on kiln performance is to prepare performance maps of appropriate subspaces of the kiln performance space. The most widely used map for this application was a graph of catalyst circulation rate versus carbon burned. Temperature and burn-off constraint curves were used to define the operating region given as shaded areas in Fig. 14. The conditions for the kiln used in Fig. 14 are given in Table IV.

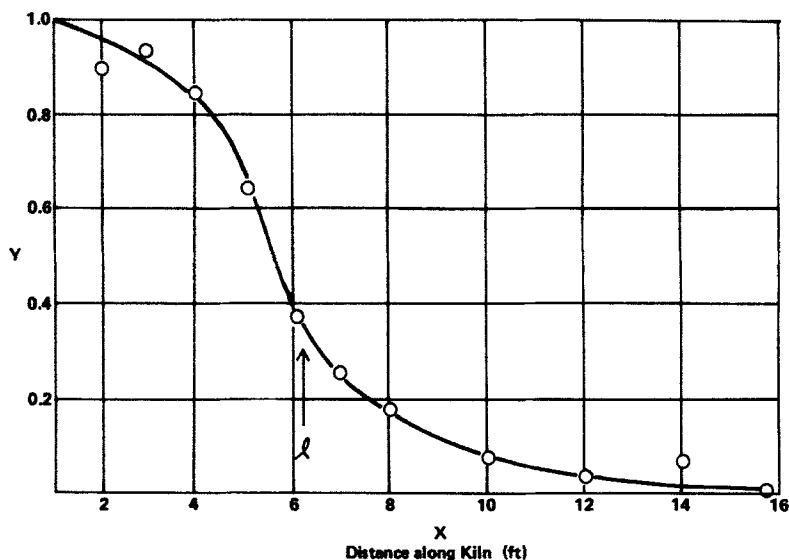


FIG. 12. Simulation of y versus x for the Beaumont T-3 kiln operating with conventional green silica-alumina catalyst. Computed results are given by the solid curve. The observed values, obtained from a vertical traverse, are given by the points. The operating conditions were as follows: flow of air up—20,700 scfm (586 scmm); flow of air down—14,900 scfm (422 scmm); air temperature at inlet—100°F (38°C); O₂ in air to kiln—21%; catalyst circulation rate—373 tons/hr (3.49×10^5 kg/hr); catalyst inlet temperature (1-ft level)—915°F (451°C); coke on catalyst (1-ft level)—1.2%.

TABLE III

A COMPARISON OF COMPUTED AND OBSERVED TEMPERATURES IN TOP ZONE OF BEAUMONT T-2 TRAVERSE OF 7/31/53

x		y	Calculated temperature		Observed temperature	
ft	in.		°F	°K	°F	°K
2	0.6096	0.95	939	777	940	777.4
3	0.9144	0.875	993	807	980	800
4	1.2192	0.83	1028	826	1030	827
5	1.529	0.675	1144	891	1125	880

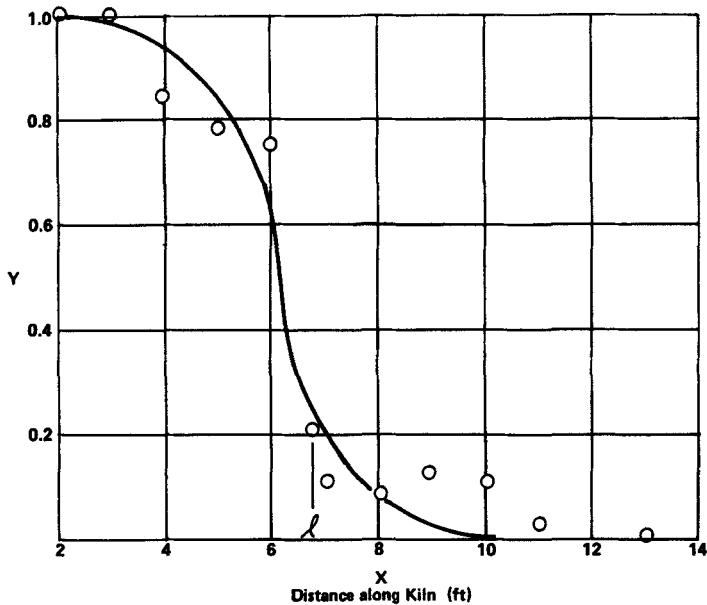


FIG. 13. Simulation of y versus x for the Buffalo kiln operating with Durabead 5. Computed results are given by the solid curve. The observed values, obtained from a vertical traverse, are given by the points. The operating conditions were as follows: flow of air up—25,500 scfm (722 scmm); flow of air down—11,500 scfm (326 scmm); air temperature at inlet—760°F (405°C); O_2 in air to kiln—18%; catalyst circulation rate—495 tons/hr (4.5×10^5 kg/hr); catalyst inlet temperature (1-ft level)—960°F (516°C); coke on catalyst (1-ft level)—1.4%.

TABLE IV

KILN OPERATING CONDITIONS USED IN FIG. 14

Flow of air up	25,000 scfm (670 n.m ³ /min)
Flow of air down	12,000 scfm (322 n.m ³ /min)
Air temperature at inlet	100°F (311 K)
Oxygen in air to kiln	21%
α (upper zone)	1.33
α (lower zone)	1.08
Location of air inlet	6.75 ft (2.057 m)
Reactor outlet temperature	920°F (766 K)
Cross-sectional area	463 ft ² (4.301 m ²)
Length of bed to cooling coils	20.5 ft (6.25 m)
Diffusivity of H_2 , temp. = 100°F	30×10^{-3} cm ² /sec

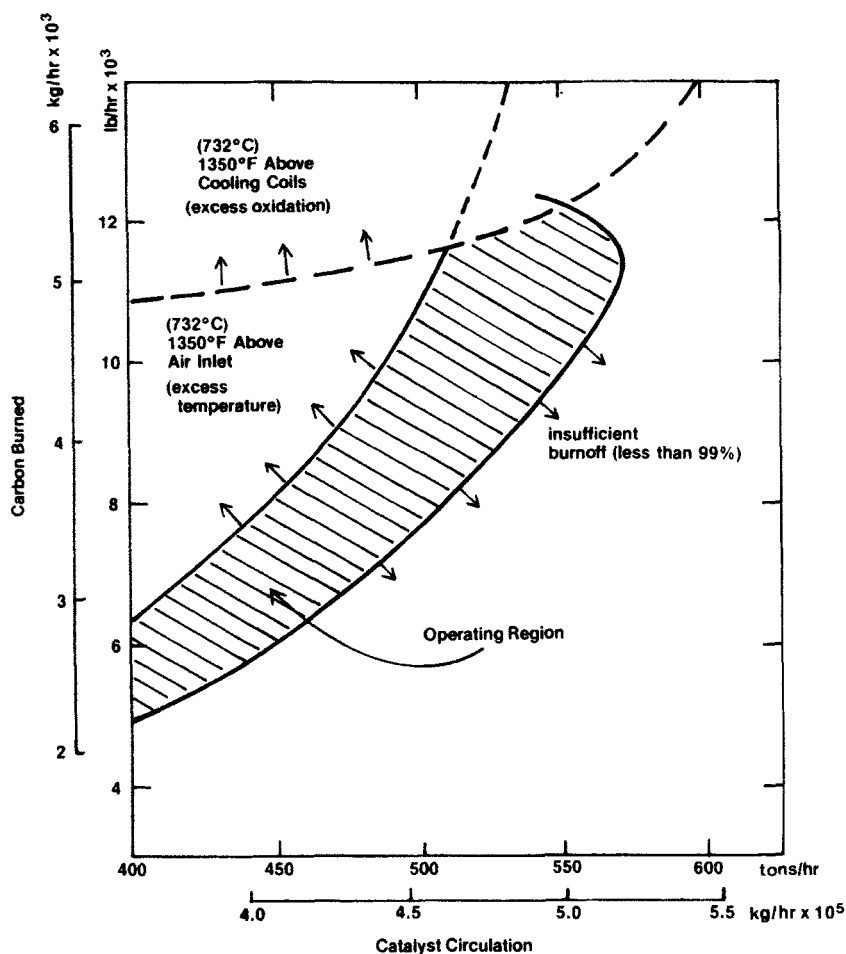


FIG. 14. Performance graph for the reference conditions given in Table IV.

The way in which the operating regions are shifted as other variables are changed is a convenient way to examine kiln performance. Figures 15 and 16 show the effect of changes in catalyst diffusivity and changes in the location of the air inlet, respectively, on the location of the operating regions for the kiln parameters given in Fig. 14. The catalyst diffusivity has considerable effect on kiln performance; the higher diffusivity catalyst allows the unit to be operated at a higher catalyst circulation rate. When the kilns were originally designed, the air inlets were placed be-

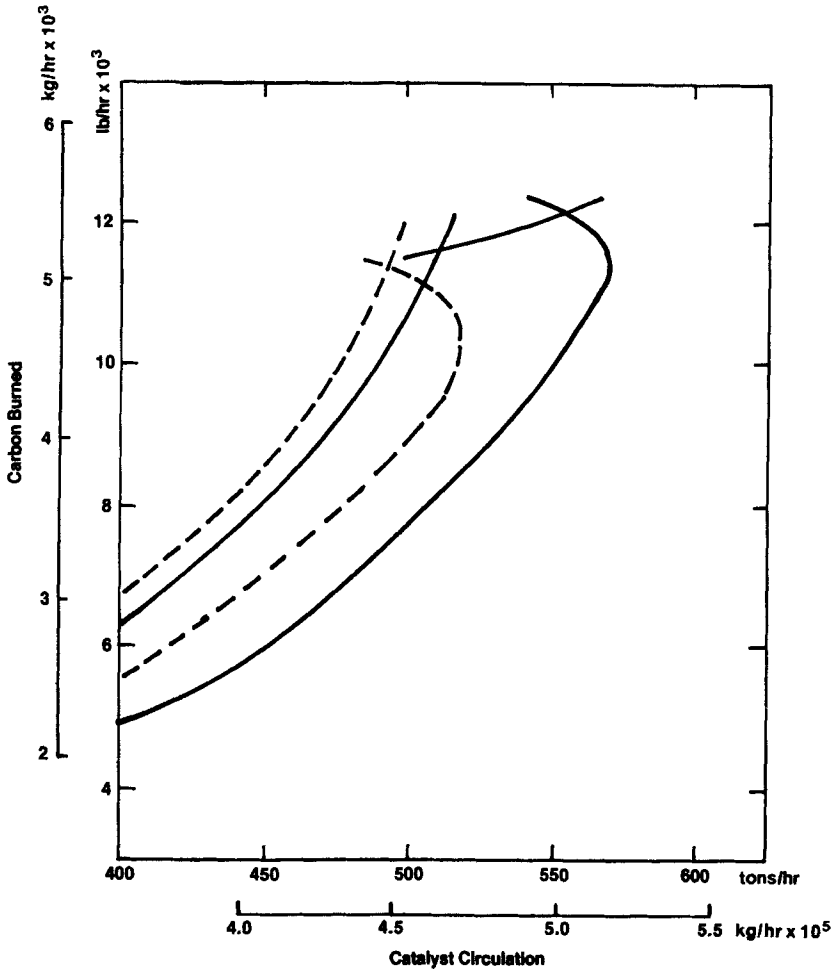


FIG. 15. A comparison of the operating region for catalysts with diffusivities D_{H_2} of 1.08×10^{-5} (---) and 3.23×10^{-5} (—) ft^2/sec (10^{-6} and $3 \times 10^{-6} \text{ m}^2/\text{sec}$). The other conditions are given in Table IV.

tween 6 and 7 ft down the kiln. Figure 16 shows that this location is not optimal for all operations. If 600 tons ($5.45 \times 10^5 \text{ kg}$) of catalyst is to be circulated per hour, the location should be at 10 ft (3 m). This procedure was used to successfully relocate the air inlet in some commercial kilns.

The original kinetic studies were neglected, but the explicit solution was accepted and found considerable use in practical kiln problems.

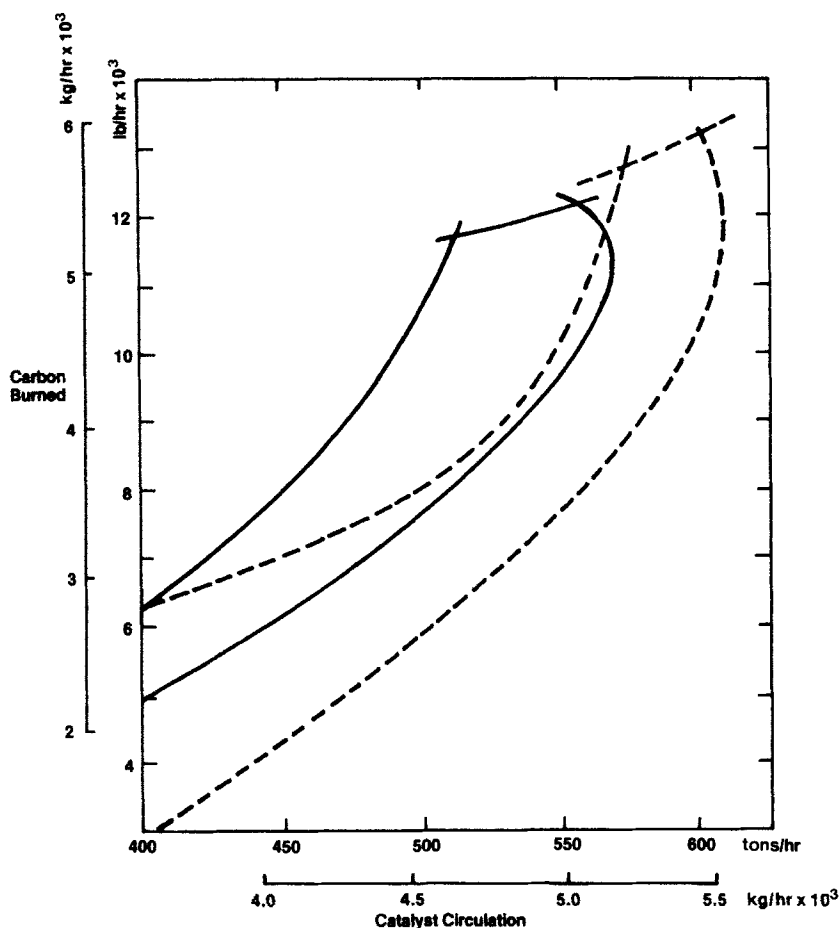


FIG. 16. A comparison of the operating regions for air inlet locations at 6.75 (—) and 10 (---) ft (2.05 and 3.05 m). The other conditions are given in Table IV.

IV. Extension of the Model for Fast and Slow Coke

A. THE EFFECT OF THE INITIAL TEMPERATURE T_i ON RESIDUAL CARBON

The explicit model can be used to determine the behavior of the TCC kiln when the initial temperature T_i is varied. A good index of the kiln performance is the distance down the kiln at which 99% of the carbon has been removed. This distance X_b is an important indicator of the extent to

which the catalyst has been regenerated when it leaves the kiln. A graph of X_b versus T_i for the kiln used for the simulation in Fig. 13 is shown in Fig. 17. The distance X_b is a strong function of T_i and the kiln performance should show a large sensitivity to T_i . This temperature T_i , which is the temperature of the catalyst after the fast coke has been burned off, is not generally known. The measured parameter on the TCC unit is the reactor outlet temperature T_R , where the coke contains both fast and slow coke. In the commercial kiln, X_b does not show a great sensitivity to T_R . As the reactor outlet temperature decreases, the amount of fast coke on the catalyst increases. On entering the kiln, the catalyst encounters a special region called the plume burner with an auxiliary air supply designed to burn as much of the fast coke as possible before the catalyst enters the kiln proper. Hence, the temperature rise due to the combustion of fast coke in the plume burner and in the upper parts of the kiln will increase the catalyst temperature. A lower reactor outlet temperature usually means a higher amount of desorbable fast coke and a higher temperature rise in the plume burner.

It was found that for a large spectrum of commercial operations, the kiln behaved as if T_i was approximately 920°F (494°C) regardless of reactor outlet temperature. This observation allowed the explicit model to be extensively used to explore the effects of some of the variables such as catalyst diffusivity and air inlet location on kiln performance. However, the absence of fast coke in the model limited its usefulness, here leading us to develop a model which included the plume burner and fast coke. This next stage of advance was not possible without numerical integration.

B. THE INCLUSION OF FAST COKE IN THE MODEL

As with slow coke, the fast coke was shown to burn at a rate that is first order in coke and approximately first order in oxygen. However, the activation energy is approximately half that of the slow coke and the frequency factor is $1.0 \times 10^3 \text{ sec}^{-1}$ in contrast to $3.7 \times 10^7 \text{ sec}^{-1}$ for slow coke. At 950°F (783 K), the fast coke burns 17 times as fast as the slow coke.

A major part of the fast coke is probably desorbed from the catalyst bed and burned in the gas phase. Even if none of the fast coke was desorbed, a calculation of the Thiele modulus η for conditions in the plume burner and the top of the first zone of the kiln shows that η is in the range 0.92–0.99. Thus, the fast coke can be assumed to burn without significant diffusion limitation.

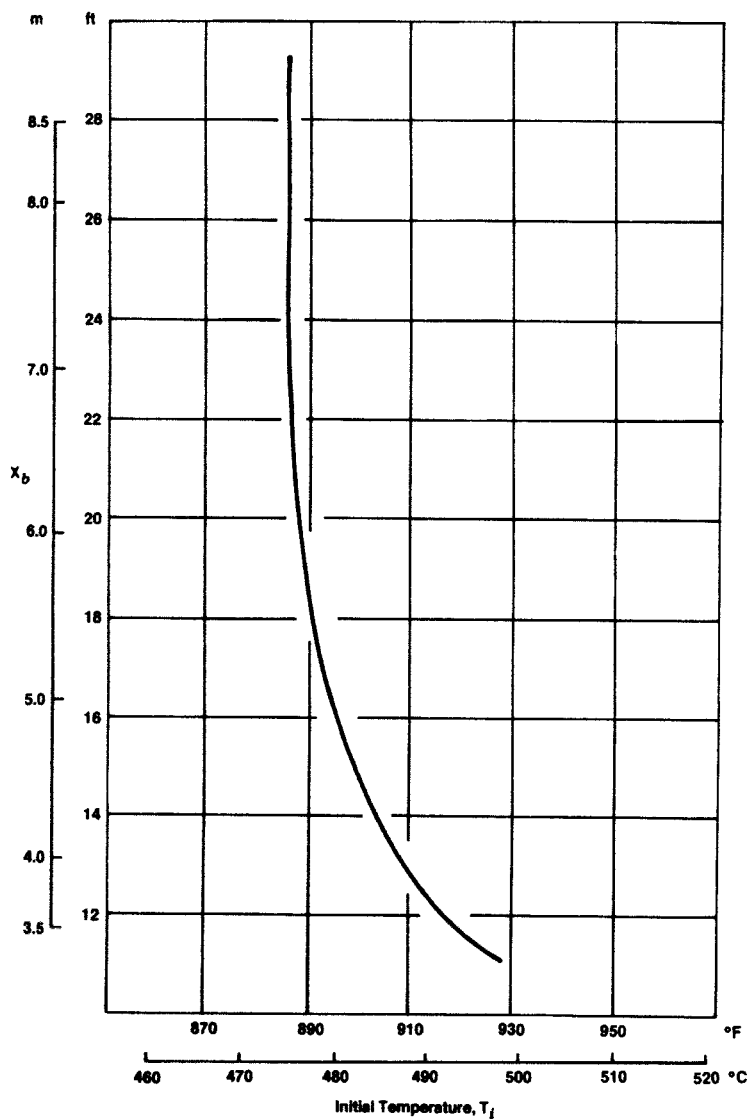


FIG. 17. The effect of catalyst inlet temperature T on the 90% burn-off distance X_b for the kiln simulated in Fig. 13.

In treating the simultaneous burning of both fast and slow coke, it is convenient for computation purposes to reformulate the slow-coke kinetics in terms of a new effectiveness factor η_T . The total rate of slow coke burning $(dy_s/dt)_T$ of Eq. (12) is set equal to $\eta_T(dy_s/dt)_I$:

$$(dy_s/dt)_T = \eta_T(dy_s/dt)_I \quad (26)$$

Using Eq. (26) in Eq. (12),

$$\{\eta_T b_s y_s z C'_{ox} [\exp(-Q_s/RT)]\}^{-1} = \{b_s y_s z C'_{ox} [\exp(-Q_s/RT)]\}^{-1} + \frac{a^2 C_c^0 (1 - y_s^{1/3})}{3 D \alpha_s z C'_{ox} y_s^{1/3}} \quad (27)$$

Solving Eq. (27) for η_T ,

$$\eta_T = \frac{3 D \alpha_s}{3 D \alpha_s + a^2 b_s C_c^0 (y_s^{2/3} - y_s) [\exp(-Q_s/RT)]} \quad (28)$$

Making the transformation from time to distance along the kiln by use of Eq. (17) gives

$$\frac{dy_s}{dx} = - \frac{\sigma \rho_b}{F_c} \eta_T b_s C'_{ox} z y_s \left[\exp\left(-\frac{Q_s}{RT}\right) \right] \quad (29)$$

for the fraction of slow coke remaining, y_s . Equation (29) is equivalent to the differential form of the integral Eq. (18). For the fraction of fast coke remaining, y_f

$$\frac{dy_f}{dx} = - \frac{\sigma \rho_b}{F_c} b_f C'_{ox} z y_f \left[\exp\left(-\frac{Q_f}{RT}\right) \right] \quad (30)$$

The coupling between Eqs. (29) and (30) is with the temperature T and oxygen z . The equation for the rate of change of temperature as a function of the distance down the kiln is given by

$$\frac{dT}{dx} = \frac{F_c}{F_c C_{pc} + F_a C_{pa} M_a} \left(W'_{cf} \Delta H_f \frac{dy_f}{dx} + W'_{cs} \Delta H_s \frac{dy_s}{dx} \right) \quad (31)$$

The heat of combustion of fast coke, ΔH_f , takes into account both CO and CO₂ formation as well as the combustion of the hydrogen in the coke. The heat of combustion of the slow coke is given by

$$\Delta H_s = [\alpha_s \Delta H_{CO_2} + 2(1 - \alpha_s) \Delta H]/\alpha_s \quad (32)$$

where $\Delta H = (\Delta H_{CO_2} - \Delta H_{CO})$. Coke loses all of its hydrogen rapidly, and this hydrogen is included in the fast-coke burning. The equation for the rate of change of oxygen as a function of distance down the kiln is

given by

$$\frac{dz}{dx} = \frac{F_c}{F_a K_o M_c} \left(\frac{W'_{cf}}{\alpha_f} \frac{dy_f}{dx} + \frac{W'_{cs}}{\alpha_s} \frac{dy_s}{dx} \right) \quad (33)$$

Computer solutions of the set of Eqs. (29)–(31) and (33) were obtained with α and ΔH_f typical of those measurements on operating kilns, since the kinetics of the conversion of CO to CO₂ had not been included into the model at this time. A low catalyst inlet temperature is used to show more clearly the effect of fast coke on kiln performance. Figure 18 shows the coke versus distance along the kiln for the fast and slow coke in the plume

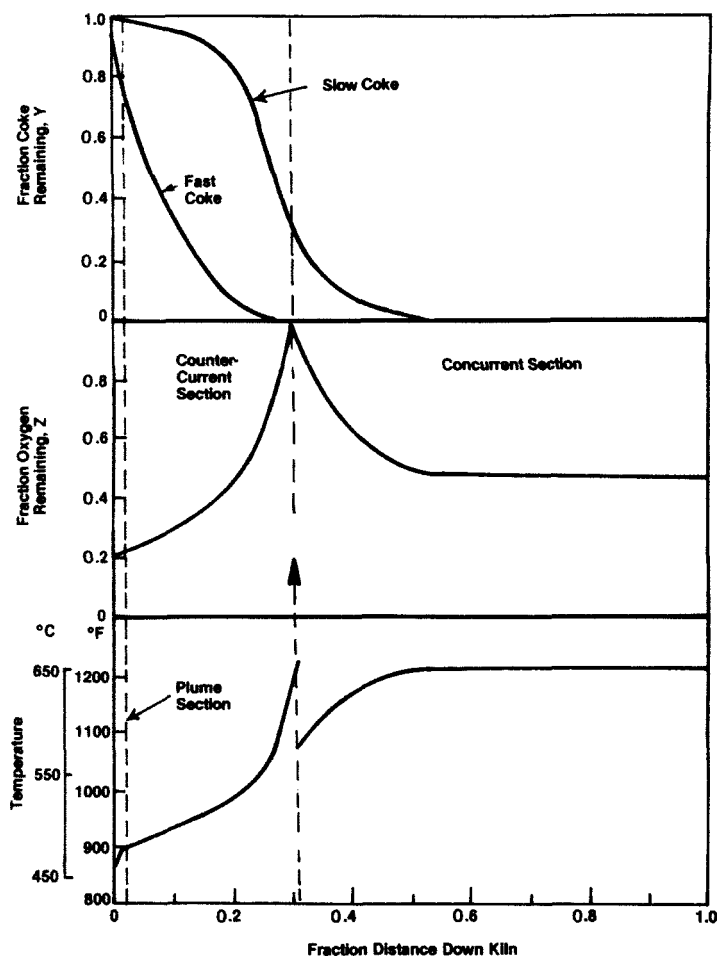


FIG. 18. Typical steady-state solution of the kiln model.

burner, the top and the bottom zones, for 1% slow coke and 0.1% fast coke. Almost no slow coke is burned in the plume burner, but 40% of the fast coke is burned.

Figure 19 shows the slow coke profiles for the top and bottom zones obtained when 0.0, 0.1, and 0.2% fast coke is present. When no fast coke is present, the catalyst does not burn clean ($\sim 0.2\%$ residue carbon at kiln exit). This is consistent with the rapid rise in burn-off distance at 875°F (469°C) seen in Fig. 17. However, the presence of 0.1% fast coke gives an essentially clean catalyst, using only 0.6 of the bottom zone. Only a quarter of the bottom zone is needed when 0.2% fast coke is present. This improvement in burn-off distance is caused by the temperature boost obtained from the rapidly burning fast coke. This temperature boost is shown by the temperature curves in Fig. 20b. The temperature of the catalyst at the top of the upper bed has increased from 875°F (741 K) to 900°F (755 K). This is sufficient to make a large improvement in burn-off distance as shown by Fig. 17.

An interesting effect occurs in the top zone of the kiln as shown in Fig. 20. In the first part of the top zone, the catalyst contains 0.2% fast coke and has a rate of burning less than the one containing 0.1% fast coke. Also the temperature boost obtained at the inlet to the top zone is less than that obtained from 0.1% fast coke. This change in response is caused by the change in oxygen concentration in the plume burner and at the top of the first zone as seen in Fig. 20a. The burning of the fast coke diminishes the oxygen concentration at the top of the first zone, thereby decreasing the rate of burning in this region. However, the subsequent temperature increase in the top zone more than compensates for this effect. The overall effect of fast coke is to accelerate the burning of the slow coke.

V. Dynamic Response Model

When operating conditions were changed, transient phenomena were sometimes observed that first move in one direction and in the reverse direction on going to the final steady state. To study these transients and to design an improved control strategy for the unit, a dynamic response model was needed. With the inclusion of the fast coke in the model, it became possible to extend the steady-state model to obtain useful dynamic response results by the addition of time-dependent accumulation terms (Weekman *et al.*, 1967).

The accumulation term for the coke (lb/hr) is given by

$$M_{c\sigma} \frac{\partial C_c}{\partial t} dx = \frac{F_c C_c^0 M_c}{\rho_b} \frac{\partial y}{\partial \theta} d\chi \quad (34)$$

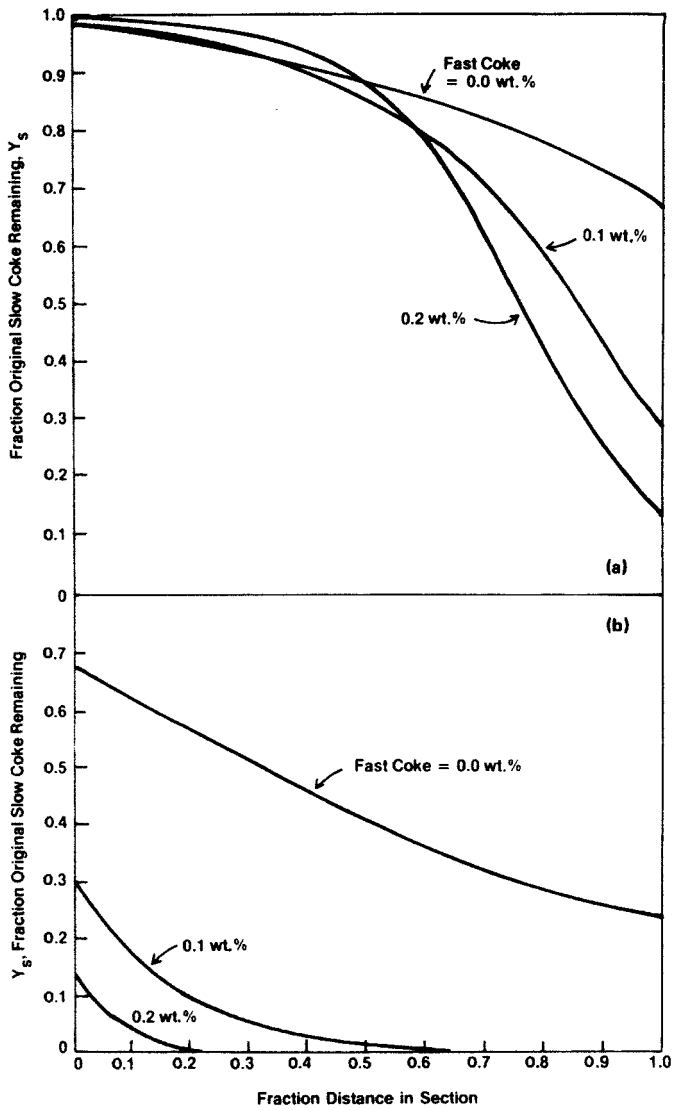


FIG. 19. Effect of fast coke on slow coke burning. All cases 1.0 wt. % original slow coke. Slow coke profiles are given for the top (a) and bottom (b) sections.

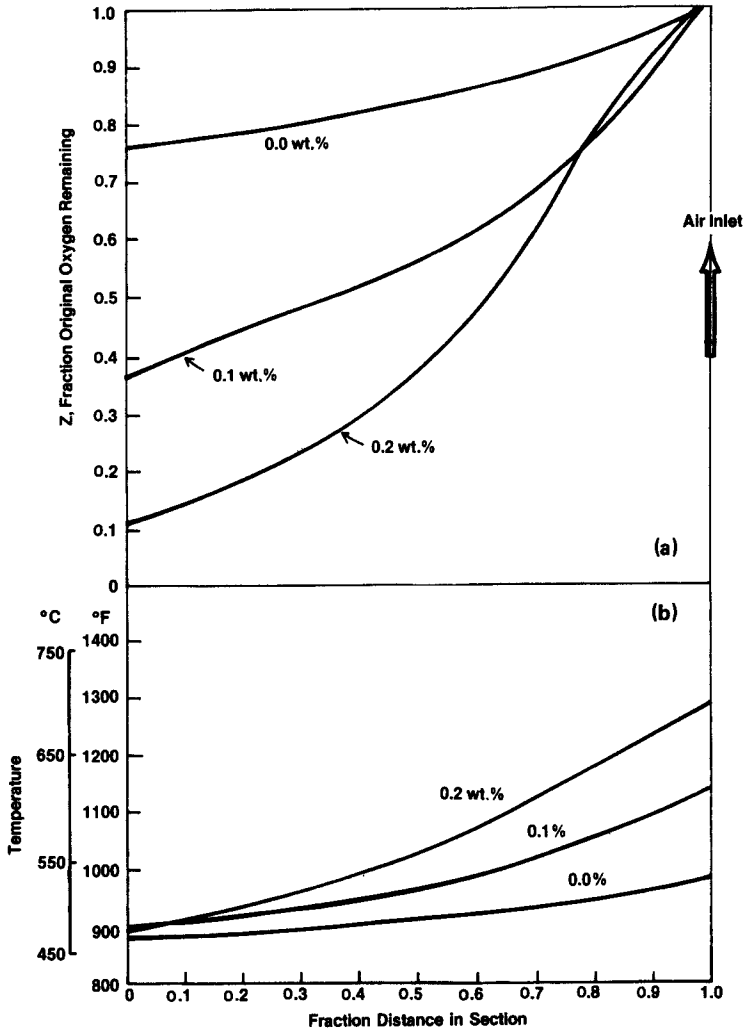


FIG. 20. Effect of fast coke on slow coke burning (1% slow coke). The profiles shown are for the top section: (a) oxygen profile; (b) temperature profile.

where θ is a normalized time relative to each kiln zone and χ is a normalized distance relative to each kiln zone:

$$\theta = (F_c / \sigma L_i \rho_b) t \quad (35)$$

$$\chi = x / L_i \quad (36)$$

where L_i is the length of the i th zone.

The flow differential for the element dx of the kiln is given by

$$\frac{F_c M_c}{\rho_b} \frac{\partial C_c}{\partial x} dx = \frac{F_c M_c C_c^0}{\rho_b} \frac{\partial y}{\partial \chi} d\chi \quad (37)$$

and the reaction term is given by

$$b \eta C_c^0 C'_{ox} z M_c V_i [\exp(-Q/RT)] d\chi \quad (38)$$

where V_i is the volume of the i th zone. Combining Eqs. (34), (37), and (38) for the fast coke, we get

$$\frac{\partial y_f}{\partial \theta} + \frac{\partial y_f}{\partial \chi} = \frac{V_i b_f \rho_b C'_{ox} y_f z}{F_c} \exp\left(-\frac{Q_f}{RT}\right) \quad (39)$$

since $\eta_f = 1$.

For the slow coke, combining Eqs. (34), (37), and (38) gives

$$\frac{\partial y_s}{\partial \theta} + \frac{\partial y_s}{\partial \chi} = \frac{\eta_s V_i b_s \rho_b C'_{ox} y_s z}{F_c} \exp\left(-\frac{Q_s}{RT}\right) \quad (40)$$

The accumulation term for the oxygen (lb/hr) is

$$\varepsilon \sigma M_{O_2} \frac{\partial C_{ox}}{\partial t} dx = \frac{\varepsilon F_c C'_{ox} M_{O_2}}{\rho_b} \frac{\partial z}{\partial \theta} d\chi \quad (41)$$

the flow term (lb/hr) is

$$F_a K_o M_{O_2} \frac{\partial z}{\partial \chi} d\chi \quad (42)$$

the reaction term is

$$\begin{aligned} & \frac{V_i b_f C_{cf} C'_{ox} M_{O_2} y_f z}{\alpha_f} \left[\exp\left(-\frac{Q_f}{RT}\right) \right] d\chi \\ & + \frac{\eta_s V_i b_s C_{cf} C'_{ox} M_{O_2} y_s z}{\alpha_s} \left[\exp\left(-\frac{Q_s}{RT}\right) \right] d\chi \end{aligned} \quad (43)$$

Combining Eqs. (41)–(43) gives

$$\begin{aligned} \frac{\varepsilon F_c C'_{ox}}{\rho_b F_a K_o} \frac{\partial z}{\partial \theta} + \frac{\partial z}{\partial \chi} &= \frac{V_i C'_{ox} z}{F_a K_o} \left[\frac{b_f C_{cf} y_f}{\alpha_f} \exp\left(-\frac{Q_f}{RT}\right) \right. \\ & \left. + \frac{\eta_s b_s C'_{cs} y_s}{\alpha_s} \exp\left(-\frac{Q_s}{RT}\right) \right] \end{aligned} \quad (44)$$

For the enthalpy, the accumulation flow and reaction terms are

$$\frac{F_c}{\rho_b} (\varepsilon \rho_a C_{pa} + \rho_b C_{pc}) \frac{\partial T}{\partial \theta} d\chi \quad (45)$$

$$(F_c C_{pc} + F_a M_a C_{pa}) \frac{\partial T}{\partial \chi} d\chi \quad (46)$$

$$b_f C'_{cf} C'_{ox} \Delta H_f M_{cf} y_f z V_i \exp(-Q_f/RT) d\chi \\ + b_s \eta_s C'_{cs} C'_{ox} \Delta H_s M_{cs} y_s z V_i \exp(-Q_s/RT) d\chi \quad (47)$$

Combining Eqs. (45)–(47), we get

$$\frac{F_c}{\rho_b} \left(\frac{\varepsilon \rho_a C_{pa} + \rho_b C_{pc}}{F_c C_{pc} + F_a M_a C_{pa}} \right) \frac{\partial T}{\partial \theta} + \frac{\partial T}{\partial \chi} \\ = \frac{C'_{ox} V_i z}{F_c C_{pc} + F_a M_a C_{pa}} \left[b_f C'_{cf} \Delta H_f M_{cf} y_f \exp\left(-\frac{Q_f}{RT}\right) \right. \\ \left. + b_s \eta_s C'_{cs} \Delta H_s M_{cs} y_s \exp\left(-\frac{Q_s}{RT}\right) \right] \quad (48)$$

To study the response of the kiln to transient conditions and to different control schemes, the set of partial differential equations (39), (40), (44), and (48) were solved using a hybrid analog–digital computer, the EAI Hydac 2000. A description of the computer and of the methods used in the solution are given in the paper by Weekman *et al.* (1967). The kiln conditions used in the simulation to be discussed are given in Table V. The dynamic model was first used to study the effect of fast coke on kiln stability.

The amount of fast coke was determined from a correlation based on observation of operating kilns. As the reactor outlet temperature changes, the amount of oil on the catalyst changes. For the usual purge conditions existing in the seal leg connecting the reactor to the kiln,

$$W_{cf} = 0.0176 - (1.92 \times 10^{-5}) T_R \quad (49)$$

where T_R is the reactor outlet temperature (°F).

As the reactor outlet temperature rises, the amount of fast coke falls. Thus, as the kiln receives more heat from the catalyst, it receives less fast coke. This leads to a self-regulatory effect that played an important role in kiln stability. This effect is seen by a comparison of Figs. 21 and 22.

Figure 21 shows the response of the temperature above the air inlets and above the cooling coils at the bottom of the bottom zone of the kiln, due to a step change in catalyst temperature T_r when no fast coke is present ($W_{cf} = 0$). Figure 22 shows that there is a large improvement in stability of the kiln temperature when fast coke [as per Eq. (49)] is present. An unexpected response to a temperature rise occurs when the fast coke is absent; the temperature above the cooling coils falls before it finally rises, and residual coke is present until ~60 min after the tempera-

TABLE V
DYNAMIC SIMULATION KILN CONDITIONS

b_f	$6.86 \times 10^{14} \text{ ft}^3/(\text{lb mole O}_2) (\text{hr})$
b_s	$6.39 \times 10^{10} \text{ ft}^3/(\text{lb mole O}_2)(\text{hr})$
C'_{ox}	$0.0001842 \text{ lb moles/ft}^3$
C_{pa}	$0.264 \text{ Btu}/(\text{lb})(^\circ\text{F})$
C_{pc}	$0.292 \text{ Btu}/(\text{lb})(^\circ\text{F})$
D	$25 \text{ cm}^2/\text{sec} (\text{H}_2\text{STP})$
$F_{a(\text{plume})}$	1900 scfm
$F_{a(\text{top})}$	$24,000 \text{ scfm}$
$F_{a(\text{bot})}$	$15,700 \text{ scfm}$
F_c	513 tons/hr
ΔH_f	$10,000 \text{ Btu/lb}$
ΔH_s	$14,087 + 10,135 (2 - 2/\alpha_s)$
M_{cf}	12
M_{cs}	16
Q_s	$37,500 \text{ cal}/(\text{gm-mole})$
Q_f	$16,500 \text{ cal}/(\text{gm-mole})$
a	0.0052 ft
$V_{i(\text{plume})}$	130 ft^3
$V_{i(\text{top})}$	3100 ft^3
$V_{i(\text{bot})}$	6900 ft^3
ρ_b	50 lb/ft^3
ρ_t	80 lb/ft^3
$\alpha_{(\text{top})}$	$1.31 \text{ lb moles coke burned/lb mole O}_2$
$\alpha_{(\text{bot})}$	$1.12 \text{ lb moles coke burned/lb mole O}_2$
ε	$.4$

ture is raised. This "wrong way behavior" is related to the difference in the speed of propagation of the concentration and temperature disturbances in the bed (Mehta *et al.*, 1981). The catalyst after this time is burned clean. The dynamic model was next used to determine the response of the kiln to certain disturbances.

The feedstock to the TCC reactor varies in its coke-forming properties. This is an important source of disturbance in the kiln operation. Figure 23 shows the effect of a 20% change in coke. The temperature above the air inlet responds with a damped oscillation of the temperature before reaching a steady state 40°F (22°C) above the previous steady state. The temperature at the bottom of the lower zone rises monotonically 75°F (42°C) to the new steady-state value. This rise in catalyst temperature will influence the performance of the reactor, since the catalyst is returned to the top of the reactor after some heat losses from cooling coils in the bottom of the kiln and in the air lift and the separator. The change of temperature

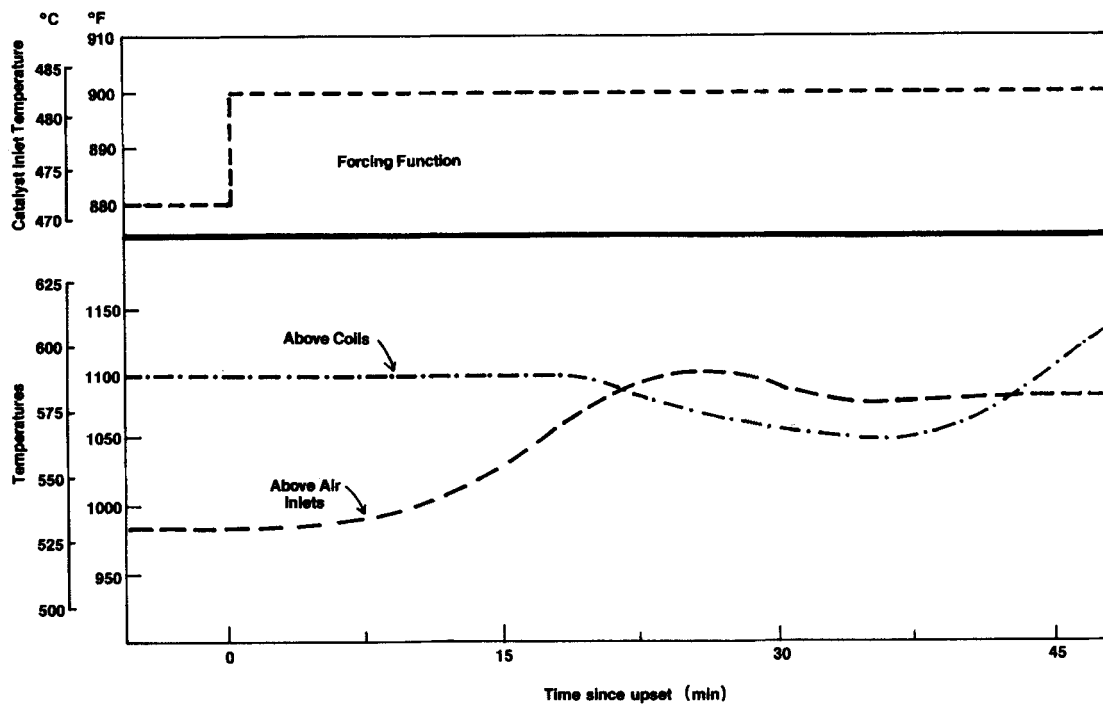


FIG. 21. Response to 20°F increase in temperature of catalyst when no fast coke is present ($K_z = 0$). Residual coke is present until ~60 min, by which time the coke is burned away.

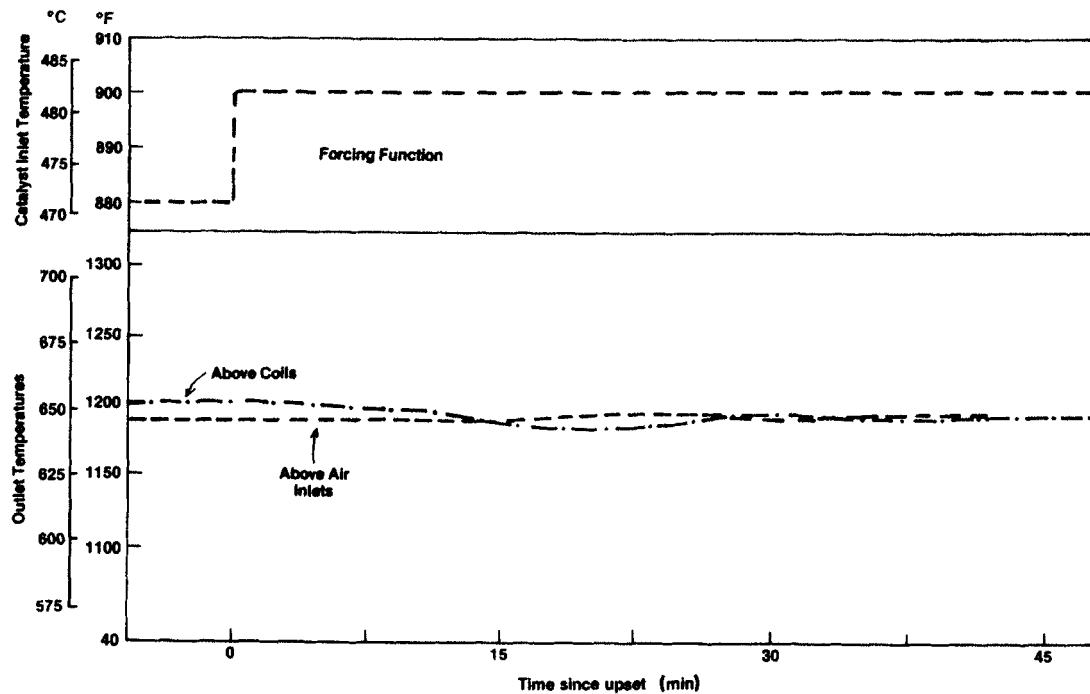


FIG. 22. Response to 20°F increase in catalyst temperature when fast coke is present in an amount given by Eq. (49).

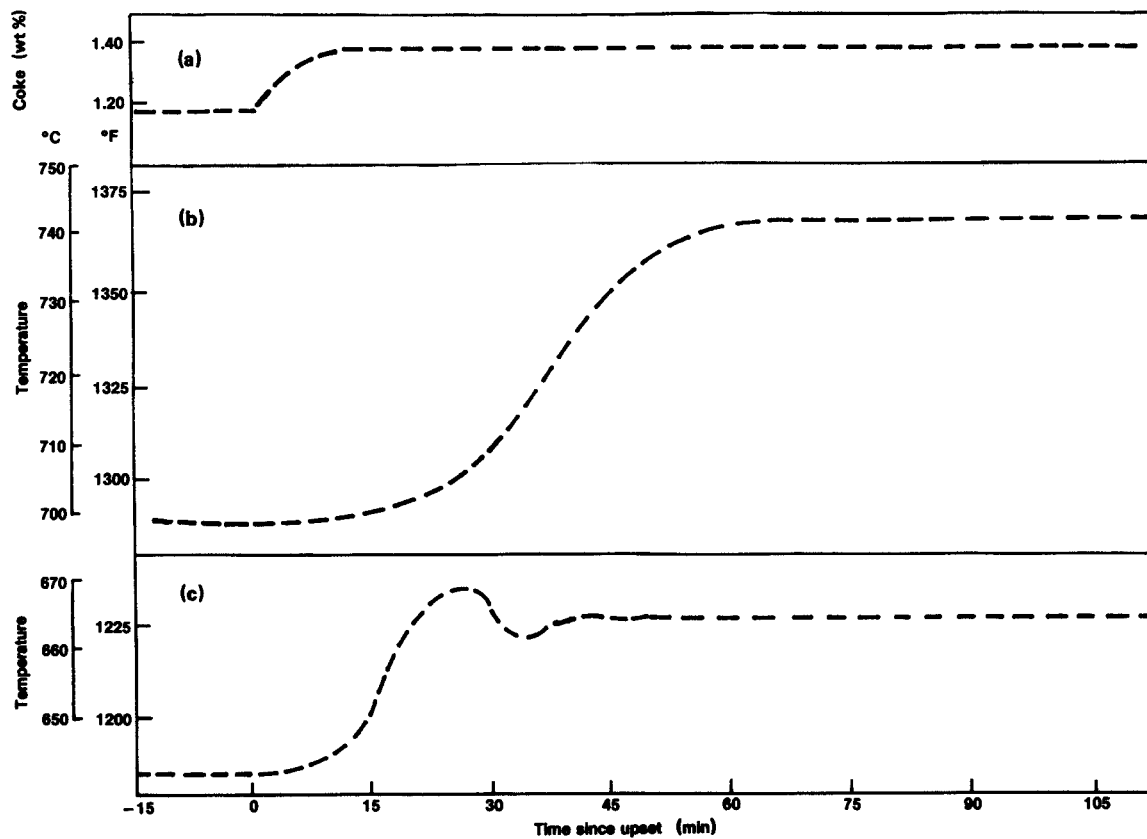


FIG. 23. Response of kiln to coke increase: (a) coke; (b) bottom of lower zone; (c) above air inlets.

of the catalyst inlet to the reactor will move the operation point of the reactor from its desired value, unless some action is taken to correct it.

Figure 24 compares the response of the catalyst above the steam cooling coils to a change in combustion air temperature with that predicted by the model. The combustion air temperature is controlled by varying the fuel gas which is injected and burned in the combustion air line by means of a line burner. Since the thermocouple employed above the coils was armored by a steel casing, it will exhibit a measurement lag. Calculations had shown that a 3-min lag was reasonable and this value gave a good match between the model prediction and the plant data.

The dynamic model was used to study and design closed-loop control systems for the kiln. Various ideas as to how to achieve effective control existed before the study began and new ideas were conceived during the study. Two systems based upon the control of combustion air temperature will illustrate this use of the model.

Since the time constant for the response of the exit kiln temperature to changes in coke level is long (see Fig. 23), a scheme was used in which the temperature above the air inlet was measured and fed to a simple linear model that predicted the kiln exit temperature from the temperature changes at the air inlet. Figure 23 shows that the temperature at the air inlet responded much more rapidly to the coke changes. The outlet temperature computed from the linear model is compared to the desired temperature and the combustion air temperature adjusted to compensate for differences. But the change in combustion air temperature is made by changing the fuel to the line burner, which changes the oxygen content of the combustion air. It would seem advisable to increase the flow rate of air to maintain the same amount of oxygen in the kiln. This adjustment was also computed and made by the control loop. The system that controlled both the combustion air temperature and maintained the amount of oxygen to the kiln constant is the closed-loop scheme (a) shown in Fig. 25.

Scheme (a) was compared to a system in which the combustion air temperature was adjusted, but the air flow rate maintained constant, thereby allowing the amount of oxygen to the kiln to vary. This system is closed-loop scheme (b) and is shown in Fig. 26.

The response of the kiln to a 20% increase in coke on the catalyst from the reactor is shown in Fig. 27 for no control and for schemes (a) and (b). The simpler scheme (b) is clearly superior to scheme (a) although steady-state considerations predicted that scheme (a) would be the better strategy. The fluctuations in the total air rate of scheme (a) that maintains a constant amount of oxygen to the kiln causes this difference and outweighs the effects of the fluctuations in oxygen amounts present in scheme (b). This comparison showed that control strategies designed

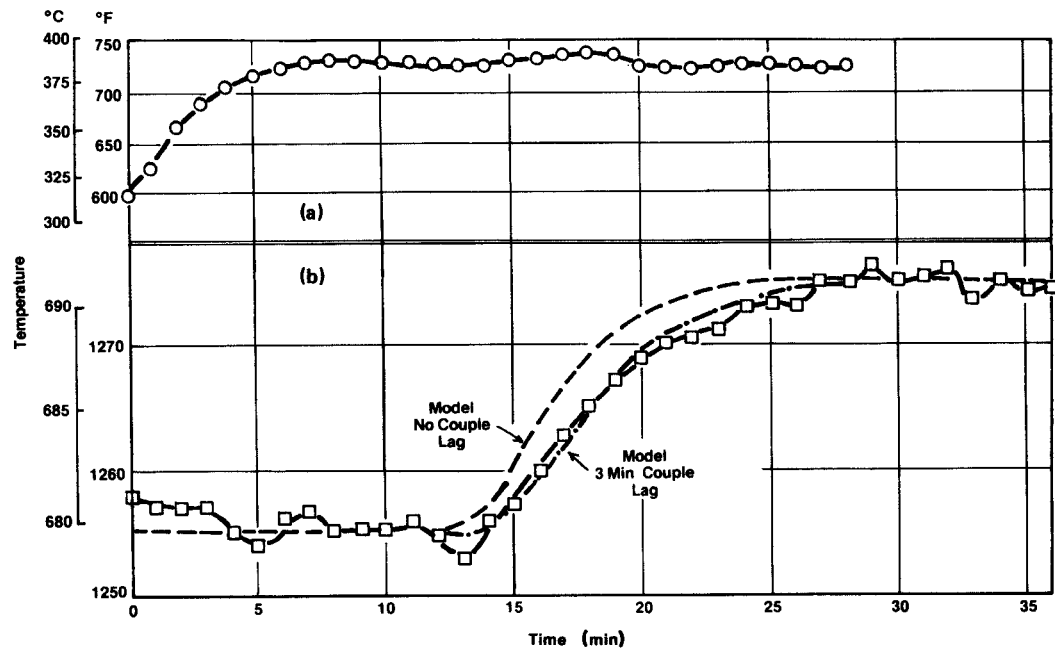


FIG. 24. Comparison of dynamic model prediction to plant performance: (○, □) plant data; (---, -.-) model prediction; (a) combustion air temperature; (b) response above coils.

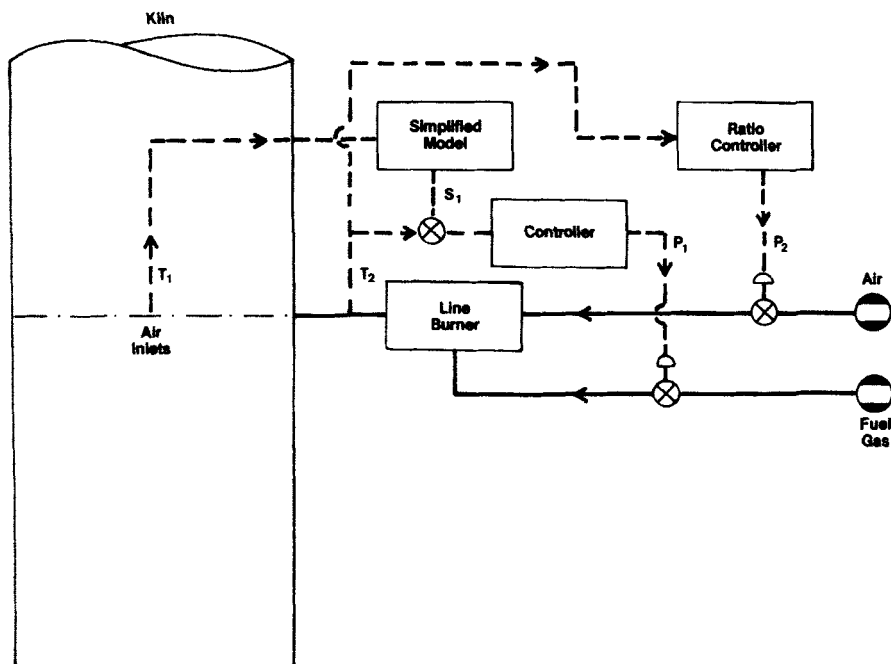


FIG. 25. Control scheme a: T_1 , average temperature at air inlets; T_2 , combustion air temperature; S_1 , desired combustion air temperature; P_1 , position of fuel gas valve; P_2 , position of air valve. Control goal: constant temperature above coils.

from steady-state considerations must be tested dynamically to show feasibility.

VI. The Inclusion of the Kinetics of the Conversion of CO to CO₂ in the Model

As the composition of the catalyst changed, the inability to predict the CO/CO₂ ratio becomes more and more limiting on the use of the model. The explicit solution was originally applied to the catalyst containing chromia (Cr₂O₃) and with relatively poorer diffusivity. With this catalyst and with the operating conditions at that time, the assumption of a constant value of α in each zone was adequate. The chromia was introduced into the catalyst early in the use of the TCC units to oxidize CO and to reduce the concentration of CO in the bottom plenum chamber and in the stack. The presence of too much CO in these parts of the unit could lead

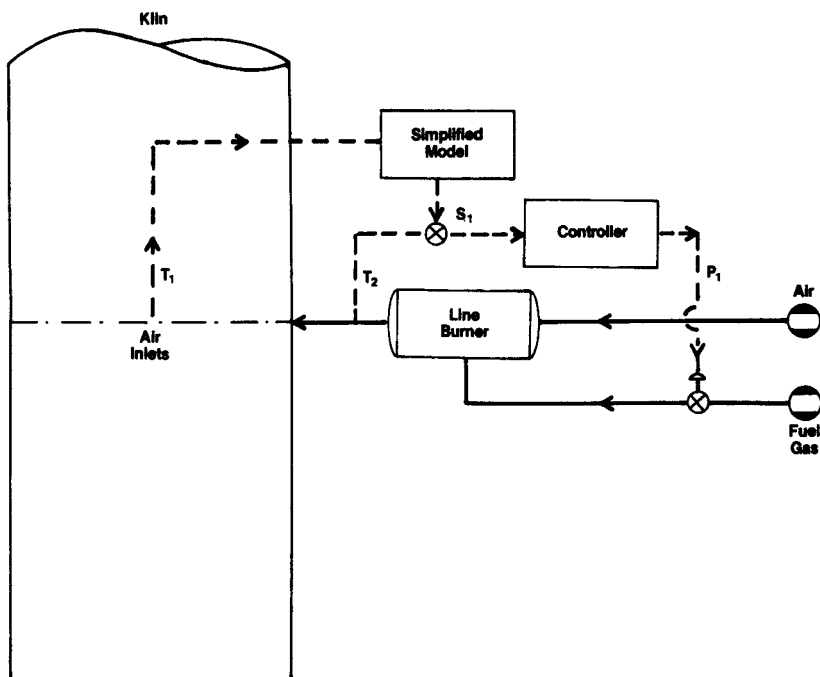


FIG. 26. Control scheme b: T_1 , average temperature at air inlets; T_2 , combustion air temperature; S_1 , desired combustion air temperature; P_1 , position of fuel gas valve. Control goal: constant temperature above coils.

to afterburning. Since no catalyst was present in the plenum and stack, a high temperature could result that could damage the unit. The presence of chromia in the cracking catalyst particles converted all the CO to CO₂ in the bottom zone of the kiln and prevented the high temperature. The value of α in the bottom zone was unity for these early uses of the model.

With the introduction of zeolites into cracking catalysts, the situation changed. The first version of the zeolite catalysts contained no chromia because it was found to be detrimental to the cracking selectivity. The value of the diffusion was also increased. These two changes led to hot spots developing in the bottom zone in regions of restrictive catalyst flow. In these regions CO burning occurred with insufficient catalyst flow to remove the heat. Large "popcorn" balls of fused catalyst resulted from the high temperatures occurring in these regions. In addition, afterburning became a problem in the plenum chambers and in the stacks. A model that included CO conversion was needed so that operating and design options could be determined to eliminate these problems.

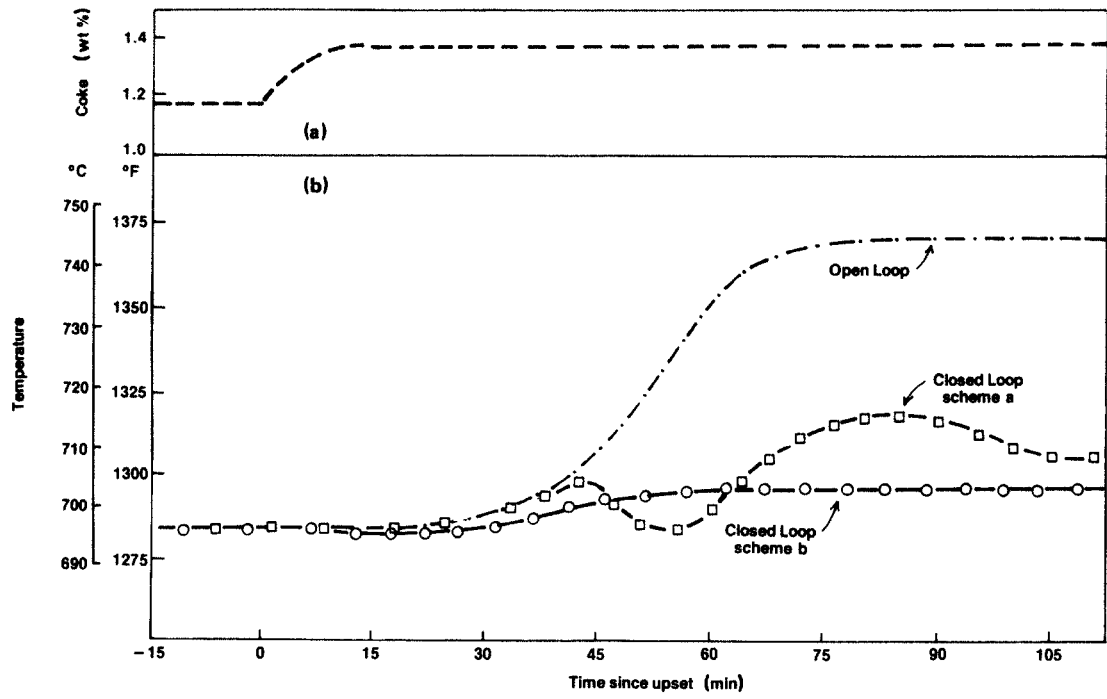


FIG. 27. Comparison of control schemes with step coke change.

A. KINETICS OF CO FORMATION AND CONVERSION

At the same time as the basic work was being done on the kinetics and diffusivity effects in coke burning, the kinetics of the processes that determined the CO/CO₂ ratio from slow coke was investigated by Weisz (1966). Studies were made of the cumulative CO₂/CO ratios for individual, whole, spherical catalyst beads. The results, shown in Fig. 28, scattered very badly.

Arthur (1951) determined that there is an intrinsic ratio of CO₂ to CO formed when graphite is burned and that this ratio is only a function of temperature. Departures from this ratio were caused by subsequent conversion of the CO to CO₂ over catalytic sites. The curve for this intrinsic

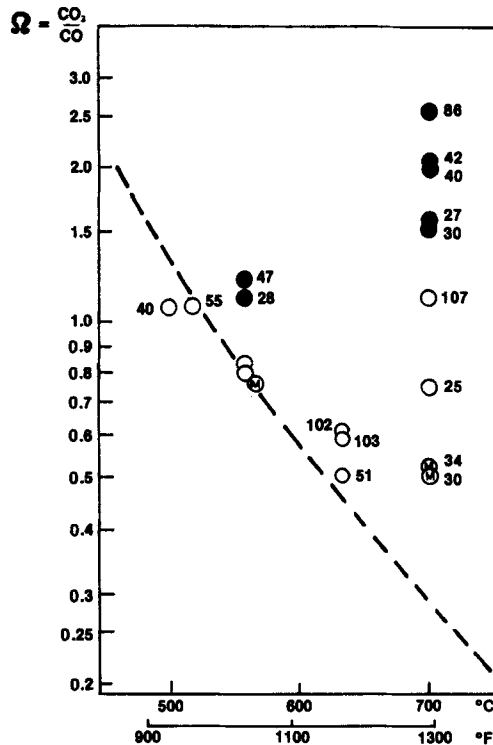


FIG. 28. The cumulative CO₂/CO ratio for coke burn-off on spherical catalyst beads versus combustion temperature in air: (○) "white" amorphous silica-alumina; (●) "green" CrO₂-containing amorphous silica-alumina; (M) macroporous "white" catalyst. The weight (mg) of the bead tested is denoted by the numerals adjacent to the respective symbol. Dashed line represents "intrinsic" ratios from carbon combustion research. From Weisz (1966).

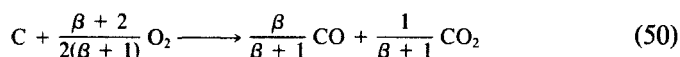
ratio found by Arthur is shown in Fig. 28. All the points lie either above this line or approximately on it.

The weight of each bead is given beside each point. Three kinds of catalyst beads are shown. The "white" beads have no chromia in them and the "green" beads have chromia. The "white" macropore beads have high values of diffusivity. The presence of chromia in the bead causes a large departure from the Arthur curve. On the other hand, the "white" beads either lie on the curve at lower temperatures or depart much less than "green" beads at higher temperatures. Furthermore, within each type of bead, the greater the weight and hence the greater the diameter, the greater the conversion of CO to CO₂. The "white" macropore beads, which have a high diffusivity, lie below the "white" ordinary beads. When the beads were crushed to a fine powder, the cumulative CO₂/CO ratio fell on the Arthur curve.

These observations are explained by the conversion of CO to CO₂ on sites active for CO conversion, as the intrinsically produced CO makes its way out of the catalyst bead by diffusion. The greater the diffusion limitation, the more the CO conversion. Weisz gave the mathematical solution for two special cases of these phenomena and demonstrated that the above interpretation was correct.

Gross (1983) expanded the mathematical treatment to the general problem required for the model and incorporated the CO conversion into the model. The treatment by Gross will be utilized because it is more general than the Weisz treatment.

The chemical reaction for the intrinsic burning of slow coke is given by



where β is the intrinsic CO/CO₂ ratio given by the Arthur curve. The quantity β is a function of temperature only and is given by

$$\beta = \beta_0 \exp(-Q_\beta/RT) \quad (51)$$

The rate of CO conversion is given by (Kozlov, 1959)

$$dC_{CO}/dt = k_{CO} C_{CO} \exp(-Q_{CO}/RT), \quad O_2 > 2\% \quad (52)$$

$$dC_{CO}/dt = k_{CO} C_{CO} C_{O_2}^{0.2} \exp(-Q_{CO}/RT), \quad O_2 < 2\% \quad (53)$$

For oxygen concentrations greater than 2%, Eq. (52) combines with Eqs. (50) and (3) to give

$$\frac{dC_{CO}}{dt} = b \frac{\beta}{\beta + 1} C_{O_2} C_c \exp\left(-\frac{Q}{RT}\right) - k_{CO} C_{CO} \exp\left(-\frac{Q_{CO}}{RT}\right) \quad (54)$$

B. DIFFUSION KINETICS

For the shell progression burning case with the burning front at the radius r_b , the differential equations for the coke-free regions of a spherical bead are

$$\frac{1}{r^2} \frac{\partial}{\partial r} \left(r^2 \frac{\partial C_{ox}}{\partial r} \right) - \frac{1}{2} k_{CO} \frac{C_{CO}}{D_{ox}} = 0 \quad (55)$$

for oxygen and

$$\frac{1}{r^2} \frac{\partial}{\partial r} \left(r^2 \frac{\partial C_{CO}}{\partial r} \right) - k_{CO} \frac{C_{CO}}{D_{CO}} = 0 \quad (56)$$

for CO.

The boundary conditions are

$$C_{ox} = C_{ox}^*, \quad C_{CO} = C_{CO}^* \quad (57)$$

at $r = a$ and at the burning front r_b ,

$$C_{ox} = 0 \quad (58)$$

Furthermore,

$$D_{CO} \frac{dC_{CO}}{dr} = - \frac{2\beta}{\beta + 2} D_{ox} \frac{dC_{ox}}{dr} \quad (59)$$

Equation (59) states that the amount of CO diffusing out is proportional to the oxygen diffusing in. The proportional function is determined by the intrinsic kinetics and is the stoichiometric ratio of CO to oxygen.

The solutions to Eqs. (55) and (56) are

$$C_{CO} = \frac{A_1}{r} \exp(mr) + \frac{A_2}{r} \exp(-mr) \quad (60)$$

$$C_{ox} = \frac{D_{CO}A_1}{2D_{ox}r} \exp(mr) + \frac{D_{CO}A_2}{2D_{ox}r} \exp(-mr) + \frac{A_3}{r} + A_4 \quad (61)$$

where $m = (k_{CO}/D_{CO})^{1/2}$ and A_1 , A_2 , A_3 , and A_4 are constants of integrations that can be evaluated from the four boundary conditions. The rate of oxygen diffusing into the spherical burning front f_s is given by

$$\begin{aligned} f_s &= 4\pi r_b^2 D_{ox} (dC_{ox}/dr)_{r=r_b} \\ &= 2\pi D_{CO} \{ A_1 [(mr_b - 1) \exp(mr_b)] \\ &\quad - A_2 [(mr_b + 1) \exp(-mr_b)] + (2D_{ox}/D_{CO}) A_3 \} \end{aligned} \quad (62)$$

The rate of oxygen utilization (f_z) is given by the rate of diffusion of oxygen across the exterior surface of the bead.

$$\begin{aligned} f_z &= 4\pi a^2 D_{\text{ox}} (dC_{\text{ox}}/dr)_{r=a} \\ &= 2\pi D_{\text{CO}} \{A_1[(ma - 1) \exp(ma)] \\ &\quad - A_2[(ma + 1) \exp(-ma)] + (2D_{\text{ox}}A_3/D_{\text{CO}})\} \end{aligned} \quad (63)$$

The amount of carbon burning is given by the amount of oxygen moving across the burning front multiplied by the intrinsic value of α : $\alpha_1 = 2(\beta + 1)/(\beta + 2)$. Thus,

$$\alpha_1 f_s = \frac{4}{3}\pi a^3 C_c (dy/dt) \quad (64)$$

Thus,

$$\begin{aligned} \left(\frac{dC_c}{dt}\right)_D &= \frac{3D_{\text{CO}}2(\beta + 1)}{2D_{\text{ox}}a^3(\beta + 2)} \left\{ A_1[(mr_b - 1) \exp(mr_b)] \right. \\ &\quad \left. - A_2[(mr_b + 1) \exp(-mr_b)] + \frac{2D_{\text{ox}}A_3}{D_{\text{CO}}} \right\} \end{aligned} \quad (65)$$

In the same way,

$$\begin{aligned} \left(\frac{dC_{\text{ox}}}{dt}\right)_D &= \frac{3D_{\text{CO}}}{2D_{\text{ox}}a^3} \left\{ A_1[(ma - 1) \exp(ma)] \right. \\ &\quad \left. - A_2[(ma + 1) \exp(-ma)] + \frac{2D_{\text{ox}}A_3}{D_{\text{CO}}} \right\} \end{aligned} \quad (66)$$

The disappearance of CO in the diffusion-limited case is given by twice the difference between Eqs. (65) and (66).

Let $(dy/dt)_D$ in Eq. (12) be rewritten as $\eta_D(dy/dt)_I$:

$$(dy/dt)_T^{-1} = (dy/dt)_I^{-1} + \eta_D^c(dy/dt)_I^{-1} \quad (67)$$

Analogous to Eq. (26), let

$$(dy/dt)_T = \eta_T(dy/dt)_I \quad (68)$$

From Eqs. (67) and (68), we get

$$\eta_T = \frac{\eta_D^c}{\eta_D^c + 1} \quad (69)$$

$$\eta_D^c = \frac{(dy/dt)_D}{(dy/dt)_I} \quad (70)$$

From Eqs. (65), (3), (70), and $C_c = yC_c^0$, we get

$$\eta_D^c = \frac{3D_{CO}2(\beta + 1)}{2D_{ox}a^3C_c^0(\beta + 2)} \times \left\{ A_1[(mr_b - 1) \exp(mr_b)] - A_2[(mr_b + 1) \exp(-mr_b)] + \frac{2D_{ox}A_3}{D_{CO}} \right\} \div \{byzC'_{ox}[\exp(-Q/RT)]\}^{-1} \quad (71)$$

In the same way the η_D for oxygen, η_D^o , is found from Eq. (66), Eq. (3) divided by α_1 , the oxygen rate equation corresponding to Eq. (70), and $C_{ox} = zC'_{ox}$:

$$\eta_D^o = \frac{3D_{CO}}{2D_{ox}a^3C'_{ox}} \times \left\{ A_1[(ma - 1) \exp(ma)] - A_2[(ma + 1) \exp(-ma)] + \frac{2D_{ox}A_3}{D_{CO}} \right\} \div \left\{ \frac{2 + \beta}{2(\beta + 1)} byzC'_{ox} \left[\exp\left(-\frac{Q}{RT}\right) + \frac{k_{CO}C_{CO}}{2} \exp\left(-\frac{Q_{CO}}{RT}\right) \right] \right\}^{-1} \quad (72)$$

From Eq. (69), we get

$$\eta_{TC} = \eta_D^c / (\eta_D^c + 1) \quad (73)$$

$$\eta_{TO} = \eta_D^o / (\eta_D^o + 1) \quad (74)$$

The introduction of the kinetics of the formation of CO and CO₂ into the model modifies the temperature equation (31) and the oxygen equation (33). The slow and fast coke burning equations are unchanged except for a change in the effectiveness factor η_T of Eq. (29) to η_{TC} given by Eq. (73). A new equation for the conversion of CO is introduced.

The equation for the rate of change of oxygen corresponding to Eq. (33) is

$$\frac{dz}{dx} = -\frac{\sigma}{F_a K_o} \left\{ \eta_{TO} \left[\frac{C'_s}{\alpha_1} b_s C'_{ox} z y_s \exp\left(-\frac{Q_s}{RT}\right) + \frac{k_{CO}}{2} C_{CO} \exp\left(-\frac{Q_{CO}}{RT}\right) \right] + \frac{C_f}{\alpha_f} b C'_{ox} z y_f \exp\left(-\frac{Q_f}{RT}\right) \right\} \quad (75)$$

The equation for the rate of change of temperature corresponding to Eq. (31) is

$$\begin{aligned}
\frac{dT}{dx} = & \frac{\sigma}{F_c C_{pc} + F_a C_{pa} M_a} \left\{ \Delta H_f b_f C'_f C'_{oxzyf} \exp\left(-\frac{Q_f}{RT}\right) \right. \\
& + \eta_{TC} [\Delta H_c + \eta_{TO} \Delta H_\Delta] \left[\frac{1}{\alpha_f} b_s C'_{ox} C'_{szy_s} \exp\left(-\frac{Q_s}{RT}\right) \right. \\
& \left. \left. + \eta_{TO} \Delta H_\Delta \frac{k_{CO}}{2} \exp\left(-\frac{Q_{CO}}{RT}\right) \right] \right\} \quad (76)
\end{aligned}$$

The additional equation for the rate of change of CO is

$$\begin{aligned}
\frac{dC_{CO}}{dx} = & \frac{\sigma \rho_a}{F_a} \left[\frac{2 - \alpha_f}{\alpha_f} b_f C'_{ox} C'_{fzy_f} e^{-Q_f/RT} \right. \\
& \left. \times \left(2\eta_{TC} - \frac{\eta_{TO}}{\alpha_f} \right) b_s C'_{ox} C'_{szy_s} e^{-Q_s/RT} + \frac{\eta_{TO}}{2} k_{CO} C_{CO} e^{-Q_{CO}/RT} \right] \quad (77)
\end{aligned}$$

These five basic equations were used by Gross to build a model including the kinetics of CO to CO₂. In addition, the Gross model accounted for (1) the water in the incoming airstream, (2) the H₂O formed during the burning of the fast coke, (3) gas density change caused by temperature variations, and (4) molar expansion of the gas during the reaction. The complete set of equations has been given by Gross (1983).

Computed results from this model are compared to actual kiln performance in Table VI and the operating conditions taken from kiln samples are given in Table VII. There are no unit factors or adjustable parameters in this model. As with the explicit model, all kinetic data are determined from laboratory experiments. Values of the frequency factors and activation energies are given in Table VIII. Diffusivity values are also included. The amount of fast coke was determined from Eq. (49). With the exception of the T-B (5/12) survey, the agreement between observed and computed values of CO, CO₂, and O₂ is very good considering that there are no adjustable parameters used to fit the model to each kiln. In the kiln survey T-212/10, the CO conversion activity of the catalyst has been considerably deactivated and a different frequency factor was used in this simulation.

When the cause of the departure of the survey T-B (5/12) was sought, it was found that afterburning was taking place in the bottom plenum of the kiln. The predicted values agreed with the observed value when the equation for the homogeneous reactions of afterburning were included in the model. These equations are (Kozlov, 1959)

$$\frac{dC_{CO}}{dx} = \frac{\sigma_\beta}{F_a} b_h C_{CO} C_{ox}^{1/4} [H_2O]^{1/2} \exp\left(-\frac{Q_h}{RT}\right) \quad (78)$$

TABLE VI

COMPARISON OF PREDICTED AND OBSERVED BEHAVIOR IN OPERATING KILNS

Kiln	ORSAT analysis						
	Predicted				Plant		
	CO	O ₂	CO ₂		CO	O ₂	CO ₂
(1) T-4 11/20	5.75	6.23	6.96	Top	6.0	7.4	6.0
	3.68	4.44	12.32	Bottom	4.4	3.3	13.7
(2) T-3 11/20	7.25	3.35	9.96	Top	7.0	1.4	8.8
	5.44	5.56	10.13	Bottom	5.3	3.4	12.5
(3) T-3 12/9	8.39	0.44	7.85	Top	8.3	1.4	8.0
	6.22	5.69	9.86	Bottom	5.6	3.9	12.6
(4) T-B 5/12	6.7	0.5	9.8	Top	6.5	3.0	9.5
	3.8	0	16.0	Bottom	0.7	0.2	19.0
(5) T-5 12/10	9.3	4.9	8.5	Top + plenum	7.3	1.9	10.8
	0.38	13.3	6.34	Bottom	0.7	13.3	5.4
(6) T-2 12/10 ^a	5.48	9.36	5.71	Top	5.6	8.4	6.0
	8.41	7.33	7.37	Bottom	8.3	7.6	7.9

^a Rate constant for CO burning lower in this case.

$$\frac{dT}{dx} = \frac{\sigma_{\beta}}{M_a C_{pa} F_a} \Delta H_{CO} b_h C_{CO} C_{ox}^{1/4} [H_2O]^{1/2} \exp \left(-\frac{Q_h}{RT} \right) \quad (79)$$

When the model was completed, it was used to explore the operating space of a typical kiln in order to obtain a better understanding of the CO concentration in the kiln and of the afterburning characteristics. A list of the parameters studied are listed in Table IX. The base operating conditions were those of T-3 12/9 of Table VII. The studies on throughput of catalyst (1d) and activity for CO burning (3a) will illustrate typical results.

The throughput of catalyst has a large effect on the amount of CO at the bottom of the lower zone as seen in Fig. 29. An increase from 500 tons/hr (4.54×10^5 kg/hr) to 700 tons/hr (6.36×10^5 kg/hr) increased the CO from about 1% to about 6%. Thus, cutting back the catalyst circulation could be used to help control afterburning in the lower plenum. The effect on the upper plenum was in the reverse direction since decreasing circulation causes more carbon to be burned in the top section, releasing more CO. However, this was a small change of an already high concentration of CO.

The afterburning and "popcorn" ball formation were so bad for the zeolite catalyst containing no chromia that chromia had to be added. A compromise between the amount of chromia added to the catalyst and the

TABLE VII
OPERATING CONDITIONS FOR TCC KILNS

	T-3 12/9	T-2 12/10	T-3 11/20	T-4 11/20	T-5 12/10	Buffalo 5/12/70
Flow of air up, scfm	14,395	22,312	16,864	21,679	51,059	13,394
Flow of air down, scfm	14,279	11,162	14,212	11,770	28,383	11,606
Air temperature at inlet, °F	540	500	800	685	580	975
Reactor outlet temperature, °F	885	921	915	883	905	897
Catalyst circulation, tons/hr	670	700	655	587	1000	514
Length of bed to cooling coils, ft	20	20	20	20	27	20
Location of air inlet from top, ft	10	6.75	10	6.75	6.75	8.0
Cross-sectional area, ft ²	463	463	463	463	964	463
Carbon on catalyst, wt. %	0.649	0.558	0.663	0.681	1.05	0.745

TABLE VIII
CARBON, CO BURNING IN TCC KILN

Rate constants	K_o (sec ⁻¹)	E_{act} (cal/gm-mole)
Fast coke	0.103×10^6	16,400
Slow coke	0.352×10^8	37,500
CO burning	0.218×10^5	20,000

Effective diffusivity in catalyst particle, $D_{H_2} = 0.0331$ cm²/sec (hydrogen at 100°F)
Diffusivity of species i is calculated from

$$D_i = D_{H_2}(M_{H_2}/M_i)^{1/2}[(T + 459)/559]^{1/2}$$

where T is temperature (°F), M_{H_2} is the molecular weight of H₂, and M_i is the molecular weight of specie i .

loss in the cracking selectivity of the catalyst was sought. The amount of chromia chosen was 0.15%, which gave a frequency factor of 4.2×10^{-9} ft³/lb/hr (12.6×10^{-10} m³/kg/hr). This choice was made before the model was constructed. The computed effect of changes in the frequency factor on the CO in the bottom of the typical kiln is shown in Fig. 30. The value of the frequency factor for the commercial catalyst in use at that time is indicated by the arrow. If the chromia content is increased by a factor of two, considerable improvement in CO content is achieved. Above this amount, the gain became much less.

TABLE IX
PARAMETERS INVESTIGATED IN INITIAL
OPERATIONS SPACE EXPLORATION

1. Process
a. Air flow rate to top and bottom
b. Position of air inlet
c. Lineburner temperature
d. Throughput of catalyst
e. Catalyst inlet temperature
2. Catalyst condition
a. Percent fast coke on catalyst
b. Coke on catalyst
3. Catalyst properties
a. Activity for CO burning
b. Diffusivity
c. Particle diameter

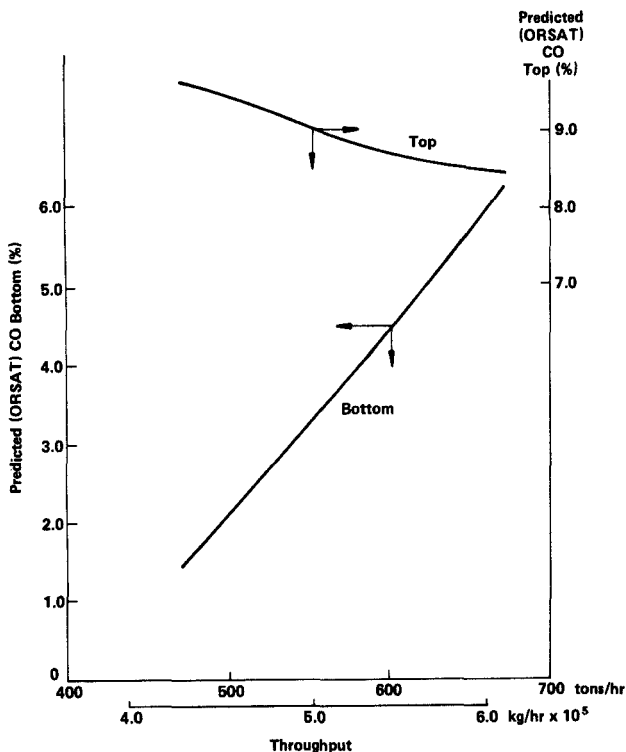


FIG. 29. Effect of catalyst throughput on CO at the top and bottom of the kiln.

Injection of cooling air into the plenum can be used to control afterburning provided sufficient air is used. This effect is shown in Fig. 31 for calculations made for the "Buffalo" kiln of Tables VI and VII. When no air is going to the plenum, some afterburning is taking place and the temperature is above 1200°F (649°C). No more afterburning occurred because the plenum was oxygen-starved. When 1000 scfm (28.3 scmm) of air was added in the plenum, the afterburning increased greatly because sufficient oxygen was now present to burn all the CO. The temperature rose to above 1700°F (927°C). When the air rate was further increased, the temperature began to drop because all the CO was burned and the effect of the additional air was to cool the plenum. When the air rate rose to 5000 scfm (141.6 scmm), the cooling effect was sufficient to stop the afterburning and at 6000 scfm (169.9 scmm) the plenum was uniform in temperature throughout.

This model completed the development of the TCC kiln model, since the TCC units were being replaced by FCC units. However, the model is

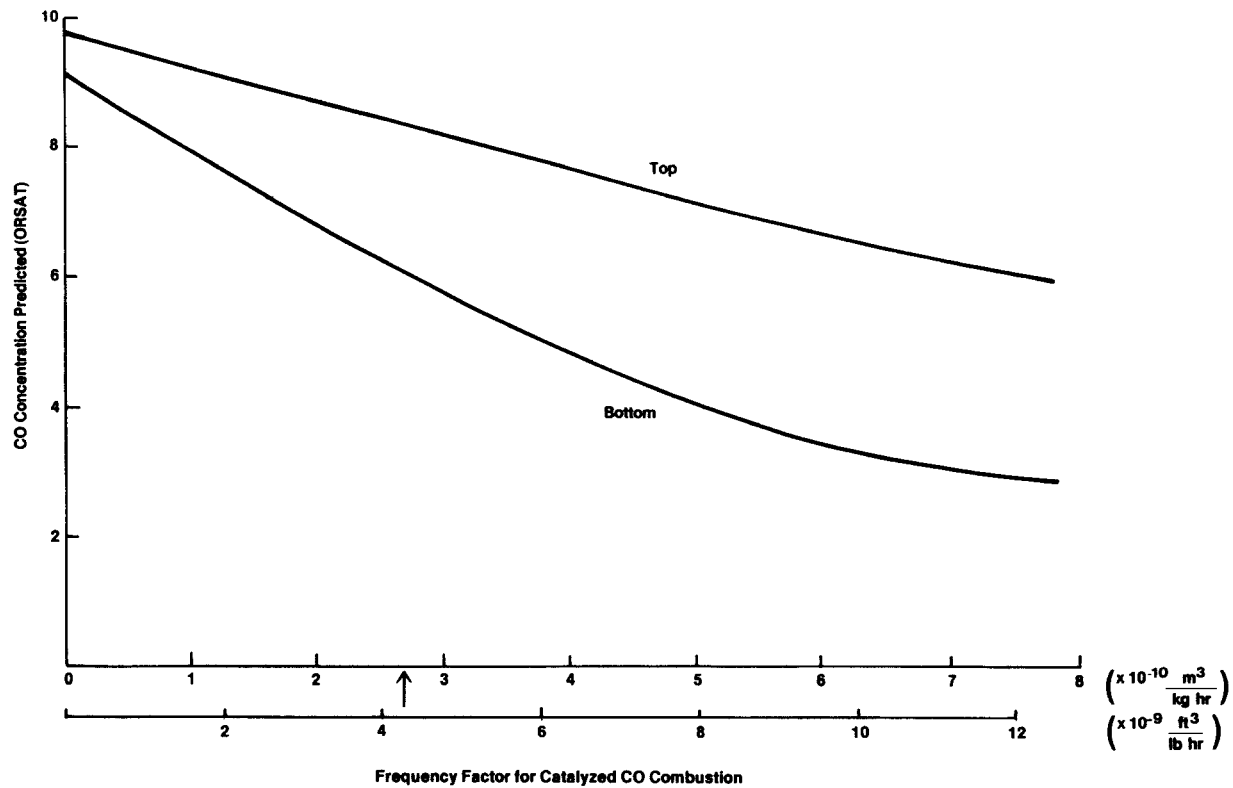


FIG. 30. Effect of CO conversion catalytic activity on CO concentration at the top and bottom of the kiln.

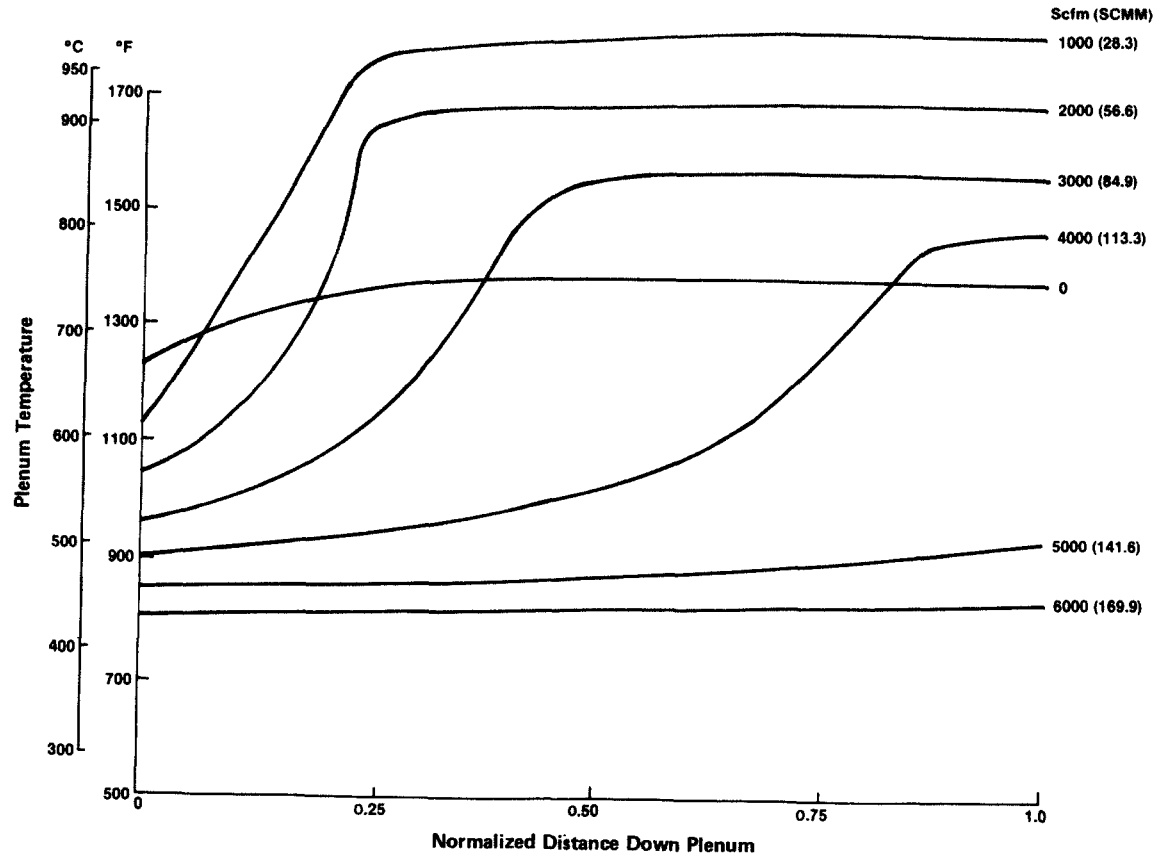


FIG. 31. Effect of adding cooling air (simulated) to the bottom plenum chamber on plenum temperature.

still in use as questions continue to arise in kiln operation for those TCC units still in existence. The basic information and the method of approach applied in the TCC kiln model enabled Weekman, Gross, and others to construct FCC regenerator models with the same successful predictive properties as the TCC model.

VII. Conclusion

The optimum design and operation of chemical reactors have progressed beyond an era of empiricism, correlations, and small extrapolations from existing knowledge of what is operable and advantageous. A more powerful tool is needed to understand the complexities, and to extrapolate with confidence into regions where no plant data exist. The wedding of mechanistic models and the computer makes possible rational design and operations, starting from fundamental knowledge of mass and energy balances, thermodynamic equilibrium, kinetics, heat and mass transfers, and fluid mechanics.

The thermofor catalytic cracker is being replaced by fluid cracking, but the lessons learned from TCC modeling and the confidence gained have not been forgotten. In fluid catalytic cracking and in reforming today, it is possible to describe the events in a reactor quite precisely, based on laboratory and pilot-plant data. A modern refinery engineer, armed with a verified mathematical model, a data bank, and a digital computer, can rapidly determine the optimum operating conditions for each change of feedstock, change of product distribution needed, or change of catalyst.

This revolution will spread to all chemical and petroleum processes that are large enough in scale to justify the investment in model building and experimental verification. Further progress needs better chemical kinetic data. The most deficient area remains in predicting the fluid mechanical and solid flow behaviors in reactors, where progress is sorely needed to round out the science of reaction engineering.

Nomenclature

a	Radius of catalyst particle, ft	C_c	Concentration of coke, lb moles/ft ³
A	Constant of integration, $y_i - YZ_i$	C_c^0	Initial concentration of coke, lb moles/ft ³
b	Frequency factor for carbon burning, ft ³ /(lb mole)(hr)	C_{CO}	Concentration of CO, lb moles/ft ³
b_h	Frequency factor for thermal CO burning, ft ³ /(lb mole)(hr)	C_{CO}^*	Concentration of CO in the gas

	phase over the catalyst particle, lb moles/ft ³	P	$F_c W_c' \Delta H / (F_c C_{pc} + F_a M_a C_{pa})$
C_{ox}	Concentration of oxygen, lb moles/ft ³	P_a	Pressure
C_{ox}^*	O ₂ concentration in gas phase over catalyst particle, lb moles/ ft ³	Q	Activation energy of carbon burn- ing, Btu/(lb mole)
C'_{ox}	Initial concentration of oxygen, lb moles/ft ³	Q_β	Activation energy for CO/CO ₂ ratio
C_{pa}	Specific heat of air, Btu/(lb)(°F) (0.26)	Q_{CO}	Activation energy of catalytic CO burning
C_{pc}	Specific heat of catalyst, Btu/ (lb)(°F) (0.29)	Q_h	Activation energy of thermal CO burning
D	Diffusion coefficient, ft ² /hr	r_1	$y^{1/3} = r_b/a$
D_{CO}	CO diffusion coefficient	r	Radial length along bead
D_{ox}	O ₂ diffusion coefficient	r_B	Radius of coke core
f	Rate of flow of oxygen through outer surface of bead, moles/hr	R	Gas constant, Btu/(lb mole)(°F)
f_s	Rate of carbon burning at bead surface	t	Time, hr
F_a	Flow of air, lb moles/hr; down- flow is positive	T	Temperature, °F or °R
F_c	Flow of catalyst, lb/hr; downflow is positive	T_a	Temperature of air at air inlet
[H ₂ O]	Concentration of water, gas phase, lb moles/ft ³	T_i	Temperature at entrance to <i>i</i> th zone
ΔH_{CO_2}	Heat of reaction for combustion of coke to CO ₂ , Btu/(lb coke burned)	T_R	reactor outlet temperature
ΔH_Δ	Heat of reaction for combustion of coke to CO, Btu/lb	V	Volume
ΔH_f	Heat of reaction for combustion of fast coke, Btu/lb	w_i	Q/RT
ΔH_s	$[\alpha_s \Delta H_{CO_2} + 2(1 - \alpha_s) \Delta H_\Delta] / \alpha_s$	W_c	Weight fraction of coke on cata- lyst, lbs coke/lb catalyst
k	Rate constant for carbon burning, ft ³ /(lb mole)(hr)	W_c'	Initial weight fraction of coke on catalyst, lbs coke/lb catalyst
k_{CO}	Rate constant for CO burning, hr ⁻¹	x	Distance along kiln, ft
K_o	Mole fraction of oxygen in air, moles O ₂ /mole air	X_b	Distance along kiln at which 99% of coke is burned off
l	Location of air inlet	y	Fraction of the original coke left on catalyst, C_c/C_c^0
L	Length of kiln, ft	y_i	Fraction of original coke remain- ing at entrance to <i>i</i> th zone
L_i	Length of <i>i</i> th zone of kiln	Y	$\alpha K_o F_a M_c / W_c F_c$, $Y > 0$ for concur- rent flow, $Y < 0$ for countercur- rent flow
m	$(k_{CO}/D_{CO})^{1/2}$	z	Fraction of O ₂ left, C_{ox}/C'_{ox}
M_a	Molecular weight of air, lb/(lb mole) = 29	GREEK LETTERS	
M_c	Molecular weight of coke, lb/(lb mole) = 12		
M_{O_2}	Molecular weight of O ₂ , lb/(lb mole) = 32	α	Moles carbon burned/moles of ox- ygen used, $\alpha = 1$ for all CO ₂ , $\alpha = 2$ for all CO
		α_1	Intrinsic value is $\alpha = 2(\beta + 1)/\beta + 2$
		β	Intrinsic CO/CO ₂ ratio
		δ	$A^{1/3}$
		ζ	$1/(y_i \tau + \mu)$
		η	Effectiveness factor
		Θ	$\alpha F_a a^3 \rho_i / 3 \sigma \tau \rho_b$
		θ	$(F_c / \sigma L_i \rho_b) t$, normalized time

μ	$RT_i/Q = 1/w_i$	Ψ	$(\alpha F_a/\tau)(C_o M_c/K)(1/b\rho_b)$
ξ	$1/[(A - y_i)\tau - \mu]$	ε	Void fraction
ρ_a	Density of the air, lb/ft ³	SUBSCRIPTS	
ρ_b	Bulk density of the catalyst, lb/ft ³		
	reactor	I	Intrinsic burning
ρ_t	Density of the catalyst beads, lb/ft ³ catalyst	D	Diffusion-limited burning
σ	Cross section of kiln, ft ²	T	Total
σ_β	Cross section of afterburning section	i	Inlet to ith zone
τ	RP/Q	s	Slow coke
χ	X/L_i , normalized distance	f	Fast coke
		h	Homogeneous gas-phase burning

References

- Arthur, J. R. (1951). *Trans. Faraday Soc.* **47**, 164.
- Caram, H. S., and Amundson, N. R. (1977). Diffusion and reaction in a stagnant boundary layer about a carbon particle. *Ind. Eng. Chem. Fundam.* **16**, 171.
- Gross, B. (1983). A kinetic model for predicting CO concentrations in moving bed regenerators. *Ind. Eng. Chem. Fundam.* (in press).
- Ishida, M., and Wen, C. Y. (1968). Comparison of kinetic and diffusional models for solid-gas reactions. *AIChEJ* **14**, 311.
- Kozlov, G. (1959). On high-temperature oxidation of methane. *Symp. (Int.) Combust. [Proc.]*, 7th, 1958 pp. 152-159.
- Mehta, P. S., Sams, W. N., and Luss, D. (1981). Wrong-way behavior of packed-bed reactors. *AIChEJ* **27**, 234.
- Prater, C. D., Moulthrop, B. L., and Wei, J. (1963). Simulation of TCC kilns in terms of fundamental parameters. *Natl. AIChE Meet.*, 1963.
- Weekman, V. W., Jr., Harter, M. D., and Marr, G. R., Jr. (1967). Hybrid computer simulation of a moving-bed catalyst regenerator. *Ind. Eng. Chem.* **56**, 84.
- Weisz, P. B. (1966). Combustion of carbonaceous deposits within porous catalyst particles. III. The CO₂/CO product ratio. *J. Catal.* **6**, 425.
- Weisz, P. B., and Goodwin, R. D. (1963). Combustion of carbonaceous deposits within porous catalyst particles. I. Diffusion controlled kinetics. *J. Catal.* **2**, 397.
- Weisz, P. B., and Goodwin, R. D. (1966). Combustion of carbonaceous deposits within porous catalyst particle. II. Intrinsic burning rate. *J. Catal.* **6**, 227.
- Wen, C. Y. (1968). Noncatalytic heterogeneous solid fluid reaction models. *Ind. Eng. Chem.* **60**(9), 34.

This Page Intentionally Left Blank

STRIPPING OPERATIONS IN POLYMER PROCESSING

Costel D. Denson

Department of Chemical Engineering
University of Delaware
Newark, Delaware

I. Introduction	61
II. Nature of the Problem.	64
III. Mass Transfer Rates in Wiped-Film Processors	67
A. Mass Transfer Coefficients for Single-Screw Extruders	68
B. Mass Transfer Coefficients for Twin-Screw Extruders	78
IV. Bubble Entrainment and Enhanced Mass Transfer	87
A. Physical and Mathematical Model	88
B. Fictitious Mass Transfer Coefficients	98
V. The Length of a Transfer Unit	99
Nomenclature	102
References	103

I. Introduction

Polymer processing operations can arbitrarily be divided into two rather broad categories which, simply stated, are those operations that are concerned with shaping polymeric materials into well-defined, end-use configurations and those that are not concerned with shaping. Profile extrusion, pultrusion, injection molding, tubular film blowing, blow molding, and fiber spinning are examples of polymer processing operations which involve shaping; and usually, the engineering analysis of these processes is concerned with describing the fluid mechanics of the process, how complex rheological behavior may affect processability, and with heat transfer when shaping involves solidification by cooling. In more sophisticated analyses, account is taken of the developing stresses during flow and how these, as well as solidification rates, influence the morphology and performance properties of the shaped structure.

Polymer processing operations which do not involve shaping are defined here as those which are concerned with the synthesis of high-molecular-weight polymers, or with affecting physicochemical changes in the nature of polymeric materials. These operations, which are most often conducted upstream from shaping operations, include the following: vapor-liquid stripping operations when the liquid phase is a molten polymer or polymer solution (devolatilization), liquid-liquid stripping operations where one liquid is a molten polymer or polymeric solution, gas absorption in molten polymers, polymerization and grafting reactions, mixing, pumping and pressurization, and filtration.

The engineering analysis and design of these operations addresses questions which are different than those addressed in connection with the shaping operations. This is illustrated in Fig. 1 which is a flow sheet, cited by Nichols and Kheradi (1982), for the continuous conversion of latex in the manufacture of acrylonitrile-butadiene-styrene (ABS). In this process three of the "nonshaping" operations are shown: (1) a chemical reaction (coagulation); (2) a liquid-liquid extraction operation which involves a molten polymer and water; and (3) a vapor-liquid stripping operation which involves the removal of a volatile component from the molten polymer. The analysis and design around the devolatilization section, for example, would deal with such questions as how the exit concentration of

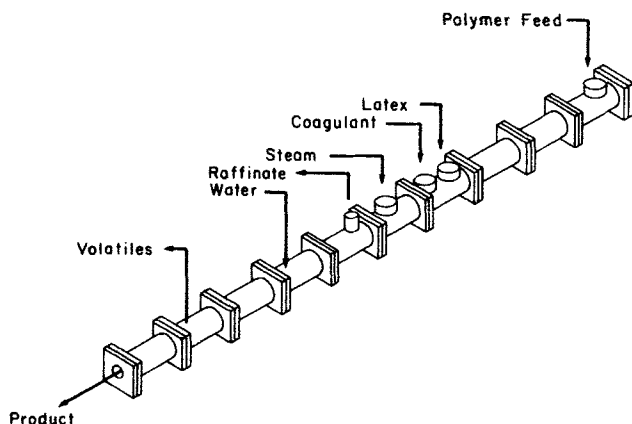


FIG. 1. Process flow sheet for the continuous conversion of latex in a counterrotating, tangential twin-screw extruder as it might be arranged for the production of acrylonitrile-butadiene-styrene polymer (Nichols and Kheradi, 1982). Polystyrene (or styrene-acrylonitrile) melt is fed upstream of the reactor zone where the coagulation reaction takes place. Washing (countercurrent liquid-liquid extraction) and solids separation are conducted in zones immediately downstream of the reactor zone. The remaining zones are reserved for devolatilization and pumping.

the volatile component is related to the throughput rate, the size of the extraction zone, the pressure in the extraction zone, the speed of the screw in the extruder, and the rheological behavior of the polymeric system.

The scientific and engineering principles which govern behavior in these nonshaping polymer processing operations have not been well articulated, and, consequently, it has not always been entirely clear as to how to proceed in the analysis and design of these operations. What is particularly noteworthy about this point is the fact that the nonshaping operations closely parallel many of the classical unit operations in the chemical process industries where analysis and design procedures are based on well-established engineering concepts, which leads one to believe that these same concepts might be applied to the analysis and design of the nonshaping operations. Polymeric materials have two features which distinguish them from the materials of usual interest in the chemical process industries: inordinately high viscosities and the property of elasticity. As a result, these materials must be processed in ways that are different than those traditionally used in the chemical process industries. New and "unusual" flow geometries must be used, and this means that the process equipment will be different. This, in turn, means that even though the scientific principles which govern behavior may be the same, the specific application of these principles may lead to quite different results.

In this article we review the current state of the art for just one of the nonshaping polymer processing operations: vapor-liquid stripping, or devolatilization as it is known in the polymer processing industries. In doing so, we show that the classical concepts and design procedures used for the traditional stripping operations are applicable to the stripping of viscous polymeric solutions. Polymer devolatilization is frequently encountered in both the synthesis of polymers and the shaping of polymeric materials to form finished goods. Condensation polymerizations, for example, require that (volatile) by-products be continuously removed during polymerization so that reverse reactions will not prevent the formation of high-molecular-weight products (Amon and Denson, 1980; Ault and Mellichamp, 1972; Pell and Davis, 1973; Secor, 1969). The removal of residual monomer in polymeric materials used for food packaging is another example of the importance of devolatilization. Some of the monomers that are used in the synthesis of these polymers are thought to be carcinogenic and therefore must be reduced to levels of the order of parts per million. And, in injection molding, it is often necessary to remove traces of moisture from the molten polymer prior to injection so as to obtain a void-free molded structure.

II. Nature of the Problem

The analysis and design of any stripping operation would be relatively straightforward provided that the velocity and concentration profiles that obtain in the extraction unit are known. Solutions to the momentum and diffusion equations provide this information, but, for most cases of interest in the chemical process industries, solutions to these equations are difficult to obtain since the flow geometry is often not well defined and flow may be both tortuous and turbulent. When these circumstances prevail, scientifically based, semiempirical relationships have often provided the basis for analysis and design procedures.

An entirely different situation exists in vapor-liquid stripping operations involving concentrated polymeric solutions. These solutions are usually viscous enough so that the creeping flow approximation can be made, and one need not be concerned with the complications which arise out of turbulence or other nonlinear behavior related to inertial effects. A further simplification results because the fluid flow boundaries in polymer processing equipment are generally well defined, and even though the shapes of these boundaries are not always simple, the equations of motion can be solved rather routinely, particularly when the polymeric solution behaves as a Newtonian fluid at the process conditions of interest. When, in addition, Fickian diffusion prevails, computation of the concentration profiles provides no great difficulty, and analysis and design can proceed in a straightforward manner.

Often times concentrated polymeric solutions cannot be treated as Newtonian fluids, however, and this tends to offset the simplifications which result from the creeping flow approximation and the fact that the boundaries are well defined. The complex rheological behavior of polymeric solutions and melts requires that nonlinear constitutive equations, such as Eqs. (1)–(5), be used (White and Metzner, 1963):

$$\tau_{ij} + \lambda_1(\Pi_\Delta)(\delta\tau_{ij}/\delta t) = \eta(\Pi_\Delta)e_{ij} \quad (1)$$

$$\eta = \eta(\Pi_\Delta) \quad (2)$$

$$\Pi_\Delta = e_{ij}e_{ij} \quad (3)$$

$$\frac{\delta\tau_{ij}}{\delta t} = \frac{\partial\tau_{ij}}{\partial t} + v_k \frac{\partial\tau_{ij}}{\partial x_k} - \tau_{kj} \frac{\partial v_i}{\partial x_k} - \tau_{ik} \frac{\partial v_j}{\partial x_k} \quad (4)$$

where η is an unspecified function which could, for example, be the power law

$$\eta = K(\frac{1}{2}\Pi_\Delta)^{(n-1)/2} \quad (5)$$

The use of nonlinear constitutive equations means that the resulting equations of motion will be nonlinear and that the determination of the velocity profiles becomes increasingly difficult. Additional complications which arise due to the finite memory and elasticity of polymer solutions and melts include the following: the generation of secondary flows because of the particular shape of a given flow geometry, and the tendency of an elastic liquid to act as a solid when the characteristic process time is much shorter than the characteristic relaxation time. This latter situation could, for example, significantly influence the efficiency of extraction equipment which operates on the basis that smooth, continuous polymeric films are mechanically generated on the wall of the extractor. If the time for formation of these films is shorter than the relaxation time of the polymeric solution, the solution could behave more like a solid than a liquid and the film could undergo rupture. In these circumstances smooth, continuous films would not be formed, and the surface area for mass transfer would be significantly different than the expected value.

The second major difference found in vapor-liquid extraction of polymeric solutions is related to the low values of the diffusion coefficients and the strong dependence of these coefficients on the concentration of solvent or monomer in a polymeric solution or melt. Figure 2, which illustrates how the diffusion coefficient can vary with concentration for a polymeric solution, shows a variation of more than three orders of magnitude in the diffusion coefficient when the concentration varies from about 10% to less than 1%. From a mathematical viewpoint the dependence of the diffusion coefficient on concentration can introduce complications in solving the diffusion equations to obtain concentration profiles, particularly when this dependence is nonlinear. On a physical basis, the low diffusivities result in low mass-transfer rates, which means larger extraction equipment.

The development of a scientific understanding of diffusion in liquid-phase polymeric systems has been largely due to Duda *et al.* (1982), Ju *et al.* (1981), and Vrentas and Duda (1977a,b, 1979) whose work in this area has been signal. In their most recent work, Duda *et al.* (1982) have developed a theory which successfully predicts the strong dependence of the diffusion coefficient on temperature and concentration in polymeric solutions. The parameters in this theory are relatively easy to obtain, and in view of its predictive capability this theory would seem to be most appropriate for incorporating concentration-dependent diffusion coefficients in the diffusion equation.

Because of the highly nonideal behavior of polymer-solvent solutions, polymer-vapor equilibrium relations account for the third major difference found in stripping operations with polymeric solutions. The appro-

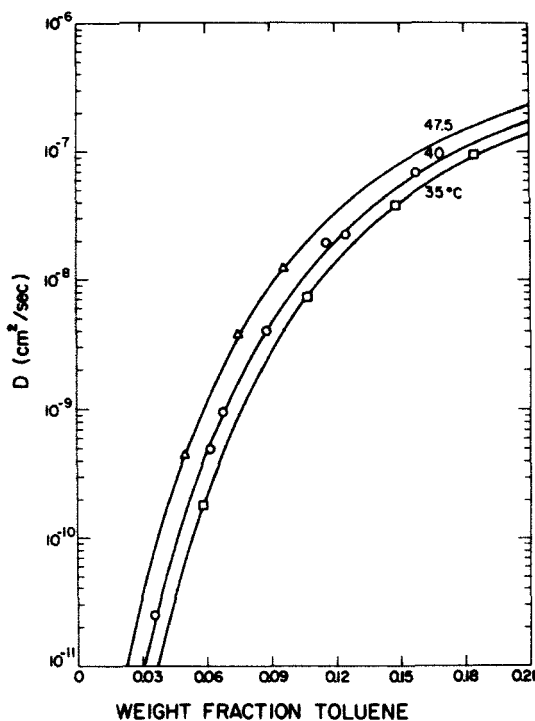


FIG. 2. Typical example of the variation of the diffusion coefficient with concentration in concentrated polymeric solutions. The system shown is poly(vinyl acetate) and toluene. (Reproduced with permission from Ju *et al.*, 1981.)

priate expression to use here is that developed by Flory (1941) and Huggins (1942):

$$\ln(P/P_0) = \ln(1 - \phi_p) + (1 - \bar{x}_n^{-1})\phi_p + \chi\phi_p^2 \quad (6)$$

For concentrated polymeric solutions, Eq. (6) can be written as

$$P = P_0\phi_s e^{1+\chi} \quad (7)$$

or

$$P = H_c w \quad (7a)$$

which is the form [Eq. (7a)] most commonly employed in engineering design. The difficulty here is the experimental determination of reliable values for the interaction parameter χ or the weight-fraction-based Henry's constant.

The most comprehensive treatment to date of the state of the art con-

cerning vapor-liquid equilibria in concentrated polymeric solutions is that due to Bonner (1975). A survey of the data available in the literature for a wide variety of polymers is presented in that work along with a discussion of both the experimental techniques used to obtain the data and the theory used to analyze and correlate the data.

None of the experimental techniques described by Bonner, however, has been capable of providing reliable vapor-liquid equilibrium data at the combined extremes of elevated temperature and reduced pressure, conditions applicable to most commercial polymer-stripping operations. This problem has been addressed by Meyer and Blanks (1982), who developed a modified isopiestic technique that could be used when solubilities are low. Although the success of this new technique was demonstrated using just polyethylene with isobutane and propane, the idea shows considerable promise for obtaining data at unusual conditions of temperature and pressure.

III. Mass Transfer Rates in Wiped-Film Processors

In commercial practice, when a volatile component must be extracted from a polymeric solution of high viscosity, say 500 P or greater, the extraction operation is almost always conducted in geometries which mechanically generate a wiped film. And here, screw extruders have played a major role.

In single-screw extruders, a screw with a finite helix angle rotates inside a cylindrical barrel (Fig. 3). Material is conveyed from the inlet to the discharge by virtue of the viscous forces which exist between the barrel wall, the fluid, and the screw. Thus, these machines are particularly well suited for the processing of highly viscous polymeric solutions. Analysis of the flow in single-screw extruders generally proceeds along the lines of unwinding the barrel and screw (Fig. 4) and treating the barrel as if it were moving and the screw as if it were stationary (Tadmor and Klein, 1970).

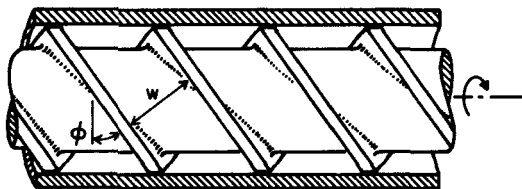


FIG. 3. Schematic view of a single-screw extruder showing a double-flighted screw in a cylindrical barrel.

exposure of fresh material at the surface of the fluid in the nip, mass is transferred to the gas phase which contains the volatile component at a lower fugacity. On the basis of an analysis by Moffatt (1964), who showed that the velocity of an infinite free surface perpendicular to a moving wall is $2/\pi$ times the wall velocity, the velocity of fluid at the surface of the nip can be approximated as $(2/\pi)V_{bx}$ and thus the exposure time for mass transfer is approximately given by

$$\theta_n = (\pi/2)(H/V_{bx}) \quad (8)$$

The second effect which results from the cross-channel component of the barrel motion is the generation of a wiped film of the polymeric solution as the solution is dragged from the nip in an adjacent screw channel through the clearance between the flight tip and the barrel. Since this film is continually generated, mass is transferred to the gas phase in a time period given by

$$\theta_f = (W - x')/V_{bx} \quad (9)$$

in circumstances, again, when the fugacity of the volatile component in the gas phase is lower than that in the solution.

1. Theory

On the basis of the simplified view of the flow patterns just described, a model for predicting mass transfer rates can be developed using penetration theory and the fact that mass is transferred simultaneously from both the nip and the wiped film. We can therefore write that the total molar mass transfer rate from an element of fluid over a length $d\lambda$ in the extruder is

$$N_t a S d\lambda = (N_n a_n + N_f a_f) S d\lambda \quad (10)$$

A mass balance across the same differential element with no axial dispersion results in

$$d(Lw)/d\lambda = -(N_n a_n + N_f a_f) S M \quad (11)$$

which can be solved to obtain a relationship between the extruder inlet and exit concentrations, the liquid flow rate, and the operating conditions once the mathematical form for the quantity in parentheses on the right-hand side of Eq. (11) is known.

A specific expression for the mass transfer rate in Eq. (11) was first developed by Latinen (1962) in a classic paper that showed how penetration theory can be applied to the analysis of devolatilization processes in single-screw extruders. The derivation presented here parallels that by Latinen but differs in some respects for reasons of clarity.

The use of penetration theory requires that the following assumptions be made:

(1) The diffusion coefficient is independent of concentration and temperature.

(2) The penetration depth for diffusion is small compared to the thickness of the liquid layer.

(3) The initial concentration of the volatile component in the wiped film is uniform and equal to the bulk concentration of the volatile component in the nip.

(4) The concentration of the volatile component in the nip is uniform as a result of the cross-channel circulatory motions even though a concentration gradient exists near the vapor-liquid interface.

In view of the above assumptions, both the wiped film and the nip can be treated as semi-infinite slabs in which diffusion is described by

$$\partial c / \partial t = D(\partial^2 c / \partial \xi_1^2) \quad (12)$$

for the wiped film and by

$$\partial \hat{c} / \partial t = D(\partial^2 \hat{c} / \partial \xi_2^2) \quad (13)$$

for the nip.

The appropriate boundary and initial conditions for a particular solution of Eq. (12) are

$$c = w\rho/M \quad \text{for} \quad t = 0 \quad (14)$$

$$c = w_i\rho/M \quad \text{for} \quad \xi_1 = 0 \quad (15)$$

$$c = w\rho/M \quad \text{as} \quad \xi_1 \rightarrow \infty \quad (16)$$

and for Eq. (13) are

$$\hat{c} = w\rho/M \quad \text{for} \quad t = 0 \quad (17)$$

$$\hat{c} = w_i\rho/M \quad \text{for} \quad \xi_2 = 0 \quad (18)$$

$$\hat{c} = w\rho/M \quad \text{as} \quad \xi_2 \rightarrow \infty \quad (19)$$

The solutions to Eqs. (12)–(19) for the wiped film and the nip are, respectively, given by

$$\frac{cM/\rho - w_i}{w - w_i} = \operatorname{erf} \frac{\xi_1}{(4Dt)^{1/2}} \quad (20)$$

$$\frac{\hat{c}M/\rho - w_i}{w - w_i} = \operatorname{erf} \frac{\xi_2}{(4Dt)^{1/2}} \quad (21)$$

From Eq. (20) the molar flux at the interface between the wiped film and the gas phase at any instant in time is given by

$$n_f = -D \frac{\partial c}{\partial \xi_1} = \frac{D(w - w_i)}{(\pi Dt)^{1/2}} \frac{\rho}{M} \quad (22)$$

whereas for the nip this flux is

$$n_n = -D \frac{\partial \hat{c}}{\partial \xi_2} = \frac{D(w - w_i)}{(\pi Dt)^{1/2}} \frac{\rho}{M} \quad (23)$$

The average molar flux at each of these surfaces is given by

$$N_f = \frac{1}{\theta_f} \int_0^{\theta_f} n_f dt = 2 \left(\frac{D}{\pi \theta_f} \right)^{1/2} \frac{\rho}{M} (w - w_i) \quad (24)$$

$$N_n = \frac{1}{\theta_n} \int_0^{\theta_n} n_n dt = 2 \left(\frac{D}{\pi \theta_n} \right)^{1/2} \frac{\rho}{M} (w - w_i) \quad (25)$$

It is often convenient to express the molar flux for mass transfer in terms of a mass transfer coefficient, and in these circumstances Eq. (10) can be written as

$$N_t a = \frac{\rho}{M} (k_L a) (w - w_i) = N_n a_n + N_f a_f \quad (26)$$

Substitution of Eqs. (24) and (25) into Eq. (26) results in

$$k_L a = \left(\frac{4 D}{\pi \theta_f} \right)^{1/2} a_f + \left(\frac{4 D}{\pi \theta_n} \right)^{1/2} a_n \quad (27)$$

which can be rearranged to

$$k_L a = 2 \left(\frac{D}{\pi} \frac{1}{\theta_f} \right)^{1/2} a_b \left(\frac{a_f}{a_b} \right) \left[1 + \left(\frac{\theta_f}{\theta_n} \right)^{1/2} \frac{a_n}{a_f} \right] \quad (28)$$

For the ideal case of smooth, continuous films on the barrel wall and a vertical interface with no curvature, the following expressions are true:

$$\theta_f = (1 - f)/pDN \quad (29)$$

$$a_f/a_b = 1 - f \quad (30)$$

$$a_n/a_f = H/W(1 - f) \quad (31)$$

When Eqs. (29)–(31) are used along with Eq. (8), Eq. (28) can be written as

$$\frac{k_L a}{a_b} = \frac{2}{\sqrt{\pi}} (DpN)^{1/2} \left[(1 - f)^{1/2} + \frac{2}{\pi} \left(\frac{H}{W} \right)^{1/2} \right] \quad (32)$$

The fraction of the channel that is partially full, f , can be approximated using Fig. 6, which is based on results developed by Squires (1958). The drag flow shape factor F_D is given by

$$F_D = \frac{L}{Q_D} = \frac{2L}{\pi D_b W H N \cos \phi} \quad (33)$$

and $k_L a/a_b$ is thus seen to depend on both N and the ratio L/N . If the channel is infinitely wide ($H/W \rightarrow 0$), F_D is identically equal to f and Eq. (32) can be written as

$$k_L a/a_b = (2/\sqrt{\pi})(DpN)^{1/2}(1 - F_D)^{1/2} \quad (34)$$

If, in addition, the holdup is low ($f \rightarrow 0$), Eq. (34) reduces to the much simpler form

$$k_L a/a_b = (2/\sqrt{\pi})(DpN)^{1/2} \quad (35)$$

Equation (35) predicts that the mass transfer coefficient increases with increases in the screw speed and the number of parallel channels on the screw. The explanation for this is rather simple and is related to the fact that each time the film on the barrel wall is regenerated and the surface of the nip is renewed, a uniform concentration profile is reestablished, which means that the driving force for mass transfer is maximized. Since the instantaneous mass transfer rate decreases with time, mass transfer rates can be maximized by keeping the exposure time as short as possible, and

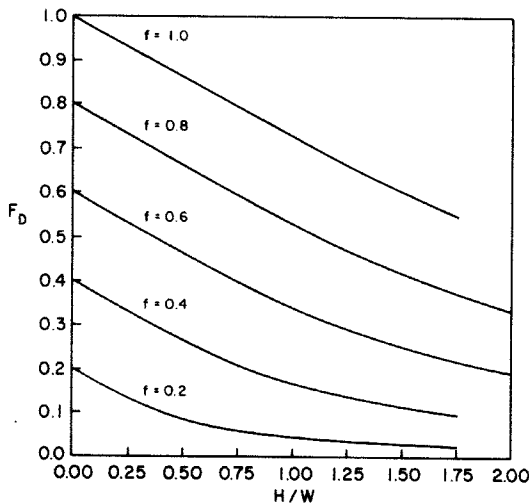


FIG. 6. Drag flow shape factors for partially filled channels in a single-screw extruder.

this is accomplished by increasing the screw speed or increasing the number of parallel channels on the screw.

The concentration of the volatile component at the exit of the devolatilization zone can be computed using Eqs. (26) and (32) along with an equation developed around a mass balance across a differential element [Eq. (11), for example].

Thus, we find

$$\ln \left(\frac{w_2 - w^*}{w_1 - w^*} \right) = \frac{-2Sa_b\lambda\rho}{L\sqrt{\pi}} (DpN)^{1/2} \left[(1-f)^{1/2} + \frac{2}{\pi} \left(\frac{H}{W} \right)^{1/2} \right] \quad (36)$$

when $w_i = w^*$. Latinen (1962) took account of axial dispersion, or back-mixing, in his mass balance and thus introduced the Peclet number, which he simply wrote as

$$Pe = u\lambda/E \quad (37)$$

In so doing, he developed (in our nomenclature) the following differential equation

$$\frac{d^2w}{d\bar{l}^2} - Pe \frac{dw}{d\bar{l}} - Pe \left[\left(\frac{k_L A_T}{\lambda} \right)_{av} \frac{\lambda\rho}{L} \right] (w - w_i) = 0 \quad (38)$$

If penetration theory is appropriate,

$$\left(\frac{k_L A_T}{\lambda} \right)_{av} = BN^{1/2} \quad (39)$$

For large values of the Peclet number, Eq. (38) reduces to Eq. (11) and the exit concentration is strongly influenced by the dimensionless group $BN^{1/2}\lambda\rho/L$ (Fig. 7). On the other hand, at low values of the Peclet number the exit concentration is hardly influenced by this dimensionless group, which means that the exit concentration is relatively insensitive to changes in the flow rate and screw speed. We shall return to this point momentarily.

Roberts (1970) has identified the exact mathematical form for axial dispersion in a screw extruder by noting that the devolatilized film is remixed with material in the bulk at an upstream position which can be determined exactly once the geometry of the system is specified. According to Roberts, the Peclet number is given by

$$Pe = 2\lambda(1 - \beta_2\Delta)/\beta_2\Delta^2 \quad (40)$$

$$\beta_2 = [V_{bx}\delta(1 - \varepsilon)]/2L \quad (41)$$

$$\Delta = (\theta_f L/WfH) + (\pi^2 D_b^2 + t^2)^{1/2} \quad (42)$$

and can be computed exactly without having to make an independent estimate. As pointed out by Roberts, the Peclet number will be a function

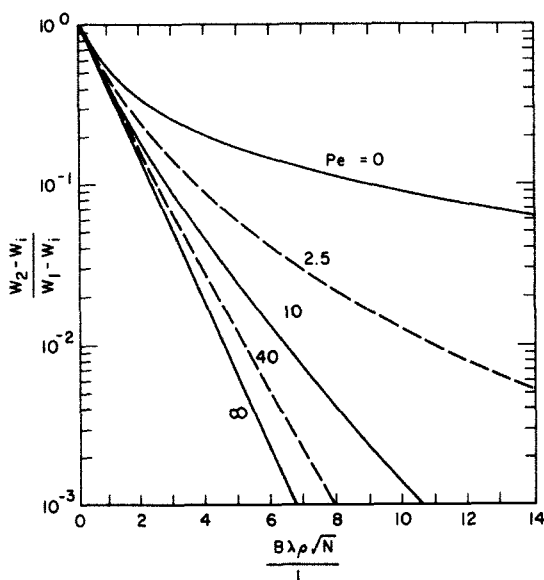


FIG. 7. Variation of the dimensionless exit concentration of the volatile component as a function of screw speed, liquid flow rate, and Peclet number. Curves were computed using Eqs. (38) and (39).

of the efficiency of the devolatilization process. If $\varepsilon = 1.0$, the Peclet number will be infinite, but if $\varepsilon = 0$, the Peclet number will have a minimum value.

2. Experimental Studies

The results of experimental studies aimed at assessing the validity of Eq. (32) have, for the most part, been inconclusive. Although the exact reasons for this are not entirely clear, certain differences between the experimental conditions employed and those upon which the model is based can be readily identified. In most studies the diffusion coefficient for the particular polymeric solution used was not known and was necessarily treated as an adjustable parameter in the theory. A subjective judgment was thus required as to whether the value of the diffusivity which described the data best was a reasonable one. Generally speaking, the resulting values were unrealistically high.

A second reason is related to an assumption employed in the reduction of the experimental data. Here, the equilibrium concentration of the volatile component in the liquid phase, w^* , was often assumed to be negligible in comparison with w , the concentration in the liquid phase. An assump-

tion of this nature would be valid if Henry's constant were large enough so that $w \gg P/H_c$. If Henry's constant is small, that is, if the volatile component is highly soluble in the polymer, such an assumption would be questionable.

Finally, a number of experimental studies have been conducted in a pressure range where the polymeric solution could "boil." The vapor bubbles thus created would provide a much larger surface area for mass transfer than the surface area of the wiped film alone. And therefore, for fixed values of the diffusivity and the driving force, predicted values for mass transfer rates would be substantially lower than the measured values. Conversely, for a fixed mass transfer rate and driving force, use of the wiped film surface area alone would require unusually high values of the diffusivity in order to obtain agreement between theory and experiment.

In a study in which styrene was stripped from polystyrene, Latinen (1962) concluded that his theory correctly described the dependence of mass transfer rates on screw speed and flow rate. This conclusion was based on the agreement obtained between the measured and predicted exit concentration of styrene over a broad range of screw speeds and flow rates (Fig. 8). But, agreement between the theoretical expression and the experimental data was obtained using a diffusion coefficient of the order of $3 \times 10^{-9} \text{ m}^2 \text{ sec}^{-1}$, at 200°C a value which is unrealistically high for this system. If the system ethylbenzene-polystyrene—which has a diffusion

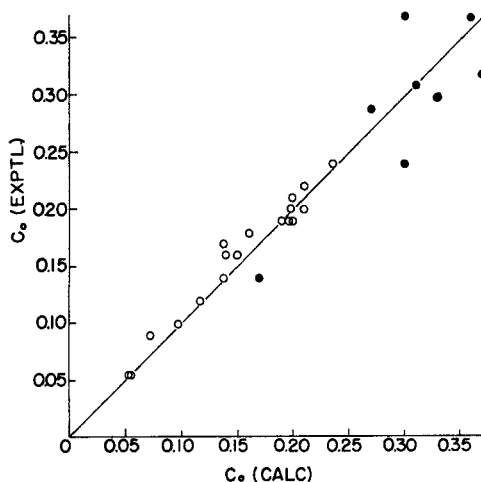


FIG. 8. Comparison of the measured and predicted exit concentrations obtained by Latinen for a styrene-polystyrene system. Reproduced with permission from Latinen (1962). Copyright 1982 American Chemical Society.

coefficient of 5×10^{-12} m²/sec at 200°C (Duda *et al.*, 1982)—is used as a basis for comparison, the Latinen value is seen to be three orders of magnitude too large. In view of the fact that Latinen's experiments were conducted at pressures which were lower than the equilibrium partial pressure of styrene in the feedstream ($H_c = 20$ –65 atm, $T = 200$ –250°C, $w_1 \leq 0.008$), vapor bubbles may have been formed and, if so, the true surface area for mass transfer would have been larger than the values used by Latinen. This, of course, would result in a high value for the diffusivity.

A second factor which may have played a role in the conclusions drawn by Latinen was that a low Peclet number (~ 10) was also required to obtain agreement with the theory. As pointed out earlier, the lower the Peclet number the less sensitive is the exit concentration to changes in the screw speed, and this could bring into question any conclusion regarding the linear dependence on the square root of screw speed.

Coughlin and Canevari (1969) have published experimental data on two systems at a variety of operating conditions: the extraction of xylene from polypropylene and the extraction of methanol from polypropylene. These studies were conducted in a single screw extruder at low pressures and w^* was assumed to be small in comparison with w . Coughlin and Canevari developed a model which they used in conjunction with their experimental data to obtain a value for the diffusion coefficient. The values that they computed were of the order of 10^{-5} m²/sec, which obviously means that the model is incorrect. Coughlin and Canevari also computed values for the mass transfer coefficient and found it to be *independent* of screw speed. This observation is particularly noteworthy since they saw no evidence of bubble formation.

We have used the Coughlin and Canevari data to compute values of $k_L a/a_b$ so as to put their results on a basis consistent with Eq. (32). We used the following equations for these calculations:

$$\frac{k_L a}{a_b} = \frac{L(w_1 - w_2)}{\lambda S a_b \Delta w_{lm} \rho} \quad (43)$$

$$\Delta w_{lm} = [(w_1 - w^*) - (w_2 - w^*)] \left[\ln \left(\frac{w_1 - w^*}{w_2 - w^*} \right) \right]^{-1} \quad (44)$$

or, for $w^* = 0$,

$$k_L a/a_b = (L/\pi D_b \lambda) \ln(w_1/w_2) \quad (45)$$

The results of these calculations are plotted in Fig. 9, where $k_L a/a_b$ is also seen to be independent of screw speed for both systems studied.

We are unable to critically comment on the numerical values of $(k_L a/a_b)$ shown in Fig. 9 since Eq. (32) cannot be used to make an independent

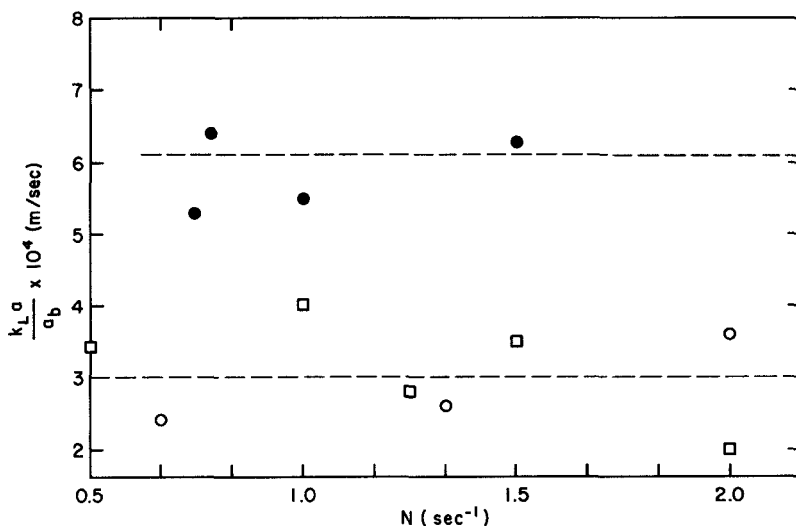


FIG. 9. Values of $k_L a / a_b$ computed from the experimental data obtained by Coughlin and Canevari (1969) in a single-screw extruder: xylene-polypropylene (□, ○); methanol-polypropylene (●). $D_b = 4.5$ (●, □), 3.5 (○) inches.

estimate because of the invariance with screw speed. Furthermore, Coughlin and Canevari (1969) is the only published work on devolatilization in single screw extruders that provides enough information for $(k_L a / a_b)$ to be computed, and so it is also not possible to compare these results with results obtained in separate studies. Insofar as future studies are concerned, however, the results shown in Fig. 9 should serve as a basis for comparison.

The extraction of styrene from polystyrene has also been studied by Biesenberger and Kessidis (1982). This study consisted of two sets of experiments. One set was conducted at atmospheric pressure, a pressure well in excess of the equilibrium partial pressure of styrene in the feed-stream. The stripping agent used was nitrogen. The other set was conducted at a pressure of 1 Torr, which was found, by visual observation, to be low enough for bubble formation and entrainment.

Biesenberger and Kessidis were able to correlate their experimental data at atmospheric pressure in terms of $N^{1/2}$ in accordance with Eq. (36) [their Eqs. (4)–(9)], but the diffusion coefficient which they computed using Eq. (36) along with the experimental data was found to be roughly $D = 10^{-9} \text{ m}^2 \text{ sec}^{-1}$ at 177°C. Again, if the ethylbenzene-polystyrene system is used as a basis for comparison, Duda *et al.* (1982) report a value of $3 \times 10^{-11} \text{ m}^2/\text{sec}$ at 178°C, which is considerably smaller than the value obtained by Biesenberger and Kessidis (1982). In the experiments con-

ducted under vacuum, experimentally measured values for the extraction efficiency were found to be independent of screw speed.

The experiments of Latinen (1962) and those of Biesenberger and Kessidis (1982), when viewed side by side (Table I), present an interesting contradiction, for which there is no obvious explanation. Both sets of investigators used the same polymer-monomer system, both used single-screw extruders, and both ran experiments at reduced pressure. Latinen found that the extraction efficiency depended on $N^{1/2}$, whereas Biesenberger and Kessidis found the efficiency to be independent of screw speed.

B. MASS TRANSFER COEFFICIENTS FOR TWIN-SCREW EXTRUDERS

In twin-screw extruders, two screws lie side by side in a common barrel that has a figure-eight pattern (Hwang, 1982). These screws may rotate in the same direction (corotating) or in opposite directions (counterrotating) and may be nonintermeshing, partly intermeshing, or fully intermeshing. In nonintermeshing twin-screw extruders, the distance between the axes of the screws (the centerline distance) is equal to or greater than the screw

TABLE I
COMPARISON OF EXPERIMENTAL CONDITIONS AND RESULTS FOR THE STRIPPING OF STYRENE FROM POLYSTYRENE IN SINGLE-SCREW EXTRUDERS

Condition	Latinen (1962)	Biesenberger and Kessidis (1982)	
Pressure (mm Hg)	5-20	1	760
Temperature (°F)	400-480	400	350
Rotational speed (min ⁻¹)	60-244	10-100	10-100
Extraction efficiency	Varies as $N^{1/2}$	Independent of N	Varies as $N^{1/2}$
w_1	≤ 0.008	0.0054	0.0054
H_c (atm, $T = 400^\circ\text{F}$)	19.7	13.6	13.6
D_b (inches)	2.5	3.0	3.0
ϕ°	18	17.7	17.7
Pe	5-12	∞	∞
λ (inches)	10-25	12.2	12.2
D m ² /sec ^a	3×10^{-9} ($T = 200^\circ\text{C}$)		10^{-9} ($T = 177^\circ\text{C}$)

^a Computed from the experimental data relating extraction efficiency and screw speed. Diffusivities determined by Duda *et al.* (1982) are $D = 5 \times 10^{-12}$ m²/sec at 200°C and 3×10^{-11} m²/sec at 178°C.

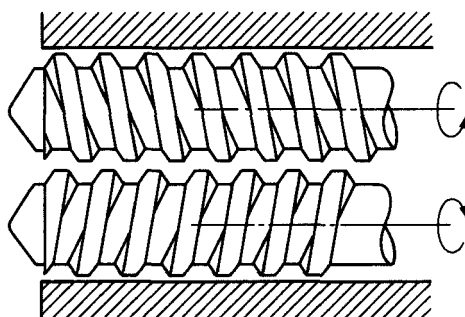


FIG. 10. Schematic representation of nonintermeshing counterrotating twin-screw extruder.

diameter. These extruders have neither self-wiping action nor positive conveying characteristics, and are usually designed to have counterrotating screws (Fig. 10).

In intermeshing twin-screw extruders (Figs. 11 and 12), the centerline distance is somewhat less than the screw diameter and the flights of one screw protrude into the channels of the other screw. In intermeshing, counterrotating twin-screw extruders, where the channels on each screw are sealed off by the flights of its mate, a positive conveying action results and these extruders operate much like gear pumps (Fig. 11). In self-wiping intermeshing, corotating twin-screw extruders the screw configuration is such that complete self-wiping between the screws can be achieved (Fig. 12). The channels are open in the down-channel direction and closed in the cross-channel direction. In these extruders, the screw crests of the corotating screws are connected together over the free wedge area. No positive conveyance—such as that which occurs in the intermeshing counterrotating extruders—is present, although partial positive conveyance is achieved because of the influence of the wedge resistance. The

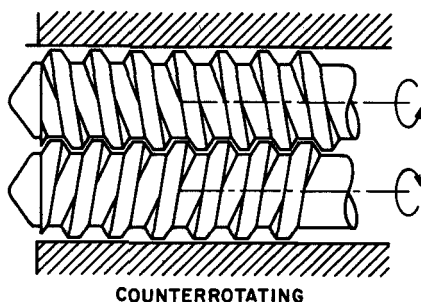


FIG. 11. Schematic representation of intermeshing counterrotating twin-screw extruder.

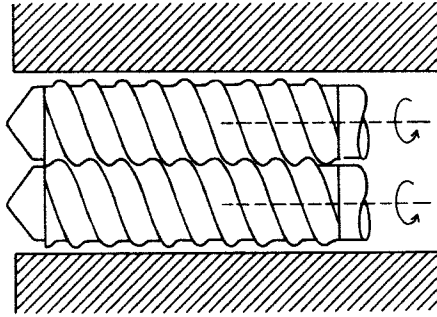


FIG. 12. Schematic representation of intermeshing corotating twin-screw extruder.

material in the parts of the channels which are away from the intermeshing zone is conveyed forward by the frictional force exerted by the barrel on the material. As the material reaches the intermeshing zone, it is brought into the intermeshing zone and then picked up by the other screw and conveyed forward further. Thus, the material is transported from the inlet to the discharge in a figure-eight pattern from one screw to the other as it moves toward the discharge.

Insofar as devolatilization processes are concerned, the three types of

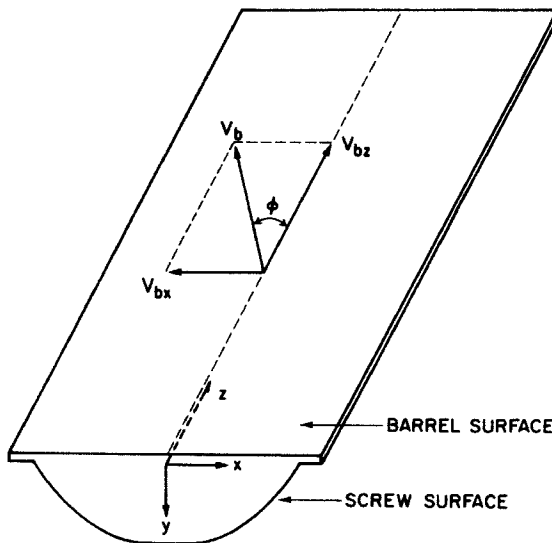


FIG. 13. Isometric view of one channel of a fully intermeshing corotating twin-screw extruder.

twin-screw extruders just described have been used, to some extent, in commercial operations. But, in view of the fact that the published scientific literature has dealt mainly with self-wiping, intermeshing corotating twin-screw extruders, we shall restrict our discussion to extraction operations in this type of extruder.

1. Theory

The constraint that the tip of one screw element wipe the flank of its mate in self-wiping, corotating twin-screw extruders leads to a unique relationship for the shape of the screw channel (Booy, 1978, 1980). Figure 13 is an isometric view of this channel and Fig. 14 is a cross section of the channel in a plane that is perpendicular to the plane which defines the helix angle. Figure 14 shows the actual shape of the channel, which is described by the following expressions:

$$h(x) = H = 2R_s - C_L \quad \text{for } 0 \leq x \leq \frac{e}{2} \quad (46)$$

$$h(x) = R_s \left\{ 1 + \cos \left[\frac{2\pi(x - e/2)}{t_s \cos \phi} \right] \right\} - \left\{ C_L^2 - R_s^2 \sin^2 \left[\frac{2\pi(x - e/2)}{t_s \cos \phi} \right] \right\}^{1/2} \quad \text{for } \frac{e}{2} \leq x \leq \frac{w}{2} \quad (47)$$

$$h(x) = 0 \quad \text{for} \quad \frac{W}{2} \leq x \leq \frac{W}{2} + \frac{e}{2} \quad (48)$$

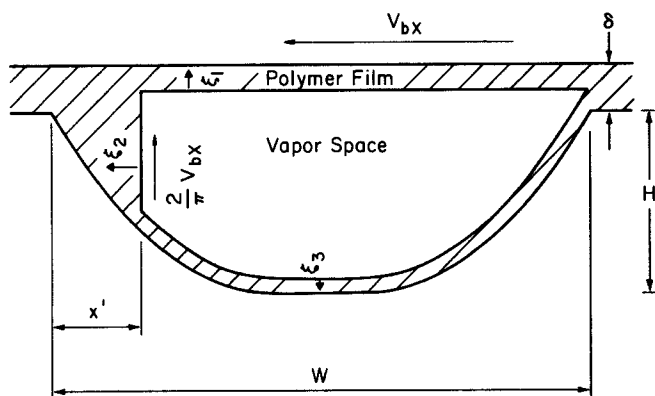


FIG. 14. Partially filled channel of intermeshing, corotating twin-screw extruder. Mass transfer occurs from the films on the screw and the barrel and from the surface of the nip.

The quantities W , e , t_s , and α are given by the following expressions:

$$W = [(t_s \cos \phi)/p] - e \quad (49)$$

$$t_s = \pi D_s \tan \phi \quad (50)$$

$$e = (t_s \alpha \cos \phi)/2\pi \quad (51)$$

$$\alpha = (\pi/p) - 2 \cos^{-1}(\rho_c/2) \quad (52)$$

The same assumptions and equations used in developing an expression for $k_L a/a_b$ for single-screw extruders can be used to describe mass transfer rates in the type of corotating twin-screw extruder considered here. In this regard, Fig. 14 is relevant, and $k_L a/a_b$ will be given by Eq. (53):

$$\frac{k_L a}{a_b} = \left(\frac{4D}{\pi \theta_f} \right)^{1/2} \left[\frac{a_f}{a_b} + \left(\frac{\theta_f}{\theta_n} \right)^{1/2} \left(\frac{a_n}{a_b} \right) + \left(\frac{\theta_f}{\theta_s} \right)^{1/2} \left(\frac{a_s}{a_b} \right) \right] \quad (53)$$

When the holdup is low ($\frac{x'}{W} \rightarrow 0$), Eq. (53) reduces to

$$k_L a/a_b \approx (4D/\pi \theta_f)^{1/2} [1 + (a_s/a_b)]$$

which can be written as

$$\frac{k_L a}{a_b} \approx \frac{2}{\sqrt{\pi}} \left[\frac{DpN}{(\frac{1}{2} + p/\pi \cos^{-1} \frac{1}{2} \rho_c)} \right]^{1/2} \left[1 + \frac{a_s}{a_b} \right] \quad (54)$$

since the exposure time is given by

$$\theta_f = (pN)^{-1} [\frac{1}{2} + (p/\pi) \cos^{-1} \frac{1}{2} \rho_c]$$

and $\theta_s \approx \theta_f$.

One major difference between single-screw extruders and fully wiping, corotating twin-screw extruders is that in the latter, a film is formed on the surfaces of the screws in addition to that on the barrel wall, and this greatly increases the surface area for mass transfer. A second major difference is due to the intermeshing zone where a significant degree of mixing is believed to occur. Mixing in the intermeshing zone thus exists along with the mixing that occurs in the screw channel because of the cross-channel motion, and therefore the concentration of volatile component in the bulk should be more uniform prior to each exposure to the vapor phase. This would have the effect of maximizing the driving force for the interphase transfer at the beginning of each exposure. In single-screw extruders where mixing occurs only in the channels, the concentration of volatile component in the bulk may not be uniform prior to each exposure and the rate of mass transfer would therefore be expected to be significantly reduced.

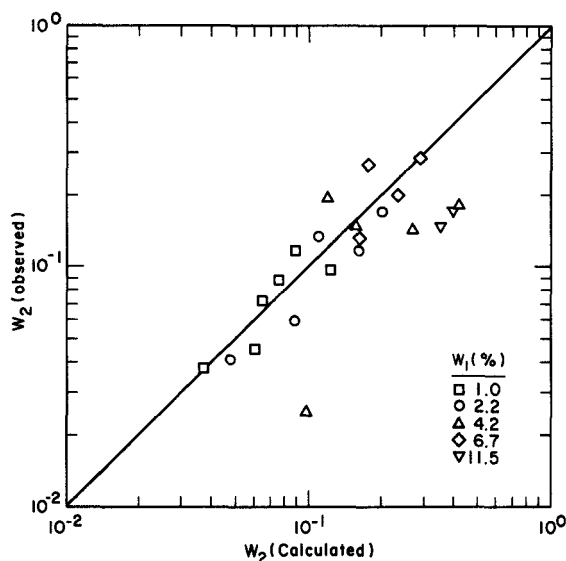


FIG. 15. Comparison of the measured and predicted exit concentrations obtained by Todd for a polystyrene polymer containing ethylbenzene as the volatile component. Data were obtained in a twin-screw extruder. From Todd (1974).

2. Experimental Studies

Published experimental studies on devolatilization rates in twin-screw extruders fall into two categories: studies conducted at pressures in excess of the equilibrium partial pressure of the volatile component in the feedstream using an inert gas as the stripping agent and those conducted at pressures lower than the equilibrium partial pressure of the volatile component.

One of the earliest published studies on extraction in twin-screw extruders was conducted by Todd (1974). In this work devolatilization was conducted under vacuum using two different polymeric systems, polystyrene in one and polyethylene in the other. In the case of polystyrene, styrene was not used as the volatile component so as to avoid problems associated with further polymerization or depolymerization; instead, use was made of mixtures of thiophene and toluene or ethylbenzene. Todd found good agreement between the measured exit concentrations of the volatile component and the predicted values using $Pe = 40$ in the solution to Eq. (38) (see Fig. 15). The value of B in Eq. (39) was not reported and it is not known whether a value was chosen to provide a fit with the data or whether it was known *a priori*. In any event, what is clear is that the exit concentration varies with $N^{1/2}$, which suggests that mass transfer is occur-

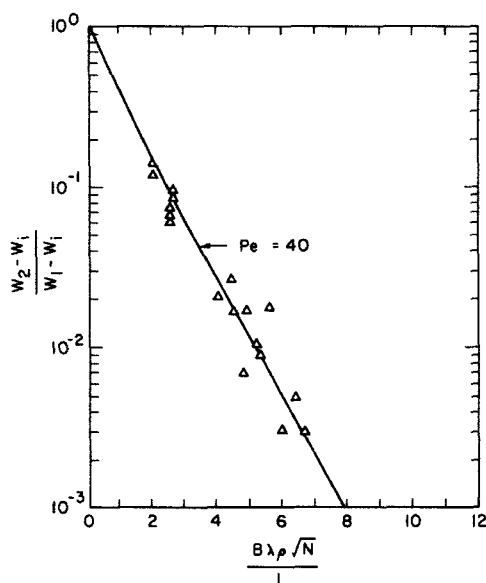


FIG. 16. Variation of the measured exit concentrations as a function of screw speed and liquid flow rate for the system cyclohexane-polyethylene. Solid line is the theoretical prediction and is based on Eqs. (38) and (39). From Todd (1974).

ring through a wiped film and that the use of reduced pressures introduced no spurious effects.

In the case of polyethylene, the volatile component was cyclohexane and here, too, good agreement was obtained between the measured exit concentration and the predicted values using $Pe = 40$ in the solution of Eq. (38) (see Fig. 16). These data also suggest that mass transfer is occurring by molecular diffusion through a wiped film since the exit concentration varies with $N^{1/2}$ in accordance with the theory. It is somewhat disconcerting, however, that the value of B used in the theoretical expression was not reported, and the question naturally arises as to whether realistic values were used to obtain the fit with the data.

Collins *et al.* (1983) have conducted the most definitive studies thus far on devolatilization. These studies were conducted at atmospheric pressure in a corotating twin-screw extruder with a transparent barrel using a polybutene-Freon system. Nitrogen was used as the stripping agent and caused to undergo both cocurrent and countercurrent flow. Mass transfer coefficients, i.e., $k_L a/a_b$, were computed from the experimental data using Eq. (43). In these studies both the diffusion coefficient and Henry's constant were known, and therefore, it was not necessary to treat the diffusion coefficient as an adjustable parameter, nor was it necessary to as-

sume that w^* was zero. Consequently, a quantitative comparison between theory and experiment could be made. These investigators found that $k_L a/a_b$ varies with $N^{1/2}$ in accordance with Eq. (54). However, the theoretical prediction [Eq. (54) with $a_s/a_b \ll 1$] was found to be higher than the experimental data by a factor of about 2 which they attributed to their assumption that the film on the barrel was continuous. In reality, $a_f/a_b \ll 1$.

Werner (1980) has studied devolatilization in corotating twin-screw extruders when the volatile component was stripped from the polymeric solution by applying a vacuum to the system. Rough estimates of the equilibrium partial pressure of the volatile component in the feedstream for each of the systems studied by Werner indicate that this pressure was less than the applied pressure, which means that bubbles could have been formed. Figure 17 shows the influence of the externally applied pressure on the exit concentration for a methyl methacrylate–poly(methyl methacrylate) system of fixed concentration. Note that the exit concentration decreases as the pressure is decreased, but seems to approach an asymptotic value at the lowest pressures studied. Werner also reported that at a fixed flow rate and feed concentration the exit concentration did not vary with screw speed (over the range 150–300 min^{-1}), which also suggests that $k_L a/a_b$ is independent of screw speed. Figure 18 is a plot of data obtained by Werner on an ethylene–low-density poly(ethylene) system and also shows that decreases in the applied pressure result in decreases in the exit concentration, but here a lower asymptote is not observed.

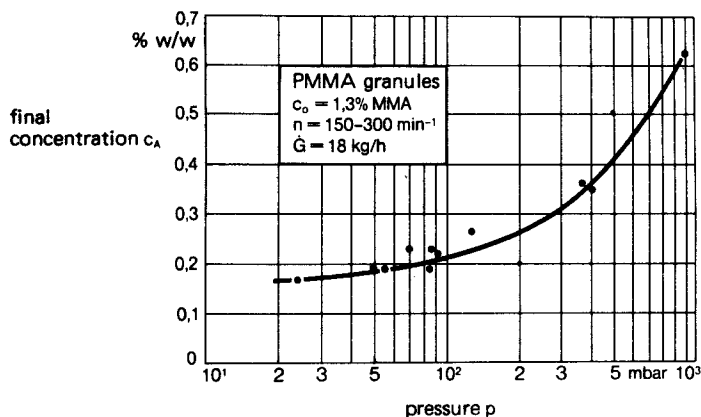


FIG. 17. Experimentally measured values of the exit concentration as a function of pressure for a polymeric solution consisting of methyl methacrylate–poly(methyl methacrylate). Data were obtained by Werner using a twin-screw extruder. (Reproduced with permission from Werner, 1980.)

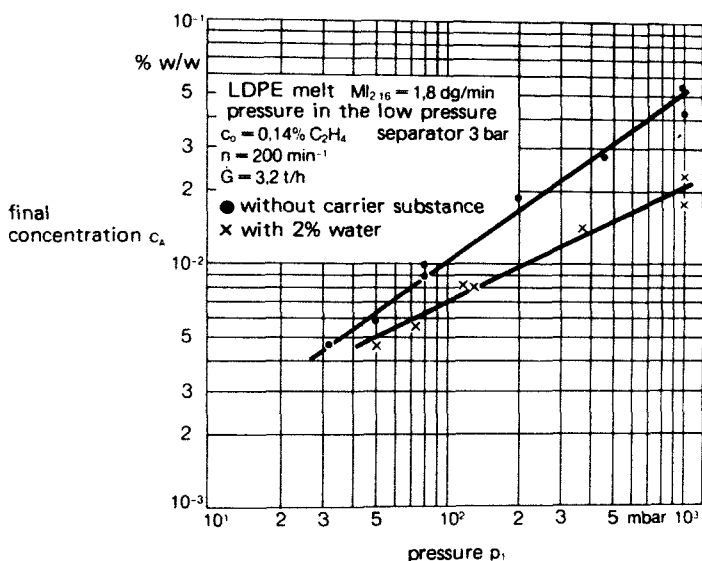


FIG. 18. Experimentally measured values of the exit concentration as a function of pressure and water content for the system ethylene–low-density poly(ethylene). Data were obtained in a twin-screw extruder by Werner. (Reproduced with permission from Werner, 1980.)

The decrease in the exit concentration with decreases in the extraction pressure seen in Figs. 17 and 18 is a consequence of the fact that the driving force for mass transfer is directly related to the partial pressure of the volatile component in the vapor phase, which, in this case, is constant and equal to the extraction pressure. In fact, reasonably good agreement between the data in Fig. 17 and the predictions of Eq. (38) can be obtained provided it is assumed that the dimensionless group $(k_L A_T / \lambda)_{av} (\lambda \rho / L)$ is independent of pressure. This point is illustrated in Fig. 19, which is a plot of Eq. (38) for $Pe = \infty$. The value used for $(k_L A_T / \lambda)_{av} (\lambda \rho / L)$ was chosen so as to obtain the asymptotic value of w_2 in Fig. 17.

Using the data shown in Fig. 17, Werner computed an average value of $2 \times 10^{-4} \text{ m sec}^{-1}$ for the mass transfer coefficient k_L by comparing these data with the solution to Eq. (38) for Pe numbers in the range 20–40, although it is not clear what value Werner used for the surface area. We have used Eq. (43), which assumes that $Pe = \infty$, to compute a value for $k_L a / a_b$ for the MMA–PMMA data shown in Fig. 17. The length of the extraction zone was not reported, and in our calculation the total length of the extruder was used ($\lambda = 0.65 \text{ m}$). The upper limit on $k_L a / a_b$ was computed to be $1.2 \times 10^{-2} \text{ m sec}^{-1}$ for the experimental runs conducted at a

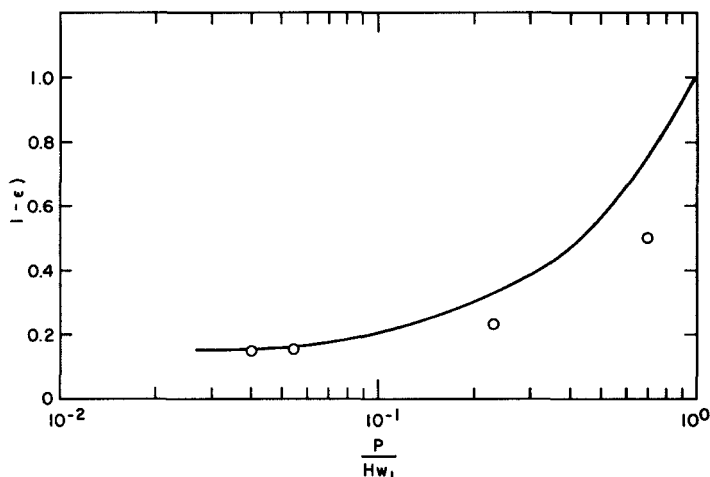


FIG. 19. Theoretical prediction (—) of the variation of the exit concentration of a volatile component with extraction pressure. The prediction is based on Eq. (38) with $[(k_L a)_{\text{avg}} \lambda \rho] / L = 0.115$. The circles are selected experimental (MMA/PMMA) data points taken from Fig. 17.

pressure of 100 mbar ($w_1 = 0.013$, $H_c = 10^5$ mbar). Since the actual length of the extraction section was probably less than the total length of the extruder, $k_L a / a_b$ should be less than $1.2 \times 10^{-2} \text{ m sec}^{-1}$. The value for k_L obtained by Werner and the value for $k_L a / a_b$ obtained from our calculations can be reconciled if $a / a_b \leq 60$. This means that either entrained bubbles were present or that the surface area of the wiped film on the screws played a dominant role.

IV. Bubble Entrainment and Enhanced Mass Transfer

Mass transfer in polymeric solutions by molecular diffusion is a comparatively slow process, and in extraction equipment where mass transfer occurs through a thin wiped film, inordinately large equipment surface areas are often required in order to obtain substantial rates of mass transfer. In commercial practice when this situation occurs, the required surface areas may, instead, be obtained by either one of two methods, both of which involve reducing the pressure in the extraction zone. In one approach the extraction pressure is fixed at a value which is less than the equilibrium partial pressure of the monomer or solvent in the polymeric solution fed to the extraction zone. In these circumstances gas bubbles

composed of the pure monomer or solvent can be formed (nearly) spontaneously by what is believed to be homogeneous nucleation. Thereafter, the monomer or solvent diffuses from the polymeric solution to the surfaces of these bubbles, which grow and ultimately rupture. Figure 20 shows the presence of such bubbles in an extruder (MacKenzie, 1979).

In a second approach, a stripping agent that is immiscible with the polymer is introduced into the polymeric solution under pressure at a position upstream from the extraction zone. If the vapor pressure of the stripping agent is higher than the equilibrium partial pressure of the solvent or monomer, gas bubbles composed mainly of the stripping agent will be formed when the mixture enters the extraction zone. Subsequently, monomer or solvent will diffuse to the surfaces of these bubbles which will grow and ultimately rupture. Two alternative advantages accrue from the use of a stripping agent. Higher extraction pressures can be employed if a stripping agent is used, or lower values of w^* can be obtained since

$$w^* = (P_a - P_f^0)/H_c \quad (P_a \geq P_f^0) \quad (55)$$

The net effect of this reduction, of course, is to increase the driving force for mass transfer in the liquid phase.

The beneficial effect that the introduction of water has on the extraction of ethylene from low-density polyethylene is shown in Fig. 18. The reduction in the exit concentration of ethylene is substantial, especially at the higher pressures, and dramatically illustrates the increase in mass transfer rates which results from the introduction of an immiscible stripping agent.

A. PHYSICAL AND MATHEMATICAL MODEL

Consider a situation in which a concentrated polymeric solution enters the extraction zone of, say, an extruder in circumstances when the pressure in the extraction zone, P_a , is less than the equilibrium partial pressure of the volatile component in the feed solution. Under these conditions the solution will be supersaturated at the extraction pressure, flashing of the volatile component will occur, gas bubbles of radius R_0 will be formed, and the concentration will immediately fall from w_1 to w_0 . If bubble formation occurs by homogeneous nucleation, the rate at which these bubbles will be formed per unit volume of solution should depend on the difference between the equilibrium partial pressure of the volatile component and the devolatilization pressure. Since this pressure difference is greatest when the solution first enters the extraction zone, the rate of formation of bubbles will at first be high; but as devolatilization pro-

ceeds and the concentration falls, this pressure difference will decrease. The rate at which bubbles are formed will also decrease.

When it is assumed that the pressure inside the gas bubbles at the time they are formed is the equilibrium pressure, then

$$P_{g0} = H_c w_0 \quad (56)$$

and, because $P_{g0} > P_a$, a mechanical driving force will be established which causes the bubbles to expand. When expansion begins, the gas pressure in the bubbles P_{g0} will decrease and a thermodynamic driving force will be established, again in accordance with Henry's law, and the volatile component will begin to diffuse to the surface of these bubbles where it will evaporate. This, in turn, reestablishes the mechanical driving force causing further expansion. Eventually, a state of both mechanical and thermodynamic equilibrium will be reached and the bubbles will attain an equilibrium radius R_e , provided rupture does not occur in the meantime.

During the period when the bubbles are growing, a dynamic situation exists in which bubbles are continually being formed and destroyed. We might anticipate, then, that the number of bubbles per unit volume of solution is rate dependent and that

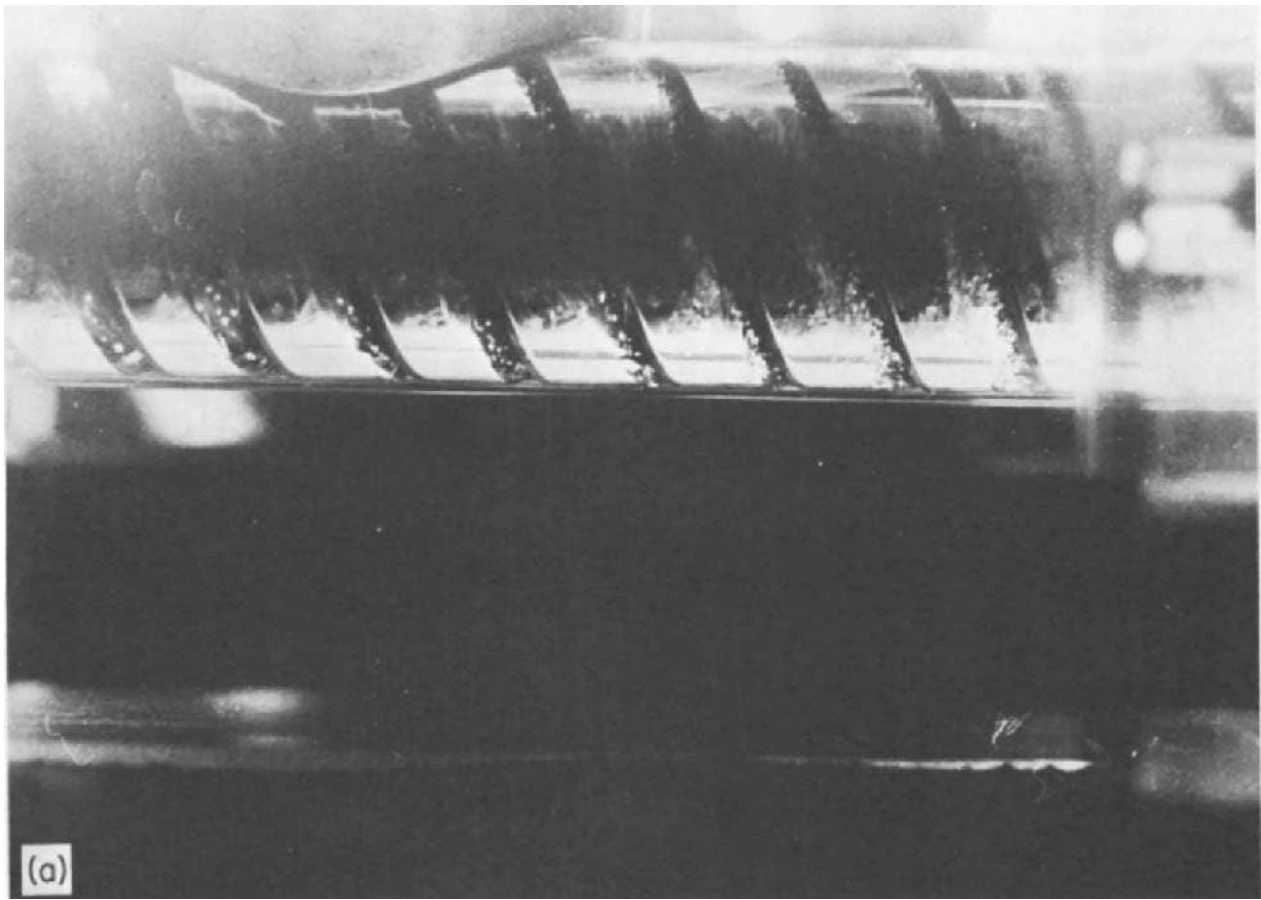
$$d\hat{N}/dt = J_F - J_D \quad (57)$$

The exact form of J_F , the number of bubbles nucleated per unit volume per unit time, is not known since there appears to be no published scientific studies which deal with nucleation rates in concentrated polymeric solutions at pressures below the equilibrium partial pressure. Blander and Katz (1975) have studied nucleation rates of pure liquids as a function of temperature at atmospheric pressure and Prud'homme (1982) has studied nucleation rates of polymeric solutions containing up to 0.60 weight fraction of polymer as a function of temperature, concentration, and polymer molecular weight at atmospheric pressure. Both sets of investigators concluded that nucleation rates seem to follow the equation

$$J_F = C \exp \left[\frac{-16\pi\sigma^3}{3kT(P_v - P_a)^2} \right] \quad (58)$$

In the absence of further evidence, a reasonable assumption is that nucleation rates in concentrated polymeric solutions as a function of pressure would also be described by Eq. (58), with P_v replaced by $H_c w$. Thus, we see that as devolatilization proceeds, w decreases and the rate at which bubbles are formed decreases.

Bubbles can disappear from the solution for a number of reasons: They can coalesce; they can simply escape from the surface of the solution; or



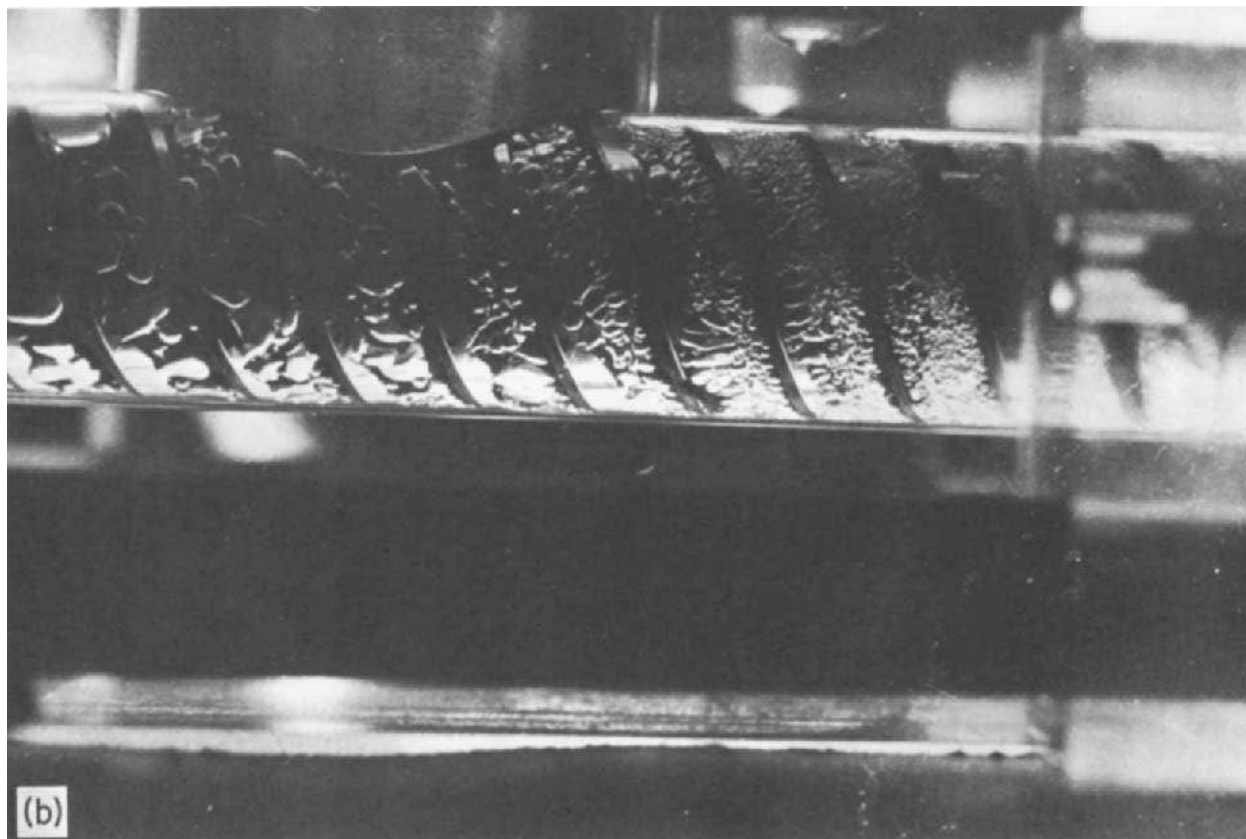


FIG. 20. Photographs taken through a transparent barrel section in a twin-screw extruder showing the presence of bubbles at an extraction pressure of 8 Torr (MacKenzie, 1979). The polymeric solution is heptane-poly(dimethyl siloxane). (a) Screw rotational speed is 15 min^{-1} . Note how bubbles are dispersed on pushing side of flight. Flow is from right to left. (b) Stationary screw. Note how the bubbles shown in (a) coalesce when the screw is stopped.

they can be mechanically ruptured. This means that J_D , the rate at which bubbles disappear per unit volume of solution, is specific to the process and the type of equipment in which the extraction operation is being conducted. In screw extruders, for example, the disappearance of bubbles could result from the mechanical action of the rotating screw, whereas in falling strand devolatilizers, where no mechanical action is present, bubble rupture may be dictated by the rheological nature of the polymeric solution (Newman and Simon, 1980). In any case, the extraction efficiency is directly dependent on the rate at which the bubbles are ruptured:

$$\varepsilon = \frac{4\pi M}{3K_T w_1 \rho} \int_0^t J_D P_g R^3 dt \quad (59)$$

And, unless the volatile component is allowed to escape from the solution after bubble rupture, no devolatilization will occur.

Equation (59), which is written around a spherical bubble, requires knowledge as to how P_g and R vary with time. The development of expressions for these variables proceeds along the following lines. First, a mass balance is made on each gas bubble:

$$4\pi R^2 N_b = \frac{d}{dt} \left(\frac{m_g}{M} \right) \quad (60)$$

which, when combined with the ideal gas law, leads to

$$N_b = \frac{1}{K_T} \left(\frac{1}{3} r \frac{dP_g}{dt} + P_g \frac{dR}{dt} \right) \quad (61)$$

If the ideas are used that an infinite sea of liquid surrounds each gas bubble and a pseudo-steady state exists, then the molar flux can be described by the familiar expression

$$N_b = (D/R)(\rho/M)(w - w_i) \quad (62)$$

Combining Eqs. (61) and (62) results in

$$\frac{1}{K_T} \left(\frac{1}{3} R \frac{dP_g}{dt} + P_g \frac{dR}{dt} \right) = \frac{D}{R} \frac{\rho}{m} \left(w - \frac{P_g}{H_c} \right) \quad (63)$$

A current mass balance on the volatile component results in an expression for w :

$$w = w_1 - \frac{4M\hat{N}P_g R^3}{3\rho K_T} - \frac{4\pi M}{3\rho K_T} \int_0^t J_D P_g R^3 dt \quad (64)$$

which upon substitution into Equation (63) gives the following result:

$$\begin{aligned} \frac{1}{K_T} \left(\frac{R}{3} \frac{dP_g}{dt} + RP_g \frac{dR}{dt} \right) \\ = \frac{D\rho}{M} \left[\left(w_1 - \frac{P_g}{H_c} \right) - \frac{4\pi M}{3K_T} \left(\dot{N}P_g R^3 + \int_0^t J_D P_g R^3 dt \right) \right] \end{aligned} \quad (65)$$

Equation (65), the working equation for mass transfer, contains two independent variables P_g and R . A second equation can be obtained from momentum transfer considerations. In the absence of surface tension forces, the momentum equations for a Newtonian fluid reduce to

$$4\eta \, dR/dt = (P_g - P_a)R \quad (66)$$

Equations (57)–(59), (65), and (66) thus constitute the governing equations for predicting the extraction efficiency when mass transfer is enhanced by the presence of entrained bubbles.

1. Simplified Analysis for Constant Bubble Population

Some useful insight can be developed concerning the influence of material properties and process conditions on devolatilization efficiency by considering the special case when the number of bubbles per unit volume of solution is constant. To fix ideas, assume that all bubbles are formed instantaneously when the solution enters the extraction zone and that no bubbles are ruptured until the very end of the process when all rupture simultaneously. Then the rate of formation can be expressed by

$$J_F = \dot{N}_0 \delta(t), \quad \delta(t) = 0, \quad t \neq 0 \quad (67)$$

and the rate of destruction by

$$J_D = \dot{N}_0 \delta(t - t^*), \quad \delta(t - t^*) = 0, \quad t \neq t^* \quad (68)$$

where $\delta(t)$ and $\delta(t - t^*)$ are Dirac delta functions. When the number of bubbles per unit volume of solution is constant, a well-defined equilibrium bubble radius exists and can be used to scale the governing differential equations (Amon and Denson, 1983). The overall mass balance, the rate of mass transfer, and the rate of momentum transfer are, respectively, given by

$$\frac{w}{w_1} = 1 - \frac{(1 - \tilde{P}_a)\tilde{P}_g\tilde{R}^3}{\tilde{P}_a(1 - \tilde{R}_0^3)} \quad (69)$$

$$\frac{1}{3} \tilde{R}^2 \frac{d\tilde{P}_g}{dt} + \tilde{R}\tilde{P}_g \frac{d\tilde{R}}{dt} = \psi \left[(1 - \tilde{P}_g) - \left(\frac{1 - \tilde{P}_a}{\tilde{P}_a - \tilde{R}_0^3} \right) (\tilde{P}_g\tilde{R}^3 - \tilde{R}_0^3) \right] \quad (70)$$

$$\frac{1}{\pi_{D\eta}} \frac{d\tilde{R}}{dt} = (\tilde{P}_g - \tilde{P}_a)\tilde{R} \quad (71)$$

where

$$\psi = \left[\left(\frac{4\pi}{3} \right)^2 \left(\frac{\bar{P}_a - \bar{R}_0^3}{1 - \bar{P}_a} \right)^2 \frac{\rho K_T}{H_c M} \right]^{1/3}$$

$$\pi_{D\eta} = \frac{t_D}{t_\eta} = \frac{H_c w_0}{\eta D \hat{N}_0^{2/3}} \quad (72)$$

The dimensionless parameter $\pi_{D\eta}$ was first identified by Amon and Denson (1983) and is a measure of whether mass transfer controls the rate of bubble growth ($\pi_{D\eta} > 1$) or whether momentum transfer controls growth ($\pi_{D\eta} < 1$).

a. *Diffusion-Controlled Bubble Growth.* In circumstances when $\pi_{D\eta} \ll 1$, Eq. (71) reduces to

$$\bar{P}_g = \bar{P}_a \quad (73)$$

which states that the bubble is in mechanical equilibrium at all times. The devolatilization efficiency is therefore given by

$$\varepsilon = \frac{w_1 - w}{w_1} = \frac{(1 - \bar{P}_a \bar{R}^3)}{1 - \bar{R}_0^3} \quad (74)$$

which results from the substitution of Eq. (73) into Eq. (69). Equation (70) reduces to

$$\bar{R} \frac{d\bar{R}}{dt} = \beta \left(\frac{1 - \bar{P}_a}{\bar{P}_a - \bar{R}_0^3} \right)^{1/3} (1 - \bar{R}^3), \quad \bar{R} = \bar{R}_0 \text{ at } \bar{t} = 0 \quad (75)$$

which has the solution

$$\frac{1}{6} \ln \left[\frac{1 + \bar{R} + \bar{R}^2}{(1 - \bar{R})^2} \right] - \frac{1}{\sqrt{3}} \tan^{-1} \left(\frac{2\bar{R} + 1}{\sqrt{3}} \right)$$

$$= \beta \left(\frac{1 - \bar{P}_a}{\bar{P}_a - \bar{R}_0^3} \right)^{1/3} \bar{t} + \frac{1}{6} \ln \left[\frac{1 + \bar{R}_0 + \bar{R}_0^2}{(1 - \bar{R}_0)^2} \right] - \frac{1}{\sqrt{3}} \tan^{-1} \left(\frac{2\bar{R}_0 + 1}{\sqrt{3}} \right) \quad (76)$$

where $\beta = [(4\pi/3)^2 (\rho K_T / H_c M)]^{1/3}$.

Figure 21 is a plot of Eq. (74), whereas Figure 22 shows the variation of bubble radius and extraction efficiency with time for specific values for the dimensionless parameters, β , \bar{R}_0 , and \bar{P}_a . Initially, the amount of volatile component remaining in the solution decreases sharply with time, but after about 80% of the material is extracted, further changes are insignificant. Thus, efforts to increase the lifetime of the bubble beyond this point would not be beneficial. The effect of pressure on extraction efficiency is shown in Fig. 23.

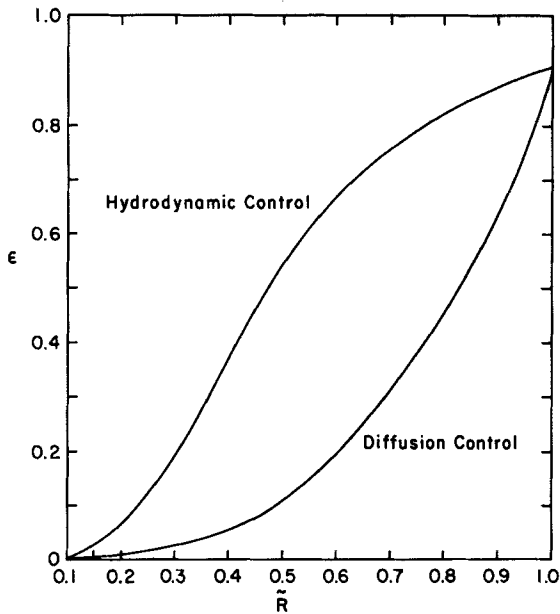


FIG. 21. Variation of the extraction efficiency with dimensionless bubble radius for diffusion-controlled and hydrodynamically controlled bubble growth when the bubble population is constant $\bar{P}_a = 0.10$, $\bar{R}_0 = 0.10$, $\beta = 5.87$.

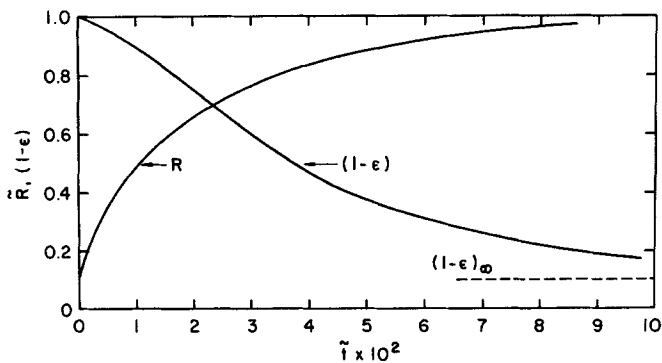


FIG. 22. Variation of the dimensionless bubble radius and extraction efficiency with dimensionless time for diffusion-controlled bubble growth when the bubble population is constant. $\bar{P}_a = 0.10$, $\bar{R}_0 = 0.10$, $\beta = 5.87$.

b. *Hydrodynamic Control of Bubble Growth.* When $\pi_{D\eta} \ll 1$, bubble growth is determined solely by the fluid mechanics and the rheological behavior of the polymeric system of interest. In these circumstances, Eq. (70) is more conveniently written as

$$\begin{aligned} & \frac{1}{3} \bar{R}^2 \pi_{D\eta} \frac{d\bar{P}_g}{d(\pi_{D\eta} \bar{t})} + \bar{R} \bar{P}_g \pi_{D\eta} \frac{d\bar{R}}{d(\pi_{D\eta} \bar{t})} \\ &= \psi \left[(1 - \bar{P}_g) - \left(\frac{1 - \bar{P}_a}{\bar{P}_a - \bar{R}_0^3} \right) (\bar{P}_g \bar{R} - \bar{R}_0^3) \right] \end{aligned} \quad (70a)$$

which reduces to

$$\bar{P}_g = \frac{\bar{P}_a(1 - \bar{R}_0^3)}{(\bar{P}_a - \bar{R}_0^3) + \bar{R}^3(1 - \bar{P}_a)} \quad (77)$$

in the limit as $\pi_{D\eta} \rightarrow 0$.

Substitution of Eq. (77) into Eq. (69) results in an expression for the extraction efficiency in terms of the bubble radius:

$$\varepsilon = \frac{(1 - \bar{P}_a)\bar{R}^3}{(\bar{P}_a - \bar{R}_0^3) + (1 - \bar{P}_a)\bar{R}^3} \quad (78)$$

and Eq. (71) reduces to

$$\frac{1}{\bar{R}} \frac{d\bar{R}}{d(\pi_{D\eta} \bar{t})} = \frac{\bar{P}_a(1 - \bar{R}^3)(1 - \bar{P}_a)}{(\bar{P}_a - \bar{R}_0^3) + (1 - \bar{P}_a)\bar{R}^3} \quad (79)$$

which has the solution

$$(\bar{P}_a - \bar{R}_0^3) \ln \left(\frac{\bar{R}}{\bar{R}_0} \right)^3 - (1 - \bar{R}_0^3) \ln \left(\frac{1 - \bar{R}^3}{1 - \bar{R}_0^3} \right) = 3\bar{P}_a(1 - \bar{P}_a)\bar{t}' \quad (80)$$

Equation (78) is plotted in Fig. 21 and Eq. (80) is plotted in Fig. 24.

A number of important conclusions can be drawn from the simplified analysis of bubble growth just presented. First, the dimensionless group $\pi_{D\eta}$ can be used as a means to assess whether the rheological properties of the polymer system control the devolatilization process or whether molecular diffusion controls the process. Thus, attempts to correlate, or analyze, performance in terms of the diffusional characteristics of the polymer system when the process is controlled by the fluid mechanics of the system would be fruitless. Second, the qualitative behavior of the extraction efficiency–time curves for diffusion control and hydrodynamic control (Figs. 22 and 24) is remarkably similar. This means that assessing the validity of a proposed model using qualitative agreement between experiment and theory may be on unsafe ground.

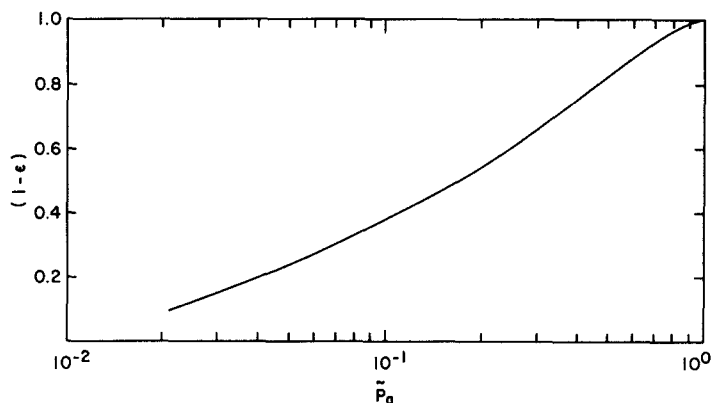


FIG. 23. Predictions of the diffusion-control model [Eq. (76)] for the influence of the extraction pressure on extraction efficiency at a fixed time. $i = 0.05$, $\bar{R}_0 = 0.10$, $\beta = 5.87$.

2. Newman-Simon Model

Some aspects of the theoretical development which have been presented here follow along the lines of an important paper by Newman and Simon (1980). Their analysis differs from the simplified analysis presented here in two respects. First, the idea that $\pi_{D\eta}$ is a measure of the type of bubble growth which occurs was not incorporated in the Newman-Simon analysis. Second, Newman and Simon used a more realistic expression for the molar flux N_b .

In place of Eq. (62), Newman and Simon used an expression based on

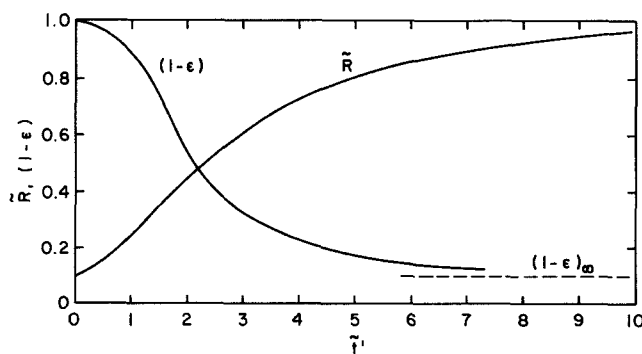


FIG. 24. Variation of the dimensionless bubble radius and extraction efficiency with dimensionless time for hydrodynamically controlled bubble growth: $\bar{P}_a = 0.10$, $\bar{R}_0 = 0.10$.

the classical penetration theory result corrected for the convective effects due to bubble expansion:

$$N_b = (7/3)^{1/2} \left[\left(\frac{D}{\pi t} \right)^{1/2} + \frac{D}{R} \right] (w - w_i) \frac{\rho}{M} \quad (81)$$

Equation (81), when combined with the ideal gas law, the momentum equation (corrected for surface tension), and the material balance equation, results in a system of differential equations that Newman and Simon solved numerically.

We have replotted one set of the Newman-Simon results in dimensionless terms in Fig. 25 for a specific set of operating conditions and physical property values ($R_0 = 0.5$ mm, $T = 230^\circ\text{C}$, $P_a = 5$ Torr). The dimensionless group π_{Dn} was determined to be $\approx 10^3$, whereas the characteristic diffusion time was found to be $t_D = 400$ sec ($\dot{N}_0 = 3860$ cm $^{-3}$, $D = 10^{-5}$ cm 2 /sec, $\eta = 10^4$ poise, $H_c = 33$ atm, $w_0 = 2.6 \times 10^{-3}$). The large value for π_{Dn} suggests that bubble growth is diffusion controlled, which means that Eq. (76) should be appropriate. As seen in Fig. 25 the difference between a plot of Eq. (76) and the Newman-Simon results is substantial, the latter predicting much higher devolatilization rates. The fact that the Newman-Simon model predicts higher rates is not surprising, given the form for N_b that they used. What is surprising, however, is that such a large discrepancy exists, which suggests that devolatilization models can be sensitive to the type of expression chosen for the molar flux.

B. FICTITIOUS MASS TRANSFER COEFFICIENTS

In circumstances when entrained bubbles are present during devolatilization, considerable ambiguity can exist with regard to the physical significance of the mass transfer coefficients. If the mass transfer coefficient is defined, or measured, in the usual way [Eq. (43)], the rate at which mass is transferred is not in any way related to diffusional processes but instead is a measure of the rate at which bubbles are rupturing or being released from solution. Thus,

$$L(w_1 - w_2) = \frac{4\pi M V_T}{3K_T} \frac{1}{t^*} \int_0^{t^*} J_D R^3 P_g dt = k_L A_T (\Delta w)_{LM} \rho \quad (82)$$

and the resulting mass transfer coefficient is a fictitious one in the sense that it may have little, or nothing, to do with diffusional processes. In fact, even for the ideal case when the bubble population is constant, a fictitious mass transfer coefficient can result. For example, if bubble growth is hydrodynamically controlled, the concentration profile of the volatile

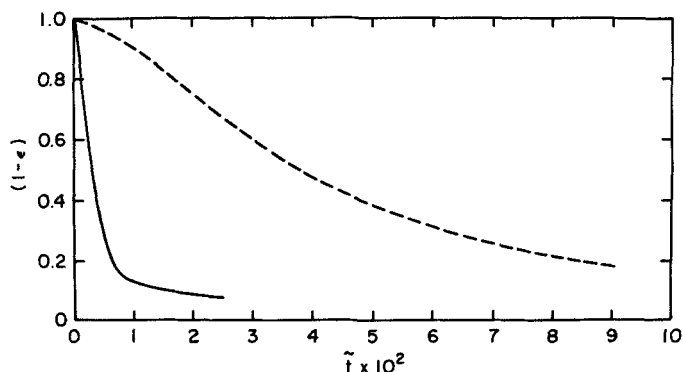


FIG. 25. Predictions of the Newman-Simon model (—) and the diffusion-control model (---) [Eq. (76)] for the bubble radius as a function of time: $\bar{P}_a = 0.08$, $\bar{R}_0 = 0.20$ for Newman-Simon model and $\bar{P}_a = 0.10$, $\bar{R}_0 = 0.20$ for the approximate model. $\beta = 5, 87$.

component in the liquid surrounding the bubble is uniform and no driving force for mass transfer by diffusion exists. In this case the rate at which mass is transferred to the bubble is determined by the hydrodynamic resistance and the hydrodynamic driving force. Mass transfer has nothing at all to do with diffusional processes.

On the other hand, if bubble growth is diffusion controlled, then the mass transfer coefficient may be meaningful. However, in this case, the surface area for mass transfer is the surface area of the bubbles entrained in the solution and this depends on the volume of liquid in the extraction zone and not on the surface area of the extraction zone. Clearly, attempts to correlate experimental data for the extraction of a volatile component from a polymeric solution containing entrained bubbles using mass transfer coefficients can be misleading or totally erroneous.

V. The Length of a Transfer Unit

A well-established concept in the design of stripping operations in the chemical processing industries is the use of equations in which the height of the unit required is expressed as the product of two terms: the number of transfer units (NTU), a measure of the difficulty of the operation to be carried out, and the height of a transfer unit (HTU), a measure of the height required in order to carry out an operation of unit difficulty. The advantage of this procedure is that the effectiveness of a particular unit is directly reflected in the value of the HTU. On the other hand, the advan-

tages of one mode of operation over another (such as countercurrent versus cocurrent) are reflected in the value of the NTU, which, for a given overall result of the process, depends on the mode of operation.

Collins *et al.* (1983) have suggested that this same concept can be applied to polymer devolatilization processes, except that the HTU might be more appropriately termed the LTU when screw extruders are used since these need not be vertical. By analogy, the following expressions can be written:

$$\lambda = (\text{LTU})(\text{NTU}) \quad (83)$$

where λ is the axial length of the extraction zone required, and

$$\text{LTU} = L/K_L a \rho S \quad (84)$$

$$\text{NTU} = \int_{w_2}^{w_1} \frac{dw}{w - w^*} \quad (85)$$

The subscripts 1 and 2 refer to liquid inlet and outlet conditions, respectively. If the mode of operation is known and the value of ε is measured, NTU can be calculated. If, in addition, λ is known or measured, then the LTU can be determined experimentally. In some cases, however, an analytic expression for the LTU can be obtained. For a wiped film processor—such as a screw extruder—in which mass transfer occurs by diffusion through a wiped film into a vapor phase that has negligible resistance, Eq. (35) can be used and the LTU is given by

$$\text{LTU} = L/(2\pi^{1/2}(DpN)^{1/2}a_b\rho S) \quad (86)$$

Equation (86) has been tested by Collins *et al.* (1983), who measured values for the LTU in an intermeshing, corotating twin screw extruder using a poly(butene)–Freon system at atmospheric pressure and nitrogen as the sweeping gas in countercurrent flow. In these experiments the length of the extraction zone was known and the NTU could be determined from measured values of the extraction efficiency. Figure 26 is a plot of these data which shows that the LTU does depend on $N^{1/2}$. Note, however, that the LTU can be large at low screw speeds when the extraction operation is conducted at atmospheric pressure and at a relatively low temperature.

As pointed out earlier, stripping operations are usually conducted under conditions of reduced pressure and in these circumstances NTU is given by

$$\text{NTU} = \ln\left(\frac{\gamma - 1}{\gamma(1 - \varepsilon) - 1}\right) \quad (87)$$

$$\gamma = H_c w_1 / P \quad (88)$$

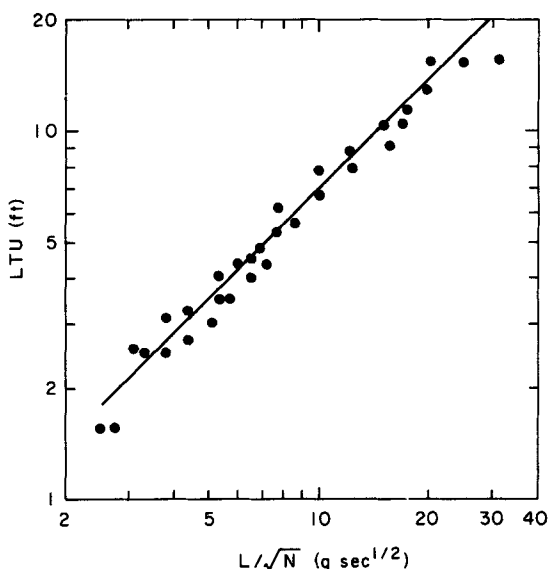


FIG. 26. The LTU as a function of L/\sqrt{N} . The line through the data is the best fit and is about 30% lower than the theoretical prediction.

$$\gamma_{\min} = 1/(1 - \varepsilon) \quad (89)$$

Equations (83) and (87)–(89) have been used to estimate values for the LTU in the studies conducted by Coughlin and Canevari (1969) and by Werner (1980). These results are summarized in Table II along with the results from the study of Collins *et al.* (1983). The results in this table provide support for the idea that the LTU can be used as a measure of the effectiveness of the extraction unit.

TABLE II
EXPERIMENTAL VALUES FOR THE LTU FOR SCREW EXTRUDERS

Investigator	System	LTU (m)	Comment
Coughlin and Canevari (1969)	Xylene–polypropylene	0.3–0.6	Single-screw extruder Reduced pressure and elevated temperatures
	Methanol–polypropylene	0.1	Independent of screw speed
Werner (1980)	Methylmethacrylate–poly(methylmethacrylate)	$\ll 0.25$	Twin-screw extruder Reduced pressure and elevated temperatures Independent of screw speed
Collins <i>et al.</i> (1983)	Polybutene–Freon	0.6–4.5	Twin-screw extruder Atmospheric pressure, $T = 20^\circ\text{C}$ Varies inversely as $N^{1/2}$

Nomenclature

Arabic Symbols

a	Surface area for mass transfer per unit volume of empty processor	K	Power law factor
a_b	Surface area of processor per unit volume of empty processor	\bar{L}	Liquid mass flow rate
a_n	Interfacial area of nip per unit volume of empty processor	\bar{l}	Dimensionless axial length (l/λ)
a_f	Interfacial area of film on wall of processor per unit volume of empty processor	l	Coordinate in axial direction
a_s	Interfacial area of film on screw per unit volume of empty processor	M	Molecular weight of volatile component
A_T	Total surface area for mass transfer	m_g	Mass of gas in bubble
B	Empirical constant in Eq. (39)	N_t	Total molar flux of volatile component
c, \hat{c}	Local molar concentration of volatile component	N_n	Molar flux of volatile component in the nip
C	Constant in Eq. (58), $3.73 \times 10^{35} (\rho^2 \sigma / M^3)^{1/2}$	N_f	Molar flux of volatile component in wiped film on barrel wall
C_L	Distance between screw centers in a twin-screw extruder	N_{fs}	Molar flux of volatile component in wiped film on screw surface
D	Molecular diffusivity	N	Screw rotational speed
D_s	Diameter of screw	\hat{N}	Number of bubbles per unit volume of solution
D_b	Diameter of barrel	\hat{N}_0	Number of bubbles per unit volume of solution initially
E	Eddy diffusivity	N_b	Molar flux of volatile component at surface of gas bubble
e	Flight width in a twin-screw extruder	n	Power law constant
e_{ij}	Deformation rate	n_f	Instantaneous molar flux of volatile component from wiped film
f	Fraction of screw channel filled with liquid	n_n	Instantaneous molar flux of volatile component from nip
F_D	Drag flow shape factor	P_a	Pressure in extraction zone
H, h	Channel depth in screw extruder	P_f^0	Vapor pressure of stripping agent or fugitive component
H_c	Henry's constant	P_g^0	Initial gas pressure in bubble
J_F	Rate of formation of bubbles per unit volume of solution	P_0	Vapor pressure of volatile component
J_D	Rate of destruction of bubbles per unit volume of solution	\bar{P}_a	Dimensionless extraction pressure (P_a/Hw_0)
k_L	Individual liquid phase mass transfer coefficient	\bar{P}_g	Dimensionless gas pressure in bubble (P_g/Hw_0)
K_T	Product of gas constant and absolute temperature	P_g	Gas pressure in bubble
		P	Partial pressure of volatile component
		p	Number of screw starts or tips

Q_D	Volumetric flow rate due to drag in screw extruder	V_{bz}	Down channel component of barrel velocity
R	Bubble radius	V_T	Total volume of liquid in extraction section
R_s	Screw radius	W	Width of channel perpendicular to screw flights in screw extruder
\bar{R}	Dimensionless bubble radius	w	Weight fraction of volatile component
\bar{R}_0	Dimensionless initial bubble radius,	w_i	Weight fraction of volatile component at interface
$\equiv \left[\frac{\bar{P}_a}{1 + (3/4\pi)[\rho \hat{V} K_T (1 - \bar{P}_a)/MHR_0^3]} \right]^{1/3}$			
R_0	Initial bubble radius	w^*	Equilibrium weight fraction of volatile component
R_e	Equilibrium, bubble radius	w_1	Weight fraction of volatile component at inlet to extraction section
S	Cross-sectional area of empty processor	w_2	Weight fraction of volatile component at exit of extractor
t	Time	w_0	Weight fraction of volatile component when bubbles are initially formed
t_D	Characteristic diffusion time	x', x	Cross-channel coordinate
t_η	Characteristic hydrodynamic time	x_k	Generalized spatial coordinate
\bar{t}	Dimensionless time (t/t_D)	\bar{x}_n	Degree of polymerization
\bar{t}'	Dimensionless time (t/t_η)		
t^*	Bubble lifetime		
T	Temperature		
t_s	Lead of screw		
u	Average axial velocity		
v_k, v_j	Velocity component		
V_{bz}	Cross channel component of barrel velocity		

Greek Symbols

α	Tip angle	$\pi_{D\eta}$	Dimensionless parameter defined in Eq. (72)
β	Dimensionless parameter defined in Eq. (76)	ρ_c	Ratio of distance between screw centers to radius of barrel
γ	Dimensionless parameter defined in Eq. (87)	ρ	Liquid density
ϵ	Extraction efficiency	σ	Surface tension
η	Viscosity	τ_{ij}	Stress
θ	Exposure time	ϕ	Helix angle
θ_f	Exposure time of film	ϕ_s, ϕ_p	Volume fraction of solvent, polymer
θ_n	Exposure time of nip	χ	Interaction parameter
λ	Axial length of wiped film processor	ψ	Dimensionless parameter defined in Eq. (72)
λ_1	Polymer relaxation time		
ξ_1, ξ_2, ξ_3	Coordinate variables		

References

- Amon, M., and Denson, C. D. (1983). *Polym. Eng. Sci.* (in press).
Amon, M., and Denson, C. D. (1980). *Ind. Eng. Chem. Fundam.* **19**, 415.

- Ault, J. W., and Mellichamp, D. A. (1972). *Chem. Eng. Sci.* **27**, 2219.
- Biesenberger, J. A. (1980). *Polym. Eng. Sci.* **20**, 1015.
- Biesenberger, J. A., and Kessidis, G. (1982). *Polym. Eng. Sci.* **22**, 832.
- Blander, M., and Katz, J. L. (1975). *AIChE J.* **21**, 833.
- Bonner, D. C. (1975). *J. Macromol. Sci. Rev. Macromol. Chem.* **C13(2)**, 263.
- Booy, M. L. (1978). *Polym. Eng. Sci.* **18**, 973.
- Booy, M. L. (1980). *Polym. Eng. Sci.* **20**, 1220.
- Collins, G. P. (1982). M.S. Thesis, University of Delaware, Newark.
- Collins, G. P., Denson, C. D., and Astarita, G. (1983). *Polym. Eng. Sci.* **23**, 323.
- Coughlin, R. W., and Canevari, G. P. (1969). *AIChE J.* **15**, 560.
- Duda, J. L., Vrentas, J. S., Ju, S. T., and Liu, H. T. (1982). *AIChE J.* **28**, 279.
- Flory, P. J. (1941). *J. Chem. Phys.* **9**, 660.
- Huggins, M. L. (1942). *Ann. N.Y. Acad. Sci.* **41**, 1.
- Hwang, B. K. (1982). Ph.D. Dissertation, University of Delaware, Newark.
- Ju, S. T., Liu, H. T., Duda, J. L., and Vrentas, J. S. (1981). *J. Appl. Polym. Sci.* **26**, 3735.
- Latinen, G. A. (1962). *Adv. Chem. Ser.* **34**, 235.
- MacKenzie, P. D. (1979). B.S. Thesis, University of Delaware, Newark.
- Meyer, J. A., and Blanks, R. F. (1982). *J. Appl. Polym. Sci.* **28**, 725.
- Moffatt, H. K. (1964). *J. Fluid Mech.* **19**, 1.
- Newman, R. E., and Simon, R. H. M. (1980). *73rd Annu. A.I.Ch.E. Meet.*
- Nichols, R. J., and Kheradi, F. (1982). Extruder coagulation and finishing of polymer latex emulsion. *Intern. Conf. Reactive Processing of Polymers, 2nd., Pittsburgh 1982.*
- Pell, T. M., Jr., and Davis, T. Q. (1973). *J. Polym. Sci., Polym. Phys. Ed.* **11**, 1671.
- Prud'homme, R. K. (1982). *75th Annu. A.I.Ch.E. Meet.*
- Roberts, G. W. (1970). *AIChE J.* **16**, 878.
- Secor, R. M. (1969). *AIChE J.* **15**, 861.
- Squires, P. H. (1958). *SPE J.* **14**, 24.
- Tadmor, Z., and Klein, I. (1970). "Engineering Principles of Plasticating Extrusion." Van Nostrand-Reinhold, Princeton, New Jersey.
- Todd, D. B. (1974). *Soc. Plast. Eng. [Tech. Pap.]* **20**, 472.
- Vrentas, J. S., and Duda, J. L. (1977a). *J. Polym. Sci., Polym. Phys. Ed.* **15**, 403.
- Vrentas, J. S., and Duda, J. L. (1977b). *J. Polym. Sci., Polym. Phys. Ed.* **15**, 417.
- Vrentas, J. S., and Duda, J. L. (1979). *AIChE J.* **25**, 1.
- Werner, H. (1980). "Devolatilization of Plastics." VDI Verlag, Berlin.
- White, J. L., and Metzner, A. B. (1963). *J. Appl. Polym. Sci.* **7**, 1869.

RAPID PHASE TRANSITIONS FROM LIQUID TO VAPOR

Robert C. Reid

Department of Chemical Engineering
Massachusetts Institute of Technology
Cambridge, Massachusetts

I.	Summary	106
II.	Introduction	112
III.	Rapid Phase Transitions between Liquefied Natural Gas and Water	113
	A. Summary	113
	B. Background	116
	C. Bureau of Mines Studies	117
	D. University of Maryland Tests	119
	E. Conoco Experiments	120
	F. Early M.I.T. Work	120
	G. Esso Program	120
	H. M.I.T. LNG Research Center	121
	I. Shell Pipeline Corporation Program	128
	J. LLNL/NWC Tests	130
	K. Overpressures from LNG RPTs	136
IV.	Smelt-Water Explosions	141
	A. Summary	141
	B. Background	143
	C. Dissolver Tank Explosions	144
	D. Laboratory Investigations	146
	E. Statistical Survey of Smelt-Water Boiler Explosions	148
	F. Description of Severe Furnace Explosion	149
	G. Argonne Molten Salt Studies	155
	H. Theories and Mechanisms	155
V.	Molten Aluminum-Water Explosions	159
	A. Summary	159
	B. Background	161
	C. Alcoa Experimental Program	162
	D. Higgins Study	166
	E. Wright and Humberstone Impact Studies	167
	F. Anderson and Armstrong Experiments	167
	G. Battelle Study	169
	H. Industrial Accidents	171

I.	Discussion	178
VI.	Reactive Metal–Water Explosions.	182
A.	Background	182
B.	Titanium Melting-Furnace Explosions.	183
C.	Tungsten Casting Explosion	186
D.	Discussion	186
VII.	Explosions with Liquid Refrigerants.	186
VIII.	Effects of Absolute Pressure on RPTs	189
A.	Dynamics of Bubble Growth	189
B.	Pressure Effects on Thermal Explosions.	193
C.	Escalation Model of Henry and Fauske	195
IX.	Appendix: Superheated Liquids.	198
	Nomenclature.	203
	References	203

I. Summary

In a number of industrial operations, there exists the possibility of contacting two different liquids—one hot and relatively nonvolatile and the other cold and more volatile. Should such an event occur, normally the more volatile liquid vaporizes and, thereby, cools the hotter liquid. In certain circumstances, however, the course of events changes dramatically, and vaporization occurs in such a brief period of time as to resemble an explosion. This *explosive boiling* may initiate shock waves that can damage equipment and injure personnel in the vicinity of the blast.

Events of this nature have been described by various terms, e.g., rapid phase transitions (RPTs), vapor explosions, explosive boiling, thermal explosions, and fuel–coolant interactions (FCIs). They have been reported in a number of industrial operations, e.g., when water contacts molten metal, molten salts, or cryogenic liquids such as liquefied natural gas (LNG). In the first two examples noted above, water is the more volatile liquid and explosively boils whereas, in the last example, the cryogenic liquid plays the role of the volatile boiling liquid and water is then the *hot* fluid.

Because of the hazards caused by such explosive boiling incidents, industry has supported research programs seeking answers to several basic questions:

(1) What is the mechanism of explosive boiling, i.e., in a liquid–liquid accident, when might one expect simple boiling and when/how does simple boiling evolve to explosive boiling?

(2) Under what conditions would a small-scale incident escalate into a coherent large-scale explosion?

(3) What can be done to prevent RPTs from occurring in industrial operations?

Definitive answers to these questions are not yet available. Only recently has there been the opportunity to collect and compare explosive boiling incidents from different industries. Also, most experiments that have been conducted to explore RPT mechanisms have been limited to relatively small-scale tests. Evidence now exists to suggest that the small-scale results may only be indicative of a trigger or initiating step, and other mechanisms need to be introduced to explain *large-scale* boiling explosions.

In this article, RPT incidents in various industries are examined. In each case, both laboratory-scale studies and industrial accidents are covered. In the former, usually only simple *spills* of one liquid upon another were conducted. The effects of a few variables were tested to determine if they were, or were not, important in achieving an RPT. The results of the small-scale experiments have led to conceptual hypotheses to clarify the initiation of an RPT—and such concepts have, in turn, provided a tentative set of criteria that must be met to achieve an RPT.

The analysis of *industrial accidents* provides an indication of the damage potential in an RPT, but, in many instances, data are fragmentary and definitive conclusions are difficult to draw. Whenever possible, the RPT criteria, developed from laboratory tests, are compared to conditions existing in industrial accidents.

For the RPT criteria noted above, we first require that the system involve two *liquids* which contact one another. RPTs are very difficult to achieve when a cold, volatile liquid contacts a hot, *solid* surface.

The second RPT criterion relates to the temperature of the hot liquid. That is, this temperature must *exceed* a threshold value before an RPT is possible. From one theory of RPTs, the *superheated-liquid* model (described later), this criterion arises naturally, and the threshold hot-liquid temperature is then equal to the *homogeneous nucleation* temperature of the colder liquid T_{sl} . This temperature is a characteristic value for any pure liquid or liquid mixture and can be measured in independent experiments or estimated from theory. From alternate RPT theories, the threshold temperature may be equated, approximately, to the hot fluid temperature at the onset of stable film boiling.

A corollary, often appended to the second RPT criterion, is that RPTs are more difficult to achieve as the temperature of the hot liquid increases beyond the threshold temperature. For very high hot-liquid temperatures, some external pressure pulse or shock becomes necessary to initiate an RPT.

These two criteria appear to suffice to achieve laboratory-sized RPTs. For *large-scale, coherent* events, however, an additional criterion is offered, i.e., the cold liquid must be prefragmented at the inception of the RPT. The prefragmentation allows an escalation of small RPTs to a larger, coherent explosion. In the time period when fragmentation is taking place, the system is in stable *film* boiling with each cold-liquid mass enveloped by a vapor film. The escalation phase then involves the (1) collapse of the vapor film (from an initiating shock) and (2) boiling of the cold liquid fragments *in the same time scale as the initiating trigger event*.

Extensive laboratory-scale studies have been conducted to investigate the triggering mechanism for RPTs when LNG, liquefied petroleum gas (LPG), and liquid refrigerants contact a hot liquid (usually water). These studies are covered in Sections III and VII. The evidence seems overwhelming that RPTs in these cases result from superheating of the cold, volatile liquid to its superheat-limit temperature where prompt homogeneous nucleation occurs in a time period of a few microseconds. (The properties of a superheated liquid and the concept of homogeneous nucleation are reviewed briefly in Section IX.)

Using the LNG studies as an example, many of the basic tenets of the superheated-liquid model may be readily tested. For example, if the hot liquid (water) temperature were *below* the expected homogeneous nucleation temperature of the LNG, then no explosive boiling incident would be expected (Criterion 2 above). Test results agree completely with this supposition. Also, for a given water temperature, the homogeneous nucleation temperature of the LNG may be varied by changing composition. Again, predicted results agree with experimental results. Thus, the theory can predict when explosive boiling is possible, but it is less useful in predicting the probability of an actual event. Experimental facts indicate that if the water temperature significantly exceeds the homogeneous nucleation temperature of the LNG, there is a low probability of an explosive boiling event. The rationale for this fact seems to be in the ease by which film boiling may be initiated between the LNG and water when the water temperature is high. With an intervening vapor film between the LNG and water, no superheating of the cryogen is then possible.

The laboratory-scale test results lead naturally to the conclusion that methane-rich LNG, as transported in commerce today, would not undergo an RPT if spills were to occur in a marine accident. Normal seawater temperatures are much higher than the superheat-limit temperature of this LNG. However, recent LNG spill tests involving up to 40 m³ of methane-rich liquids have, on occasion, produced strong RPTs (see Section III,J). In some of these incidents, the RPTs may have occurred after preferential evaporation of the methane to leave an LNG "heel" much

richer in ethane and propane. That is, the LNG composition changed such that its superheat-limit temperature rose and became equal to the ambient water temperature. In the more severe RPTs, however, this explanation seems incomplete. Referring to the third RPT criterion stated earlier, it is probable that the large-scale, coherent RPTs occurred as a result of significant prefragmentation of the LNG and, at some point, a *trigger shock* developed within the LNG–water masses. The trigger could have resulted from small masses of LNG preferentially losing methane to form ethane–propane-rich liquids which, as noted above, can explosively boil by the homogeneous nucleation mechanism. The sharp pressure wave emanating from the local trigger shocks would then propagate through the entire LNG–water system, and, if conditions were appropriate, result in an escalation to a coherent explosion.

Experimental data and theoretical considerations suggest that water pressures developed in LNG–water RPTs are significantly less than critical pressure of the LNG. Measured values have not exceeded 10–20 bar. Average overpressures in the air show a rapid decay with distance and are approximately equivalent to values expected from the detonation of a few tenths of a kilogram of TNT (see Section III,K).

Whereas one might classify the LNG–water studies as a response to a concern that industrially sized operations *might* result in a large-scale spill on water with subsequent RPTs, studies of *molten salt–water explosions* were carried out because industrial accidents *had* taken place. Emphasis has been placed on events occurring in the paper industry where molten smelt is produced in recovery boilers. This smelt is primarily a mixture of sodium chloride, sodium carbonate, and sodium sulfide. In normal operations, the molten smelt is tapped from the furnace, quenched, treated, and recycled to the wood digestors. Accidents have taken place, however, when water inadvertently contacted molten smelt with severe explosions resulting. The smelt temperature is much higher than the critical point of water: ~ 1100 K compared to 647 K (see Section IV).

Laboratory investigations into the mechanism of smelt–water explosive boiling events have been primarily of value in delineating the effect of smelt composition on the sensitivity of the salt in producing RPTs. For example, pure molten sodium carbonate has never led to explosive boiling. Addition of either (or both) sodium chloride or sodium sulfide lead to smelts which are more prone to explosive boiling. Investigators experimented with many additives both to the smelt and to the water in an attempt to obtain less sensitivity. Most had little or no effect.

The superheated-liquid model introduced earlier to explain LNG–water RPTs was not considered applicable for smelt–water explosions since the very large temperature difference between the smelt and water would, it

was predicted, lead to prompt film boiling and a very low probability of subsequent liquid-liquid contact. Only very recently has a modified superheat theory model been proposed to overcome the original objections. In this development, it was suggested that, upon initial contact between smelt and water, there is both mass *and* heat transfer at the interface. The movement of salt into the water phase then provides a "bridge" which can be heated well above the normal homogeneous nucleation temperature for pure water (~ 577 K). It was then proposed that the concentrated salt bridge is the zone where homogeneous nucleation could occur.

In Section IV, the available data for smelt-water explosions are summarized. Also, Table XII is presented, listing many industrial boiling incidents involving smelt and water. The energetics of these accidents are hard to quantify, but descriptions are provided for several well-documented events to indicate the damage potential. It would appear that an RPT is highly localized and rarely is there significant damage reported at distances exceeding about 10 m from the blast. Within the localized zone, however, there are numerous reports of damage to structural beams, walls, and furnace tubes.

The metals-processing industries, particularly those producing aluminum, have also been plagued by explosive-boiling incidents. Alcoa has carried out several test programs directed primarily at effecting means to prevent such accidents in casting plants. In most tests, molten aluminum was dropped into water and the subsequent events recorded. Many variables were studied such as water temperature, drop height, and nozzle diameter. The principal result of these investigations was to show that water containers, suitably coated with an organic-based paint, would normally not lead to explosions when molten aluminum was spilled into the container. Use of such paints in aluminum plants has indeed reduced the frequency of explosions, but many still occur.

Experimental test results for molten aluminum-water RPTs are described in Section V. Also shown is a tabulation of most documented aluminum-water explosive boiling incidents (see Table XIV). In many accidents, the quantity of water was quite small, e.g., some resulted when *wet* aluminum ingots were loaded into melting furnaces containing molten aluminum. In contrast, one notes that few, if any, serious events have ever been obtained when *small quantities* of aluminum were contacted with a large mass of water. Since laboratory tests were often carried out in the latter fashion, most of these have produced negative results.

As with the smelt-water case, if an RPT did take place, the event was localized and rarely was damage severe far from the site of contact. Modeling molten aluminum-water incidents (and, in fact, other molten metal-water explosions such as in the steel industry) has not been partic-

ularly successful. The aluminum temperature was sufficiently high to lead to immediate film boiling upon contact with water so that superheated-liquid models did not appear particularly plausible. With the new concept of a salt bridge as suggested by investigators of smelt-water accidents, one may hypothesize that a similar type of event may be occurring in the aluminum-water cases. Here, however, the bridge might be an aluminum oxide-hydrate which would form at the interface between water and metal. Evidence for this idea is, at present, slim. It is known that aluminum-saltwater incidents are more easily achieved than when pure water is used. Also, coatings of lime on the vessel walls can lead to violent explosive boiling. In this case it is possible that some reaction product between the lime, aluminum, and water may provide the necessary bridge.

In Section VI, a brief summary is given for RPT incidents in industries handling molten *reactive* metals such as titanium and zirconium. Only a few serious explosive boiling events have been documented. In most of these, a significant quantity of molten metal contacted water *and*, simultaneously, there was an external shock such as an electrode falling into the metal-water mixture. In the few known incidents, damage was extensive but quite localized. Due to the reactive nature of the metal, however, subsequent hydrogen fires often compounded the problem and led to extensive damage.

A common theme developed in this article is that many RPTs can be explained by stipulating that the colder, more volatile liquid is heated, without boiling, to its homogeneous nucleation temperature where prompt vaporization occurs. This sequence then leads to a sharp, but localized, shock. Laboratory-scale studies are concerned primarily with conditions affecting this initial event. Yet there are undoubtedly other mechanisms which could produce similar end results, and some of these alternatives are described.

Assuming, however, that the superheated liquid idea is correct, it is of interest to investigate the subsequent vapor-bubble growth processes that occur after homogeneous nucleation of liquid to vapor. This problem is treated in Section VIII and follows the developments of Henry and Fauske. The interesting conclusion reached is that the *strength* of a superheated-liquid explosion should be strongly correlated with the system pressure. That is, at high pressures, vapor bubble growth rates are relatively low and dominated by the rate of heat transfer into the growing bubble. At low pressures, however, the bubble growth rates are high and inertially controlled. While few data exist to indicate the effect of system pressure, those that are available seem to indicate that at high system pressures, RPTs are difficult to initiate and, instead, only rapid (nonexplo-

sive) boiling ensues. These results provide further evidence that homogeneous nucleation mechanisms play a key role in triggering an RPT.

Following a trigger shock, subsequent events seem to be controlled by other phenomena. (In most small-scale tests, *only* the trigger step was studied.) We noted in the third RPT criterion that, to produce large-scale, coherent explosions, the local trigger event may lead to an escalation if the cold liquid is sufficiently prefragmented and located in close proximity to the trigger region. Little is known about this escalation mechanism.

At the present time, there is a fair understanding about the initiation of RPTs in various systems, but in some instances, particularly for metal-water accidents, the theory is poorly developed and untested in controlled laboratory experiments. The area of escalation of a small-scale RPT to a large, coherent explosion has been developed into a logical picture, but again proof tests on a large scale are not available.

This article does not cover the extensive research carried out to delineate the cause and severity of RPTs possible in nuclear reactor accidents. Although there is not universal agreement, the general consensus is that the superheated liquid concept can explain many of these events and, more importantly, can indicate when RPTs are *unlikely* to occur in hypothetical reactor accidents.

II. Introduction

Rapid-phase transitions are events in which there is a very fast transformation from an initial phase to another, more stable phase. Of primary interest here are transitions from liquid to vapor, but the definition would still be applicable for other transformations such as those from vapor to liquid and liquid to solid.

In the liquid-to-vapor phase change, the key element is time. If significant vaporization occurs in a short time period, the process can, and usually does, resemble an explosion. If the liquid quantities are not small, concomitant shock waves emanating from the site of vapor formation may result in personnel injury or equipment damage.

"Explosive" boiling is certainly not the normal event to occur when liquids are heated. Thus, the very rapid vaporization process must be explained by theories other than standard equilibrium models. For example, if two liquids are brought into contact, and one is relatively nonvolatile but at a temperature significantly above the boiling point of the second liquid, an explosive rapid-phase transition sometimes results. Various models have been proposed to describe such transitions. None has been

completely successful in light of the many experimental results known for rapid-phase transitions in different liquid-liquid systems.

In the sections which follow, we have summarized the available facts for rapid-phase transitions in several systems of industrial interest:

- (1) LNG-water;
- (2) water-smelt (molten inorganic salts);
- (3) water-aluminum (molten);
- (4) water-reactive metals (e.g., molten titanium);
- (5) liquefied refrigerants-water (or oil).

In these examples, the first-named component is the one which boils explosively.

For small-scale experiments, the LNG and liquid refrigerant cases are analyzed using a model which assumes that the volatile liquid (or some part of it) is superheated to a temperature at which homogeneous nucleation occurs. Such nucleation is very rapid and the event resembles an explosion. An attempt is made to employ this same model to explain RPTs in the water-smelt, water-aluminum, and water-reactive metal cases, but data to make definitive conclusions are lacking.

The superheated liquid concept, in any case, may only supply a local trigger to initiate the RPT. Other ways to trigger such events are possible, e.g., detonation of small explosive charges can sometimes be employed. To produce large-scale, coherent RPTs, the trigger may cause collapse of vapor films in adjacent masses of volatile liquid and lead to the escalation of the small triggering event.

Since most experiments designed to study RPTs have been on a very small scale, it is possible that the importance of the triggering step has been overemphasized. Few data exist, however, to formulate reliable models for large-scale RPTs.

III. Rapid Phase Transitions between Liquefied Natural Gas and Water

A. SUMMARY

In certain instances, when LNG contacts ambient water, explosive vaporization occurs with concomitant shock waves both in the air and water. While isolated instances of such events were recorded as early as 1956, it was during the 1968-1969 Bureau of Mines tests that the phenomena first attracted wide interest. In these experiments, three explosive

events were recorded; one destroyed a laboratory test tank and two were noted when spilling LNG on an open pond.

These results stimulated a number of studies, both in industry (Conoco, Esso, Shell Pipeline) and in academia (University of Maryland, M.I.T.). The objective was, primarily, to delineate the mechanism that led to these explosive events. The results of many small-scale experiments, primarily conducted by Shell Pipeline Corporation and M.I.T., led to the hypothesis that the apparent explosion was, in fact, a very rapid vaporization of superheated LNG. Contact of LNG, of an appropriate composition, with water led to the heating of a thin film of the LNG well above its expected boiling temperature. If the temperature reached a value where homogeneous nucleation was possible, then prompt, essentially explosive vaporization resulted. This sequence of events has been termed a *rapid phase transition* (RPT), although in the earlier literature it was often described by the less appropriate title of *vapor explosion*.

A better understanding of the RPT phenomena led to definitive rules to indicate when an RPT was or was not possible in an actual spill. To employ these rules, one had to estimate the so-called superheat-limit temperature T_{sl} of the LNG, i.e., the temperature to which the LNG could be heated before undergoing an RPT. Thermodynamic stability theory as well as many laboratory measurements made it possible to estimate T_{sl} values for LNG of known composition. In fact, to a high degree of accuracy, the T_{sl} could be approximated as 0.89 times the mole-fraction-average critical temperature of the LNG—when the external pressure was 1 bar. Then, it was postulated, and proved experimentally, that the water temperature had to *exceed* T_{sl} for an RPT to occur. However, it was also shown from numerous tests that if the water temperature were significantly higher than T_{sl} (about 10–15% on an absolute temperature basis), the probability of an RPT then diminished essentially to zero for simple spills carried out in the laboratory. Apparently, high water temperatures led to the rapid establishment of film boiling with the vapor layer shielding the bulk LNG from direct contact with the water. Methane-rich LNG fits into this category and no RPTs would be expected from small-scale spills upon ambient water.

Pure liquefied propane has a value of T_{sl} around 326 K (53°C). Thus, one must heat water to at least this temperature before an RPT results. When, however, one does use water of this temperature, the probability of attaining an RPT is essentially 100%.

Some effort has been expended in obtaining RPTs from methane-rich LNG by *impacting* water on a cryogen surface. The rationale for such tests is to eliminate the vapor film and cause direct liquid–liquid contact. Little success has, however, been achieved for any LNG, but one can

modify dramatically the behavior of pure liquefied ethane. This cryogen with a $T_{sl} \sim 269$ K (-4°C) has never been known to undergo an RPT in simple spills on ambient water, but will most definitely do so when water is impacted on it.

Also, methane-rich LNG can undergo a *delayed* RPT following a spill. That is, since methane is preferentially vaporized, the residual liquid will enrich and may attain such a composition that it will then undergo an RPT. In all cases where this delayed event has been reported, the spill size has been much larger than normally used in laboratory experiments.

The late 1970s produced little new research. The mechanism was thought to be well understood and, since LNG transported in tankers would be methane-rich, there was little concern from industry. It came somewhat as a shock to discover that, in large spill tests such as those carried out at China Lake, RPTs of a rather violent nature could occur even with methane-rich LNG. One is prone to forget that in essentially all previous tests, the maximum spill size would be measured in liters rather than cubic meters.

For *large* spills which undergo an RPT, one must reconsider the initial assumption that only with LNG of an appropriate composition would one achieve an RPT. Thus, the concept of a "large-scale, coherent" RPT was developed. In these cases, the superheat concept may still play an important role, i.e., to trigger the RPT. Other triggering sources are, however, also possible. Current concepts of *large-scale* RPTs require the following set of circumstances:

- (1) Significant prefragmentation of the LNG must occur before the onset of an RPT. In the prefragmentation state, the LNG would exist in stable film boiling.

- (2) The water-LNG interface temperature, computed by assuming intimate contact, must exceed the value of T_{sl} for the LNG.

- (3) A trigger must exist to produce a significant pressure pulse. The trigger may result from a portion of the LNG superheating and attaining T_{sl} or it may be caused by other means.

The pressure wave propagating through the premixed LNG and water collapses the vapor film surrounding the LNG. Intimate liquid-liquid contact occurs and, since the interface temperature is above T_{sl} , rapid heat transfer and vaporization occur. The time scale of the vaporization is comparable to that of the trigger step. Propagation and escalation then result.

Concerning the projected energetics from LNG RPTs, Shell Pipeline measured overpressures from small-size ($0.1 \text{ m}^3 = 30$ gallons) spills both in the air and under water. From calibration tests in their spill apparatus,

they estimated that a strong RPT had the energy equivalent of some 0.4 MJ or about 0.1 kg TNT. With this assumption, one can project the expected air overpressure versus distance. Except for a few spills which generated somewhat higher values, the vast majority of Shell Pipeline's overpressures fall below the predicted values. The results show that beyond about 10 m, overpressures are less than about 7 kPa or 1.0 psi. With scatter, most overpressures measured at China Lake and at Maplin Sands range between 0.1 and 1.0 kg TNT equivalent. Overpressures in the water are larger and may reach tens of bars near the source of the RPT. No data exist, however, that show that pressures exceed those comparable to the vapor pressure of the LNG at T_{sl} .

B. BACKGROUND

The earliest reported observations of RPTs between LNG and water were made by Constock Liquid Methane Corporation at Bayou Long, Louisiana in 1956. LNG was intermittently pumped through 300 m of 10-cm uninsulated aluminum tubing supported on a floating stanchion 1 m above the water surface. Flow rates of 0.2 m³/min were maintained for periods of several days and on occasions exceeded one m³/min for a period of several hours. It is estimated that about 3700 m³ of LNG were spilled in a period of about 3 months during which 3 or 4 very audible eruptions—loud enough to be heard 0.5 km away—occurred. Since none of these events damaged standard window glass panes erected less than 15 m from the spill area, it was concluded that this phenomenon was unlikely to constitute a hazard.

The same type of event may have been observed at Amarillo, Texas during tests associated with transportation hazards of LNG for the API 6A6 (LPG/LNG) subcommittee of the API Tanker Committee. A 0.03-m³ quantity of LNG was being pumped into a cooling pond. It was "heaved into the air" and was reported to have reacted "explosively" on contact with the water.

The Wisconsin Gas Co., while draining LNG from a storage tank, noted explosions as the liquid flowed into a nearby pond. Ice chunks were ejected and carried some 30–40 m from the spill site.

A similar occurrence was noted by the Memphis Light, Gas and Water Division. They had built an earthen reservoir 1.5 m in diameter by 30 cm deep into which LNG was periodically poured and ignited to provide experience to operators in extinguishing fires. On one occasion, there was about 2–3 cm of water in the bottom of the reservoir when some 0.2 m³ of LNG was poured into it. The LNG was successively ignited and extin-

guished several times, and there was perhaps 3 cm of LNG remaining on top of the ice. The LNG residue was left to evaporate when there occurred what appeared to be an "explosion." Dirt and ice were thrown some 10–15 m from the reservoir.

Similar events were also observed in 1965 when LNG came in contact with water during the cool-down of the Transco frozen in-ground storage cavern at Hackensack, New Jersey (Enger and Hartman, 1972a–d). At the completion of construction, there was a water leak of about 0.2 m³/min through the lower part of the cavern surface which had been grouted rather than frozen. A small electrically driven pump had been left in the bottom to remove water. It was assumed that ice, formed after LNG addition, would prevent further leakage of water. Cool-down was begun by spraying LNG into the upper part of the cavern. However, temperatures did not drop as rapidly as anticipated and LNG fell to the bottom of the cavern.

Six and one half hours later, an RPT "explosion" occurred and the water pump stopped. Although the pump was subsequently restarted, it was disconnected after a second event. In the next 3 days, 10 similar events were recorded. During a typical one, the cavern roof and truss shook and the safety vents were forced open. The gauge pressure in the cavern (nearly 5.6×10^4 m³ in volume) increased from about 500 to 3700 Pa within a few seconds.

A series of experiments were run to find the probable cause of these explosive events. A 20-liter bucket was placed on the ground and a second bucket placed on a stand above it with a remotely actuated tipping device. In alternate experiments, water was poured on LNG and LNG on water. "Foamed ice" was formed, but no "explosions" occurred. The tests were extended by adding either additional LNG or water after the initial mixing of LNG and water had taken place. The further addition of LNG had no effect. However, when water was added to an already mixed quantity of LNG and water, an explosive event occurred which threw the contents of the bucket upward about 5 m.

C. BUREAU OF MINES STUDIES

The first well-publicized incident wherein an LNG spill on water produced an explosive vaporization took place during the 1968–1969 tests carried out by the U.S. Bureau of Mines Safety Research Center in Pittsburgh (Burgess *et al.*, 1970, 1972). Under contract to the U.S. Coast Guard, they were studying the spreading and vaporization rates of LNG on water.

While carrying out the spill tests, three unexplained "explosions" occurred in isolated incidents while pouring the LNG onto water. In the first incident, a 0.6-m-long \times 0.3-m-wide \times 0.3-m-deep aquarium was being used in small-scale experiments. The LNG was poured via a remotely actuated dumping apparatus from an open-mouth Dewar above the aquarium. An aluminum ramp had been placed just below the surface of the water in the aquarium to minimize mixing of the LNG with the water during pouring. Fifty-five spills were made without any indication of a violent reaction between the LNG and water. Then, during the 56th spill test, approximately 3 sec after the first LNG-water contact, an explosive event destroyed the apparatus. There was no ignition of the vapor.

The second incident occurred during a large-scale spill test on an artificial pond, approximately 60 m in diameter and 7 m deep. In one spill, when 0.26 m³ of LNG were being poured from a height of about 0.6 m out of an open-mouth insulated container, an "explosion" occurred which immediately dispersed most of the spilled LNG. A frame-by-frame study of the motion picture taken of the spill indicated the event was triggered no more than $\frac{1}{8}$ sec after LNG-water contact and that the first was followed by two others in rapid succession as the container emptied. One observer reported that "this explosion might have been equivalent to a stick of dynamite." No damage was done to the exterior of the metal container. An interior plastic liner which projected a few centimeters from the container was cracked in an exposed portion. This explosive event was a single occurrence in a total of 12 large-scale spills.

The third incident occurred during a vapor dispersion test on the same artificial pond. LNG was being discharged at a steady rate of 0.045 m³/min through a 3.8-cm-diameter pipe into an inverted 0.56-m-diameter steel drum. The drum was suspended with its open end about 0.5 m above the water and contained internal diffuser plates to distribute the LNG flow evenly. What was described as a "moderate explosion" occurred approximately 5 min after commencing the LNG spillage from the drum. The drum was rocked slightly but remained undamaged.

To understand better the nature of these explosive events, the Bureau of Mines (Burgess *et al.*, 1972) carried out the following additional experiments:

- (1) *Liquid propane spills into 341 K water.* Explosive vaporization always occurred and the delay between the start of the spill and the event was typically 0.2 sec. Strain-gauge pressure transducers were located 7.6 cm under the water interface and also in the air, 1.38 m from the spill container. The overpressure data are shown in Table I. The highest overpressure measured in the water was 410 kPa (60 psi) and the highest

TABLE I
OVERPRESSURE OF SPILLS OF LIQUID PROPANE INTO 341-K WATER^a

Propane (liters)	Diameter of water surface (cm)	Air		Water	
		Pressure (kPa ^b)	Impulse (kPa msec)	Pressure (kPa)	Impulse (kPa msec)
6	25	4.3	2.1	28	46
6	25	4.3	2.1	28	46
6	25	1.7	3.6	140	750
6	25	2.4	4.2	250	800
4.5	46	1.7	5.8	200	125
5	46	1.7	2.4	310	225
6	46	2.2	12.2	110	530
6	60	2.8	—	410	480
6	60	1.1	1.1	40	20
6	60	5.5	14.0	300	1400

^a From Burgess *et al.* (1972).

^b 1 kPa = 0.145 psia.

impulse 1400 kPa msec (0.2 psi sec). Burgess pointed out that such an impulse should accelerate 6 liters of liquid propane to a velocity of about 100 m/sec, and this is close to what was observed.

(2) *LNG spills on hydrocarbons.* Explosive boiling was obtained with spills of LNG on pentane or hexane (pure or layered on water). No pressure measurements were given.

(3) *Weathered LNG on water.* Erratic results were reported. The highest probability of an "explosion" resulted when the most weathered LNG was used.

The 1970 Bureau of Mines report stimulated research in several industrial and academic laboratories.

D. UNIVERSITY OF MARYLAND TESTS

Garland and Atkinson (1971) at the University of Maryland reported on many small tests in which a methane-rich LNG (95.1% CH₄, 3.0% C₂H₆, 0.8% C₃H₈, 0.3% C₄H₁₀, 0.1% C₅H₁₂, 0.7% CO₂, 0.01% N₂) was spilled upon water, water-organic mixtures, and pure organic liquids. No "explosions" were noted with spills upon water, although they did occur when the water was coated with *n*-hexane or toluene films. The principal conclusion reached in the study was that the concentrations of the heavier constituents of LNG were very important in determining whether or not

“explosions” occurred when LNG spilled on water. One interesting result reported by these authors relates to overpressure measurements made when LNG was spilled on *n*-hexane. (The transducer was positioned above the surface of the liquid.) In a glass vessel, the first spill generated a ΔP of about 4 bar. Without replacing the hexane, another spill was made and, in this case, the ΔP rose to about 9 bar. A third spill onto the same hexane gave $\Delta P > 10$ bar and the vessel broke. Carrying out the same test in a polypropylene container, the ΔP values for four sequential spills were 3, 8, 19, 28 bar! No explanation was given for the variation in ΔP , but the hexane composition (and temperature) would have varied from spill to spill.

E. CONOCO EXPERIMENTS

A few LNG¹ spill tests on *organic liquids* carried out at Conoco by Yang (1973) led to reproducible “explosions.” When saturated hydrocarbons from C₅ through C₈ (including many isomers) were used, immediate “explosions” were noted. Delays of 5 sec or longer were recorded before they occurred on methanol, acetone, or methyl ethyl ketone. Few or none were recorded for higher alcohols or for hydrocarbons above C₈ (or benzene).

F. EARLY M.I.T. WORK

Nakanishi and Reid (1971) at M.I.T. reported on pour tests with a liquid mixture of methane (92.7%) and nitrogen (7.3%). “Explosions” were reported for spills upon *n*-pentane, *n*-hexane, methylcyclohexane, and toluene. None were found for spills on *n*-butanol, benzene, *p*-xylene, solid *n*-hexane, mercury, or water (fresh or saline). It might be noted that the freezing points of benzene, toluene, and *p*-xylene are 5.5, -95, and 13°C, respectively. The fact that an “explosion” could be obtained with toluene but not with the other two organic liquids suggested that the ease of freezing the hot liquid surface was an important factor in determining whether an “explosion” could occur.

G. ESSO PROGRAM

Holt and Muenker (1972) at Esso carried out small-scale spills of LNG on ambient water and developed “compositional maps” delineating areas

¹ 90.1% CH₄, 5.4% C₂H₆, 2.1% C₃H₈, 0.6% *i*- and *n*-butane with the residual primarily N₂ and CO₂.

where "explosions" would result. They normally occurred only in low-methane-content LNG. A few tests were made with R12(CCl_2F_2) in 333-K water and only a mild eruption was noted. With R22 (CHClF_2), however, in 333-K water, the refrigerant sank and then underwent a violent and rapid vaporization that shattered the vessel. LNG was also found to undergo explosive boiling when spilled on gasoline layered over water.

H. M.I.T. LNG RESEARCH CENTER

The experiments described previously led to the hypothesis that the explosive boiling was due to local superheating of the LNG in contact with water (Enger and Hartman, 1972a-d; Nakanishi and Reid, 1971; Katz and Sliepcevich, 1971; Katz, 1972). The event was then renamed as a *rapid phase transition* (RPT) rather than as a vapor "explosion." To test this hypothesis, Porteous and Reid (1976) at the M.I.T. LNG Research Center undertook a series of experiments using both pure cryogenes and mixtures. The spills were carried out by tripping a Dewar flask containing the liquid hydrocarbon onto the surface of a liquid, usually water. Normally 500 cm^3 of hydrocarbon were used. The water area contacted was about 200 cm^2 . RPTs were monitored with a high frequency quartz pressure transducer located in the bottom of a polycarbonate hot-liquid container. The pressure signal was fed to an oscilloscope equipped with a camera and to a high-speed magnetic tape recorder triggered automatically by a signal greater than the initial baseline.

Spills were made with six pure hydrocarbons on water and other substances, over a wide range of temperatures, as shown in Table II. Given an appropriate substrate and temperature, all of the cryogenes would undergo an RPT when spilled.

The reproducibility of the RPT $[(100)(\text{number of spills that ended in an RPT})/(\text{total number of spills})]$ varied from 100 to 12%. At temperatures less than those necessary for an RPT, there was generally nucleate boiling and sometimes the substrate froze. The temperature of the transition from nucleate boiling to an RPT was quite sharp. At temperatures above the RPT region, film boiling took place. However, the temperature of this transition was not definite. The transition would often take the form of decreased reproducibility and RPT intensity at higher temperatures.

Five binary-hydrocarbon mixtures of ethane or ethylene with heavier hydrocarbons were studied (Table III). The only substrate used in these studies was water. If an RPT did not occur, ice always formed rapidly. When *n*-butane or *n*-pentane was the heavier component, RPTs were 100% reproducible over a particular composition range. This was not, however, true if the heavier component were propane.

TABLE II
SPILLS OF PURE ALKANES AND ALKENES

Cryogen	Substrate	Substrate temperature (K)	Result (reproducibility)
Ethane	Water	278–313	Boiling, ice forms
	Ammonia–water	271–297	Boiling, no ice forms
	Methanol	{ 264–305	Eruptions
		{ 306–331	Weak RPTs (100%)
	Methanol–water	{ 276–295	Boiling, foamy slush
		{ 296–304	RPTs (100%)
{ 303–319		Popping	
{ 319–325		Boiling, ice forms	
Propane	Water	{ 326–334	RPTs (85%)
	Ethylene glycol	{ 335–356	Popping, occasional RPT
		{ 317–358	Boiling
Isobutane	Water	358–372	Occasional popping
	Ethylene glycol	{ 298–348	RPTs (12%)
		{ 352–377	Nucleate boiling
		{ 379–393	Violent boiling
		{ 370–373	Film boiling, popping
		{ 374–379	Violent boiling
	Ethylene glycol–water	{ 381–388	RPTs (100%)
			Film boiling
<i>n</i> -Butane	Water	363–372	Boiling, popping
	Propylene	{ 303–312	Boiling, ice forms
{ 313–316		Popping	
{ 317–346		RPTs (100%)	
{ 347–363		Film boiling	
Isobutylene	Ethylene glycol	{ 376–378	Eruptions
		{ 379–408	RPTs (100%)

In addition to binary mixtures, the ethane–propane–*n*-butane ternary system was studied (see Fig. 1). Spills were also made with mixtures containing methane. The addition of as little as 10 mole % methane inhibited RPTs and none were ever obtained with methane concentrations in excess of 19 mole %.

Attempts were made to record both the delay time before an explosion and the overpressure of each RPT. Peak pressures were generally found to be about 6–8 bar and occurred within 4 msec from the start of an RPT.

One variation to the usual experimental procedure was tried. In this test, liquid ethane was impacted on a 293-K water surface. This was accomplished by evacuating the air space between the water container and an ethane reservoir above. When the ethane reservoir was broken by

TABLE III
COMPOSITIONS OF BINARY MIXTURES SPILLED ON WATER WITH AN RPT

Mixture	Water temperature (K)	RPT range, mole percent heavy component	Percent reproducibility
Ethane:propane	293	15–30	75
	278	4.5–8	100
Ethane: <i>n</i> -butane	283	4.5–8	100
	293	2.5–9	100
	303	4.5–16	100
Ethane: <i>n</i> -pentane	293	2–9	100
Ethylene: <i>n</i> -butane	293	9–23	100
Ethylene: <i>n</i> -pentane	293	5–18	100

driving a rod through the bottom, a very violent, immediate RPT resulted. No pressure transducer was in place for this test. Note that this impact test gave quite different results from those obtained by simply pouring liquid ethane onto a water surface, in which case no RPT ever resulted. The ethane–water impactation results were later verified by Jazayeri (1977). A similar, but much less violent, RPT resulted when liquid methane was used rather than ethane. Other impact studies at the LNG Research Center are described later.

The data reported in the Porteous–Reid study coupled with those of other investigators strengthened the hypothesis that hydrocarbon–water RPTs could originate from the rapid nucleation of vapor when a liquid was heated well above its expected boiling point.

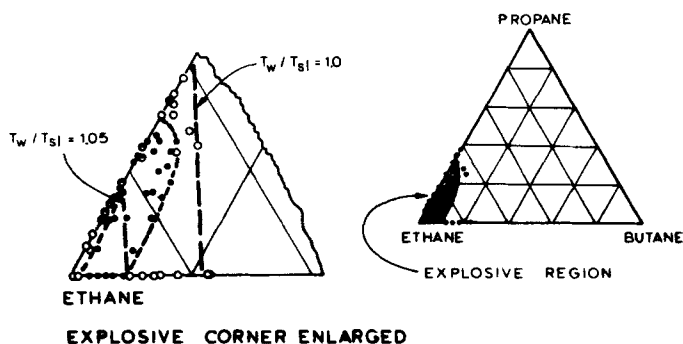


FIG. 1. RPT compositions for an ethane–propane–*n*-butane system on 293-K water: (●) explosion; (◐) pop; (○) boil.

In all laboratory-scale RPTs, the following salient facts stand out:

(1) Liquid-liquid contact is necessary, i.e., no coherent solid interface can be present. (Ice fragments on the surface of water will not prevent an RPT; the surface must be *covered* by ice.)

(2) There exists a sensitive lower limit of temperature for the hot liquid; below this limit, RPTs do not occur.

(3) Although, after contact, there may be a delay of a few milliseconds to a few hundred milliseconds, the time scale of the RPT is very short and is usually less than 5 msec. In large spills such as those at China Lake,² delay times are more difficult to quantify, but the RPT time scales still appear to be very small.

(4) The probability of an RPT depends upon the composition of the more volatile, cold liquid (e.g., ethane poured on water simply boils whereas ethane with a few percent *n*-butane undergoes a violent RPT).

(5) Impacting the cold, volatile liquid upon the hot liquid may lead to destructive RPTs or to RPTs that would not have occurred if the liquids were contacted in a gentler fashion.

(6) The probability of an RPT decreases when the hot liquid is initially at a much higher temperature than the critical lower limit temperature.

(7) If the temperature of the hot liquid interface is low enough to cause freezing of the surface, or even to form a viscous slush, RPTs are then rare.

These facts indicate that the hot liquid temperature should be equal to, or greater than, the homogeneous nucleation temperature of the cold, volatile liquid. The homogeneous nucleation temperature or the limit-of-superheat temperature T_{sl} has been measured for many hydrocarbons and hydrocarbon mixtures (Blander and Katz, 1975; Porteous and Blander, 1975; Porteous, 1975).

For an external pressure of one atmosphere, T_{sl} is about 0.89–0.90 times the critical temperature of a pure hydrocarbon. For hydrocarbon mixtures, the superheat-limit temperature may be closely approximated by a mole fraction average of the homogeneous nucleation temperature of the pure components.

This theory then indicates that the ratio $T_{\text{hot liquid}}/T_{sl}(\text{hydrocarbon})$ should exceed 1.00 for an RPT to occur. In fact, we might expect that the lower limit ratio of 1.00 might be somewhat higher since, in theory, when the hot liquid contacts the cold liquid, the interfacial temperature would be the more important value.

This interfacial temperature is less than the bulk temperature of the hot

² See Section III.J.

liquid. Commonly it is estimated to be that value which would result if two "slabs" at different, but uniform, temperatures are suddenly brought into contact. In this case, approximately

$$T_{\text{interface}} = T_{\text{hot,bulk}} - \Delta T \quad (1)$$

$$\Delta T = (T_{\text{hot,bulk}} - T_{\text{cold,bulk}})[\psi/(1 + \psi)] \quad (2)$$

$$\psi = [(k_f \rho_f C_f)/(k_h \rho_h C_h)]^{1/2} \quad (3)$$

The subscripts f and h refer to the cold and hot fluids, k is the thermal conductivity, ρ is the density, and C is the heat capacity. If the hot fluid is water and the cold fluid is a typical hydrocarbon, $\Delta T \sim 10\text{--}20^\circ\text{C}$. Then, to achieve a $T_{\text{interface}} \sim T_{sl}$, since $T_{\text{hot,bulk}} > T_{\text{interface}}$, one might expect the lower limit $T_{\text{hot,bulk}}/T_{sl}$ to be slightly larger than unity before an RPT would result.

The upper-limit temperature of the hot liquid where RPTs are not probable and film boiling occurs is less definite. Data from laboratory-scale experiments shown below indicate that a value equal to $1.10T_{sl}$ is not a bad approximation.

To summarize, this very simple theory indicates that, for small-scale hydrocarbon spills on water, RPTs may occur if

$$1.00 < [T_w/T_{sl}(\text{hydrocarbon})] < 1.10$$

As the superheat-limit temperature of light hydrocarbons can be closely approximated as 0.89 times the critical temperature, an equivalent statement would be

$$0.89 < [T_w/T_c(\text{hydrocarbon})] < 0.98$$

For mixtures, a pseudocritical temperature would be used and estimated as the mole fraction average of the critical temperatures of the pure components.

Table IV presents a summary of the explosive range for the experiments reported by Porteous and Reid. Although there is a spread of T_H/T_{sl} somewhat beyond the 1.00–1.10 range noted above, in most cases there is excellent agreement.

Only in the case of methanol is there a substantially different result. This is readily explained since the thermal conductivity of methanol is less than that for water and ΔT [in Eq. (1)] would be larger, so that the bulk methanol temperature must be higher to attain the necessary interfacial temperature to achieve an RPT.

The few examples shown when $T_w/T_{sl} < 1.00$ may indicate nucleation occurred heterogeneously at the interface before the bulk homogeneous nucleation temperature was achieved.

TABLE IV
EXPLOSIVE RANGES FOR HYDROCARBON SPILLS

Hydrocarbon	Hot liquid	Temperature of hot liquid T_H (K)	RPT range T_H/T_{sl} (hydrocarbon)
Ethane	Methanol	306–331	1.14–1.23
	Methanol–water	296–304	1.10–1.13
Propane	Water	326–334	1.00–1.02
Isobutane	Ethylene gly- col–water	374–379	1.04–1.05
	Water	371	0.98–?
<i>n</i> -Butane	Ethylene gly- col–water	387–398	1.03–1.06
	Water	317–346	0.97–1.06
Propylene	Ethylene glycol	379–408	1.03–1.10
Isobutylene	Water	293	1.02–1.06
Ethane–propane	Water	278	1.00–1.01
Ethane– <i>n</i> -butane	Water	283	1.02–1.04
		293	1.05–1.08
		303	1.06–1.11
		293	1.04–1.08
Ethane– <i>n</i> -pentane	Water	293	1.05–1.08
Ethylene– <i>n</i> -butane	Water	293	1.05–1.14
Ethylene– <i>n</i> -pentane	Water	293	1.02–1.08
Ethane–propane– <i>n</i> -butane	Water	323	1.08–1.13
Methane–ethane– propane– <i>n</i> -butane	Water		

While it appears that the bulk water (or hot fluid) temperature must be above $T_{sl}(\text{hydrocarbon})$, the upper limit is impossible to define. [The (T_w/T_{sl}) value of 1.10 used previously is only approximate.] As an example, in small-scale tests, liquid methane will not undergo an RPT when poured on water at any temperature. If the water were at 293 K, $T_w/T_{sl} = 293/166 = 1.76$; i.e., the ratio is far above unity.

Yet methane could have an RPT with water if there were some way to collapse the protective vapor film, perhaps by impaction upon the water surface at high velocity. Liquid nitrogen will even show an RPT if so impacted on water (Anderson and Armstrong, 1972). Extremely violent and immediate RPTs are also obtained when liquid ethane is impacted on water. In all these cases, good liquid–liquid contact is assured and, if the hot fluid temperature is greater than T_{sl} , RPTs are possible.

But, even if the criterion shown above indicates an explosion can oc-

cur, it may not. Water may freeze or some other event may occur to cause vapor to form and prevent the liquid from superheating.

The simple criteria noted above are shown in Figs. 2 and 3. The water was assumed to be 298 K. Lines representing a constant value of the $T_w/T_{sl}(\text{mixture})$ are shown for 1.0, 1.05, and 1.10. No RPTs would be expected where T_w/T_{sl} is less than about 1.00. Most RPTs occur when this ratio lies between 1.00 and 1.05.

In some cases, the initial LNG composition may lie in a region where RPTs are improbable (e.g., LNG with a high methane concentration), but boiling removes methane preferentially and the residual liquid composition would be enriched in ethane and higher hydrocarbons. In this case the LNG may reach the RPT region. These events would be referred to as *delayed* RPTs, and they are possible unless surface ice has formed. Spills on open water do not lead to extensive ice formation and just such a delayed RPT was noted in one of the ESSO tests sponsored by the American Petroleum Institute (Feldbauer *et al.*, 1972). Seven cubic meters of LNG (with a methane content of about 85%) were spilled in Matagorda Bay, Texas, in about 25 sec. A strong RPT occurred about 17 sec after the termination of the spill. In the next 15 sec, other, smaller RPTs resulted.

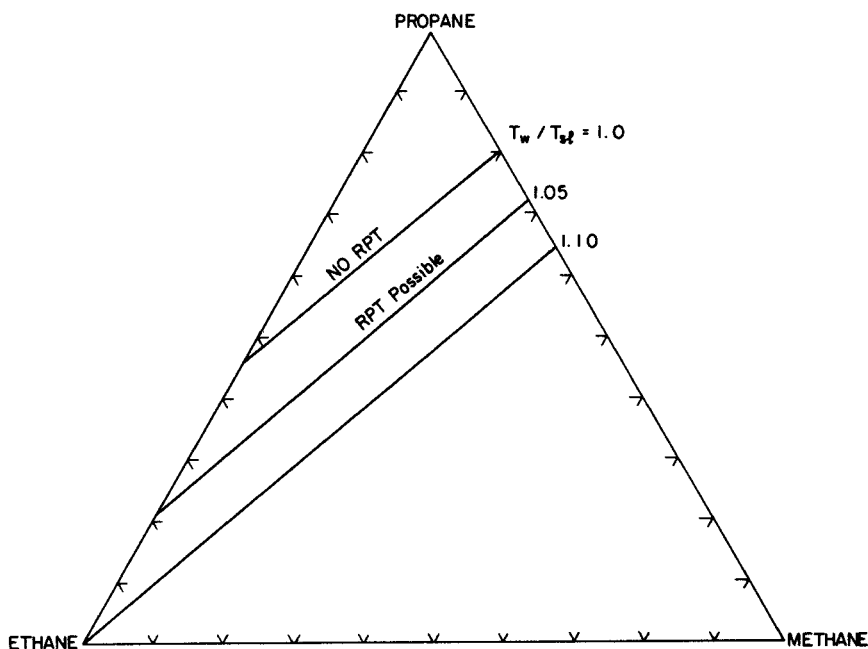


FIG. 2. RPT regions for a methane-ethane-propane system on 298-K water.

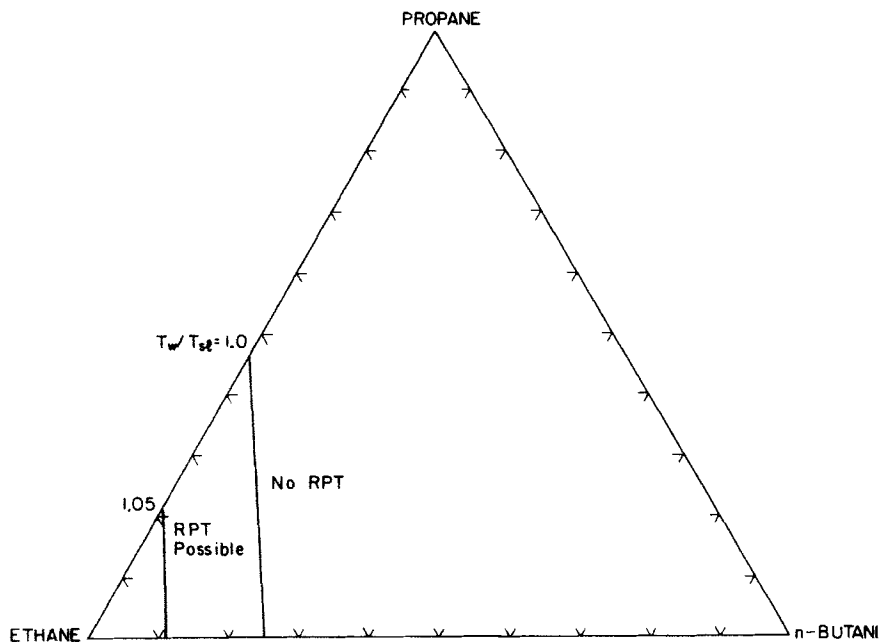


FIG. 3. RPT regions for an ethane-propane-*n*-butane system on 298-K water.

It is reemphasized that the M.I.T. tests and conclusions were based on small-scale laboratory spills of LNG. As will be seen later, the superheat theory requires modification when large LNG spills are considered.

I. SHELL PIPELINE CORPORATION PROGRAM

Enger and Hartman (1972a-d) carried out extensive studies at the Shell Pipeline Corporation. The work was divided into two phases. In the first, or exploratory part, a few small-scale LNG spills were made on water ranging from 273 to 356 K; no RPTs were noted. Also in the same phase, several pure liquefied gases were spilled on water. A brief summary of their results is shown in Table V.

These results are in excellent agreement with the data in Table II and IV. As noted earlier, the hot liquid temperature divided by the critical temperature of the liquefied gas would be expected to be in the range of 0.89-0.90 for an RPT to occur.

In the second phase of their studies, Enger and Hartman concentrated primarily on hydrocarbon mixtures. They made 255 spills, normally with 2-liter quantities on a water surface 900 cm² in area.

TABLE V
RESULTS OF SPILLS OF LIQUEFIED GASES ON WATER^a

Liquefied gas	Water temperature range where RPTs were recorded (K)	Temperature/critical temperature of liquefied gas
R-22	319–355	0.87–0.96
Isobutane	366–372	0.90–0.91
Propane	326–343	0.88–0.93
Propylene	315–348	0.86–0.95
Ethane	No RPTs	—
Nitrogen	No RPTs	—

^a From Enger and Hartman (1972a–d).

A number of tests were also carried out with liquefied ethane containing various amounts of heavier hydrocarbons. The compositions where RPTs were reported are given in Table VI. Also shown is the ratio T_w/T_{sl} which, from previous tests, would be expected to be slightly greater than unity for an RPT to occur. The agreement is excellent. Note also that, for pure ethane, $T_w/T_{sl} \sim 1.09$, yet no RPT results if this liquefied gas is simply poured into water. The value $T_w/T_{sl} \sim 1.09$ is close to the upper cutoff of the ethane binaries in Table VI. While theory would still indicate that RPTs are possible, they do not often occur when the water temperature is much above the superheat limit temperature of the liquefied gas.

The rule that, for an RPT to occur,

$$1 \leq T_w/T_{sl} \leq 1.1$$

TABLE VI
BINARY MIXTURES CONTAINING ETHANE SPILLS ON
297 ± 12 K WATER^a

Second component	Boiling temperature (K)	Mole percent of second component for an RPT	T_w/T_{sl} range ^b
Propane	231	42–19	1.01–1.06
Isobutane	261	4	1.09
<i>n</i> -Butane	273	23–2	1.01–1.09
Isopentane	301	11–2	1.04–1.09
<i>n</i> -Pentane	309	12–2	1.03–1.09

^a From Enger and Hartman (1972a–d).

^b $T_w = 297$ K.

appears to fit most of the other spill experiments reported by Enger and Hartman. The rule also is applicable for dilute salt solutions, but for saturated salt solutions, they report that RPTs were rare. Again one should note that all spills were with relatively small amounts of LNG.

Enger and Hartman also reported overpressures measured from RPTs. These are discussed later when the energetics of LNG RPTs are considered.

J. LLNL/NWC TESTS

Since 1978, *large-scale* LNG spill tests have been conducted by a joint team from Lawrence Livermore National Laboratory (LLNL) and the Naval Weapons Center (NWC) (Koopman *et al.*, 1981). The test site was located at NWC, China Lake, California. The program, sponsored primarily by the Department of Energy, had as its principal objective the acquisition of data to aid in modeling both vapor dispersion and thermal radiation effects (from LNG vapor cloud fires).

LNG was stored on site in a large insulated tank (see Fig. 4). Prior to a test the tank was either self-pressurized or pressurized with nitrogen gas, and some liquid is forced into 53 m of 25-cm-diameter pipe before the control valve. A small by-pass line around the control valve permitted LNG to enter the final 41 m of transfer piping in order to lower its temperature. Following the cool-down, the control valve was opened to allow liquid to flow and spill onto the surface of a small pond. The horizontal

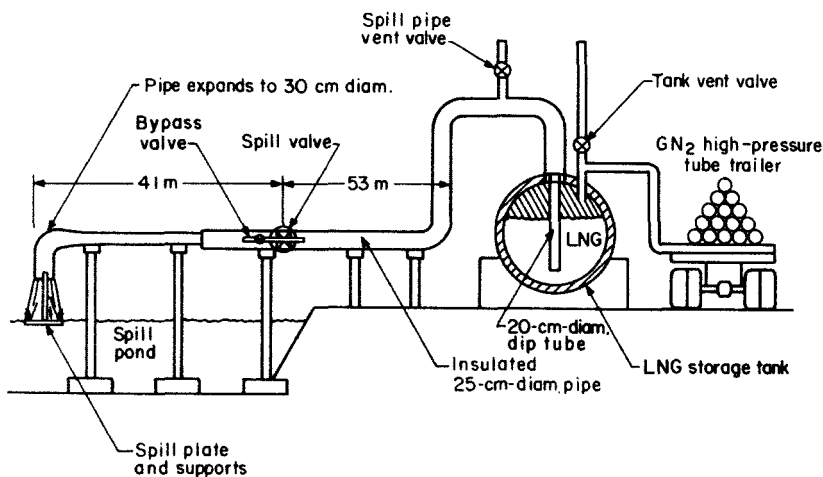


FIG. 4. The 40-m³ LNG spill facility at the NWC.

transfer pipe had a bend just prior to the exit to direct the liquid flow downward into the water, but penetration was diminished by the employment of a flat spill plate normally located at or slightly below the water surface.

Small RPTs were observed several times during the early tests in 1978. These occurred at the beginning of the spill, i.e., soon after full liquid flow was initiated. The early tests (the AVOCET series) spilled some 4.5 m³ of LNG at rates of about 3.5 m³/min. Impact velocities were estimated to be on the order of 1.5 m/sec, and LNG storage tank analyses (prior to a test) indicated that total hydrocarbons higher than methane were less than 9%. The AVOCET RPTs were attributed to the presence of a highly enriched LNG "heel" left in the transfer pipe after the cool-down period. In these tests the transfer pipe was slightly lower at the storage tank than at the spill point. Enrichment of the cool-down LNG would take place with the enriched heel being flushed out of the line when full liquid flow was started.

In 1980 the BURRO test series was conducted. These were much larger, with spills up to 40 m³ at injection rates of 12–18 m³/min. In all cases, the LNG tank liquid had a composition of over 83 mole % methane. The first five tests were conducted with no indication of an RPT. In BURRO-6, motion pictures clearly showed several strong RPT events late in the spill and at a location near the outer edge of the ice which formed on the pond around the spill pipe. Three RPTs were particularly sharp and water and LNG were violently ejected into the air; no instrumentation was operating to indicate overpressures either in the water or air, and no structural damage was done to the test facility.

In BURRO-9, the last test in the 1980 series, rather severe RPTs were noted throughout the test. Mud, water, ice, and LNG were thrown from the pond and loud noises were heard. The splash plate (ca. 23 kg) was blown from its supports and later found some 57 m from the pool. The transfer pipe, positioned by vertical steel supports anchored in heavy cast-concrete blocks, was moved and tipped. A postaccident analysis indicated that, in the cool-down period, enrichment of some LNG may well have occurred in the transfer line. Thus, at the start of the test, some RPTs might have been expected—and were, indeed, observed. The unusual result of the BURRO-9 test was the continuation of the RPTs during the entire test, i.e., when the high-methane content storage liquid was being spilled.

A summary of the BURRO test series parameters is given in Table VII. The column entitled spill-plate location needs some comment. In BURRO-2 through -8, the location of the spill plate relative to the water level changed due to normal pond evaporation. That is, the pond depth

TABLE VII
BURRO SERIES SUMMARY

Test	RPT	Time of occurrence	Ambient temp. (°C)	Spill volume (m ³)	Average spill rate (m ³ /min)	Spill-plate location	LNG composition (mole percent)		
							CH ₄	C ₂ H ₆	C ₃ H ₈
2	Several large	Late in spill	36.8	34.3	11.9	Below water (~5 cm)	91.3	7.2	1.5
3			34.0	34.0	12.2	Below water (~5 cm)	92.5	6.2	1.3
4			35.4	35.3	12.1	Below water	93.8	5.1	1.1
5			41.2	35.6	11.3	At water level	93.6	5.3	1.1
6			39.5	27.5	12.8	?	92.8	5.8	1.4
7	Numerous, very large	Throughout entire spill	33.8	39.4	13.6	Above water	87.0	10.4	2.6
8			33.2	28.4	16.0	Above water	87.4	10.3	2.3
9			35.4	24.2	18.4	Below water (~5 cm)	83.1	13.9	3.0

was greatest at the start of the series and it is believed that for BURRO-2, the depth was about 5 cm below the water surface. As the runs progressed, the height of the plate relative to the receding liquid level changed so that in BURRO-7 and -8, it was *above* the water surface. It is again not clear if these facts are important in explaining the severity of the BURRO-9 RPTs. One might, however, conjecture that the RPT events during BURRO-9 began with a few early RPTs from the enriched transfer line heel. These events led to the failure of one or more of the holding bolts on the spill plate. LNG could then penetrate deeper into the water.

It was fortunate that, for the BURRO-9 test, RPTs were anticipated and a pressure transducer was located in the air about 30 m from the LNG injection point. The reflected overpressures at various times are shown in Table VIII. Also given on the same table are the TNT equivalents assuming a free-air, point-source explosion. Some equivalents were significantly higher than noted in the smaller Shell Pipeline tests.

The test data for the 1982 test series (COYOTE) are shown in Table IX. As indicated, RPTs were noted in only a few spills. Test 9 in the COYOTE series was made with liquid nitrogen. No RPTs were reported. (In some of the preliminary tests carried out early in the program with this cryogen, incidents were seen that resembled an RPT.)

No overpressures were measured in the COYOTE series.

In Tables VII and IX, the initial LNG compositions are shown. In all cases, these compositions were well within the range of values wherein one would have predicted that the LNG would not undergo an RPT with simple, small spills on water. Of course, after injection into the water, the LNG composition will vary as boiling proceeds. As an example of this

TABLE VIII
TIME OF OCCURRENCE AND MAGNITUDES OF THE MAJOR BURRO-9 RPTs

Time ^a (sec)	Static pressure ^b (Pa)	TNT equiv. ^c (g)	Time ^a (sec)	Static pressure ^b (Pa)	TNT equiv. ^c (g)
6.5	1700	65	46.0	1700	65
7.1	2100	115	54.1	1700	65
9.2	3700	530	54.9	1800	80
21.4	7900	3400	66.9	2600	215
35.1	10,000	6300	72.7	700	65
43.2	1400	41			

^a $t = 0$ indicates the start of spill valve opening.

^b Measured at distance of 30 m, multiply by 1.45×10^{-4} to obtain psi; pressures are reflected values.

^c Equivalent free-air point source explosion of TNT.

TABLE IX
COYOTE SERIES SUMMARY

Test	RPT	Time of occurrence	Ambient temp. (°C)	Spill volume (m ³)	Average spill rate (m ³ /min)	Spill plate depth (cm)	LNG composition (mole percent)		
							CH ₄	C ₂ H ₆	C ₃ H ₈
1	Small	Early	30	14	6	30	81.7	14.5	3.8
	Large	Late							
2	Small	Early	27.6	8	16	2.5	70.0	23.4	6.6
3	—	—	22.8	14.6	13.5	2.5	79.4	16.4	4.2
4a	Small	Early	22.4	3.8	6.8	25	78.8	17.3	3.9
4b	—	—	20.6	6.0	12.1	25	78.8	17.3	3.9
4c	Large	Early	20.2	5.2	18.5	25	78.8	17.3	3.9
5	Large	Delayed	17.2	28	17.1	6	74.9	20.5	4.6
6	—	—	15	22.8	16.6	5	81.8	14.6	3.6
7	—	—	13.6	26	14.0	33	99.5	0.5	—
8a	—	—	12.8	3.7	7.5	33	99.7	0.3	—
8b	—	—	12.7	5.4	14.2	33	99.7	0.3	—
8c	—	—	12.3	9.7	19.4	33	99.7	0.3	—
9 ^a									
10a	—	—	10.6	4.6	13.8	36	70.2	17.2	12.6
10b	—	—	10.6	4.5	19.3	36	70.2	17.2	12.6
10c	Small	Early	11.6	5.0	18.8	Removed	70.2	17.2	12.6

^a Test 9 made with liquid nitrogen; no RPTs were noted.

variation, Figs. 5 and 6 have been drawn. The initial LNG composition was chosen to be 85% methane, 10% ethane, and 5% propane. As illustrated by the initial linear line in Fig. 5, during most of the boiling process, the vapor is essentially pure methane. Only after the methane content is nearly zero does the ethane begin to vaporize. During this period, as seen from Fig. 6, the ethane and propane compositions increase. Ethane shows a maximum value of 65 mole % before it too begins to decrease. Eventually the liquid consists of pure propane.

Also shown in Fig. 5 are the loci of compositions of LNG where the criterion

$$T_w/T_{sl} = 1.0$$

applies. Three water temperatures are noted. For example, starting with the 85–10–5 LNG in Fig. 5, during evaporation the LNG composition will intersect the $T_w/T_{sl} = 1.0$ lines where an RPT is probable. If the water temperature were 288 K, this intersection is given at a methane content of about 3 mole %. From Fig. 6, this corresponds to a condition where 85% of the LNG has evaporated. Thus, if the China Lake RPTs are to be interpreted as being the result of the homogeneous nucleation of the LNG (as a trigger or as the main event), then most of the LNG would have been

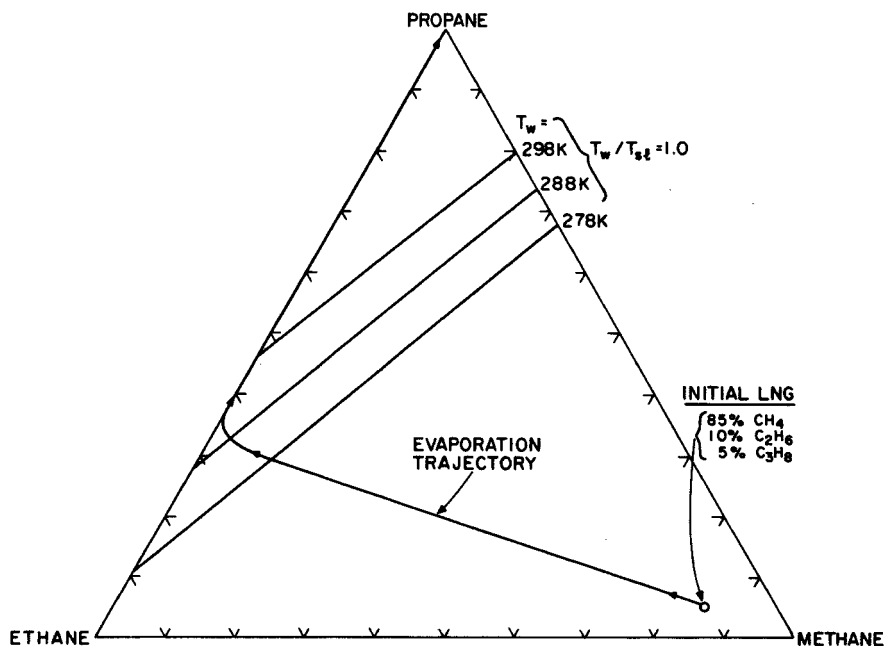


FIG. 5. Variation in LNG composition during evaporation.

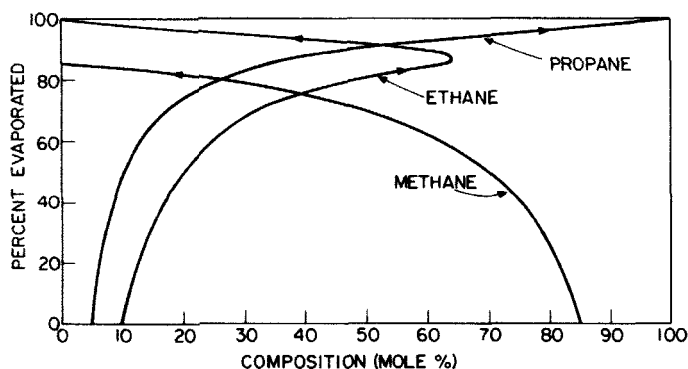


FIG. 6. LNG composition as a function of fraction evaporated of initial LNG: 85% methane, 10% ethane, 5% propane.

lost in any individual LNG mass before conditions were favorable for homogeneous nucleation.

K. OVERPRESSURES FROM LNG RPTs

Few investigators have reported overpressures from LNG spills. In Table I, the Bureau of Mines data for propane RPTs on water were shown, and in Table VIII, the LLNL/NWC results from one large LNG spill are given. In other sections, isolated overpressures are noted, but the data are sparse and the accuracy uncertain.

The most complete set of overpressure measurements was obtained by Enger and Hartman in the Shell Pipeline study. The data were collected using a spill tank 1.5 m deep and 2.1 m in diameter. The tank was made of 6.3-mm mild steel plate with 12-mm-diameter circumferential reinforcing rods spot-welded to the exterior. The capacity was 5.3 m³, but during the tests the water depth was held constant at 1 m (3.8 m³). The LNG was contained in a 0.13-m³ Dewar made from 6.3-mm mild steel with a stainless steel inner liner. The annulus was evacuated. When spilling, the Dewar lip was about 0.75 m above the water surface.

Pressures were determined from piezoelectric transducers. One was located in the middle of the spill tank, 70.1 cm below the water surface. The maximum peak pressure which could be measured was about 70 bar.³

Two air transducers were located on poles, 11 and 31 m from the tank center, slant range, and 7 and 27 m, horizontal range, respectively. Two other air transducers were set at various locations but always in a line-of-

³ 70 bar = 7 MPa ~ 1000 psi; 0.7 bar = 7×10^4 Pa ~ 10 psi

sight to the tank center water surface. All air transducers had a range of 0–0.7 bar.

Additional information resulted from an array of burst discs set 70 cm below the water surface in the central area of the tank.

For calibration purposes, data were obtained in tests where small charges of RDX explosive were detonated either 2.5 or 30 cm below the water surface, i.e., either 67.6 or 39.6 cm above the pressure transducer and burst discs. The measured overpressures were compared to those expected from such explosives assuming an “ideal” case of a spherical source and negligible effects of the tank and air–water interface (West *et al.*, 1972). These data allowed Enger and Hartman to estimate *calibration factors* to be applied to the measured output voltages from the transducers to allow the readings to be converted directly into pressure units. These factors have been employed to convert the original data; the results are given in Table X.

The most energetic RPT is listed first in this table. It is interesting to note the detailed description of this event. Observers about 0.3 km distant compared the noise to a strong sonic boom and remarked that windows rattled. The experimental team outside the instrumentation shack some 15 m from the spill noted a loud sound but no physical discomfort was experienced nor was there residual ringing of the ears. The spill Dewar and forklift were rocked back about 2 m but the Dewar was undamaged. The spill tank, weighing ~4 tons, was moved along the asphalt pavement some 10 cm but no other damage was done. The hollow wooden door of the instrument shack was slightly split around the hasp; two glass windows facing the spill tank were undamaged.

Enger and Hartman give other overpressure data, particularly from spills of liquefied propane on hot water. These overpressures were of the same order of magnitude as those noted for LNG.

In interpreting their RPT data, Enger and Hartman estimate that during the short period of liquid–liquid contact prior to an RPT, some 4 J/cm² was stored in the liquefied gas. About half of this was assumed to be available for mechanical work. An adiabatic expansion model was developed and, with the estimated heat transfer and *measured* overpressures, the *source* overpressures ranged from about 25 to 100 bar. Also, the overpressure data for RPTs for spills of about 0.1 m³ (~30 gallons) LNG indicated a source energy of about 0.4 MJ (~0.1 kg TNT). They caution, however, about comparing RPT events to chemical explosions because the energy release—and gas production—rates are quite different in the two cases.

An overpressure–distance graph has been drawn in Fig. 7. Plotted as the ordinate is the *reflected* pressure in pascals. The Shell Pipeline results

TABLE X
PEAK OVERPRESSURE DATA FROM LNG SPILLS ON WATER^a

Spill (m ³)	Volume (gallons)	LNG temp. (K)	Air transducer data (Pa/m)		Water transducer data (kPa)	Shock velocity (m/sec)
1.2×10^{-1}	32	124	$3.1 \times 10^4/3.4$	$2.6 \times 10^4/11$	$2.5 \times 10^3/31$	
3.8×10^{-3}	1	180	$2.9 \times 10^3/6.4$		$1.2 \times 10^3/23$	
3.8×10^{-3}	1	179	$8.3 \times 10^2/6.4$		$6.2 \times 10^2/23$	
3.8×10^{-3}	1	131	$1.2 \times 10^3/6.4$		$2.0 \times 10^2/23$	
7.6×10^{-2}	20	131	$5.0 \times 10^3/7.3$	$1.1 \times 10^4/11$	$1.9 \times 10^3/31$	
1.9×10^{-2}	5	147	$1.2 \times 10^3/7.3$	$2.1 \times 10^3/11$	0/31	
1.9×10^{-2}	5	180	$8.3 \times 10^2/7.3$	$4.1 \times 10^2/11$	0/31	
3.8×10^{-2}	10	148	$1.7 \times 10^3/7.3$	$7.0 \times 10^3/11$	$4.1 \times 10^2/31$	
4.7×10^{-2}	12.5	146	$2.5 \times 10^3/7.3$	$6.2 \times 10^2/11$	0/31	
1.1×10^{-2}	3	127	$5.4 \times 10^3/5.0$	$4.1 \times 10^2/11$	0/31	440
1.9×10^{-2}	5	131	$1.2 \times 10^3/5.8$	$1.2 \times 10^3/11$	0/31	
2.3×10^{-2}	6	144	$1.7 \times 10^3/5.8$	$2.1 \times 10^3/11$	$4.0 \times 10^2/31$	240
1.9×10^{-2}	5	125	$2.1 \times 10^3/5.8$	$1.5 \times 10^3/11$	$4.0 \times 10^2/31$	<700
6.6×10^{-2}	17.5	—	$2.7 \times 10^3/5.8$	$3.1 \times 10^3/11$	$8.3 \times 10^2/31$	1860
2.8×10^{-2}	7.5 ^b	155	$1.7 \times 10^3/5.8$	$1.5 \times 10^3/11$	0/31	1380
						420
						390
						410

1.1×10^{-1}	30	137	$2.5 \times 10^3/5.8$	$1.5 \times 10^3/11$	$2.0 \times 10^2/31$		
1.1×10^{-1}	30	133	$2.8 \times 10^4/5.8$	$8.3 \times 10^3/11$	0/31	$270 < P < 3450$	
1.9×10^{-2}	5	125	$2.1 \times 10^3/5.8$	$7.5 \times 10^3/11$	0/31		
6.8×10^{-2}	18	134	$3.7 \times 10^3/5.8$	$2.9 \times 10^3/11$	$4.0 \times 10^2/31$	$2800 < P < 7000$	
3.8×10^{-3}	1	141	$4.6 \times 10^3/5.8$	$2.9 \times 10^3/11$	0/31	$800 < P < 1600$	
2.7×10^{-2}	7	125	$2.1 \times 10^3/5.5$	$1.2 \times 10^3/5.7$	$4.0 \times 10^2/11$	< 830	370
3.8×10^{-3}	1	139	$1.5 \times 10^3/5.5$	$1.2 \times 10^3/5.7$	$8.3 \times 10^2/11$	$830 < P < 1600$	
1.9×10^{-2}	5	152	$4.0 \times 10^2/5.5$	$6.0 \times 10^2/5.7$	$4.0 \times 10^2/11$	< 830	
3.8×10^{-2}	10	152	$1.7 \times 10^3/5.5$	$2.5 \times 10^3/5.7$	$3.3 \times 10^3/11$	$1600 < P < 3600$	360
7.6×10^{-2}	20	152	$8.3 \times 10^2/5.5$	$1.2 \times 10^3/5.7$	$6.0 \times 10^2/11$	$2700 < P < 3600$	370
5.7×10^{-2}	15	150	$7.5 \times 10^3/5.5$	$3.3 \times 10^3/5.7$	$2.7 \times 10^3/11$	< 830	380
9.5×10^{-2}	25	150	$3.7 \times 10^3/5.5$	$7.0 \times 10^3/5.7$	$4.1 \times 10^3/11$	$1600 < P < 2800$	380
1.1×10^{-1}	30	154	$6.8 \times 10^3/5.5$	$3.5 \times 10^3/5.7$	$3.3 \times 10^3/11$	< 7000	380
7.6×10^{-3}	2	123		$2.3 \times 10^3/5.7$	$1.6 \times 10^3/11$	> 1200	

^a From Enger and Hartman (1972a-d).

^b C₂ + C₄ mixture.

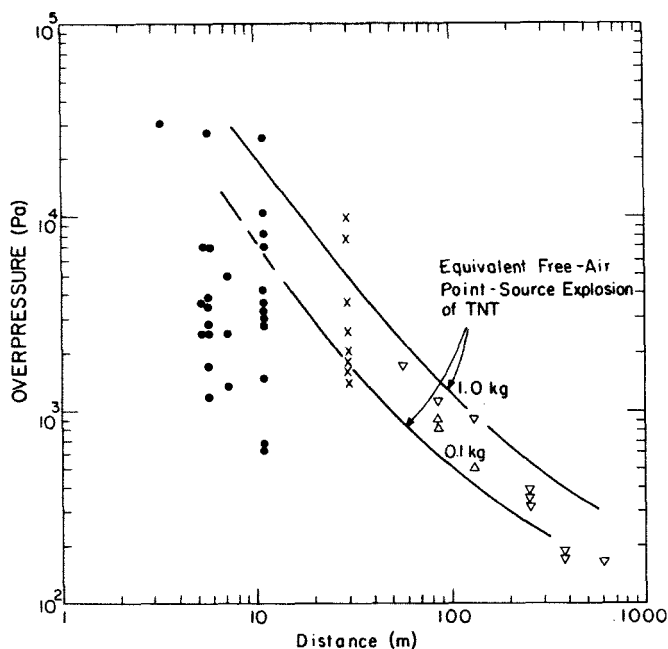


FIG. 7. Overpressures from LNG RPTs. Note: All pressures are reflected values: (●) Shell Pipeline, 1972 tests; (x) LLNL/NWC China Lake tests, 1980; (▽) Shell Research Maplin Sands tests, 1980, outside visible cloud; (△) Shell Research Maplin Sands tests, 1980, inside visible cloud.

scatter over a wide range with the three highest overpressures between 2×10^4 and 3×10^4 Pa (2.9–4.3 psi). Most values were, however, less than 10^4 Pa even when the distance was less than 10 m. The highest Shell Pipeline overpressures would be approximately equivalent to a free-air 1.0 kg TNT explosion. To show this, a curve is drawn to illustrate expected reflected overpressures from this size charge of explosive. Also shown is a similar curve for 0.1 kg TNT. The vast majority of the Shell Pipeline data fall below this latter curve. Recent Shell Research studies at Maplin Sands also yielded overpressures (Nguyen, 1982). Some of their data are shown in Fig. 7. Expressed in terms of TNT equivalent, their results indicate values of 0.1–0.4 kg.

Also noted in Fig. 7 are the overpressures measured in the large China Lake spills (Table VIII). The overpressures cover a wide range, with the maximum pressure (10^4 Pa) corresponding to about 6.3 kg TNT.

The Bureau of Mines overpressure data for propane spills on hot water fall well below the solid curve; Shell Pipeline data for this system are also low.

Thus, it would appear that overpressures experienced in the air from LNG RPTs for spills less than about 30 m³ are not particularly large unless one is very close to the spill site. Overpressures in the water are much larger, as shown in Table X from transducer measurements about 0.7 m from the surface. In fact, in one instance, the overpressure in the water exceeded the critical pressure of the LNG; this would not have been expected from the superheated liquid model.

IV. Smelt–Water Explosions

A. SUMMARY

Smelt, a molten salt mixture containing primarily Na₂CO₃, is a product of chemical recovery furnaces in the paper-pulp industry. Due to an accident, either in an operational sense or from a failure of some furnace equipment, boiler water may contact the smelt within the furnace confines. Experience has shown that contacts can lead to an explosion⁴ with concomitant shock waves that may cause significant damage. Also, smelt quenching outside the furnace to form “green liquor” has, on occasion, resulted in similar explosions. The Institute of Paper Chemistry and various technical societies affiliated with the paper industry have conducted or monitored a number of research programs to delineate the mechanism of these smelt–water explosions and to recommend techniques to eliminate them through simple, yet viable, process modifications.

Research into the smelt–water explosion phenomenon began in 1955 with studies on the quenching of soda smelt. It was discovered that if the smelt were pure Na₂CO₃, no explosions resulted, but the addition of NaCl or NaOH in concentrations of about 10% led to explosive smelts. Explosions were more severe when green liquor (a salt solution) was used instead of water. Further dissolver tank experiments were made in 1956 with kraft smelt. This smelt differs from a soda smelt in that the concentration of Na₂S is significantly higher. Kraft smelts were shown to be more prone to explosions and the sensitizing action of Na₂S was cited as the cause. As in the earlier soda smelt studies, it was found that NaCl and/or NaOH greatly sensitized the smelt and increased the probability of an explosion after contact with water.

Various theories were suggested to explain the explosions (e.g., free metallic sodium, hydrogen generation), but all were later proved to be

⁴ The term “explosion” is used in most instances in this section rather than rapid phase transition in accordance with the literature in this area.

inadequate. The dissolver-tank explosion problem was, in effect, eliminated by the use of steam shatter jets to disperse the entering smelt into small globules which would rapidly solidify. No recent literature pertains to dissolver-tank explosions.

Laboratory investigations of smelt–water incidents within the recovery boilers were carried out from 1960 to 1980. These added to the basic store of data, but few new results were obtained. It was confirmed that molten sodium carbonate would not explode when contacted with water, but many other salts added to the Na_2CO_3 led to explosive smelts. As in the earlier programs, studies concentrated on NaCl , NaOH , and/or Na_2S as additives. A few compounds were also identified as desensitizers, e.g., CaCO_3 , NaAlO_2 , and Fe_2O_3 , although these were not sufficiently effective to be used to prevent explosions in plant operations. Suggestions were tendered that their efficacy was related to the greater ease of gas formation (CO_2) at the smelt–water boundary. Similarly, some chemicals were found which, when dissolved in the water, inhibited explosions, e.g., ammonium salts or polyethylene glycols. On the other hand, many dissolved salts exacerbated the explosion; green liquor was also placed in this class.

Chemical reactions were shown to play a minor role in a smelt–water explosion, although gas samples from kraft smelt–water incidents showed that hydrogen evolution could be correlated with Na_2S content. There was general agreement that the explosion mechanism was physical in nature.

A few attempts were made to measure the overpressures from explosions. Pressures were not high, but the rise time to the pressure maximum was short (ca. 1–2 msec) and the shock quite localized. The highest quoted overpressure was about 20 bar a few centimeters from an explosion (Nelson, 1973).

Apart from the laboratory studies, statistical surveys of actual recovery boiler explosions have shown that such incidents are relatively rare and, in the United States occur, on the average, about once every 100 years of boiler operation. All explosions have been traced to events which allowed water to enter the furnace and contact the smelt, e.g., broken water tubes or dilute liquor feed. A listing of the presumed causes of all known smelt–water explosions is given in Table XII.

Few in-depth studies have been made of actual furnace smelt–water explosions and, therefore, it is difficult to delineate expected overpressures and impulses. One case history is presented to indicate in a qualitative fashion the type of damage in a large explosion.

As noted earlier, no viable theories of the smelt–water explosion had been widely accepted during the early period of investigation. Nelson in

1973 proposed that when the molten smelt contacted liquid water, the latter was heated to its superheat-limit temperature where homogeneous nucleation occurred. From other studies, primarily on the LNG–water interactions, it was known that such a homogeneous nucleation process would proceed with explosive violence (see Section III). The model of Nelson further hypothesizes that the initial superheat-limit explosion(s) would lead to rapid mixing of the smelt and water and would enhance the steam yield. Nelson's theory was questioned since smelt temperatures were much higher than the superheat-limit temperature of water, and, in addition, the theory could not differentiate between various smelts. The superheat theory was modified by Shick (1980), wherein he suggested that the contact of smelt and water led to *both* heat and mass transfer fluxes. On the water side, a strong salt solution would be formed, and it is expected that such solutions have significantly higher superheat-limit temperatures than pure water. Thus, higher water solution temperatures could be achieved and the thin film of saltwater heated to the superheat limit. This modified theory also indicated why fused Na_2CO_3 was nonexplosive, i.e., Na_2CO_3 has an inverse temperature–solubility curve with essentially zero solubility at temperatures below the critical point of water. NaCl , NaOH , Na_2S , and other sensitizers, on the other hand, show continuous solubility and vapor pressure curves with maximum values of pressure well in excess of the critical point of water.

This salt-gradient theory deserves further attention. It is possible that the concepts may be applicable to vapor explosions in different industries.

B. BACKGROUND

To prepare a wood pulp, there is usually a digestion step to hydrolyze the lignins and to separate the cellulose fibers. The kraft and soda processes are the topics of this section. In both, an alkaline solution of NaOH and Na_2CO_3 (with Na_2S in the kraft process) is fed with wood chips to the digester, which operates at an elevated pressure and temperature. The waste stream, after pulp separation, must then be treated to recover and recycle the feed chemicals. This product stream is known as black liquor. It is concentrated in an evaporator, and the organic portion is then burned in a recovery boiler, where the inorganic chemicals are melted. The molten salt product is referred to as *smelt*. It is dissolved to form green liquor and, after subsequent causticizing steps, is recycled to the digestors.

The smelt–water explosion problem is of primary interest in kraft recovery furnaces where, from operational error or an equipment failure,

water contacts smelt on the furnace floor. However, some research has been carried out to study explosions in the dissolving operation where smelt is converted to green liquor.

Research studies conducted in both areas are reviewed in this section.

C. DISSOLVER TANK EXPLOSIONS

Molten salt (smelt) tapped from black liquor boilers is quenched and dissolved to form green liquor in tanks near the boiler. On occasion, explosions have resulted which severely damaged the dissolver tank. (These events are different from the smelt–water boiler explosions described later.)

Sallack (1955) was the first to publish a study of dissolver-tank explosions. He was motivated by incidents which occurred in a soda pulp operation with a dissolver tank 4.3 m in diameter and 3.7 m tall. Molten smelt entered the tank at the top and was to be broken up with a jet of recirculating green liquor. Agitation of the bulk liquid was also accomplished by air jets. Operation was normally smooth, but if a boiler upset led to a sharp increase in smelt flow, then the smelt–green liquor breakup operation was inefficient and unbroken slugs of smelt could enter the bulk green liquor in the tank. Explosions could then occur.

To understand the phenomenon better, Sallack carried out a number of laboratory tests wherein he poured about 170 g of smelt into water or green liquor. He also varied the composition and temperature of the smelt. His principal findings were as follows:

- (1) No explosions could be achieved with pure molten Na_2CO_3 .
- (2) The probability of an explosion was 100% if the sodium carbonate were mixed with more than 7 wt. % NaCl or 10 wt. % NaOH .
- (3) Explosions with green liquor were more violent than those with water, and, for both, an increase in temperature reduced the severity and probability of an explosion.

Whereas Sallack was concerned with soda smelts, Nelson and Kennedy (1956a,b) were interested in kraft smelts in which sodium sulfide was present in significant amounts. In Table XI, typical analyses are shown for both types of smelts.

The experimental procedure followed by Nelson and Kennedy was very similar to that used by Sallack, and their results agreed with Sallack's conclusions in regions of overlap. With kraft smelts an explosion was easier to achieve and the presence of Na_2S was cited as a possible

TABLE XI
TYPICAL ANALYSIS OF SODA AND KRAFT SMELTS^a

	Soda (wt. %)	Kraft (wt. %)		Soda (wt. %)	Kraft (wt. %)
Na ₂ CO ₃	92.5	69.0	NaOH	1.6	—
Na ₂ SO ₄	0.8	3.5	NaCl	1.3	2.0
Na ₂ SO ₃	0.2	1.6	K (as K ₂ CO ₃)	1.5	5.3
Na ₂ S ₂ O ₃	1.0	0.7	Insoluble	0.1	0.6
Na ₂ S	1.0	17.3			

^a From Nelson and Kennedy (1956a,b).

reason. Kraft smelts could be sensitized (i.e., from a nonexplosive domain to an explosive one) with small quantities of NaCl or NaOH. Three types of dissolver-tank incidents were cited: an *instantaneous* one which occurred as soon as the smelt contacted with water, a *short-delay* type wherein the smelt had to fall to the bottom of the test vessel, and a *delayed* explosion that took place several seconds after the smelt had reached the vessel bottom and had coalesced to a larger mass. Normally, the more violent incidents took place in delayed cases.

In agreement with Sallack, if the water or green liquor temperature were high, the explosion probability decreased, but he cites one anomalous case: "a composition which gave an immediate violent surface explosion in cold water produced a terrifically violent deep explosion in hot quenching water. The blast was heard more than $\frac{1}{4}$ mile away" (100 g of smelt was used).

There had been some suggestions that explosions were due to free metallic sodium in the smelt. This hypothesis was disproved by adding oxidizers (KNO₃ or Na₂O₂) to the smelt with no significant changes noted in the explosion pattern.

Explosions could not be obtained with smelt poured into transformer oil.

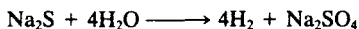
Whereas these early experiments provided interesting data, no mechanism was developed to explain the explosion phenomenon. In fact, since the 1950s there has been little interest in conducting further studies in dissolver tanks because the addition of efficient steam-shatter jets at the smelt entrance has effectively eliminated explosions in this section of the process. Further studies were directed to the explosions which took place within the recovery boiler as a result of water contacting the smelt on the furnace floor.

D. LABORATORY INVESTIGATIONS

1. *Rogers et al. Study*

Rogers *et al.* (1961) melted mixtures of Na_2CO_3 , Na_2SO_4 , and Na_2S in a closed 23-cm-diameter, 1.8-m-long pipe. Smelt quantities ranged around 9 kg and about 3.7 kg of water or green liquor was injected *under* the surface of the smelt. A manometer in the side of the pipe yielded a quantitative assessment of the pressure pulse in an explosion. The water-injection pressure was high (31 bar). Gas samples could be taken after an explosion.

Rogers *et al.* confirmed that the presence of Na_2S in Na_2CO_3 could lead to an explosive smelt; they also showed that the concentration of hydrogen in the vapor increased with the quantity of sodium sulfide originally present. It was suggested that Na_2S reacted with water as follows:



and the hydrogen played a key role in the explosion. [Later work (Combustion Engineering, 1966) has shown, however, that the explosion sequence is unchanged even if air is replaced by nitrogen, so any $\text{H}_2\text{--O}_2$ reaction is normally neglected.]

To indicate the magnitude of the pressure pulse, their most violent explosion occurred with a smelt consisting of 20% Na_2S , 75% Na_2CO_3 , and 5% Na_2SO_4 . Green liquor was injected. The pressure rose 27 kN/m² (4 psi) and the exit gas contained about 8% hydrogen.

2. *Research by Combustion Engineering*

Combustion Engineering (1966) carried out a laboratory program that produced additional information on the smelt–water explosion. As with the Rogers *et al.* study, water was injected under smelt. Beginning with a base of nonexplosive, fused Na_2CO_3 , they showed that the molten salt could be sensitized by addition of Na_2S , NaCl , NaOH , other halide salts, aluminum borate, etc. However, with explosive smelts, the sensitivity could be reduced with CaCO_3 or sodium aluminate. Also, ammonium sulfate or polyethylene glycol solutions usually quenched smelt with no or less violent explosions. This finding led to two patents (Nelson and Norton, 1969; Nelson, 1971).

The research results clearly indicated that the smelt–water explosion yielded a localized, high-energy shock wave which moved at velocities of over 700 m/sec. The maximum pressure rise was achieved in about 1 msec. These facts were related to the results found in real boiler explosions in descriptive terms as “there were 3–4 inch depressions 3 to 6 feet

across the strongly supported furnace floor tubes and localized deformation of heavy wide-flange beams below." (A similar *case history* description is given later in Section IV,F.)

They also proved that explosions could occur in nitrogen-rich atmospheres and no flame was seen (even when viewed in a darkened room). A few experiments showed that explosions could often be eliminated if "enough" dissolved material such as methyl or ethyl alcohol, acetone, or ammonia were used in the quench water. Conversely, dissolved "stable" salts such as NaCl increased the violence of an explosion. (Green liquor would also be included in this list.)

3. Lougher *et al.* Study

Lougher *et al.* (1968) reviewed the situation, presented some additional data, and developed recommendations for further work. They examined existing theories to explain smelt-water explosions and rejected all. They too noted that sodium aluminate in the smelt reduced the probability of an incident and also stated that CaCO_3 and Fe_2O_3 were effective. Most other additives (and over 90 were studied) either led to more violent explosions or were ineffective. No correlation of the smelt additive results was given. Also, water with various additives such as surfactants, starch, sucrose, glycerine, and hydroxymethyl cellulose still exploded when contacted with a sensitized smelt.

One of the more interesting aspects of the Lougher *et al.* study was the discussion section dealing with the vapor pressure of water in salt solutions. Using the data of Keevil (1942), they pointed out that hot pressurized water could dissolve significant amounts of some salts and attain vapor pressures well in excess of the critical point of water (647 K). This led them to suggest that heats of solution may play a role in the explosive mechanism, especially if such enthalpy changes are highly exothermic. No definitive mechanism was, however, developed. We will return to the general idea of smelt-water solutions later when the recent theory of Shick is described.

4. Krause *et al.* Study

Krause *et al.* (1973) carried out the last detailed U.S. experimental investigation of the smelt-water explosion phenomenon. A large number of experiments were conducted with variations in the smelt composition. The scale was quite small with 0.03–1 g quantities of water injected at high velocity (20–30 m/sec) onto the surface of the smelt. A few tests were also made with small drops (0.8–0.3 g) of water on the end of a ceramic tube that was dropped into the smelt. Some information concerning pres-

sure pulses was obtained from a transducer on the end of an alumina rod that penetrated the smelt. Peak pressures were near 280 kN/m^2 (40 psi) within 1–2 msec after injection. (It is also stated in the report that Combustion Engineering, in earlier tests, found pressure rises from $690\text{--}1200 \text{ kN/m}^2$ a few centimeters above the melt during an explosion.)

The general conclusions from this study are quite similar to those reported earlier, i.e., pure fused Na_2CO_3 is nonexplosive, but this melt can readily be sensitized with NaCl , NaOH , or Na_2S . Even K_2CO_3 , Na_2SO_4 , and Na_2SO_3 were mild sensitizers.

A detailed study of the physical properties of various smelts (viscosity, surface tension, density, and sonic velocity) led to the conclusion that there were no significant differences in these properties with explosive or nonexplosive smelts.

Other studies showed that those smelts which could release CO_2 at a high rate after contact with water were less explosive. This finding was related to the known fact that gas-evolving chemicals (CaCO_3 , NaAlO_2) were effective inhibitors.

A model based on inertial restraints was developed, but it has not been widely accepted since it does not explain many of the experimental facts for smelt–water explosions.

A final laboratory study was described by Shick and Grace (1982) as being carried out in Sweden (Bergman and Laufke, 1981). From 10 to 100 g of water were injected into 10–30 g of smelt. In some tests subsurface injection was used at pressures of 10 bar, whereas in others a ceramic capsule with water was burst under smelt with electric fuses. Smelts of a wide range of compositions could be exploded with the subsurface injection. Comparison of explosion intensities to those produced by TNT or black powder (as judged from pressure–time traces) suggested that 1 kg of water was equivalent to 0.03–0.2 kg TNT or 0.3–2 kg black powder.

E. STATISTICAL SURVEY OF SMELT–WATER BOILER EXPLOSIONS

Taylor and Gardner (1974) and, more recently, Grace and Taylor (1979) have made detailed statistical analyses of the reported smelt–water explosions in modern recovery boilers operating in the United States and Canada. There have been 77 incidents in the period from January 1958 through July 1979. Of these 77 explosions, 55 occurred in the United States and 22 in Canada. The time period covered 5120 boiler-years of operation in the United States and 1070 boiler-years in Canada.

Over 80% of all operating boilers have never experienced an explosion; thus, the phenomenon should be viewed as a relatively infrequent event.

In the operation of a recovery boiler, the inorganic fraction of the fuel (black liquor) ends up as a molten mixture of inorganic salts (smelt) with some unburned carbon. The presence of this molten salt in the boiler results in a hazardous situation if it were to be contacted with water or a dilute black liquor. Essentially all boiler explosions have, therefore, resulted from an accident wherein water did contact the smelt. About one-third of the explosions can be traced to an operational situation where the fuel (black) liquor was very dilute (or even pure water) and this fluid fell to the furnace floor to contact smelt. In another one-third of the cases, a water tube failed and allowed direct ingress of water into the boiler. The remaining third were assigned to miscellaneous events—all of which allowed water to enter.

Explosions occurred more frequently during start-up operations and in new, or relatively new, boilers. Somewhat surprisingly, the frequency of incidents was also significantly higher in the larger boiler sizes. No correlation was noted between explosion frequency and operating pressure.

Table XII presents the date, the qualitative estimate of damage, and the cause of all reported explosions (112) from 1948 through 1979 (Grace and Taylor, 1979).

F. DESCRIPTION OF SEVERE FURNACE EXPLOSION

The following was excerpted from a damage report of a smelt–water explosion.

The recovery boiler in question was heavily damaged and all four water walls and most of the furnace floor had to be replaced. The explosion opened up all four corners of the furnace from the firing gun level (third floor) to the roof (~30 m), and buck stays were sheared off at the corners. Some openings were as wide as 1.2 m about halfway up the wall. The water walls were displaced over 1 m and left a corrugated pattern in the walls where they were constrained by buck stays.

The most severe damage was on the front wall. The displacement was such to impact against the walkways and I-beam supports. Supporting I beams, 15–20 cm flange to flange, were twisted and deformed. A concrete walkway on the fifth floor was moved about 1 m and essentially demolished.

The damage continued to the top of the furnace, but screen and superheater tubes were not damaged. One soot blower was blown onto the roof of an adjoining building and another knocked loose.

The floor of the furnace underwent considerable deformation. The floor beams were 52 cm from top to bottom with a 33-cm-wide flange. One such beam had a 20-cm permanent deflection.

TABLE XII
BLACK LIQUOR RECOVERY BOILER EXPLOSION LIST^a

Date	Amount of damage	Water source	Cause of explosion
8/14/48	Major	Wall tube	Unknown
10/21/48	Negligible	Unknown	Unknown
2/2/51	Major	Wall tube	Failure of feedwater supply—cause unknown
3/4/51	Major	Wall tube	Stud pushed from wall tube by bar and sledge hammer
11/30/51	Severe	Floor tube	Overheating—cause unknown
11/17/55	Extensive	Wall tube	Smelt pushed stud from wall tube
5/21/58	Moderate	Water hose	Water used to wash flame arrester on vent gas system entered furnace
9/21/58	Moderate	Floor tube	Unknown
6/19/59	Slight	Floor tube	Unknown
8/17/59	Major	Gen. tubes	External corrosion of generating tubes under accumulated dust on mud drum
9/14/60	Negligible	Wall tube	Unknown
11/25/60	Moderate	Feedwater or plant water system	Superheater was filled with water to locate superheater leak for repair while smelt still molten in furnace (furnace down at time)
4/12/61	Moderate	Soap handling	Talloy soap was being fired separately from black liquor when weak black liquor beneath soap entered pump suction
11/4/61	Moderate	Black liquor system	Firing weak black liquor
12/3/61	Very major	Screen tube	Overheating as a result of tube blockage from unknown causes
8/25/62	Moderate	Black liquor system	Firing weak black liquor without burner tips in place
10/12/62	Slight	Unknown	Water from wash-up hose
10/6/63	Major	Gen. tube	Boiler was operated with a known tube leak until an orderly shut-down and repair could be arranged. Explosion occurred after small leak became a big one when wall of tube fell out
11/30/63	Slight	Water-cooled door	Refractory covering over cooling coil failed, exposing coil to either overheating or accelerated corrosion

TABLE XII (Continued)

Date	Amount of damage	Water source	Cause of explosion
5/25/64	Major	Talloyl spent acid system	Spent acid from talloyl operation was added directly to furnace separately from black liquor fuel
6/23/64	Major	Screen tube	A chunk of accumulated debris fell from upper furnace onto screen tube, breaking it off adjacent to a tube support
8/13/64	None	Floor tube	Smelt leak through furnace floor eroded or corroded floor tubes
8/17/64	Slight	Floor tube	Use of air lances
1/11/65	Moderate	Black liquor system	Attempted to stop smelt leak in corner of furnace bottom by quenching with heavy black liquor
3/18/65	Moderate	Black liquor system	In course of shutdown for superheater leak, char bed was flooded with heavy black liquor which probably became dilute from lack of evaporation in venturi scrubber as shutdown proceeded
8/14/65	Slight	Black liquor system	Firing weak black liquor
12/28/65	Slight	Black liquor system	Firing weak black liquor
1/30/66	Moderate	Screen tube	Overheating when instrument lines exposed to cold weather froze, making feedwater controls and drum level indicator inoperative or unreliable.
4/13/66	Unknown	Water jacketed air nozzle	Cooling water leak (cause of leak unknown)
5/12/66	Moderate	Black liquor system	Firing weak black liquor
8/19/66	Moderate	Black liquor system	Firing weak black liquor
10/6/66	Moderate	Water hose or piping	Cooling char bed with primitive "stream-water" spray at supposedly safe interval after shutdown
10/25/66	Moderate	Floor tube	Use of air lances
4/27/67	Moderate	Black liquor system	Firing weak black liquor

(continued)

TABLE XII (Continued)

Date	Amount of damage	Water source	Cause of explosion
8/12/67	Moderate	Black liquor system	Firing weak black liquor
9/14/68	Negligible	Wall tube	Unknown
1/25/69	Major	Cross-connection to plant water system	Dilution of black liquor to guns through cross-connection to water lines to facilitate washing dual black liquor headers
5/4/69	Major	Screen tube	Unknown
7/8/69	Slight	Steam condensate	Black liquor to guns became diluted by condensate through an auxiliary line in the liquor system
7/30/69	None	Floor tube	Smelt leak; 2 tubes blistered, smelt eroded floor tubes
10/30/69	Moderate	Superheater tube	Superheater tube parted from vibration fatigue, causing carryover of boiler water from steam drum and into furnace through superheater leak
5/1/70	Severe	Screen tubes	Overheating following partial plugging of tubes from inadequate feedwater treatment
6/14/70	Major	Plant water system	Foam produced in ACE cascade evaporator during water-washing carried out into furnace through primary air system
2/21/71	None	Floor tube	Smelt leak through floor eroded or corroded floor tubes
5/2/71	Major	Wall tube	Overheating from unknown causes
6/21/71	Major	Screen tube	Overheating caused by incomplete removal of debris following acid wash of boiler
7/4/71	None	Wall tube	Welded attachments to wall tubes pulled out
7/25/71	Slight	Screen tube	Overheating caused by incomplete removal of debris following acid wash of boiler
10/11/71	Major	Plant water system	Cross-connection between soot-blowers and plant water lines admitted water through soot-blowers
11/16/71	None	Wall tube	Overheating resulting from partial blockage of wall tube from unknown causes
11/23/71	Unknown	Black liquor system	Firing weak liquor on start-up

TABLE XII (Continued)

Date	Amount of damage	Water source	Cause of explosion
12/5/71	Severe	Water hose	In attempting to clear plugged dust hopper by water washing, hopper filled with water and overflowed into furnace
1/13/72	Minor	Wall tube	Faulty repair work
8/14/72	Minor	Hose	Falling debris washed down by fire hose after furnace had been down 24 hr exposed molten smelt which exploded with wash-up water
3/2/73	Severe	Black liquor system	Firing weak liquor
4/13/73	Slight	Wall tube	Rod driven through wall tube
4/25/73	Minor	Screen tube	Internal corrosion caused wall tube to pull out of lower screen header
7/8/73	None	Hose	Using water lance to clear plugged smelt spout
7/11/73	Very major	Plant water system	Water being used to water-wash cascade evaporator and black liquor header around furnace entered furnace because (1) liquor guns were left in firing position when not firing liquor and (2) one liquor gun valve was inadvertently left open
12/2/73	None	Smelt spout	Smelt spout leak sprayed fine stream of water into furnace
12/16/73	Minor (5 days)	Wall tube	Three $\frac{1}{4}$ -inch holes 6 ft above floor, corrosion
1/7/74	Moderate	Wall tube	External corrosion of wall tube on casing side. After initial failure, tube broke in two, allowing steam and water to enter furnace
7/21/74	None	Floor tube	Overheating failure due to faulty construction weld downstream of failure, $\frac{1}{4}$ -inch deep metal projection into tube
1/16/75	Moderate	Spout	Hole developed in smelt spout and allowed water to enter into the furnace
5/6/75	None	External	Water entered furnace through liquor system from two possible sources: (a) liquor meter wash water; (b) liquor feed pump seal water
12/30/75	Heavy (6 months)	Smelt spout	Leaking smelt spout due to improper cooling system

TABLE XII (Continued)

Date	Amount of damage	Water source	Cause of explosion
1/11/76	Moderate	—	Assumed to be weak liquor.
3/19/76	None	Auxiliary fuel tank	Water entered furnace through oil guns
3/22/76	None	Auxiliary fuel tank	Water entered furnace through oil guns
5/18/76	Slight	Screen tube	Plugged screen tube ruptured after acid cleaning
6/14/76	Heavy (90 days)	Superheater tube	Carryover from sheared S/H tube
7/2/76	Heavy (11 weeks)	Black liquor	Firing weak liquor: liquor diluted from pump sealing water
8/17/76	Slight	Ruptured downcomer tube	Water impingement from soot-blower
8/26/76	Heavy (41 days)	Floor tube	Detachment of welded bracket between floor and wall tube
12/8/76	Heavy (4 months)	Ruptured side wall tube	Short term overheating resulting in ductile failure
8/18/77	Moderate (14 days)	Screen tube	Screen tube separation caused by falling salt cake
8/19/77	Heavy (6 months)	Washwater from I.D. fan flowed to cascade	The unit has 2 I.D. fans in parallel. One down for repair was washed, allowing water to enter cascade which diluted liquor
8/30/77	Moderate (10 days)	Erratic liquor flow	No pressure part failure. Explosion believed due to erratic liquor flow and temperature condition
11/18/77	Slight (5 days)	Washwater ring header	Boiler shut down to repair economizer leak. Wash water accidentally admitted to furnace ring header through a liquor gun into residual smelt
1/17/78	Slight	Front wall tube	Welded windbox attachment pulled loose from a vertical front wall tube. Water entered windbox and was carried to smelt bed
10/14/78	Moderate (3 weeks)	Pinhole leak floor tube	Faulty weld on membrane bar between floor tubes, made 10–15 yr earlier
3/12/79	Major	Floor tube	Defective tube
5/16/79	—	Wall tube	Overheat
7/23/79	—	Wall tube	Overheat-blockage

^a From Grace and Taylor (1979).

In a somewhat different type of furnace that suffered from a *combustion-gas* explosion, the floor beams, which were similar in size, were deflected at most 2–3 cm. A structural analysis of this explosion led to the conclusion that peak pressures were in the order of 30–40 kN/m² (5–6 psi). Comparing the two damage descriptions, it is obvious that the smelt–water explosion generated pressures well in excess of 40 kN/m² on the floor.

G. ARGONNE MOLTEN SALT STUDIES

Anderson and his co-workers at the Argonne National Laboratory (Anderson and Armstrong, 1972, 1973; Anderson *et al.*, 1975; Anderson and Bova, 1975) described experiments in which water was mixed with molten sodium chloride.

In the small-scale tests, water was jetted into the salt both from above and below the interface. Explosions were erratic with many tests simply producing water vapor which ejected the salt. In some tests, high-speed photography was employed and, at the highest framing speeds (13,000 fps), the explosion, if it occurred, took place within the time of a single frame, i.e., <77 μ sec. No definitive conclusions were drawn except that, if an explosion did occur, it was very short in duration and rather destructive.

A few larger-scale tests were planned wherein a larger mass of water would be driven into a mass of molten NaCl. All tests were negative and photography showed that a few “leading” drops of water would always contact the salt, explosively boil, and drive the descending water column back so as to prevent it from contacting the salt!

H. THEORIES AND MECHANISMS

Whereas the wealth of small-scale test data indicated, generally, which smelt compositions might be expected to undergo an explosion if contacted with water, no reasonable mechanism had been developed to explain the phenomenon. It was agreed that the explosive event was of a physical nature with a large quantity of steam being generated in a short period of time. Chemical reactions between the smelt and water were expected to occur, but their contribution to the event was shown to be minimal. Nelson (1973) first proposed that the process might involve the superheating of water in thin films near the smelt–water interface. His concept was based to some degree on similar “vapor explosions” re-

ported when LNG “vapor exploded” in contact with water (see Section III).

For the smelt–water case, Nelson suggested the water in contact with the very hot smelt was, initially, separated by a thin vapor film. Either because the smelt cooled—or because of some outside disturbance—there was a collapse of the vapor film to allow direct liquid–liquid contact. The water was then heated to the superheat-limit temperature and underwent homogeneous nucleation with an “explosive” formation of vapor. The localized shocks either led to other superheat-limit explosions elsewhere in the smelt–water mass or caused intense local mixing of the smelt and water to allow steam formation by normal heat transfer modes.

While the mechanism proposed by Nelson explained many of the characteristics of a smelt–water explosion, it had one very serious drawback, i.e., the smelt temperature was significantly higher than the expected superheat-limit temperature of water (1100–1200 K compared to 577 K). For LNG–water, it was shown earlier in Section III that if the water temperature were much higher than the superheat-limit temperature of the LNG, explosions were then rarely noted. For such cases, the film-boiling mode was too stable and collapse of this vapor film was unlikely.

Another limitation to the simple superheat model was that it could not explain why smelts of varying compositions behaved so differently, i.e., some were nonexplosive while others were very explosive.

Shick (1980) proposed a modified superheat theory to retain many of the elements of the original Nelson concept, but he introduced the idea that salt and water concentrations vary across the interface. In other words, he suggested that, in addition to the very large temperature gradient across the smelt–water interface, there is a mass flux of salt into the water and a water flux into the smelt. As a consequence of this mass transfer, the hot water film then contains dissolved salts and may be heated to a much higher temperature before homogeneous nucleation can occur. Thus, film boiling would be delayed and a relatively thick saltwater layer would have formed before any explosive vaporization occurred. He also noted that the water flux into the smelt might lead to smelts with significantly lower melting points so that crystallization would be delayed.

To buttress his arguments, Shick recalled the fact that all experimental data show that molten sodium carbonate is nonexplosive in contact with water. He notes “nor do its (Na_2CO_3) concentrated solutions have a significantly higher boiling point than water.” Another way to express this reasoning is to consider the data of Waldeck *et al.* (1932). They measured the solubility of Na_2CO_3 in high-temperature water. Some of their data are shown in Table XIII. For this material, the solubility decreases with temperature and becomes zero below the critical point of

TABLE XIII
SOLUBILITY OF Na_2CO_3 IN WATER^{a,b}

<i>T</i> (K)	Weight percent Na_2CO_3	<i>T</i> (K)	Weight percent Na_2CO_3
323	32.0	548	13.2
373	30.9	573	8.4
418	28.1	594	4.8
453	25.0	621	0.0
498	20.7		

^a From Waldeck *et al.* (1932).

^b The transition from monohydrate to anhydrous occurs at 385 K at 1.29 bar.

water (647 K). Waldeck *et al.* also measured the vapor pressure of saturated Na_2CO_3 solutions and showed that the vapor pressure lowering was very small even in regions where the concentrations of Na_2CO_3 were large.

Based on data of this nature, Shick concluded that little, if any, Na_2CO_3 would move to the high-temperature water phase and, even if this were to occur, the volatility (and superheat-limit temperature) of water would be unaffected.

Contrast the situation of Na_2CO_3 with that of pure NaCl which, when molten, is known to explode violently with water. The NaCl– H_2O phase diagram has been developed by Keevil (1942), Morey and Chen (1956), and Ölander and Liander (1950), and reviewed by Morey (1957).

The pressure–temperature–composition diagram presented by Morey is shown in Fig. 8. The vapor pressure of pure water (on the P – T projection) terminates at the critical point (647 K, 220 bar). The continuous curve represents saturated solutions of NaCl in water, i.e., there is a three-phase equilibrium of gas–solution–solid NaCl. The gas-phase pressure maximizes over 400 bar at around 950 K. Ölander and Liander's data for a 25 wt. % NaCl solution are shown, and T – X and P – X projections given. At the pressure maximum, the solution phase contains almost 80% NaCl.

Thus, these data clearly show that NaCl and water are miscible over a wide temperature–composition range.

Returning to Shick's argument, developed further by Shick and Grace (1982), if the water film accumulates salt, the pressure is depressed but, even more important, they suggest that the 1-bar superheat limit temperature may be significantly increased over the value for pure water (~ 577 K). The rationale for this assertion stems from considering the P – V iso-

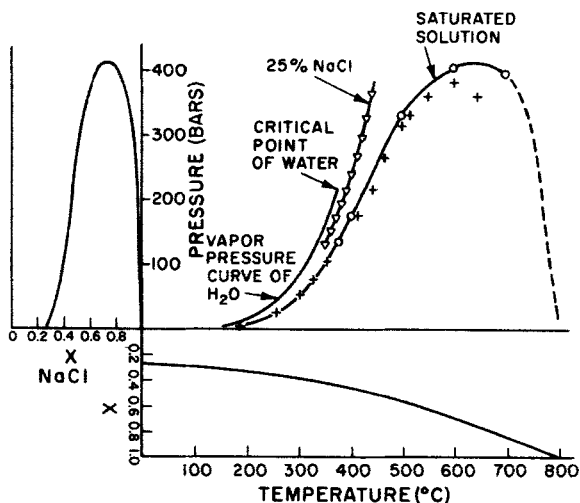


FIG. 8. The system H₂O-NaCl: (+) Keevil (1942), (O) Morey (1957), (∇) Ölander and Liander (1950). [From Morey (1957).]

therms for water and NaCl solutions (Yayanos, 1970). Without going into detail, the argument proceeds along the following line. Yayanos presented an equation to correlate specific volumes of liquid water—or NaCl solutions—with pressure. Using the approximate criterion that $(\partial P/\partial V)_T = 0$ at the superheat limit, then they show that NaCl solutions have a higher tensile strength than pure water. That is, using their equations, one calculates the tensile strength of pure water to be ~ 2300 bar at 298 K and to increase with NaCl concentration. Extrapolating this result to the compressive region, Shick and Grace estimate the 1-bar superheat-limit temperature of NaCl solutions can be several hundred degrees higher than pure water.

Assuming the argument is valid, it would then be possible to contact fused NaCl (or, presumably NaOH, Na₂S, or smelts with these constituents) with water and to state that the resulting explosion stemmed from a homogeneous nucleation of a *solution* of salt in water. Their hypothesis therefore explains qualitatively the effect of variations in smelt composition on explosivity. It also clarifies the result that green liquor normally explodes more violently than pure water since, in the former, there are dissolved salts (of the NaCl type) to enhance the salt effect at the interface.

The theory of Shick and Grace deserves careful attention. One practical result has been a renewed interest in developing smelt desensitizers which react with molten Na₂CO₃ to liberate CO₂ since it is well known that the

presence of gases (dissolved or free) greatly reduces the probability or severity of a superheat-limit explosion.⁵

Finally, it has often been stated that the maximum pressure which could exist at the source of a superheat explosion is that equivalent to the vapor pressure of the cold liquid at its superheat-limit temperature. For most organic liquids this value would be ~ 30 bar. For pure water, it rises to ~ 90 bar. For concentrated salt solutions, much higher values are possible.

V. Molten Aluminum-Water Explosions

A. SUMMARY

Inadvertent contact of molten aluminum and water may lead to an event termed a thermal explosion.⁶ These incidents may produce little vapor, but they are accompanied by sharp, local shocks which are potentially damaging to personnel and equipment. Although not a major problem to aluminum producers, they do occur in casting plants, and it is important that preventative measures be enforced. The same general comments apply to other metal processing industries such as steel and copper.

The lead in studying both the cause and prevention of molten metal-water thermal explosions has been taken by Alcoa. The Aluminum Association also sponsored several research programs both at Alcoa and at Battelle-Columbus. The Argonne National Laboratory has carried out experiments with molten aluminum and water.

The test programs which are summarized in detail in this section were usually *not* planned to test a causative mechanism. Rather, they were carried out to determine the effect of variables which were thought to be important in initiating the event. The results were normally reported only as explosions achieved or, conversely, not achieved.

In most tests, molten aluminum was poured into a vessel containing water. In a few instances, however, water was injected onto or below a pool of aluminum. The first type of experiment would model one of the more familiar types of industrial accidents, i.e., one in which an ingot break or a furnace leak allowed molten aluminum to contact a source of

⁵ A patent (Nelson, 1978) also advocates the use of a high-surface-area powder coated with an antiwetting agent to promote nucleation of the water.

⁶ A thermal explosion is the metal industry's term for "explosive boiling" or "rapid-phase transition."

water. Neither test scheme appropriately models the more common type of industrial accident, i.e., one in which damp—or even wet—solid metal is fed to a furnace holding molten aluminum (see Table XIV).

The aluminum spill tests in water led to effective plant preventative schemes wherein organic coatings were placed on all solid surfaces which, in the event of an accident, might be in contact with molten metal and water. Use of such coatings has greatly diminished the frequency of thermal explosions.

Experiments also indicated that under circumstances where a significant quantity of *molten* aluminum could *not* contact a *wetted surface*, explosions were rare. Thus, small spills, or spills which required the metal to fragment or pass through considerable distances in air or water before contacting a wet, solid surface, seldom led to explosions. On the other hand, if molten aluminum were to contact wet, rusty steel (or steel with inorganic salts on it), explosions were more likely.

Most small-scale aluminum spills produced negative results. To promote explosions, several investigators attempted to “trigger” the explosion by the use of detonators or other such devices in the vicinity of the aluminum–water mixture. Success was usually achieved if the trigger shock wave were sufficiently strong. Explosions were obtained in these cases even though the vessel walls and bottom were covered with an organic coating.

Several studies attempted to determine whether chemical reactions were occurring at the aluminum–water interface. The finding that there was some light emission and local high temperatures led to the conclusion that reactions do occur, and they may be of more importance in the more violent explosions.

Few models have been advanced to explain the mechanism of the thermal explosion, and of these, only one seems to fit most of the available experimental data.

In this article, we suggest that a modified superheated-liquid model could explain many facts, but the basic premise of the model has never been established in clearly delineated experiments. The simple superheated-liquid model, developed for LNG and water explosions (see Section III), assumes the cold liquid is prevented from boiling on the hot liquid surface and may heat to its limit-of-superheat temperature. At this temperature, homogeneous nucleation results with significant local vaporization in a few microseconds. Such a mechanism has been rejected for molten metal–water interactions since the temperatures of most molten metals studied are above the critical point of water. In such cases, it would be expected that a steam film would encapsulate the water to

isolate it from the hot metal. Superheating of the liquid water could not then occur.

A modified superheat theory was proposed by Shick to explain molten salt (smelt)–water thermal explosions in the paper industry (see Section IV). (Smelt temperatures are also above the critical point of water.) In Shick's concept, at the interface, salt diffuses into water and water into the salt to form a continuous concentration gradient between the salt and water phases. In addition, it was hypothesized that the salt solution on the water side had a significantly higher superheat-limit temperature and pressure than pure water. Thicker, hotter saltwater films could then be formed before the layer underwent homogeneous nucleation to form vapor.

This model may possibly be adapted to metal–water thermal explosions if one assumes that there are reactions between the molten metal and water (and substrate) that form a soluble salt bridge across the interface between the two liquids. This salt solution would then be the material which could superheat and, when finally nucleated, would initiate the thermal explosion. As noted, the model rests on the premise that there are chemical reactions which occur very quickly between metal and water to form soluble products. There is experimental evidence of some reactions taking place, but the exact nature of these is not known. Perhaps, in the case of aluminum, the hydroxide or hydrated oxides form. With substrates covered by rust or an inorganic salt [e.g., $\text{Ca}(\text{OH})_2$], these too could play an important role in forming a salt solution.

To prove or disprove such a modified superheated-liquid model, experiments are necessary to delineate the rates and products of reaction between molten metals and water in a high-temperature environment with and without substrates which could participate in the reaction.

B. BACKGROUND

It is common knowledge in industries handling molten metal that contact of the metal with water may lead to severe explosions, although, fortunately, in most cases, only mild steam evolution is observed. Most incidents to date have been reported in aluminum or steel plants, but copper and nickel smelters as well as other less common metals have been involved in isolated cases. One of the earliest recorded explosions in the aluminum industry resulted when, in 1949, a company was experimenting with the casting of a new high-strength alloy (S. G. Epstein, personal communication, 1979). Expecting possible "bleed-outs" of molten aluminum from breaks in the skin of the incompletely solidified ingot, a steel

collector pan holding about 0.14 m³ (36 gallons) of water was placed in the casting pit. A heavy bleed-out did occur and a violent explosion resulted.

This accident led to a concerted effort by the aluminum industry to study the phenomenon and to find preventative measures. Basic studies have been funded by the Aluminum Association for research at Battelle Memorial Institute, ITT Research Institute, and the Alcoa Research Laboratories.

Besides the aluminum industry, the nuclear power industry has been interested in molten aluminum–water explosions due to the presence of aluminum metal in some boiling water reactors. Certain accident scenarios lead to a meltdown of the reactor core with concomitant contact of molten aluminum and water.

C. ALCOA EXPERIMENTAL PROGRAM

Results from extensive test programs on molten aluminum–water explosions have been reported by Long (1957), by Hess and Brondyke (1969), and by Hess *et al.* (1980). In almost all experiments, molten aluminum, usually 23 kg, was dropped into water from a crucible with a bottom tap (see Fig. 9). In only a few tests was there instrumentation to indicate temperatures, pressures, delay times, etc. The test results were normally reported as *nonexplosive* or *explosive*—and if the latter, qualitative comments were provided on the severity of the event. A large number of parameters were varied, and several preventative schemes were tested. Over 1500 experiments were conducted. Some of the key results are summarized below.⁷

1. Variation in the Molten Aluminum

All other conditions being held constant, there appeared to be a minimum required mass of aluminum to cause an explosion, but an excess over this critical quantity did not lead to more damaging events. The critical mass was in the range of 4–5 kg for normal tests.

Higher aluminum temperatures usually increased the probability of an explosion. This was especially true if the depth of water in the water tank were also increased.

Certain aluminum alloys, notably 2011,⁸ were more prone to lead to explosions and these were often quite violent. This alloy forms stable oxides more rapidly than most other types. Also, alloys of aluminum with

⁷ To some degree, the test summary has been abstracted from findings compiled by Dr. Walter E. Wahnsiedler of Alcoa.

⁸ Nominal composition: 5.5% Cu, 0.4% Pb, 0.4% Bi, 93.7% Al.

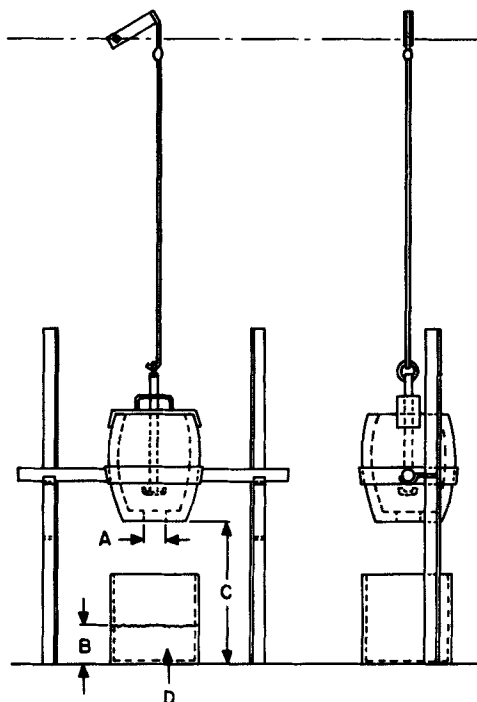


FIG. 9. Alcoa test site details: A, tap diameter; B, water depth; C, drop height; D, water vessel.

5% lithium have been shown to be very sensitive and readily produce explosions when poured into water. Explosion frequencies for commercially pure aluminum with or without beryllium, silicon, or sodium, were not statistically different.

2. Pour Variations

The tapping hole had to be large to lead to an explosion. Few resulted when the diameter was less than about 6.4 cm. Diameters up to 10 cm were studied.

For most tests, if the drop height were too high (≥ 3 m), no explosions resulted. Also, inhibition was obtained when a steel grid (spacing ~ 2.5 cm) was placed between the crucible and water surface.

3. Water Variations

No explosions resulted if the water depth were less than about 5 cm. Splatter and steam formation were observed instead.

No explosions resulted if the water depth exceeded about 70 cm (but this depth could vary with the size of spill studied). For intermediate depths, the probability of an explosion was related both to the depth and to the initial aluminum temperature. For deeper pools, a higher temperature was necessary.

The explosion incidence decreased as the water temperature was raised, particularly over 330 K.

Generally, soluble oils prevented explosions except in very cold water. Some wetting agents increased the probability while others decreased the probability of an explosion.

Water with dissolved salt was more likely to lead to explosions, and the water temperature was less significant. (Related tests with molten KCl-NaCl mixtures poured into water led to explosions even for deep water pools or when soluble oils were present.)

4. *Water Vessel*

Unless some external shock source was employed, it was found that molten aluminum had to reach the vessel bottom before an explosion could occur. In these cases, organic coatings and paints (except silicones) prevented explosions. Many coatings were studied (see, in particular, Hess *et al.*, 1980) and, when evaluated on many tests of applicability, durability, and nonexplosive characteristics, it was recommended that epoxy, coal-tar epoxy, and bituminous paints be used. Silicone, graphite, and inorganic coatings, in general, did not prevent explosions.

The size of the square water vessel was varied from 16.5 cm to 61 cm on a side with little variation in the probability of an explosion. A few tests carried out in vessels 122 cm on a side led to explosions which appeared to be milder. (The effect of water depth was noted earlier.)

With no externally imposed shocks, no explosions were ever found (even with 1100-K aluminum) for vessels whose *bottoms* were aluminum, glass, glass-coated, oxide-coated glass, or rough glass. For the aluminum bottoms, the roughness was varied up to 0.12 μm .

It was more difficult to achieve an explosion in a clean stainless steel vessel compared to carbon steel.

Rough surfaces or those covered with inorganic coatings (aluminum hydroxide, gypsum, silicones, etc.) or rust were much more prone to explode. $\text{Ca}(\text{OH})_2$ coatings produced particularly violent events. Even lime coated *over* an *organic* paint led to an explosion.

Concrete vessels were somewhat less prone to explosions; sand blasting the surface reduced the incidence.

Preheated steel vessels, particularly if rough, were prone to have explo-

sions. This may have been due to the formation of rust during the heating step.

Vessels with walls uncoated with an organic protective layer, but with *bottoms* coated, did not undergo an explosion.

Bare spots in the organic coating on the vessel bottom allowed explosions to occur. Spots were as small as 5×5 cm.

5. *Initiating Event*

In most tests, no external trigger was used. Explosions did or did not occur depending on the variables discussed above. In some tests, however, external shocks were used in an attempt to turn normal "nonexplosive" tests into "explosive" ones.

Explosions were obtained in glass vessels when small explosive charges were detonated on the vessel wall. 1.6 g (or more) of Primacord or 5 g of Detacord were tried. Similar shocks led to violent explosions even for systems which had organic coatings on the bottom.

Strong "hammer" blows on the outside of the vessel wall often initiated explosions even in cases where organic coatings covered the bottom. There was a threshold energy for an explosion to result; for the Alcoa test scale, it was about $19 \text{ m} \cdot \text{kg}$ ($137 \text{ ft} \cdot \text{lb}$) although only about one-half of this energy probably reached the water. Such an impact would lead to overpressures less than 0.5 bar.

6. *Other Comments*

If an explosion resulted, the peak pressure usually occurred within 1 msec after initiation.

Spills of molten magnesium yielded results similar to those of aluminum, but fires often followed the event.

In most instances, no light was visible. In a few of the more violent tests, there were flashes of light and these were assumed to result from chemical reactions.

Temperatures measured in the vessel bottom during an explosion sometimes exceeded the inlet molten metal temperature. Such findings were most common for the more violent explosions.

The importance of "prefragmentation" to the probability or violence of an explosion is not clear. Hess and Brondyke (1969) describe one incident where motion pictures were taken for a transparent plastic water vessel that had a steel bottom:

a layer of molten aluminum covered the bottom of the container to a depth of about 3 in. before the blast. The layer was fairly uniform. A careful look at the film indicated

the top surface of the metal had crusted, except where the incoming stream of molten metal entered the pool. [p. 96]

Briggs (1976), in studies at Winfrith in the United Kingdom, also describes the interaction in similar terms:

The metal stream enters the water and is surrounded by a thick vapour film. The metal reaches the base of the vessel, spreads radially across the base and then up the walls of the vessel. Interaction is triggered a few hundred milliseconds after the initial entry of metal into the vessel. Typically, the metal/water zone will have spread about 100 mm up the wall at the time of the interaction. The first visual indication of interaction is the disappearance of detail in a small zone near the base of the vessel. [p. 80]

It is clear that the Alcoa research teams have provided a valuable data base to examine the mechanism of aluminum–water explosions. However, before considering proposed theories, the research studies at Argonne National Laboratory and elsewhere are summarized.

D. HIGGINS STUDY

In 1955, Aerojet-General Corporation issued a report (Higgins, 1955) that described a few experiments in which molten aluminum (and other metals) were poured into water. The water vessel was a vertical 30-cm-diameter, 25-cm-long pipe with a steel bottom plate. The water depth was 23 cm. Metal was dropped from an overhead crucible, usually with a free fall of 51 cm before contacting the water. A barium titanate crystal pressure transducer was located in the side of the water vessel about 13 cm below the water surface.

For the pure aluminum tests (99.0% minimum purity), two tests were run in initial experiments using a glass-sided water tank. Each spill was only 0.15 kg. Motion pictures indicated that most of the aluminum entered as an irregular “blob.” Steam bubbles formed about the metal and collapsed. No explosions were obtained. In other tests, with the steel-pipe water vessel, No. 6 blasting caps were detonated after the aluminum entered the water. (The caps were located in the center of the pipe at the same level as the pressure transducer.) The cap detonation fragmented the metal, but no explosions were obtained.

Higgins quotes unpublished work at both Aerojet and DuPont that aluminum–water explosions were difficult to obtain, but alloys of aluminum with small amounts of lithium, sodium, or uranium were quite reactive.

Tests made by Higgins using 95% Al–5% Li were made both with and without blasting caps. Drops varied from 0.025 to 0.15 kg. Without blasting caps, there was only popping with an occasional flame. With blasting

caps, the event was violent and "extensive chemical reaction [was] reported."

It is difficult to draw many conclusions from this study. Drop masses were far below those considered minimal in the Alcoa tests; also the drop height was large and the water deep. Judging from the Alcoa studies, one would not have expected any thermal explosions to result with pure aluminum. The presence of lithium apparently could change even small systems from a nonexplosive to a potentially explosive one if a sufficiently energetic external shock were also imposed.

It might also be noted that under similar conditions, molten nickel or stainless steel spills into water were also nonreactive. Pure zirconium or Zircaloy-2 (1.5% Sn, 0.1% Fe, 0.1% Cr, 0.05% Ni, 98.25% Zr) were, however, explosive when 1-kg pours were made and blasting caps were used to initiate the event.

E. WRIGHT AND HUMBERSTONE IMPACT STUDIES

Wright and Humberstone (1966) presented a brief description of water impact studies on molten aluminum. The experiments were carried out *in vacuo* with moving water columns striking a molten aluminum surface with an impact pressure of 1.4 MPa (200 psi). The aluminum pool was about 7 mm deep. The result was a violent disruption with the generation of high pressures, the highest recorded being 20 MPa (2900 psi) when the initial aluminum was at 1220 K.

For the highest-temperature explosion (1220 K, 20 MPa), the pressure rise time was about 40 μ sec with a decay-time constant of 3 msec.

Chemical reactions between water and aluminum were considered but no definite conclusions were reached.

F. ANDERSON AND ARMSTRONG EXPERIMENTS

In studies conducted at the Argonne National Laboratory, Anderson and Armstrong (1981) describe various experiments where water and molten aluminum were brought into intimate contact. The object was to collapse any steam film and monitor subsequent events.

In the initial test series, water was injected at low velocity onto the surface of the aluminum or, as a variation, under the surface. Various injection pressures were used, but only splashing resulted. Next, the experiments were repeated with very high-velocity water jets (up to 400 m/sec) into a crucible containing 0.13 kg of aluminum. The impact pres-

sure was about 80 MPa. Whereas the splashing was more violent (up to 60% of the aluminum was lost), no thermal explosions were noted.

The technique was then changed to entrap a small mass of water under a molten aluminum surface and simultaneously to overpressure the system. In this manner it was hoped to collapse steam films around the water. The actual procedure employed a small glass sphere containing water. The sphere was moved beneath the aluminum surface and broken by impulsively loading the system from a falling steel cylinder which impacted on a graphite toroid immediately above the molten aluminum. About 0.7 g of water was released into 1 kg of aluminum at 1170 K and pressurized to about 8 MPa. No explosions were detected.

By modifying the procedure described above to explode a wire in the water sphere while the system was under compression, they did attain explosions. Measuring the rebound of the cylinder and the loss of aluminum, they could estimate the work produced by the event. Assuming the maximum energy transfer to the water would occur by constant volume heating to the aluminum temperature, followed by an isothermal, reversible expansion, they estimated an efficiency of about 25%. Clearly the exploding wire led to an immediate and effective dispersal of the water.

Other tests were carried out in which aluminum was poured into water while, at the same time, exploding a wire in the water. Early scoping tests were carried out in Pyrex and stainless steel vessels with 0.9 kg of water and 0.1 kg of aluminum. Quite violent explosions were obtained in both Pyrex and stainless steel when the bottom was covered with a rusty steel plate. In cases where no such plate was present, no or small explosions resulted.

Further aluminum pour tests were made in a heavy-wall stainless steel tank fitted with Lucite side windows. The tank was supported on a force transducer and pressure transducers were located on either end. In a test, after the spill, there was a predetermined delay and then the wire was exploded. The aluminum usually had puddled on the tank bottom before the wire explosion and steam bubbles could be seen. The shock from the wire explosion usually collapsed the film and, following this, the aluminum expanded. If the shock were sufficiently energetic, the aluminum soon fragmented and expelled the water from the tank in a thermal explosion. In such cases, the force transducers on the bottom ranged from 5 to 10 N · sec. (The exploding wire alone led to impulses around 1 N · sec.) Efficiencies of an explosion calculated as indicated above were low.

In a final set of experiments in which aluminum was dropped into water, care was taken to determine if any light were emitted—i.e., if so, this would be indicative of a chemical reaction. As before, exploding

wires were used to supply the trigger shock. In a total of 25 tests, light was seen in three and an analysis of the color spectrum indicated temperatures of 2600–3000 K. The source was diffuse and not strong. It was conjectured that the reaction



might have occurred. (Note no net volume change is involved.) As the energy release from experiments in which light was seen was no different from those with no light, it was concluded that chemical reactions, if they did result, were not a major contributor to the explosion event.

G. BATTELLE STUDY

Lemmon (1980) summarized a study carried out at Battelle-Columbus in which molten aluminum was dropped into water in a manner very similar to that used in the Alcoa program. The aluminum crucible had an 8-cm-diameter tap hole, and the water vessel was square, 30 cm on a side, and 25 cm deep. It was constructed of mild steel with one or more Plexiglas sides to allow observation. 5- to 20-kg drops of aluminum (1000–1330 K) were made. The height between the tap hole and vessel bottom varied from 48 to 53 cm. The water depth was 15 cm, and the water temperature ranged from 286 to 297 K. Fifty-four tests were run and, in many, high-speed photography was used to record any events.

In the first set of experiments, the water vessels had rusted bottoms. Of the 21 tests, 14 produced explosions, but no correlation of explosion probability could be deduced. It was reported that, in all tests, molten aluminum reached the bottom of the vessel. High-speed movies showed that the entire explosion sequence “between the first visible disturbance in the system to a full-scale chemical reaction was very rapid (on the order of 600 μsec).” Note that the word “chemical” was used in the quote. Lemmon suggests that chemical reactions play a key role in the explosion phenomenon, particularly for violent incidents. The proof that chemical reactions are important stems from the finding that strong explosions produced light and, also, limited spectrographic data indicated local temperatures in excess of 3000 K. The emphasis on chemical reactions was not stressed in the work of other investigators.

The second series of experiments used vessels with bottoms made of Pyrex glass (coated or uncoated) or aluminum. No explosions were produced with any combination even when coatings of Fe_2O_3 , Fe_3O_4 , and $\text{Ca}(\text{OH})_2$ were applied to the glass vessels. (In one test there may have

been a mild interaction with iron oxide scale on the bottom of a glass pan.)

The final set of experiments employed external sources to provide a shock wave in the water during or immediately following a spill of molten aluminum. Usually the shock was caused by the detonation of a small charge of explosive in the water.

It was found that the stronger the shock (i.e., an increased amount of explosive), the more violent the subsequent explosion. Below a certain level, no explosion occurred.

In some tests, the shock was transmitted to the system through an aluminum rod with an external detonation. This technique often led to severe explosions.

In all shock-initiated tests, the probability of a violent incident increased with an increase in the temperature of the aluminum. In many instances, explosions could be obtained even in *glass*-bottomed vessels or vessels with an *organic coating*. The aluminum on the bottom would explode violently with completion in about 600 μ sec. (There may, however, have been a 1- to 2-msec delay after the detonation of the explosive charge before the large explosion.)

Since the Battelle study places a strong focus on the importance of chemical reactions, some discussion of their spectrographic results would seem warranted. Spectra were obtained for explosions occurring in glass-bottomed vessels:

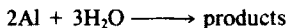
(1) Doublets at 3944 and 3961 Å were attributed to excited Al.

(2) An intense emission line at 5900 Å was believed to be the unresolved sodium doublet (5890 and 5896 Å). The appearance of sodium emission spectra is probably related to the presence of this element in the glass bottom.

(3) Four bands (4471 to 5079 Å) were interpreted as AlO.

(4) All lines (bands) were superimposed on a continuum due to incandescent Al_2O_3 and Al.

Lemmon indicated that the adiabatic temperature expected for the reaction



was about 3500 K. (Most Al goes to Al_2O_3 but about 1.7% AlO was calculated to be formed.) No excited hydrogen was found in the spectra or in other experiments when Al was burned in a hydrogen-oxygen flame.

Based to some degree on the finding of the AlO lines and on the fact that light was seen, they concluded that reaction of aluminum and water does occur.

H. INDUSTRIAL ACCIDENTS

The aluminum industry has maintained careful records of most molten metal–water accidents. Many of these are summarized in Table XIV to indicate the general types of events. Also noted is the approximate damage due to each incident.

Many explosions appear to have resulted from the accidental introduction of wet feed to a furnace holding molten aluminum. The damage from such explosions varied widely. In some cases, there was only minor splash. In others, there was extensive damage to the furnace. There did not seem to be any correlation between the amount of water introduced and the resulting damage—but in essentially all cases the water quantity was believed to be small.

In other incidents, molten aluminum was accidentally spilled and contacted water or wet substrates. The reported damage varied from very minor to quite extensive. In all cases, the initial event was a sharp, local shock. The actual conditions (and quantities of metal and water involved) then seemed to dictate whether the overall incident was severe or mild.

In no case were there sufficient data to estimate reliable overpressures and impulses from the explosion. From the description of some events, it would appear that they might have been large. However, injury reports, even from many of the more severe accidents, do not substantiate this concept because workers in the area were either not injured or, if injured, were usually burned or hit by shrapnel.

In Table XV, some data are given for molten metal–water explosions *not* involving aluminum. In most of these cases, the quantity of metal was large. Because only the more serious explosions are reported, these tend to illustrate the most damaging type of event. Again, it is interesting to note that usually only small quantities of water were involved.

Illustrative of one of these events, we quote below the summary of the first accident in Table XV as given in a report by Health and Safety Executive (1975, p. 31):

At about 1.25 am on the fourth of November 1975 the foreman at the Queen Victoria Blast Furnace, Appleby-Frodingham Works started a cast that was intended to fill two torpedo ladles. Conditions at the time were normal; the shift manager was in attendance.

Shortly before 2.00 some 175 tonnes of metal had been run into the first torpedo and the iron stream diverted to the second ladle. Some 10 to 15 minutes later the blow pipe at the No. 3 tuyere position started to burn down on the side facing on to No. 2 tuyere hearth cooler. The burning developed rapidly with intense flame and sparks despite efforts by the furnace keeper to cool the pipe by spraying it with water.

Whilst the pipe was burning down, a substantial water leak from the furnace or fittings was observed. The source of the leak could not be identified because the face of the

TABLE XIV
BRIEF DESCRIPTIONS OF SOME ACCIDENTS IN THE ALUMINUM INDUSTRY

Description and probable cause	Damage
<i>Accidents While Loading Furnaces</i>	
Charge of aluminum metal being added to melting furnace when explosion occurred. Cause believed to be due to water which had accidentally entered charge bucket	Minor. Spray of molten aluminum started small fire
While charging solid aluminum "sows" to a melting furnace containing molten aluminum, an explosion occurred. Analysis of other "sows" from this batch indicated a few had cavities which were filled with water	Extensive. Much of furnace dome destroyed
Scrap was being charged into a large aluminum melting furnace (~22,000 kg). During one addition, an explosion resulted. Later examination indicated the scrap had not been adequately preheated or dried and may have been moist	Roof damaged but did not fail
As above. During charging of scrap aluminum into a remelt furnace, an explosion resulted. A careful analysis of the accident revealed that there may have been some sludge-covered wet pit scrap charged	Impressive. Noise heard 5 km away. Furnace roof blown off and walls damaged. But workers in the area only received minor injuries
As above. An explosion resulted when charging aluminum scrap into a large melting furnace containing 14,000 kg of metal. The explosion was immediate after the scrap addition. An extensive investigation failed to find any definite cause, but judging from similar accidents, it was concluded that moisture had been present in the scrap	Extensive. The furnace door was blown off, the roof was destroyed, and the back wall buckled. Some 2000 kg of aluminum spilled on the concrete floor with significant spalling. Personnel injuries resulted primarily from aluminum splash, not shock waves
As above. "Sows" were being charged to an aluminum melting furnace. One led to an immediate explosion. (It was recovered intact during cleanup.) Investigation showed that some of the sows had moist ammonium nitrate adhering to their surface. (The sows had been shipped on a railroad car used previously to carry fertilizer.) The water and not the salt was cited as the accident cause	Impressive. Transite roof blown off and corrugated siding lost. Many windows shattered. Workers in the furnace area were burned, but they did not receive severe shocks. Some 1000 kg of molten metal lost
As above. 500-kg sows of aluminum were being added to a holding furnace when an explosion occurred. The explosion was immediate upon contact of the sow with the molten metal. It	Impressive. Loud noise, molten metal spray, unmelted aluminum bars (ca. 15 kg) thrown out onto

TABLE XIV (Continued)

Description and probable cause	Damage
<p>was determined later that the sows were contaminated with ammonium nitrate</p> <p>A crane holding a bucket of scrap aluminum and sows (10,000 kg) was loading into a holding furnace which contained some 12,000 kg of molten aluminum. Upon opening the clam shells, an immediate explosion occurred. The furnace was cooled and most sows were recovered intact. There was no evidence of foreign material in the charge. It was considered likely that one sow had a shrinkage cavity which contained some water</p>	<p>roof. No strong shock wave noted</p> <p>Moderate. One sow was ejected about 40 m; the clam shells became unhooked and fell</p>
<p>Two large blocks of aluminum, each weighing about 600 kg, were being loaded into a furnace. Later investigation ascertained that one block had a small amount of water (about "a teaspoonful"). When this block entered the molten aluminum, an explosion occurred</p>	<p>Moderate. Significant splashing within and without the furnace</p>
<p>As above. While charging aluminum pig to a remelting furnace, an explosion took place. An investigation could find no definite cause, but the pigs had been shipped in railroad cars which had ammonium nitrate fertilizer. It is also possible that water had become entrapped in some pigs</p>	<p>Moderate. A large hole was blown in the furnace roof and the molten metal splashed in the vicinity of the furnace</p>
<p>About 15 min after loading a 900-kg aluminum sow into a melting furnace, an explosion occurred. Later investigation showed the sow had a hidden internal cavity which could have held 0.015 m³ of water</p>	<p>Moderate. The unmelted sow was blown out and metal splashed around furnace</p>
<p>As above. Apparently the sow, although preheated, still contained water</p>	<p>Moderate. Some 3600 kg of aluminum blown from furnace</p>
<p>As above, except aluminum scrap was being loaded. An explosion resulted. It was suspected that there was water in the scrap</p>	<p>Mild. Some splash</p>
<p>As above. Magnesium was being added to molten aluminum. Moisture in the charge was suspected.</p>	<p>Mild. Some splash</p>
<p>300-kg aluminum ingots were being loaded into a large melting furnace. An explosion resulted. Moisture on the ingots was suspected even though they had been preheated</p>	<p>Moderate. 9000 kg of aluminum lost</p>
<p>Aluminum scrap (with moisture?) was being loaded in a melting furnace when an explosion resulted</p>	<p>Moderate. Severe splash</p>

(continued)

TABLE XIV (Continued)

Description and probable cause	Damage
A 900-kg aluminum ingot was loaded into a remelt furnace. It may have had moisture (?); an explosion occurred	Mild. Light splash
A charge of copper and chrome hardener was being added to an aluminum furnace. An explosion occurred immediately after loading. No cause was determined	Mild
Aluminum scrap was added to a remelt furnace. An immediate explosion resulted. Later examination indicated there was foreign material in the scrap. Water may have been in a bottle whose pieces were recovered	Extensive. Severe splash. Roof fell in. Wall of the building had a hole blown in it (shrapnel?)
As above. During aluminum scrap loading, two explosions resulted	Mild
During scrap loading in an aluminum remelt furnace, an explosion resulted. Moisture in scrap suspected	Extensive. Furnace destroyed, building heavily damaged
Wet scrap fed to remelt furnace. An explosion took place	Extensive. Furnace destroyed.
As above. 1700 kg of aluminum scrap (wet?) was being loaded when explosions occurred	Extensive. Furnace destroyed. Building and adjacent furnace severely damaged
<i>Ingot Bleed-Out</i>	
Aluminum ingots being cast developed cracks. Cooling water entered and contacted molten aluminum	Minor. Shrapnel caused injuries to some personnel
During casting of small ingots, one developed a leak (bleed-out) and contacted water near an unpainted (slightly rusty) steel plate. An explosion resulted	Moderate. 1000–1500 kg of aluminum were blown from the casting box and damaged the unit
An aluminum ingot which had just been cast was submerged below water. The skin covering the top apparently broke, thereby exposing molten metal. An explosion resulted	Extensive, particularly to equipment
A bleed-out occurred from aluminum molds and contacted water. An explosion resulted	Extensive. The casting unit and adjacent portions of the building were destroyed
A vessel holding about 0.14 m ³ of water was contacted with molten aluminum during a bleed-out from an ingot. An explosion took place	Extensive
<i>Loss from Furnace or Holding Vessel</i>	
Leak in a reduction pot allowed molten aluminum to flow into basement. Leak stopped, explosion occurred about ½ hr later. Water of unknown origin contacted pool?	Mild. 3 × 3 m section of concrete floor lifted

TABLE XIV (Continued)

Description and probable cause	Damage
During casting of 37-cm ingots, due to a failure of equipment, molten aluminum was allowed to flow into water (depth unknown). An explosion resulted. The equipment was coated with an approved material, but some bare areas may have been present. Also there were external shocks from equipment falling against the vessel with aluminum and water	Extensive damage both to casting unit and auxiliary equipment
Failure of a flow-metering rod in a casting operation led to the flow of aluminum into a pool of water. Two separate explosions resulted	Mild. Splash of aluminum to roof (15 m) and some minor damage to casting unit
The spout on a holding furnace broke during casting and molten aluminum fell into a pool of water. An explosion resulted	Mild. Some splashing of aluminum
An aluminum-manganese alloy was being melted in a refractory crucible. Due to an accident to the crucible, molten metal spilled into the furnace pit which contained water. An explosion resulted	Extensive. The furnace was destroyed, building siding and roofing were torn off, and a nearby furnace was damaged. Personnel in the area, however, were only slightly injured
During casting, a leak in the pouring trough allowed molten aluminum to fall on a wet floor. An explosion occurred	Mild. Splash
A bad leak occurred in a melting furnace while casting. Significant quantities of aluminum may have contacted wet surfaces both on the superstructure of the casting machinery and in the bottom of the casting pit. Several explosions took place	Very extensive. Several fatalities, many injuries. Two furnaces completely destroyed; considerable damage to casting building and to nearby structures. Primary shock damage in 60-m radius
<i>Wet Mold</i>	
Aluminum poured into mold containing material suspected to have some $MgCl_2$. An explosion occurred. It is believed that the salt was sufficiently hygroscopic to have been damp at the time of the event	Minor. Aluminum spray
Molten aluminum was poured into a mold. The mold had not been preheated and may have contained some moisture	Moderate
Molten aluminum was cast into a damp mold when an explosion took place	Moderate. Some splash
While tapping aluminum into a crucible, an explosion resulted. Analysis showed foreign debris in the crucible bottom	Mild. Some splash

(continued)

TABLE XIV (Continued)

Description and probable cause	Damage
Molten aluminum was cast into a moist mold and an explosion resulted	Mild. Some splash
An explosion took place when molten aluminum ran into a damp mold	Mild. Light splash
Explosion in damp mold during casting	Mild
As above. Crane was filling mold with molten aluminum	Mild
Aluminum was being cast when an explosion occurred. It was concluded that metal contacted a salt deposit which was damp	Mild
<i>Miscellaneous</i>	
At the start of a casting operation, an explosion occurred when a metering rod was inserted into the tap hole to control the flow. Such rods are coated to prevent molten metal from sticking; indications are that, in this case, the coating was not sufficiently dry before use	Very minor
An aluminum scrap fire developed near a melting furnace. Fire departments responded and sprayed water on the flames. Suddenly the pot furnace exploded. It is presumed that water from the fire hoses entered the furnace which contained about 900 kg of molten aluminum	Extensive. Severe damage to furnace; roof blown off; windows within 100 m were broken. Firemen injured but there were no fatalities
Ingots 0.3×1 m in cross section were being cast when one ingot stuck and water was trapped in the hanging section. Molten aluminum flowed into the cavity and an explosion resulted	Moderate. Molten aluminum was thrown to the roof and splashed some 20 m from the casting pit. The molds were damaged
In the casting of an aluminum alloy, one of the molds did not seat properly. A workman began to hammer it down when an explosion occurred. Water had apparently entered the mold by splashing up. The effect of "pounding" the mold is not known	Moderate. Significant splashing within and without the furnace
An explosion occurred when molten aluminum ran through a trough that was wet	Mild. Some shrapnel
A dipping ladle (which may have been wet) was inserted into molten aluminum. An explosion resulted	Mild
A water leak allowed a spray to contact unsolidified aluminum ingots to cause an explosion	Mild. Some splash
While cutting aluminum with a torch, a moisture pocket was encountered. An explosion occurred	Mild
Water (origin unknown) entered a remelt furnace to cause an explosion	Extensive both to furnace and building

TABLE XV
SOME TYPICAL ACCIDENTS IN THE STEEL AND COPPER INDUSTRIES

Description and probable cause	Damage
During steel casting, a fire resulted which damaged the water cooling system. A water stream joined the molten iron runner to result in an explosion	Extensive. Severe shock wave
A ladle with 27,000 kg of molten iron was being transferred by a crane when the ladle slipped and spilled the iron onto the wet floor. An explosion resulted	Extensive. Shock waves and significant splash
A railroad car with a molten iron ladle (90,000 kg) derailed and spilled the iron onto damp ground with snow and puddles. An explosion resulted	Very extensive. Noise heard in 16-km radius with heavy damage to buildings and to windows
During operation of a basic oxygen furnace, ^a while tipping the furnace, a rumbling sound was heard and soon after an explosion took place. It was believed that foreign material was introduced with scrap feed	Extensive. 200,000 kg of steel thrown out
Molten iron slag spilled onto wet sand to cause an explosion	Moderate. Roof and siding blown off building
Water entered a reverberatory furnace containing molten copper and an explosion resulted	Extensive. Furnace destroyed. Much shrapnel
A stainless steel electric melting furnace developed a water leak in the water-cooled rings. Water entered the furnace and an explosion took place	Moderate. Much of furnace damaged
Molten iron spilled on wet sand and an explosion resulted	Moderate. Building roof lifted 15 cm
A ladle carrying molten steel slipped and allowed about 45 kg of metal to fall into a trough of water. An explosion resulted	Extensive. Severe shock waves. Concrete floor cracked. Major damage to roof and walls

^a A number of water-molten steel explosions in basic oxygen furnaces were described in three papers: McFarlane (1970), Brenner (1970), and Wolff (1970). In most incidents, the water-cooled oxygen lance provided the source of water although other water sources, including the water-cooled hood used to collect gases, occasionally leaked. In many instances, leaking water simply collected as a pool on top of (solidified) slag and then boiled. Explosions were more commonly noted when some further incident occurred such as slag cracking or during movement of the furnace that then allowed water to contact *molten* steel and slag.

furnace was obscured by flame. For the same reason men could not approach the leak to take remedial action. The leak of water was under pressure and fell outwards from the furnace towards the edge of the hob; from the hob the water ran down the slope of the cast house floor joining eventually with the iron runner. Water entered the full torpedo ladle.

Within a few minutes of the blow pipe starting to burn down progressive action was being taken by the furnace crew to bring the furnace off blast so that a new pipe could be fitted.

Shortly before 2.47 am instructions from the shift manager were passed via Traffic Control to a loco driver and shunter to remove the full torpedo ladle from the vicinity of the furnace. Traffic personnel were made aware that water was running into the torpedo. As the loco was coupled to the ladle, water was seen to be coming from the iron runner. An explosion occurred as the ladle was moved. An eye witness identified the throat of the ladle as the seat of the explosion. The incident was timed at 2.47 am.

As a result of the explosion there were four immediate fatalities and 15 hospital admissions. Subsequently a further seven employees died as a result of injuries received.

At the time of the explosion 23 persons were working in the Queen Victoria furnace area. This number included four extra helpers standing by to assist in changing No. 3 blast pipe.

Casting to the second torpedo was still proceeding at the time of the explosion.

I. DISCUSSION

A number of experimental facts have been introduced in the preceding sections. To discuss these results, let us first limit our attention to those tests which used *no external shock* such as a charge of high explosive to initiate an explosion. In these instances it seems clear that to have a *high probability of an explosion between molten metal* (aluminum in most instances) *and water, one must have a situation where a reasonably large quantity of molten metal contacts a wetted, solid surface*. Thus, spills (1) with small amounts of metal, (2) with long metal drop paths in air and/or water, (3) with low rates of flow of metal into water, and (4) with metal temperatures near the solidification point would not normally lead to a large molten metal mass on a wet vessel bottom. Because most (laboratory) tests were conducted in a manner to spill molten metal into water, this initial criterion would indicate that *small-scale* tests would be unproductive—as indeed they were. For essentially all industrial accidents, this criterion was, however, easily met. Small metal spills in industrial plants would not be expected to lead to an explosion and, therefore, they were never reported. On the other hand, many industrial accidents occurred when loading wet metal into a pool of molten metal. These situations do fit

the criterion stated above of a wet surface in contact with a large mass of molten metal.

Next, and apparently of critical importance, even if the first criterion is met—the wet surface must have the appropriate chemical/physical characteristics to allow the explosion sequence to continue. This step, often noted as the “trigger,” is normally prevented if the wet surface is covered with an organic coating or with materials such as oil or grease. Presumably in such cases, steam forms via a film-boiling mechanism and there is a concomitant disintegration of the coating. The trigger step also appears to be blocked if the wet surface is made of glass or aluminum.⁹ On the other hand, coatings of rust and most inorganic salts or paints favor the trigger step. Clean carbon steel, stainless steel, and concrete may or may not allow the trigger step. In all cases where the trigger can take place, the probability of its occurrence is increased if the physical state of the wet surface is rough.

Higher water temperatures seem to reduce the ease of triggering. This may be due to the simple fact that less water is trapped on the surface. Inorganic salts dissolved in the water act in an opposite manner and increase the explosion probability. The vessel cross section does not appear to be a significant variable.

An explosion that results from the trigger occurs in a very short time scale. High-speed photography clearly indicates significant fragmentation, but it is again not clear whether a certain degree of fragmentation is *necessary* for a strong explosion or whether the fragmentation is the *result* of the strong shock that forms the trigger. It would seem obvious that *any* fragmentation could only increase the evolved vapor and exacerbate the damage potential.

Viewed in the light of these findings, molten metal–water explosions show strong similarities—and dissimilarities—to other types of explosions (e.g., smelt–water, LNG–water). Current theories for these other systems often invoke the concept of forming a superheated liquid in the more volatile liquid which, if it can attain the homogeneous nucleation temperature, will vaporize in a very short time period to form a strong local shock, i.e., trigger the event. This concept appears to be well substantiated in the LNG–water case where laboratory-scale tests have been conducted to test the effect of specific variables such as LNG composition and water temperature. The results (Section III) agree very well with theoretical predictions. For the smelt–water case, only recently has there

⁹ Explosions with wet aluminum ingots in an aluminum melting furnace are clearly exceptions.

been developed a viable theory to explain how smelt (a mixture of molten salts such as NaCl , Na_2CO_3 , and Na_2S) could superheat water when the initial smelt temperature greatly exceeds the homogeneous nucleation (or superheat-limit) temperature of water (~ 577 K). This theory, described in Section IV, suggests that at the interface between the smelt and water, both mass and heat transfer processes occur. On the water side, a concentrated salt solution forms. Other data indicate that such solutions may have significantly higher superheat-limit temperatures than pure water. Thus, thicker, high-temperature superheated liquid layers may form and, if these then subsequently nucleate, a strong local explosion can result.

It is possible that this theory can be adapted to explain molten metal–water thermal explosions although many needed data are still unavailable. One might presume that, at the molten metal–wet surface interface, there is some chemical reaction. Possibly that of the metal plus water or metal plus surface to lead to localized formation of salt solutions. These may then superheat until homogeneous nucleation occurs. The local temperature and pressure would then be predicted to be far in excess of the critical point of pure water (220 bar, 647 K) and a sharp, local explosion could then result. Fragmentation or subsequent other superheat explosions would then lead to the full-scale event.

In favor of this general concept are the experimental facts that inorganic compounds, present either in the water or as deposits on the wet vessel wall, increase the probability of an explosion. Also, as noted by Lemmon (1980) and by Anderson and Armstrong (1981), some “light” from surface chemical reactions has been observed, particularly in the more violent incidents. Molten metal dropping through pure water—or in contact with water on an organic (or aluminum or glass) substrate—is notably unexplosive. However, one of the most destructive of all the Alcoa tests occurred when metal was dropped into a vessel with $\text{Ca}(\text{OH})_2$ coated over steel. Temperatures in the bottom rose above the temperature of the molten aluminum at the initiation of the explosion. The salt-gradient theory as applied to this case would suggest that the $\text{Ca}(\text{OH})_2$ or some reaction product dissolved in the water near the molten aluminum and led to the formation of a superheated salt solution. [The solubility of $\text{Ca}(\text{OH})_2$ in water decreases with increasing temperature.] Maischak and Feige (1970) proposed that the $\text{Ca}(\text{OH})_2$ (or iron rust in other cases) may have reacted with the aluminum in a thermite sense to provide sufficiently high local temperatures to favor the highly exothermic aluminum–water reaction.

One other interesting fact is given by Lipsett (1966) in discussing metal–water thermal explosions. He quotes work by Elgert and Brown, who

contacted molten aluminum with water and found very localized pressures in excess of 1 kbar. An analysis of the gases evolved indicated about 0.2% of the aluminum had indeed reacted to form the oxide (hydroxide ?) and hydrogen.

The salt-gradient theory may explain why Anderson and Armstrong (1981) were unable to obtain explosions by injecting water into aluminum, but the small scale of their tests may also have been a factor. Also, when they attempted to collapse the steam film for a slug of water below a molten aluminum surface, their negative results could have been due to the fact that all surfaces were glass. Alcoa tests had proved that glass was a very unreactive substrate. We also note that Anderson and Armstrong (1981) obtained explosions much more readily when aluminum and water were contacted on a "rusty steel plate."

One experiment which does not seem to fit into the network of the salt-gradient theory was that of Wright and Humberstone (1966), who impacted water on molten aluminum and obtained explosions. These results are at variance with those of Anderson and Armstrong, but the latter worked at 1 bar whereas the former used a vacuum environment. It might be possible that, under vacuum, it is much easier to achieve intimate contact between the aluminum and water and, under these conditions, there may be sufficient reaction between the aluminum and water to allow soluble aluminum salts to form. This salt layer could then form the superheated liquid which is heated to the homogeneous nucleation temperature and explodes.

Extending this concept, we now consider those experiments which led to molten aluminum-water explosions *without* the presence of a wet, solid surface. In all of these there was an *external shock* applied to the system—usually in the form of an exploding wire or a detonator. As presumed by the investigators, these artificial shocks could be very effective in collapsing steam films.

Other theories have been advanced to explain molten metal-water explosions. These are usually developed in terms of some change in the mode of heat transfer. For example, Dewing (1980) proposed that transitional boiling could occur on the container surface where both water and molten aluminum are present. As illustrated in Fig. 10, heat flow from the molten metal to the water occurs in the container wall. This unstable boiling phenomenon may cause strong, local shocks and initiate a large-scale explosion. This model places emphasis on both the heat transfer and surface characteristics of the container wall. Organic paints would then be effective in preventing explosions by hindering the necessary heat transfer. The proposed model is interesting and deserves serious consideration.

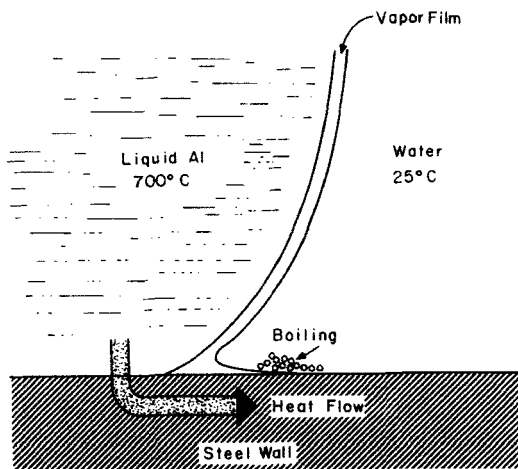


FIG. 10. Transitional boiling model of Dewing.

VI. Reactive Metal–Water Explosions

A. BACKGROUND

In casting or processing reactive metals such as titanium, tungsten, and molybdenum, incidents have occurred in which molten metal contacted water. In some instances, explosions have resulted. There have been no published papers describing such accidents.¹⁰

Few in-depth studies have been made for any single accident; in no case were the energetics developed to yield information on “TNT equivalents” nor were overpressures determined. The accidents were at industrial or government production plants and rarely was there an opportunity for an immediate on-site inspection after an incident.

In all documented cases, the accidents took place during melting and casting in an arc furnace (either vacuum or at a low argon pressure). The metal to be cast was prepared as a consumable electrode by compressing and welding sponge metal. The crucibles were constructed of copper and cooled by water circulation. Melting was achieved by a high-amperage arc between the electrode and the molten metal pool. The process was described in a Bureau of Mines report (Anonymous, 1968).

When accidents are analyzed, the initial event is usually the failure of

¹⁰ Robert A. Beall, former Director of Research at the Bureau of Mines, Albany (OR) Research Center, has, however, collected most of the available information, and he has made his files available for inspection.

some portion of the copper crucible wall because of inadequate cooling or misalignment of the electric arc. This leads to water entering the crucible since its pressure exceeds that in the crucible. Mild steam explosions normally result, and, later, there may be a hydrogen fire from gas produced by the metal-water reaction. An explosion—with significant damage potential—appears to require a second, sequential event that involves some shock applied to the water-molten metal mix. As an example, in one case described below, a crucible developed a water leak and, somewhat later, there was a failure of the electrode cables. This allowed the heavy electrode to fall into the mix, and an explosion occurred.

In an accident report prepared by Robert Beall, he concludes:

Of important consideration is the fact that water leaks in arc furnaces of this type have occurred occasionally in the various melting establishments without any serious explosion resulting therefrom. In a few reported instances, steam buildups have been noted but not of serious consequence. It must be pointed out that the affair here reported required the coincidental occurrence of a water injection, intimate mixing with molten metal, and very possibly, tamping of the mixture by the falling electrode. Such a chain of circumstances can lead to a powerful explosion rather than the customary quiet extinguishing of the arc.

To indicate more details on several case studies, the accident reports have been abstracted below.

B. TITANIUM MELTING-FURNACE EXPLOSIONS

1. *Case I*

Titanium sponge was being melted in a consumable-electrode arc furnace. The furnace had an argon atmosphere slightly above atmospheric pressure. The metal accumulated in a water-cooled copper crucible (41.9 cm i.d., 44.5 cm o.d. about 2 m long). The ingot weighed about 10^3 kg. (The sponge metal was first formed into an electrode and melted in a smaller arc furnace to form an ingot which then became the consumable electrode noted above.)

No previous history of any malfunction in this furnace was noted. The copper crucible had been used for 4 previous runs; the normal lifetime for such crucibles was 40–50 billets. The run was almost completed when the accident occurred.

Just prior to the incident, an adjustment was made on the cooling water flow as the outlet temperature was rising.

The first explosion occurred without warning. One man 14 ft from the furnace was knocked off his feet. No fire or smoke was reported. About 5 sec later a second and more violent explosion occurred. The entire area

around the furnace was enveloped in flame for a brief period. Sheet metal was blown off the building walls, but window damage was not extensive. Cinder blocks in the intermediate area were cracked but not fragmented.¹¹ Injuries to personnel were apparently caused by burns (4 eventually died). The crucible was blown from the furnace and fell on the floor, spilling molten titanium. The main explosion also caused the crucible to bulge [internal pressures of 40–55 bar (600–800 psi) were estimated], and the steel water jacket was torn loose and wrapped back on itself. All water cooling lines were severed.

Although no definite cause could be ascertained, it was generally agreed that there was a burn-through of the crucible (possibly by misdirection of the arc). This allowed water (under pressure) to enter the crucible and contact the molten titanium. A minor (steam) explosion resulted and the burst disc blew. The heavy electrode was lifted up and then fell back into the water–titanium mix. A later, final explosion resulted when the crucible fell on the floor to allow a water–titanium contact.

Some hydrogen was probably generated when the water initially contacted the titanium; it was estimated that only 150 g of water need have reacted to create a pressure of 70 bar in the crucible. Thus, only a very small quantity of water could have been involved.

Since crucible failures have occurred in numerous instances in the industry—with minor steam explosions, the violence of the event described above is believed to be due to the electrode falling into the water–metal mixture. Somehow, the steam–liquid water–molten titanium mixture changed character from a relatively slow increase in pressure to a sharp shock wave.

2. Case II

The furnace and remelting operation was similar to that described in Case I. The crucible diameter was, however, somewhat larger (~50 cm).

The incident began during a normal run when the operator noted an electrical short not long after the start of the melt. Standard shutdown procedures were initiated, and the titanium electrode was retracted at a rate of about 30 cm/min using a chain hoist. During shutdown, what proved later to be a water leak into the crucible occurred with a concomitant pressure rise. Three rupture discs failed at about 4 bar. Some 2 min

¹¹ There is an inconsistency in the accident reports and one stated: "Window panes and sash were broken and two sections of brick and cement block partition walls were demolished." This same report estimated that blast pressures on the walls were less than 1 psi with the wave highly directed.

later, when the electrode was about 75 cm above the molten titanium–water mix, the chain-hoist retracting mechanism failed and the electrode (and holder), weighing about 4500 kg, fell. Quoting from the accident report: “Immediately thereafter a violent explosion occurred which caused a considerable amount of structural damage to the enclosing vault and adjacent portions of the melt-shop buildings.”

Apparently a vault had been constructed around the superstructure of the furnace. It was 4.5×6 m in cross section and 4 m high. It was constructed of 20-cm-wide flange beams on 0.8 m (front) and 1 m (sides) centers faced on both sides with 10-mm steel plates and filled with dry sand. The explosion displaced the walls about 6 cm. The top of the vault which was supported by a 30-cm beam on top of a 20-cm beam was deflected about 8 cm. Steel doors mounted to slide in angle-iron tracks were blown off. A number of 1.9-cm bolts holding the door tracks were sheared “cleanly.” The furnace was driven down into the concrete floor and a penetration of some 10 cm was measured.

One might note the striking similarity between Cases I and II. In both, a crucible failure allowed water to enter and mix with molten titanium. Steam (and hydrogen) formed and the pressure increased so as to bulge the crucible and rupture the safety discs. Tamping the water–metal mix by the fall of the electrode then caused a major explosion. No injuries resulted in the Case II incident because the vault walls provided protection. No data were available to allow an estimation of blast pressures, but as described, the vault construction maintained its integrity and the wave was forced to exit from the bottom.

3. *Case III*

For Cases I and II above, the furnaces were located in the United States. In the 1960s, a severe explosion in Great Britain was partially documented. Apparently the furnace was similar to the one noted in Case I, but argon at about 0.25 bar was used. The bottom cooling plate in the crucible failed and water was allowed to enter. No mention is made of a second event in the accident report. The incident is described as follows:

About three tons of control gear together with a (ton) block of titanium were projected upwards through several feet. Hundreds of square feet of glass and panelling were removed from the roof and walls of the building. The water jacket, made of $\frac{1}{4}$ inch steel, was blown apart.

There was no containment, but blast shields prevented severe injuries to personnel.

C. TUNGSTEN CASTING EXPLOSION

In March 1961, a casting furnace was in operation melting a 98% W-2% Mo alloy to be centrifugally cast. Melting was proceeding normally, and the run was nearly completed. The casting furnace had been in operation several minutes.

Near the termination of melting, the arc penetrated the bottom of the skull and copper crucible, permitting molten tungsten alloy and water to come into intimate contact. The pot contained approximately 137 kg of molten tungsten with a pot water pressure of 2.8 bar. The intimate contact between the metal and water resulted in a steam pressure surge that caused the metal to be ejected from the crucible up the stinger stack and out into the operating area. The pressure buildup lifted the floating stinger lid sufficiently to permit particles of metal to be spewed out and deflected downward onto the top of the furnace deck and general operating area. The crucible had approximately a 5×8 cm oval hole in the bottom where burnthrough occurred. Both view ports in the stinger housing were severely cracked from contact with metal particles. Neither of the view ports were detached from their mounts. The primary cause of injury to operators was the rain of metal particles from the stinger stack.

D. DISCUSSION

Very few molten metal-water explosions are well documented; essentially no data are available to estimate the overpressures or force-time relationships. The few incidents which have been described in any detail suggest that a two (or more)-step sequence is involved. First, contact is made between water and molten metal. Second, the mix is tamped or a shock wave occurs near the mix. The resulting explosion is sharp and has an associated blast wave.

While the incidents described earlier are quite severe, it is difficult to describe them as major explosions. Even with the largest ingot diameter and with an efficient tamp (by electrode cable failure), a rather simple vault enclosure was sufficient to contain the blast wave and shrapnel.

No analysis has been carried out to clarify the mechanism of the explosion.

VII. Explosions with Liquid Refrigerants

Several studies have been carried out in which liquid refrigerants were contacted with either water or oils. In view of the similarity of such

systems to those involving liquefied hydrocarbons, the test results are of value to determine if they are in agreement or disagreement with the superheat-liquid concept developed in Section III.

Five refrigerants have been studied. Some property values are shown in Table XVI.

Fauske (1973) showed that drops of R-11 could be injected into warm water (~ 343 K) with little boiling. The drops, being more dense than water, fell to the bottom of the vessel. No explosions were noted. Also, for R-11 and (R-21), Chukanov and Skripov (1971) measured the superheat-limit temperatures (see Table XVI).

Several investigators studied R-12. Holt and Muenker (1972) and Rausch and Levine (1973) made simple spills of this cryogen into water. The highest water temperature used by both teams was ~ 342 K and weak explosions were noted. From Table XVI, it can be seen that this water temperature was barely within the range of the superheat-limit temperature, so no or only minor explosions might have been expected. Henry *et al.* (1974) spilled R-12 on top of a hot mineral oil. For oil temperatures less than about 409 K, there was little interaction except rapid boiling. Above 409 K, explosions resulted. Henry *et al.* state that this oil temperature would lead to an interface temperature [see Eq. (1)] close to the expected homogeneous nucleation temperature (~ 345 K) so that the explosions were to be expected.

Rausch and Levine (1973) spilled R-114 on hot ethylene glycol. Explosions were reported if the glycol temperature exceeded about 386 K. They estimated the interface temperature between the R-114 and glycol to be about 354 K. Thus, explosions were noted when the *bulk* glycol temperature exceeded the expected homogeneous nucleation temperature, T_{sl} , even though the interface temperatures were less than T_{sl} .

Most experiments using liquid refrigerants have been made with R-22,

TABLE XVI

PROPERTIES OF LIQUID REFRIGERANTS

Refrigerant	Structure	T_b (K) ^a	T_c (K)	P_c (bar)	T_{sl} (K) ^b
R-11	CCl_3F	297	471	44.1	422
R-12	CCl_2F_2	243	385	41.2	345
R-21	CHCl_2F	282	452	51.7	406
R-22	CHClF_2	232	369	49.8	327
R-114	$\text{C}_2\text{Cl}_2\text{F}_4$	277	419	32.6	375

^a Normal boiling temperature.

^b Approximate superheat-limit (homogeneous nucleation) temperature at a pressure of 1 bar.

and the data have been thoroughly summarized by Anderson and Armstrong (1977).

Enger and Hartmann (1972a-d) observed explosions with R-22 poured into water at temperatures from about 320 to 355 K. Rausch and Levine (1973) found no explosions if the water temperature was below 322 K. Holt and Muenker (1972) noted explosions for water temperatures >333 K. Quoting the last authors:

[The experiments were] most impressive since R-22, being heavier than water, immediately sinks beneath the water and in a split second a single explosion is observed. [p. 27]

The results of Enger and Hartmann, Rausch and Levine, and Holt and Muenker are in surprisingly good agreement, and their lower water temperature threshold values are close to the expected superheat-limit temperature of R-22 (~ 327 K).

Anderson and Armstrong (1977) summarize a number of other studies carried out at the Argonne National Laboratory and elsewhere in which there was contact between R-22 and water (or R-22 and mineral oil) (see Henry *et al.*, 1974, 1976; Board *et al.*, 1974). In these studies, pressure transients were measured. Anderson and Armstrong have summarized these data in Fig. 11. Note that for water temperatures below about 350 K, the pressure rise upon contact is small. Above a water temperature of about 350 K, which corresponds to a calculated interface temperature of

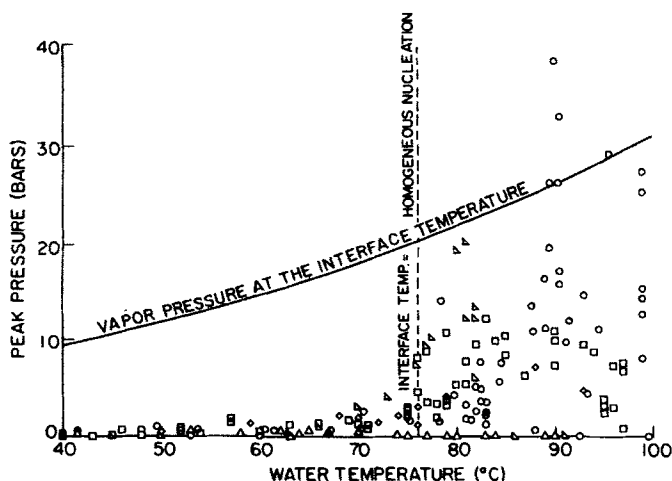


FIG. 11. Refrigerant-22 water contact experiments. Homogeneous nucleation temperature of R-22 $\sim 54^{\circ}\text{C}$. Interface temperature is 54°C when bulk water temperature $\sim 76^{\circ}\text{C}$. (O) Armstrong; (□) Board, saturated R-22; (◇) Board, 116°C R-22; (Δ), Armstrong, 68°C R-22; (▲) Henry, saturated R-22. [From Anderson and Armstrong (1977).]

327 K, there is a significant increase in pressure and values of 30 bar (or higher) were recorded. Assuming that the water-R-22 interface temperature had to attain the superheat-limit value before an explosion occurred, these data are in remarkable agreement with T_{sl} in Table XVI. Also shown in Fig. 11 is the vapor pressure of R-22 calculated for the interface temperature between the water and the saturated R-22 (232 K). Essentially all measured pressures fall below this curve, and this suggests that the maximum pressure transient corresponds to the vapor pressure determined in this manner. (Another limit could be chosen as the critical pressure of R-22, ~50 bars, but this value significantly exceeds any measured pressure.)

The data for Fig. 11 are at 1 bar initial pressure. The effect of the absolute value of the system pressure is discussed in Section VIII.

The experimental data presented above are in good agreement with the superheated liquid model described in Section III. The fact that similar findings were reported by a number of experimentalists in different laboratories, using various spill techniques and test geometries, argues strongly that there is a definite threshold temperature for the hot liquid to lead to a vapor explosion. Further, the general consensus is that this threshold value (at the interface or in the bulk hot liquid) is close to the expected superheat-limit or homogeneous nucleation temperature.

VIII. Effects of Absolute Pressure on RPTs

As will be described later in this section, for several types of small-scale tests where RPTs would be expected, an increase in the absolute system pressure had a profound effect in suppressing such incidents. As often noted in previous sections, one current theory to explain RPTs invokes the concept of the colder liquid attaining its superheat-limit temperature and nucleating spontaneously. In an attempt to explain the pressure effect on the superheating model, a brief analysis is presented on the dynamics of bubble growth and how this process is affected by pressure. The analysis is due largely to the work of Henry and Fauske, as attested to by the literature citations.

A. DYNAMICS OF BUBBLE GROWTH

Let us consider a superheated liquid which has attained the limit of superheat and a vapor embryo forms *in equilibrium* with the liquid. The bubble radius is r_0 , the pressure in the bulk liquid is P_0 , and the temperature is T_0 . Assume the liquid is pure.

The vapor embryo, or bubble, is in *unstable* equilibrium and will either collapse or grow. We are only interested in those that follow the latter path. The "chemical" criteria of equilibrium between the bubble and liquid state that the temperature and chemical potential of the material in the bubble are equal to those in the superheated liquid, i.e.,

$$T_0 = T^B \quad (4)$$

$$\mu_0 = \mu^B \quad (5)$$

The latter equality can be related to the bubble pressure P^B and the liquid pressure by

$$P^B = P_{vp}(T_0) \exp[(V^L/RT)(P_0 - P_{vp})] \quad (6)$$

where P_{vp} is vapor pressure of the liquid at T_0 . Since the liquid is superheated, $T_0 > T_b$, where T_b is the normal boiling temperature of the liquid at P_0 . In fact, $T_0 - T_b$ is the *superheat* of the liquid phase.

The exponential term in Eq. (6) is normally only slightly less than unity ($P_0 < P_{vp}$) and is often neglected. For the discussion given below, we will also follow this procedure.

The "mechanical" criterion of equilibrium states that

$$P^B - P_0 = 2\sigma/r_0 \quad (7)$$

Since the initial vapor bubble is very small at the homogeneous nucleation temperature, P^B greatly exceeds P_0 .

Most treatments of bubble growth dynamics assume that, as the bubble expands, Eq. (7) is still valid although the pressure may drop due to the expansion from both temperature variations in the bubble and the increase in radius—to lessen the surface forces, i.e., at any time in the growth,

$$P(r) = P^B - 2\sigma/r \quad (8)$$

Here, r is the bubble radius, P^B is the pressure inside the bubble, $P(r)$ is the pressure in the liquid at the bubble boundary, and $P(r) > P_0$.

As soon as the bubble expansion causes $P(r)$ to exceed P_0 , one can express the dynamics of the event as

$$r(d^2r/dt^2) + (\frac{3}{2})(dr/dt)^2 = [P(r) - P_0]/\rho^L \quad (9)$$

Equation (9) assumes the liquid is nonviscous and incompressible.

As one limiting case, let us assume no heat transfer limitations so that the pressure *inside* the bubble is invariant at $P_{vp}(T_0)$. Then, using Eqs. (8) and (9), as shown by Plesset and Zwick (1954),

$$\begin{aligned} (dr/dt)^2 = & (dr/dt)_0^2/r^* + (4\sigma/3\rho^L r_0)[1 - (r^*)^3] \\ & - (2\sigma/\rho^L r)[1 - (r^*)^2] \end{aligned} \quad (10)$$

where $(dr/dt)_0$ is the *initial* velocity of movement of the bubble wall when growth just begins and $r^* = r_0/r$. We are interested in the growth velocity dr/dt .

The value of dr/dt is relatively insensitive to the value of $(dr/dt)_0$ as shown by Prosperetti and Plesset (1978). Also, if we choose $r \gg r_0$, then r^* is a small number. Equation (10) then simplifies to

$$dr/dt = \{(\frac{2}{3}\rho^L)[P_{vp}(T_0) - P_0]\}^{1/2} \quad (11)$$

or

$$r \sim \{(\frac{2}{3}\rho^L)[P_{vp}(T_0) - P_0]\}^{1/2} t \quad (12)$$

Equation (11) or (12) is often termed the Raleigh solution for inertial controlled bubble growth.

The actual motion of the bubble deviates markedly from that predicted by Eq. (11) or (12) because the expansion allows vaporization to occur at the bubble boundary and this cools the liquid near the bubble. The heat transfer at the bubble boundary is found by solving the energy equation. In the liquid phase, if R is measured from the bubble center,

$$\partial T/\partial t + (r/R)^2(\partial r/\partial t)(\partial T/\partial R) = (\alpha/R^2)(\partial/\partial R)[R^2(\partial T/\partial R)] \quad (13)$$

$$(4\pi r^2 k)(\partial T/\partial R)_{R=r} = \Delta H_v(\partial/\partial t)[(\frac{4}{3})\pi r^3 \rho^v] \quad (14)$$

where α is the thermal diffusivity and k is the thermal conductivity of the liquid. ΔH_v is the enthalpy of vaporization and is assumed to be temperature independent. ρ^v is the vapor density inside the bubble and varies with the temperature and pressure in the bubble.

In reality, Eqs. (13) and (14) should be solved simultaneously with Eqs. (8) and (9), but no analytical solution is available. However, we can examine the asymptotic solutions to Eqs. (13) and (14) to determine the bubble growth rate when heat transfer limits the growth, i.e., when $P(r) \sim P_0$ and $T^B \sim T_b$ so no inertial effects are present. For this extreme,

$$dr/dt \sim k(T_0 - T_b)/\Delta H_v \rho^v(\alpha t)^{1/2} \quad (15)$$

Here, ρ^v is evaluated at P_0 , T_b . Integrating,

$$r \sim 2(\alpha t)^{1/2} \text{Ja} \quad (16)$$

where Ja is the Jacob number, and

$$\text{Ja} = k(T_0 - T_b)/(\rho^v \Delta H_v \alpha) \quad (17)$$

In the thermally controlled regime, the radius increases with the square root of time.

Thus the *initial* growth is largely controlled by inertial restraints and the radius increases linearly with time [Eq. (12)], whereas at long times heat transfer considerations become predominant and the growth is given by Eq. (16). The actual variation of r with t is less than either of these two asymptotic extremes (see Theofanous, 1969).

In Fig. 12, we show the computed values of bubble radius for superheated liquid propane at two pressure levels: 1 and 5 atm. Consider the inertial rate first. At 1 atm, liquid superheated propane attains the limit of superheat at about 328 K, where the vapor pressure is ~ 18.9 atm. With Eq. (12), $r_{\text{inertial}} \sim 52t$ m, where t is in seconds. At 5 atm, the driving force $[P_{\text{vp}}(T_0) - P_0]$ is less than that at 1 atm, but the difference is slight. Thus, the 1 and 5 atm radii are shown as a single line in Fig. 12.

For the thermally controlled growth curve, Eq. (16) was used and the properties of liquid propane were estimated at T_0 [328 K at 1 atm and 322 K at 5 atm]. Over this small temperature range, the variation in most properties was small. However, ρ^v , the density of the vapor in the growing bubble, is proportional to the pressure so that the Ja number [Eq. (17)]

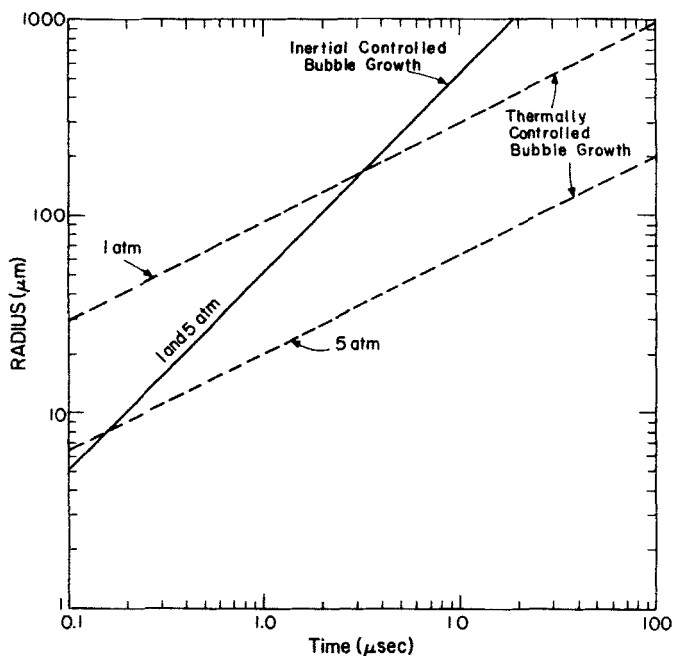


FIG. 12. Bubble growth for superheated propane.

is approximately inversely proportional to pressure. This is the reason for the large difference in the two thermally controlled growth curves in Fig. 12. In a physical sense, more mass must be evaporated at higher pressures for the same bubble volume increase. This results in lower growth rates since the thermal properties of the liquid and the temperature driving force are not greatly different for the two cases.

From Fig. 12, the important conclusion is reached that pressure effects can play an important role in establishing the controlling regime for bubble growth. Higher pressures cause a more rapid transition from inertial to thermal control and a lower growth rate after this transition. This is the same argument developed by Henry and his colleagues (see, for example, Henry and McUmbert, 1977).

B. PRESSURE EFFECTS ON THERMAL EXPLOSIONS

In the preceding section, a simple analysis of the growth of a vapor embryo in a superheated liquid showed that the level of the ambient pressure could play an important role in controlling the rate of expansion of the vapor bubble, i.e., high ambient pressures led to predictions that heat transfer rates would limit the growth process soon after expansion began. Inertial controlled expansion played a smaller role at high pressures. To examine the effect of pressure, three experimental programs have been conducted. These are described briefly below.

Henry and McUmbert (1977) reported on the systems R-22¹²-water and R-22-oil. They constructed an apparatus in which R-22 could be poured into water or mineral oil at various ambient pressures controlled by the pressure of argon gas in the system. Separate units were used for the water and oil tests. They demonstrated that they could achieve thermal explosions at 1 bar, in agreement with earlier tests (see Section VII). However, no such events were observed at system pressures of 2.2 or 8 bar even though the hot liquid temperature was varied over a wide range.

They argue that, at the higher pressures, the rate of bubble growth is smaller and any prefragmentation would have to be into a very small drop size to allow these drops to be disintegrated and thereby provide a means to escalate any small events.

Henry (1978) and Henry *et al.* (1979) describe other experiments where elevated pressures eliminated thermal explosions between water and molten sodium chloride. Two kilograms of NaCl were heated to melt temperatures between 850 and 1200°C and dropped into a tank of water at 20, 50,

¹² R-22 is refrigerant-22, CHClF_2 .

or 90°C. The system pressure was varied from 1 to 40 bar. The water-to-melt ratio was 15:1.

A typical test sequence is shown in Fig. 13 for a NaCl temperature of 850°C and water at 50°C. Pressure signatures are shown for overpressures of 1, 5, and 10 bar. For the 1-bar case a rather violent explosion was noted with deformation of the test vessel. At 5 and 10 bar, the pressure increases are slower and indicate "long-term" vaporization was occurring. As with the R-22 tests, an increase in system pressure led to a significant change in the behavior of a vapor explosion.

In the third study, Miyazaki and Henry (1978) carried out vapor bubble growth experiments with water drops in hot silicone oil under various pressures of argon gas. As conducted, the oil temperature was set so that the interface temperature was below the homogeneous nucleation temperature of water. When bubbles did appear, their growth was followed by

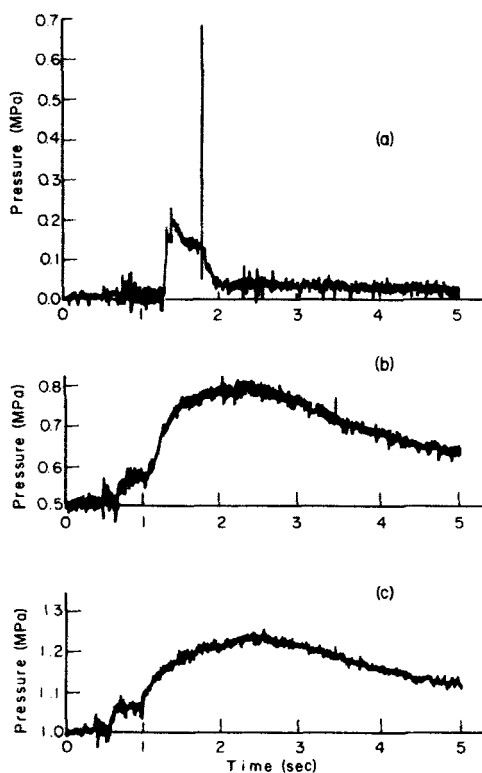


FIG. 13. NaCl-H₂O interaction: effect of ambient pressure. $P_0 = 0.1$ (a), 0.5 (b), 1.0 (c) MPa. System parameters: NaCl, mass = 1.7 kg, $T = 850^\circ\text{C}$; H₂O, mass = 15 kg, $T = 50^\circ\text{C}$. [From Henry *et al.* (1979).]

high-speed photography. They found that bubble growth rates were suppressed as the system pressure was increased, in agreement with the concepts described above for bubble growth dynamics.

C. ESCALATION MODEL OF HENRY AND FAUSKE

Henry and Fauske (1975, 1976) have proposed a model to describe the events leading to a *large-scale* vapor explosion in a *free contact* mode. Their initial, necessary conditions are that the two liquids, one hot and the other cold, must come into intimate contact, *and* the interfacial temperature [Eq. (1)] must be greater than the homogeneous nucleation temperature of the colder liquid. Assuming the properties of both liquids are not strong functions of temperature, the interface temperature is then invariant with time. Temperature profiles within the cold liquid may then be computed (Eckert and Drake, 1972) as

$$[T(x) - T_i]/(T_i - T_0) = \text{erf}[x/2(\alpha t)^{1/2}] \quad (18)$$

where x is the distance into the cold liquid at time t ; α is the thermal diffusivity of the cold liquid; $T(x)$ is the temperature at x ; T_0 is the bulk cold liquid temperature; and T_i is the interface temperature determined from Eq. (1). In Fig. 14 (Henry and Fauske, 1975), three temperature profiles are shown for the system R-22 (CHClF_2) and water, where the water temperature is such as to give an interface temperature of 60°C . The bulk R-22 is at its 1 bar boiling point: -41°C . In this case the interface is slightly above the expected homogeneous nucleation temperature of R-22: 54°C .

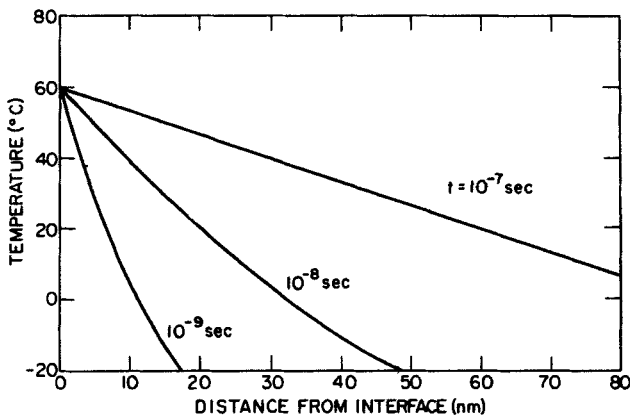


FIG. 14. Thermal boundary-layer development. Freon-22, $T_i = 60^\circ\text{C}$. After Henry and Fauske (1975).

From nucleation theory (see Section IX), one can estimate the expected rate of formation of critical-sized vapor embryos in a liquid as a function of temperature. This rate is a very strong function of temperature and changes from a vanishingly low value a few degrees below the homogeneous nucleation temperature to a very large value at this temperature.

Theory also allows one to estimate the size of these unstable embryos at the moment of inception. The critical size has been given by Eq. (7). Assuming P_0 is 1 bar and P^B is the vapor pressure of R-22, Fig. 15 shows the value of D_0 ($= 2r_0$) as a function of temperature.

Considering Figs. 14 and 15 together, assume time $t \sim 10^{-7}$ sec. At a distance $x \sim 5$ nm from the interface, the temperature is slightly less than 60°C , but D_0 is greater than 5 nm as can be seen by superimposing both figures (as in Fig. 16). The intersection of D_0 and the $t = 10^{-7}$ sec curves (point A) yields the location of the smallest vapor embryo which can be formed. Note no intersections are possible when $t = 10^{-8}$ or 10^{-9} sec, so nucleation cannot occur. If the vapor embryo at A could grow infinitely fast to the second intersection (point B), the embryo would then be too large for the local temperature and it would collapse.

The Henry and Fauske model employs curves similar to Fig. 16. Immediately upon initial contact, they assume that there is rapid pressurization at the interface. Nucleation in this vicinity is then prevented [P_0 in Eq. (7) is large and so is D_0] until the pressure is acoustically relieved by the wave moving to a free surface and returning. During this period, the thermal boundary layer in the cold liquid continues to develop. At relief, there still may be no intersection of the t - D_0 curve (in Fig. 16), so until such a time

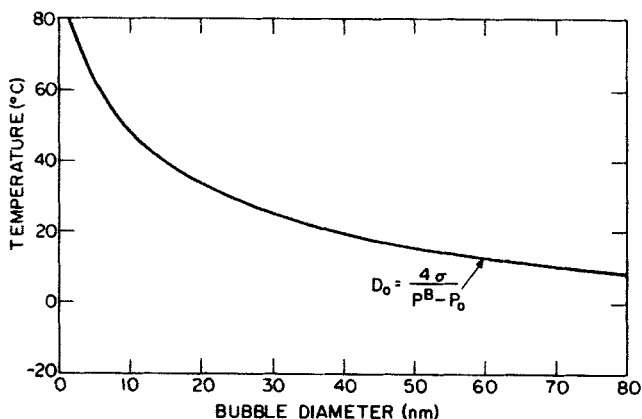


FIG. 15. Critical bubble diameter for Freon-22; $T_i = 60^\circ\text{C}$. [After Henry and Fauske (1975).]

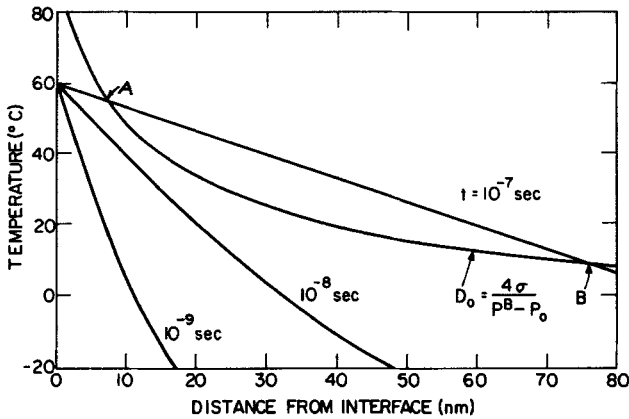


FIG. 16. Thermal boundary-layer development and critical bubble size for Freon-22; $T_i = 60^\circ\text{C}$. [After Henry and Fauske (1975).]

that this occurs, no nucleation is possible. Finally, when there is nucleation, there is assumed to be another delay period while a pressure gradient is developed within the liquid. Growth then begins and is, initially, inertially controlled, i.e., see Eq. (12), at least until point B is reached.

Their argument then proceeds along the following lines. During the growth from A to B, there is a characteristic time. They estimate the number of other vapor embryos which will develop during this time. They state that if more than about 10^9 embryos form per square centimeter in this period, they will result in interference at the maximum stable diameter (point B) and vapor blanketing will result on that portion of the surface. The energy transfer is then terminated and no escalation can occur.

With this model, it is predicted that there should be a liquid drop size which, if too large, will result in long delay times and excessive numbers of new embryos to vapor blanket the surface. Thus, small drops (or thin layers) are more prone to escape termination by vapor blanketing. Also, if experimental variables are modified so as to reduce the growth rate of embryos from A to B, e.g., by increasing pressure, again one would expect a lower probability of escalation. These two predictive conclusions appear to be substantiated by experiment.

Escalation is, however, encouraged for cases where the initial coolant liquid is sufficiently fragmented so that initial embryo growth is rapid and without excessive interference due to other embryos (which would increase the local pressure and, thereby, reduce the growth rate). If the fragmentation is such that very small drop sizes are present, then during the inertial growth of vapor embryos, the bubble radius will reach the

interface and burst. This phenomenon will result in an increase of system pressure, but, at the same time, smaller drops are formed which can then nucleate and grow even at the higher system pressure.

Escalation has been achieved.

The model also predicts that if the interface temperature exceeds the *critical* temperature of the colder liquid, vapor blanketing should always result and no rapid phase transitions could occur.

While there are many aspects of the model which can be questioned, the basic concepts are realistic and the predictive results are of value. They can be summarized as follows:

(1) Two liquids in contact must yield an interface temperature which exceeds the homogeneous nucleation temperature of the cold liquid. The bulk temperature of the cold liquid may be saturated or subcooled.

(2) Sufficient prefragmentation must be achieved during the contact (or in any subsequent boiling) to produce small drops. The critical drop size can be estimated and may be shown to be smaller as the system temperature rises.

(3) Increases in system pressure lead to more rapid vapor blanketing of small drops so, to obtain rapid phase transitions at elevated pressures, more extensive prefragmentation is necessary.

(4) If the interface temperature exceeds the critical temperature of the cool liquid, vapor blanketing prevents escalation.

These conclusions hold only for a *free contact* model. Contact in shock tubes or with external triggers are excluded.

Other escalation models have been proposed (see Bankoff, 1978), but most do not emphasize conditions (1) and (4) above which are, however, supported by experimental evidence.

IX. Appendix: Superheated Liquids

Superheated liquids are liquids which exist at temperatures above their equilibrium boiling point at the system pressure. These liquids are metastable in a thermodynamic sense, i.e., they are stable with respect to small perturbations on the system, but if the perturbation is sufficiently large, superheated liquids will partially vaporize and form a final, more stable state, usually consisting of vapor and residual liquid.

The basic reason why superheated liquids can exist is that the nucleation step requires that a vapor embryo bubble of a minimum size must be achieved. Vapor embryos less than the critical size are unstable and tend

to collapse. Only when examining the behavior of very large numbers of embryos in their dynamic growth and decay processes is it possible to show that there is a finite probability of forming embryos of the appropriate (critical) size that can then grow to macroscopic size bubbles.

Increasing the temperature or lowering the pressure on a superheated liquid will increase the probability of nucleation. Also, the presence of solid surfaces enhances the probability because it is often easier to form a critical-sized embryo at a solid-liquid interface than in the bulk of the liquid. Nucleation in the bulk is referred to as *homogeneous* nucleation whereas if the critical-sized embryo forms at a solid-liquid (or liquid-liquid) interface, it is termed *heterogeneous* nucleation. Normal boiling processes wherein heat transfer occurs through the container wall to the liquid always occur by heterogeneous nucleation.

The key to attain the high superheats associated with homogeneous nucleation is, therefore, to prevent spurious heterogeneous nucleation from container walls or from suspended motes. To study superheated liquids, experimental techniques usually involve the "encapsulation" of the liquid by another, less volatile liquid (Trefethen, 1957). The latter liquid is chosen so that it is immiscible but wetted by the superheated liquid, i.e., there is a low or zero contact angle. The liquid-liquid interface should then approach one that is microscopically smooth; heterogeneous nucleation is then prevented, and any vapor embryos which form will do so in the bulk of the superheated liquid. The bubble column developed by Moore (1956, 1959) and by Wakeshima and Takata (1958) has been widely used to study superheated liquids. One variation of this column is shown in Fig. 17. The host or nonvolatile liquid is the continuous phase in a vertical glass column. The column is wrapped with heating wire in such a manner as to develop a stable vertical temperature gradient. A small drop (ca. 0.5 mm in radius) of the test liquid is injected into the bottom of the column. As the host fluid has been chosen to be more dense than the test liquid, the injected drop rises slowly. The temperature of the host fluid at the point of injection is below the expected boiling point of the test liquid. However, during the ascent of the drop into warmer regions of the host liquid, the test liquid eventually becomes superheated. Nucleation to vapor is, however, prevented by the lack of heterogeneous sites. The main purpose of the bubble column is to determine just how far one can superheat a given liquid before *homogeneous* nucleation occurs.

As will be seen later, there is a maximum superheat and at this point the liquid attains the *superheat-limit temperature* or *homogeneous nucleation temperature* and nucleation is prompt. Denoting this limit as T_{sl} , we note it is a function of pressure and material tested.

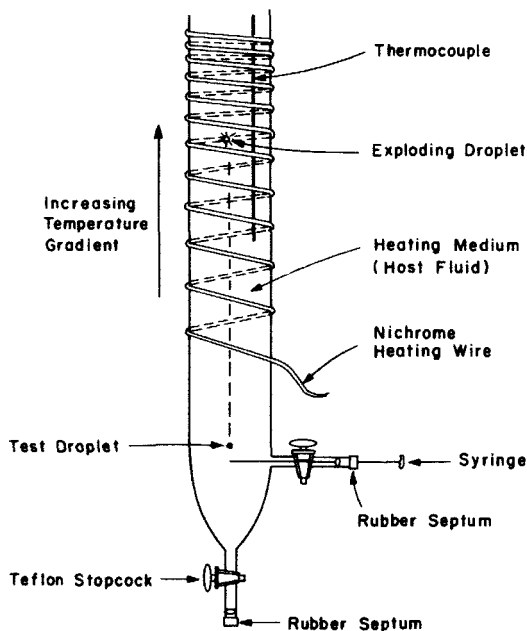


FIG. 17. Bubble column.

T_{sl} may be estimated by two very different theoretical routes. From *thermodynamics*, one can derive the necessary criteria (Beegle, 1973; Beegle *et al.*, 1974). To use these relations, an applicable equation of state for the material is all that is required, i.e., one only needs a relationship between P , V , T , and composition for the liquid. The results of applying this technique can be generalized in a deceptively simple way, e.g., to a reasonable approximation:

$$T_{sl} = T_c[(0.11P_r) + 0.89] \quad (19)$$

where T_c is the critical temperature, P_c is the critical pressure, and $P_r = P/P_c$. For example, with propane, $T_c = 369.8$ K, $P_c = 42.5$ bar. When the system pressure is, say, 1 bar, $T_{sl} = 330$ K or 57°C . This value is only a degree or so higher than measured values of T_{sl} for this material.

A second technique for estimating T_{sl} involves a detailed consideration of the sequential rate processes to form vapor embryos in a superheated liquid (see Volmer and Weber, 1926; Farkas, 1927; Becker and Döring, 1935; Zel'dovich, 1943; Moore, 1959). This method does not yield an *absolute* value of T_{sl} ; rather it allows one to estimate the probable *rate* of formation of *critical-sized embryos* in a superheated liquid at any given temperature and pressure. If the rate is *very* low, within the time scale of

an experiment one concludes *no* nucleation would occur. On the other hand, if the rate is *very* high, then one assumes that T_{sl} has been exceeded. One must make some judicious choice of a rate which would correspond to T_{sl} . This procedure is not as indefinite as it might appear since the calculated rate of nucleation is a very strong function of temperature as will be illustrated below.

The rate of nucleation is given, approximately, as

$$J = Nf \exp(-\Delta B/kT) \quad (20)$$

$$\Delta B = \left(\frac{4\pi}{3}\right) \pi \sigma^3 / (P^B - P^L)^2 \quad (21)$$

where J is the expected rate of formation of critical-sized vapor embryos per unit volume; f is a "frequency" factor which, in general, is on the order of 10^{11} sec^{-1} ; N is the number density of molecules in the superheated liquid; ΔB is the availability change in forming a critical-sized embryo (Modell and Reid, 1982); σ is the surface tension of the liquid; P^B is the pressure inside the vapor embryo; P^L is the system pressure; and k is Boltzmann's constant.

N and f are not strong functions of temperature, but this is not true for σ and P^B . As temperature increases, σ decreases and P^B increases. Both effects tend to make the exponential term larger. In fact, near T_{sl} , it is not uncommon for J to vary 3 to 4 orders of magnitude per degree! As an example, consider pure diethyl ether at a pressure of 1 bar. The normal boiling temperature is 307.7 K. If this liquid were to be heated to about 410 K, J , as calculated from Eq. (20), is about $10^{-29} \text{ nuclei/m}^3 \cdot \text{sec}$. This is a negligibly small number and one would conclude that homogeneous nucleation would not occur. Another way to visualize this value is to examine J^{-1} , i.e., $10^{29} \text{ m}^3 \cdot \text{sec}$. If one had 1 m^3 of superheated liquid ethyl ether at 410 K, an average waiting time of 10^{29} sec ($\sim 10^{21} \text{ yr}$) would elapse before one would note the formation of a bubble from homogeneous nucleation! (This value is only valid for comparison purposes; ionizing radiation and other very minor perturbations would initiate nucleation long before this in a real situation.)

However, if the temperature were raised from 410 to 420 K, then $J \sim 10^{14} \text{ nuclei/m}^3 \cdot \text{sec}$. Now J is a very large number and nucleation is prompt, with a "waiting period" of $\sim 10^{-14} \text{ sec}$ for a cubic meter of superheated ether!

Clearly the "experimental" value of T_{sl} lies between 410 and 420 K. A J value of $10^6 \text{ nuclei/cm}^3 \cdot \text{sec}$ is often used to define T_{sl} . With this as a criterion, $T_{sl} \sim 418\text{--}419 \text{ K}$, which is in excellent agreement with experimental results using bubble columns (Skripov, 1974).

T_{sl} is also a function of composition. For example, let us consider a

superheated liquid mixture of ethane and *n*-butane at 270 K and 1 bar. For reference, at this pressure, the boiling temperatures of ethane and *n*-butane are 184.5 and 272.7 K, respectively. Using Eqs. (20) and (21), one can estimate the expected rate of bubble formation as a function of composition:

$T = 270 \text{ K}, \quad P = 1 \text{ bar}$	
Mole fraction of ethane in liquid	Expected rate of formation of critical-sized vapor embryos (number/m ³ · sec)
0.88	3×10^{-15}
0.90	2×10^{-7}
0.92	5×10^{-1}
0.94	3×10^5
0.96	1×10^{10}
0.98	2×10^{14}
1.0	9×10^{17}

Considering these results, it would be predicted that superheated liquid mixtures of ethane and *n*-butane with less than about 92% ethane would not have attained T_{sj} . Above this composition, prompt nucleation would be expected. Experiments seem to substantiate the lower limit prediction. At about 95% ethane, violent rapid phase transitions occur when this cryogen contacts water near its freezing temperature. Compositions close to (and including) pure ethane would be predicted to have very prompt nucleation, yet simple spills of such a cryogen on water do not lead to any dramatic result, i.e., simple film boiling results. It is believed that, in such cases, nucleation is so rapid that, at the interface, vapor forms to "insulate" the bulk ethane from the water. As indicated in Section III, one can obtain explosive rapid phase transitions with pure liquid ethane by *impacting* ethane with water. The presumption then is that the vapor blanket at the interface collapses to allow liquid-liquid contact. Superheating of the liquid ethane can then occur and lead to bulk nucleation.

This brief commentary on superheated liquids has indicated that they are readily formed if one prevents heterogeneous nucleation of vapor embryos. Also, there is a limit to the degree of superheat for any given liquid, pure or a mixture. This limit may be estimated either from thermodynamic stability theory or from an analysis of the dynamics of the formation of critical-sized vapor embryos. Both approaches yield very similar predictions although the physical interpretation of the results from both differ considerably.

For those wishing to learn more about superheated liquids, there are several general reviews (Blander and Katz, 1975; Skripov, 1974; Reid, 1976, 1978a,b,c; Eberhart *et al.*, 1975).

Nomenclature

ΔB	Availability change to form embryo	t	Time
D_0	Initial bubble diameter	T	Temperature
f	Frequency factor in nucleation	T_0	Temperature in bulk liquid
ΔH_v	Enthalpy of vaporization	T^B	Temperature in bubble
J	Rate of formation of critical-sized embryos per unit volume	T_b	Normal boiling point
J_a	Jacob number [Eq. (17)]	T_w	Temperature of water
k	Boltzmann's constant or thermal conductivity	T_{sl}	Superheat-limit temperature
N	Number density of molecules	T_c	Critical temperature
P	Pressure	V	Specific volume
P_0	Pressure in bulk liquid	x	Distance
P^B	Pressure in bubble		
P_{vp}	Vapor pressure		
P_c	Critical pressure		
P_r	P/P_c		
r	Radius		
r_0	Radius of original embryo		
r^*	r_0/r		
R	Gas constant or distance from center of embryo		

GREEK LETTERS

α	Thermal diffusivity
μ	Chemical potential
μ_0	Chemical potential in bulk liquid
μ^B	Chemical potential in bubble
ρ	Density
ρ^L	Density in liquid
ρ^v	Density in bubble
σ	Surface tension
ψ	Parameter in Eq. (3)

ACKNOWLEDGMENTS

This review was made possible only through the help of many individuals who provided unpublished reports and critical, but valuable, suggestions during its preparation. In particular, I would like to thank Dr. Richard P. Anderson (Argonne National Laboratory), Drs. Robert E. Henry and Hans K. Fauske (Fauske & Associates), Dr. Thomas M. Grace (Institute of Paper Chemistry), Dr. Thomas McRae (Lawrence Livermore National Laboratory), and Dr. Walter E. Wahnsiedler (Alcoa).

Financial support was provided by the Gas Research Institute, Exxon Research and Engineering, and the National Science Foundation.

References

- Anderson, R. P., and Armstrong, D. R. (1972). "Experimental Study of Vapor Explosions," LNG-3, Sess. VI, Pap. 3. Washington, D.C.
- Anderson, R. P., and Armstrong, D. R. (1973). Comparison between vapor explosion

- models and recent experimental results. *AIChE-ASME Natl. Heat Transfer Conf.*, 1973, Atlanta, Georgia.
- Anderson, R. P., and Armstrong, D. R. (1976). "Combined Physical-Chemical Explosions," ANL-76-87. Argonne Natl. Lab., Argonne, Illinois.
- Anderson, R. P., and Armstrong, D. R. (1977). R-22 vapor explosions. *Pap., Winter Annu. Meet., ASME*, 1977.
- Anderson, R. P., and Armstrong, D. R. (1981). Experimental study of small scale explosions in an aluminum-water system. *Pap., Winter Annu. Meet., ASME*, 1981, New York.
- Anderson, R. P., and Bova, L. (1975). "Final Report on the Small Scale Vapor Explosion Experiments Using a Molten NaCl-H₂O System," ANL/RAS 75-6. Argonne Natl. Lab., Argonne, Illinois.
- Anderson, R. P., Armstrong, D. R., Bova, L., and Gebner, R. H. (1975). "Report on Large Scale Vapor Explosion Experiments Using a Molten NaCl-H₂O System," ANL/RAS 75-5. Argonne Natl. Lab., Argonne, Illinois.
- Anonymous (1968). Cold-mold arc melting and casting. *Bull.—U.S. Bur. Mines* **646**.
- Bankoff, S. G. (1978). Vapor explosions: A critical review. Keynote address. *Heat Transfer, Int. Heat Transfer Conf.*, 6th, 1978, Toronto, Canada.
- Becker, R., and Döring, W. (1935). The kinetic treatment of nucleus formation in supersaturated vapors. *Ann. Phys. (Leipzig)*[5] **24**, 719, 752.
- Beegle, B. L. (1973). Stability analysis of multicomponent systems. S.M. Thesis, Massachusetts Institute of Technology, Cambridge.
- Beegle, B. L., Modell, M., and Reid, R. C. (1974). Thermodynamic stability criterion for pure substances and mixtures. *AIChE J.* **20**, 1200.
- Bergman, S. G. A., and Laufke, H. (1981). "Recovery Boiler Explosions," SPCI-Rep. No. 35. The Swedish Steam Users Association, Stockholm, Sweden.
- Blander, M., and Katz, J. L. (1975). Bubble nucleation in liquids. *AIChE J.* **21**, 833.
- Blander, M., Hengstenberg, D., and Katz, J. L. (1971). Bubble nucleation in *n*-pentane, *n*-hexane, *n*-pentane + hexadecane mixtures, and water. *J. Phys. Chem.* **75**, 3613.
- Board, S. J., Hall, R. W., and Brown, G. E. (1974). "The Role of Spontaneous Nucleation in Thermal Explosions: Freon/Water Experiments," RD/BIN 3007. Central Electricity Generating Board, Berkeley Nuclear Laboratories, Great Britain.
- Brenner, G. A. (1970). Explosions in basic oxygen furnaces. II. *Trans. AIME, Open Hearth Proc.*, 1970 p. 89.
- Briggs, A. J. (1976). Experimental studies of thermal interactions at AEE Winfrith CSNI Spec. Meet. *Sodium Fuel Interact. Fast React.*, 3rd, 1976, Tokyo, Japan.
- Briscoe, F. (1978). "LNG Water Vapour Explosions—Estimates of Yields and Pressures," Sess. 2A. *LNG/LPG Gas Conf.*, 6th, 1978, Monte Carlo, Monaco.
- Buchanan, D. J., and Dullforce, T. A. (1973). Mechanism for vapour explosions. *Nature (London)* **245**, 32.
- Burgess, D. S., Murphy, J. N., and Zabetakis, M. G. (1970). Hazards associated with the spillage of liquefied natural gas on water. *Rep. Invest.—U.S. Bur. Mines* **RI-7448**.
- Burgess, D. S., Biordi, J., and Murphy, J. (1972). "Hazards of Spillage of LNG into Water," PMSRC Rep. No. 4177. U.S. Bur. Mines.
- Chukanov, V. N., and Skripov, V. P. (1971). Kinetics of homogeneous nucleation in F-11 and F-21 superheated liquid freons. *Tr. Ural. Politekh. Inst. im. S.M. Kirova* **189**, 48.
- Combustion Engineering, Inc. (1966). "Summary Report on the Nature of and Remedies for Explosive Reaction(s) Between Smelt and Water in Kraft Chemical Recovery Furnaces." Inst. Pap. Chem., Appleton, Wisconsin.
- Dewing, E. W. (1980). The initiation of molten aluminum-water explosions. *Memo., AIME Meet.*, 1980, Las Vegas, Nevada.

- Eberhart, J. G., Kremsner, W., and Blander, M. (1975). Metastability of superheated liquids; AD753561, bubble nucleation in hydrocarbons and their mixtures. *J. Colloid Interface Sci.* **50**(2), 369.
- Eckert, E. R. G., and Drake, R. M., Jr. (1972). "Analysis of Heat and Mass Transfer," Chapter 4. McGraw-Hill, New York.
- Enger, T., and Hartman, D. E. (1972a). "LNG Spillage on Water," Tech. Prog. Rep. 1-72. Shell Pipeline Corp.
- Enger, T., and Hartman, D. E. (1972b). Mechanics of the LNG-water interaction. *Pap., Am. Gas Assoc. Dist. Conf.*, 1972.
- Enger, T., and Hartman, D. E. (1972c). Explosive boiling of liquefied gases on water. *Pap., Mater. Res. Counc. Conf. LNG Importation Terminal Saf.*, 1972, Boston, Massachusetts.
- Enger, T., and Hartman, D. E. (1972d). "Rapid Phase Transformations during LNG Spillage on Water," Pap. 2, Sess VI, LNG 3. Washington, D.C.
- Farkas, L. (1927). The velocity of nucleus formation in supersaturated vapors. *Z. Phys. Chem.* **125**, 236.
- Fauske, H. K. (1973). On the mechanism of uranium dioxide—sodium explosive interactions. *Nucl. Sci. Eng.* **51**, 95.
- Feldbauer, G. F., Heigel, J. J., McQueen, W., Whipp, R. H., and May, W. G. (1972). "Spills of LNG on Water," Rep. No. EE61E-72. Esso Res. Eng. Co.,
- Garland, F., and Atkinson, G. (1971). "The Interaction of Liquid Hydrocarbons with Water," AD753561. Dept. of Transportation, U.S. Coast Guard, Washington, D.C.
- Grace, T. M., and Taylor, M. L. (1979). "Analysis of Explosion Data." Inst. Pap. Chem., Appleton, Wisconsin.
- Health and Safety Executive (1975). "The Explosion at Appleby-Frodingham Steelworks, Scunthorpe." HM Stationery Office, Great Britain.
- Henry, R. E. (1978). "Test Plan: Large Scale Molten Salt-Water Vapor Explosion Studies to be Conducted at Ispra, Italy," NUREG/CR-0728, ANL-79-20. Argonne Natl. Lab., Argonne, Illinois.
- Henry, R. E., and Fauske, H. K. (1975). Energetics of vapor explosions. *Am. Soc. Mech. Eng. [Pap.]* **75-HT-66**.
- Henry, R. E., and Fauske, H. K. (1976). Nucleation characteristics in physical explosions. *Spec. Meet. Sodium Fuel Interact. Fast React.*, 3rd, 1976, Tokyo, Japan.
- Henry, R. E., and McUmber, L. M. (1977). Vapor explosion potentials under LWR hypothetical accident conditions. *Proc. Light Water React. Saf. Meet.*, 1977, Sun Valley, Idaho. CONF-770708, pp. 414–425.
- Henry, R. E., Gabor, J. D., Winsch, I. O., Spleha, E. A., Quinn, D. J., Erickson, E. G., Heiberger, J. J., and Goldfuss, G. T. (1974). Large scale vapor explosions. *Proc. Fast React. Saf. Meet.* 1974, Argonne, Illinois. Conf. 740 401-P2, p. 922.
- Henry, R. E., Fauske, H. K., and McUmber, L. M. (1976). Vapor explosions in sub-cooled freon. *Spec. Meet. Sodium-Fuel Interact. Fast React.*, 3rd, 1976, Tokyo, Japan.
- Henry, R. E., Hohmann, H., and Kottowski, H. (1979). The effect of pressure on NaCl-H₂O explosions. *Proc. CSNI Spec. Meet. Fuel-Coolant Interact. Nucl. Saf.*, 4th, 1979, Bournemouth, England.
- Hess, P. D., and Brondyke, K. J. (1969). Causes of molten aluminum-water explosions. *Met. Prog.* **95**(4), 93.
- Hess, P. D., Miller, R. E., Wahnsiedler, W. E., and Cochran, C. N. (1980). Molten aluminum/water explosions. In "Light Metals 1980" (C. McMinn, ed.), p. 837. (Proceedings of Technical Sessions Sponsored by TMS Light Metals Committee at 190th AIME Annual Meeting.)

- Higgins, H. M. (1955). "A Study of the Reaction of Metals and Water," AECD-3664. Aerojet-General Corp., Azusa, California.
- Holt, R. J., and Muenker, A. H. (1972). "Flameless Vapor Explosions in LNG-Water and Other Cryogen-Hot Liquid Systems," Reps. No. GRU.1GPR.72 and GRU.2GPR.72. Esso Res. Eng. Lab., Linden, New Jersey.
- Jazayeri, B. (1977). Impact cryogenic vapor explosions. S.M. Thesis, Chem. Eng., Massachusetts Institute of Technology, Cambridge.
- Katz, D. L. (1972). Superheat-limit explosions. *Chem. Eng. Prog.* **68**(5), 68.
- Katz, D. L., and Sliepcevich, C. M. (1971). LNG/water explosions. Cause and effects. *Hydrocarbon Process.* **50**(11), 240.
- Keevil, N. B. (1942). Vapor pressure of aqueous solutions at high temperatures. *J. Am. Chem. Soc.* **64**, 841.
- Koopman, R. P., Cederwall, R. T., Ermak, D. L., Goldwire, H. C., McClure, J. W., McRae, T. G., Morgan, D. L., Rodean, H. C., and Shinn, J. H. (1981). Description and analysis of BURRO series 40-m³ LNG spill experiments. *Lawrence Livermore Lab. [Rep.] UCRL UCRL-53186*.
- Krause, H. H., Simon, R., and Levy, A. (1973). "Smelt-Water Explosions," Final reports to Fourdrinier Kraft Board Institute, Inc. Battelle Laboratories, Columbus, Ohio.
- Lemmon, A. W. (1980). Explosions of molten aluminum and water. In "Light Metals 1980" (E. McMin, ed.), p. 817. (Proceedings of Technical Sessions Sponsored by TMS Light Metals Committee at 190th AIME Annual Meeting.)
- Lipsett, S. G. (1966). Explosions from molten metals and water. *Fire Technol.* **2**, 118.
- Long, G. (1957). Explosions of molten aluminum in water-cause and prevention. *Met. Prog.* **71**(5), 107.
- Lougher, E. H., Blue, G., Goddard, S., Gurev, H. S., Miller, J. F., Putnam, A. A., and Simon, R. (1968). "Feasibility Study on Smelt-Water Explosions," Summary report to Fourdrinier Kraft Board Institute, Inc. Battelle Memorial Institute, Columbus, Ohio.
- McFarlane, D. M. (1970). Explosions in basic oxygen furnace. I. *Trans. AIME, Open Hearth Proc.*, 1970 p. 88.
- Maischak, K.-D., and Feige, W. (1970). Sources and prevention of Al-H₂O explosions. *Neue Huette* **15**(11), 662.
- Miyazaki, K., and Henry, R. E. (1978). Effects of system pressure on the bubble growth from superheated water droplets. In "Topics in Two Phase Heat Transfer and Flow" (S. G. Bankoff, ed.). Am. Soc. Mech. Eng., New York.
- Modell, M., and Reid, R. C. (1982). "Thermodynamics and Its Applications," 2nd ed. Prentice-Hall, Englewood Cliffs, New Jersey.
- Moore, G. R. (1956). Vaporization of superheated drops in liquids. Ph.D. Thesis, University of Wisconsin, Madison.
- Moore, G. R. (1959). Vaporization of superheated drops in liquids. *AIChE J.* **5**, 458.
- Morey, G. W. (1957). The solubility of solids in gases. *Econ. Geol.* **52**, 227.
- Morey, G. W., and Chen, W. T. (1956). Pressure-temperature curves in some systems containing water and a salt. *J. Am. Chem. Soc.* **78**, 4249.
- Nakanishi, E., and Reid, R. C. (1971). Liquid natural gas-water reactions. *Chem. Eng. Prog.* **67**(12), 36.
- Nelson, H. W. (1971). Preventing physical explosion due to the interaction of liquid water and molten chemical compounds. U.S. Patent 3,615,175.
- Nelson, H. W. (1973). A new theory to explain physical explosions. *Tappi* **56**(3), 123.
- Nelson, H. W. (1978). Method of preventing explosions using a smelt water explosion inhibitor. U.S. Patent 4,106,978.

- Nelson, H. W., and Kennedy, E. H. (1956a). What causes Kraft dissolving tank explosions. *Pap. Trade J.* **140**(29), 50.
- Nelson, H. W., and Kennedy, E. H. (1956b). What causes Kraft dissolving tank explosions. *Pap. Trade J.* **140**(30), 30.
- Nelson, H. W., and Norton, C. L. (1969). Method of preventing smelt-water explosions. U.S. Patent 3,447,895.
- Nguyen, V. T. (1982). Shell Research Centre, Thorton, England.
- Ölander, A., and Liander, H. (1950). The phase diagram of sodium chloride and steam above the critical point. *Acta Chem. Scand.* **4**, 1437.
- Plesset, M. S., and Zwick, S. A. (1954). The growth of vapor bubbles in superheated liquids. *J. Appl. Phys.* **25**, 493.
- Porteous, W. M. (1975). Superheating and cryogenic vapor explosions. Ph.D. Thesis, Massachusetts Institute of Technology, Cambridge.
- Porteous, W. M., and Blander, M. (1975). Limits of superheat and explosive boiling of light hydrocarbons, halocarbons and hydrocarbon mixtures. *AIChE J.* **21**, 560.
- Porteous, W. M., and Reid, R. C. (1976). Light hydrocarbon vapor explosions. *Chem. Eng. Prog.* **72**(5), 83.
- Prosperetti, A., and Plesset, M. S. (1978). Vapour-bubble growth in a superheated liquid. *J. Fluid Mech.* **85**, 349.
- Rausch, A. H., and Levine, A. D. (1973). Rapid phase transformations caused by thermodynamic instability in cryogens. *Cryogenics* **13**(4), 224.
- Reid, R. C. (1976). Superheated liquids. *Am. Sci.* **64**, 146.
- Reid, R. C. (1978a). Superheated liquids: A laboratory curiosity and, possibly, an industrial curse. *Chem. Eng. Educ.* **12**(2), 60.
- Reid, R. C. (1978b). Superheated liquids: A laboratory curiosity and, possibly, an industrial curse. *Chem. Eng. Educ.* **12**(3), 108.
- Reid, R. C. (1978c). Superheated liquids: A laboratory curiosity and, possibly, an industrial curse. *Chem. Eng. Educ.* **12**(4), 194.
- Rogers, C. E., Markant, H. P., and Bluehosh, H. N. (1961). Interactions of smelt and water. *Tappi* **44**(2), 146.
- Sallack, J. A. (1955). An investigation of explosions in the soda smelt dissolving operation. *Pulp Pap. Mag. Can.* **56**(10), 114.
- Shick, P. E. (1980). Concentration-gradient trigger mechanism for smelt-water explosions. *Pap., Am. Pap. Inst. Annu. Recovery Boiler Comm. Meet., 1980, Chicago, Illinois.*
- Shick, P. E., and Grace, T. M. (1982). "Review of Smelt-Water Explosions," Proj. 3473-2. Inst. Pap. Chem., Appleton, Wisconsin.
- Skripov, V. P. (1974). "Metastable Liquids" (translated from the Russian by R. Kondor). Wiley, New York.
- Taylor, M. L., and Gardner, H. S. (1974). Causes of recovery boiler explosions. *Tappi* **57**(11), 76.
- Theofanous, T., Biasi, L., Isbin, H. S., and Fauske, H. (1969). A theoretical study on bubble growth in constant and time-dependent pressure fields. *Chem. Eng. Sci.* **24**, 885.
- Trefethen, L. (1957). Nucleation at a liquid-liquid interface. *J. Appl. Phys.* **28**, 923.
- Volmer, M., and Weber, A. (1926). Nucleus formation in supersaturated systems. *Z. Phys. Chem.* **119**, 277.
- Wakeshima, H., and Takata, K. (1958). On the limit of superheat. *J. Phys. Soc. Jpn.* **13**, 1398.
- Waldeck, W. F., Lynn, G., and Hill, A. E. (1932). Aqueous solubility of salts at high temperatures. I. Solubility of sodium carbonate from 50 to 348°. *J. Am. Chem. Soc.* **54**, 928.

- West, H. H., Hashemi, H. T., and Sliepcevich, C. M. (1972). LNG—Water explosions: A distributed source. *Pap., 27th Annu. Pet. Mech. Eng. Conf., New Orleans, Louisiana*.
- Witte, L. E., and Cox, J. E. (1972). Questions about LNG explosions. *Hydrocarbon Process.* **51**(3), 67.
- Wolff, L. R. (1970). Explosions in basic oxygen furnaces. III. *Trans. AIME, Open Hearth Proc.*, 1970 p. 94.
- Wright, R. W., and Humberstone, G. H. (1966). Dispersal and pressure generation by water impact upon molten aluminum. *Trans. Am. Nucl. Soc.* **9**, 305.
- Yang, K. (1973). LNG-superheat-limit explosion of LNG-organic liquid systems. *Nature (London)* **243**, 221.
- Yayanos, A. A. (1970). Equation of state for P-V isotherms of water and NaCl solutions. *J. Appl. Phys.* **41**, 2259.
- Zel'dovich, Ya. B. (1943). On the theory of new phase formation: Cavitation. *Acta Physicochim. URSS* **18**, 1.

ATMOSPHERIC DIFFUSION THEORY

John H. Seinfeld

Department of Chemical Engineering
California Institute of Technology
Pasadena, California

I.	Introduction	210
II.	Fundamental Equations of Turbulent Diffusion	212
III.	Mean Concentration from an Instantaneous Source in Stationary, Homogeneous Turbulence	218
	A. Lagrangian Approach	218
	B. Eulerian Approach	222
IV.	Mean Concentration from Continuous Sources	224
	A. Lagrangian Approach	224
	B. Eulerian Approach	230
	C. Summary of Continuous Point Source Solutions	233
V.	Point Source Diffusion Formulas Based on a Gaussian Distribution	233
	A. Lagrangian Approach	235
	B. Eulerian Approach	238
	C. Line and Area Source Solutions	243
	D. Fluctuating Plume Model	247
VI.	Validity of the Atmospheric Diffusion Equation.	250
VII.	Meteorological Parameters Characterizing the Atmospheric Boundary Layer.	253
	A. Estimation of the Monin-Obukhov Length.	255
	B. Estimation of Surface Roughness	256
	C. Determination of the Friction Velocity u_*	259
	D. The Convective Boundary Layer	260
VIII.	Dispersion Parameters in Gaussian Models.	261
	A. Spatial and Temporal Averaging	262
	B. Determination of σ_y and σ_z	265
	C. Dispersion Coefficients in Convective Conditions.	268
	D. Determination of $\overline{D_y^2}$ and $\overline{D_z^2}$	271
	E. Determination of $\overline{Y^2}$ and $\overline{Z^2}$	272
	F. Averaging Time Considerations.	273
IX.	Parameters in the Atmospheric Diffusion Equation	275
	A. Mean Wind Speed.	275
	B. Vertical Eddy Diffusion Coefficients	276
	C. Horizontal Eddy Diffusion Coefficient.	285
	D. Solutions of the Steady-State Atmospheric Diffusion Equation	286

X.	Monte Carlo Simulation of Turbulent Diffusion	288
A.	Elements of Monte Carlo Simulation of Turbulent Diffusion	288
B.	Application of the Monte Carlo Method to a Continuous, Elevated Line Source	291
XI.	Summary	294
	References	295

I. Introduction

A particularly serious environmental problem facing densely populated areas of the world is that of air pollution. The problem is both pervasive and difficult to control. An important element of a rational approach to improve the situation is a reliable means for evaluating the air quality impact of alternative control measures.

Whether the prediction scheme is a simple chart, a formula, or a complex numerical procedure, there are three basic elements that must be considered: meteorology, source emissions, and atmospheric chemical interactions. Despite the diversity of methodologies available for relating emissions to ambient air quality, there are two basic types of models. Those based on a fundamental description of the physics and chemistry occurring in the atmosphere are classified as *a priori* approaches. Such methods normally incorporate a mathematical treatment of the meteorological and chemical processes and, in addition, utilize information about the distribution of source emissions. Another class of methods involves the use of *a posteriori* models in which empirical relationships are deduced from laboratory or atmospheric measurements. These models are usually quite simple and typically bear a close relationship to the actual data upon which they are based. The latter feature is a basic weakness. Because the models do not explicitly quantify the causal phenomena, they cannot be reliably extrapolated beyond the bounds of the data from which they were derived. As a result, *a posteriori* models are not ideally suited to the task of predicting the impacts of substantial changes in emissions.

The various elements that must be linked as part of an *a priori* methodology for relating emissions to air quality are shown in Fig. 1, where the mathematical model provides a framework for integrating the following basic components.

(1) A kinetic mechanism describing the rates of atmospheric chemical reactions as a function of the concentrations of the various species present.

(2) A source description giving the temporal and spatial distributions of emissions from significant pollutant sources within the airshed.

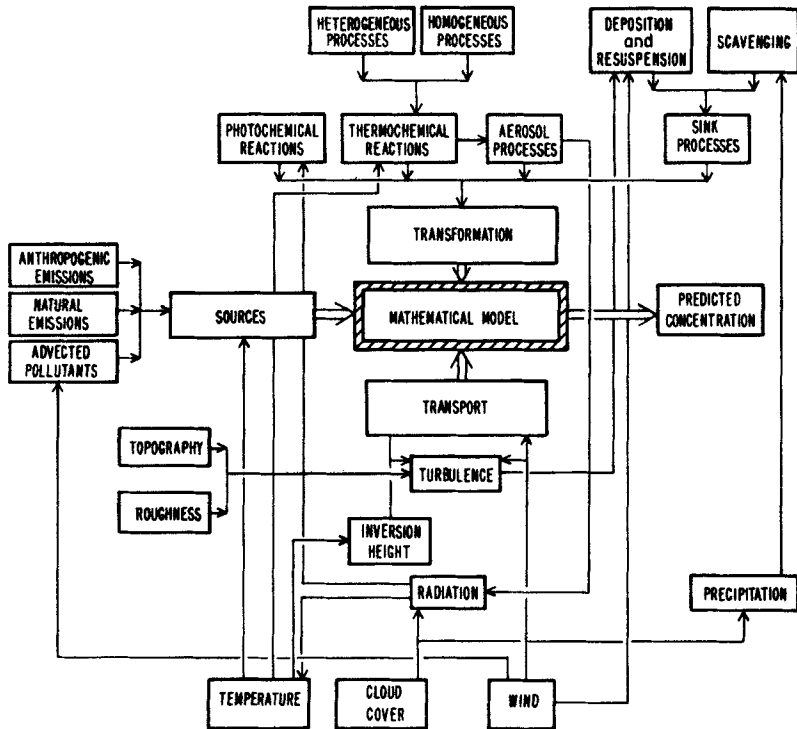


FIG. 1. Components of a mathematical model of air pollution.

(3) A meteorological description, including wind speed and direction at each location in the airshed as a function of time, vertical temperature structure, and radiation intensity.

The fundamental basis for virtually all *a priori* mathematical models of air pollution is the statement of conservation of mass for each pollutant species. The formulation of a mathematical model of air pollution involves a number of basic steps, the first of which is a detailed examination of the basis of the description of the diffusion of material released into the atmosphere. The second step requires that the form of interaction among the various physical and chemical processes be specified and tested against independent experiments. Once the appropriate mathematical descriptions have been formulated, it is necessary to implement suitable solution procedures. The final step is to assess the ability of the model to predict actual ambient concentration distributions.

The expression for the concentration of an emitted species is often referred to as an air quality model. Such an expression, or model, enables

a calculation of the concentration expected to result from a given material release under given meteorological conditions. Although there exists a large number of air quality models in the literature, virtually all are based on the few essential equations arising from atmospheric diffusion theory.

The theoretical foundation for understanding the diffusion of airborne matter was first laid by Taylor (1921) in his historic paper "Diffusion by Continuous Movements." Within the last 30 years or so, concern for environmental protection has heightened the interest in atmospheric diffusion theory to the point where there now exist hundreds of publications on the subject as well as several comprehensive treatises (Gifford, 1968; Monin and Yaglom, 1971; Csanady, 1973; Pasquill, 1974).

The object of this article is to present a concise development of the key elements of atmospheric diffusion theory leading to the formulas in common use for carrying out atmospheric diffusion calculations. The article is intended to be a unified treatment of the subject that introduces the principal ideas and shows many of the important derivations of atmospheric diffusion theory. An attempt has not been made to provide a comprehensive, evaluative literature review of current work in atmospheric diffusion theory, although we will have occasion to refer to much of the recent literature. One purpose of this article is to present usable formulas for performing atmospheric diffusion calculations. In doing so, we have not endeavored to survey in a detailed way the experiences of others gained in use of the formulas. A relatively thorough list of recent references is provided for the reader who desires to pursue the subject further.

II. Fundamental Equations of Turbulent Diffusion

The basis of the description of turbulent diffusion is the species conservation equation (Bird *et al.*, 1960):

$$\partial c_i / \partial t + \mathbf{u} \cdot \nabla c_i = D_i \nabla^2 c_i + R_i + S_i \quad (2.1)$$

where c_i is the molar concentration of species i in air, \mathbf{u} is the fluid (air) velocity vector ($\mathbf{u} = [u, v, w]$), D_i is the molecular diffusivity of species i in air, $R_i = R_i(c_1, c_2, \dots, c_n, T)$ is the rate of formation of i by chemical reactions, a function in general of all n species concentrations and the temperature T , and $S_i = S_i(x, y, z, t)$ is the rate of introduction of i from sources in the fluid.¹ R_i may also be a function of solar radiation intensity.

¹ Sources of material also enter the mathematical description as boundary conditions. It is convenient to use S_i to represent sources as occurring within the fluid, the most notable case being point sources.

We will generally not be concerned here with chemical reactions, so the R_i term can be omitted, in which case the subscript i denoting species is no longer required.² In addition, for the turbulent flows of interest the molecular diffusion term in Eq. (2.1) may be neglected. [Although for the spatial scales of interest to us the molecular diffusion term may be neglected, molecular and turbulent diffusion are not independent, linearly additive, physical processes (Saffman, 1960).] As a result of the above two simplifications, Eq. (2.1) becomes

$$\partial c / \partial t + \mathbf{u} \cdot \nabla c = S \quad (2.2)$$

Equation (2.2) can be considered as the fundamental governing equation for the concentration of an inert constituent in a turbulent flow. Because the flow in the atmosphere is turbulent, the velocity vector \mathbf{u} is a random function of location and time. Consequently, the concentration c is also a random function of location and time. Thus, the dispersion of a pollutant (or tracer) in the atmosphere essentially involves the propagation of the species molecules through a random medium. Even if the strength and spatial distribution of the source S are assumed to be known precisely, the concentration of tracer resulting from that source is a random quantity. The instantaneous, random concentration, $c(x, y, z, t)$, of an inert tracer in a turbulent fluid with random velocity field $\mathbf{u}(x, y, z, t)$ resulting from a source distribution $S(x, y, z, t)$ is described by Eq. (2.2).

The solution of Eq. (2.2) can be expressed as³

$$c(x, y, z, t) = \int_{-\infty}^{\infty} \int_{-\infty}^{\infty} \int_{-\infty}^{\infty} \int_0^t G(x, y, z, t | x', y', z', t') \\ \times S(x', y', z', t') dt' dx' dy' dz' \quad (2.3)$$

where G is termed a stochastic Green's function (Adomian, 1963) because it serves to convert a deterministic "input" $S(x, y, z, t)$ into a stochastic "output" $c(x, y, z, t)$. G is, in fact, the concentration at (x, y, z) at time t that results from an instantaneous point source of unit strength at (x', y', z') at time t' for one "experiment."⁴ The stochastic nature of the turbulent field is embodied in G , that is, given knowledge of the random velocity field, the equation governing G (Morse and Feshbach, 1953; Özisik, 1980):

$$\partial G / \partial t + \mathbf{u} \cdot \nabla G = \delta(x - x') \delta(y - y') \delta(z - z') \delta(t - t') \quad (2.4)$$

can be solved to give one realization of the tracer "experiment."

² Although atmospheric chemical reactions are a subject of great interest and importance, they are not discussed in this article.

³ This solution applies for zero initial concentration.

⁴ In order for Eq. (2.3) to be dimensionally consistent, G must have units of $[\text{length}]^{-3}$.

What is really desired, of course, is not the random concentration resulting from one realization of the flow, but the expected (mean) value resulting from an entire ensemble of flows with identical macroscopic conditions. Letting $\langle c(x, y, z, t) \rangle = E\{c(x, y, z, t)\}$ and then taking the expected value of Eq. (2.3) leads to

$$\begin{aligned} \langle c(x, y, z, t) \rangle = & \int_{-\infty}^{\infty} \int_{-\infty}^{\infty} \int_{-\infty}^{\infty} \int_0^t E\{G(x, y, z, t|x', y', z', t')\} \\ & \times S(x', y', z', t') dt' dx' dy' dz' \end{aligned} \quad (2.5)$$

(Specifying S as a deterministic function implies that the inevitable randomness in S is negligible when compared to the mean emission rate and to the effect of the randomness of the turbulent field on c .)

Equation (2.5) can be interpreted physically as follows. $E\{G\}$ is just the probability density p that a particle released at location (x', y', z') at time t' will be at location (x, y, z) at time t , the transition probability density,

$$p(x, y, z, t|x', y', z', t') = E\{G(x, y, z, t|x', y', z', t')\} \quad (2.6)$$

so that Eq. (2.5) can be expressed in terms of p ,

$$\begin{aligned} \langle c(x, y, z, t) \rangle = & \int_{-\infty}^{\infty} \int_{-\infty}^{\infty} \int_{-\infty}^{\infty} \int_0^t p(x, y, z, t|x', y', z', t') \\ & \times S(x', y', z', t') dt' dx' dy' dz' \end{aligned} \quad (2.7)$$

Equation (2.7) is sometimes taken as the starting point for the so-called *Lagrangian* description of turbulent diffusion. In the Lagrangian description the concentration is related not to the velocity at a fixed point, i.e., $\mathbf{u}(x, y, z, t)$, but to the velocity of particles that move with the fluid. Thus, the probability density function p expresses the probability that a particle released at (x', y', z') at time t' will arrive at (x, y, z) at time t . Equation (2.1) is a *Eulerian* description because it gives c at a fixed point in space as a function of the local values of the velocity vector \mathbf{u} . The interpretation of p as the expected value of the stochastic Green's function, $E\{G\}$, provides a connection between the Eulerian and Lagrangian descriptions. In the Lagrangian approach Eq. (2.7) is usually taken as the starting point, where p is to be specified.

Statistical properties of c other than the mean can be obtained from Eq. (2.3). For example, the cross-correlation between the concentrations at two different locations and times,

$$R(x_1, y_1, z_1, x_2, y_2, z_2, t_1, t_2) = E\{c(x_1, y_1, z_1, t_1)c(x_2, y_2, z_2, t_2)\} \quad (2.8)$$

can be determined from

$$\begin{aligned}
 & R(x_1, y_1, z_1, x_2, y_2, z_2, t_1, t_2) \\
 &= \int_{-\infty}^{\infty} \cdots \int_{-\infty}^{\infty} \int_0^{t_1} \int_0^{t_2} E\{G(x_1, y_1, z_1, t_1 | x', y', z', t') \\
 &\quad \times G(x_2, y_2, z_2, t_2 | x'', y'', z'', t'')\} \\
 &\quad \times S(x', y', z', t') S(x'', y'', z'', t'') dt'' dt' dx'' \cdots dz' \quad (2.9)
 \end{aligned}$$

The autocorrelation of the concentration at the same point at different times is obtained from Eq. (2.9) by setting $x_1 = x_2$, $y_1 = y_2$, and $z_1 = z_2$, and the mean square concentration is obtained from Eq. (2.9) by setting $t_1 = t_2$ in addition to $x_1 = x_2$, $y_1 = y_2$, and $z_1 = z_2$. Thus, the mean square concentration is given by

$$\begin{aligned}
 E\{c(x, y, z, t)^2\} &= \int_{-\infty}^{\infty} \cdots \int_{-\infty}^{\infty} \int_0^t \int_0^t E\{G(x, y, z, t | x', y', z', t') \\
 &\quad \times G(x, y, z, t | x'', y'', z'', t'')\} \\
 &\quad \times S(x', y', z', t') S(x'', y'', z'', t'') dt'' dt' dx'' \cdots dz' \quad (2.10)
 \end{aligned}$$

The variance of the concentration distribution is

$$\text{Var}\{c(x, y, z, t)\} = E\{c(x, y, z, t)^2\} - E\{c(x, y, z, t)\}^2 \quad (2.11)$$

Of the various statistical properties of the concentration other than the mean, the variance is of the most interest.

Let us return for the moment to Eq. (2.2). In atmospheric problems it is impossible to solve the equations of motion analytically. Under these conditions information about the instantaneous velocity field \mathbf{u} is available only from direct measurements or from numerical simulations of the fluid flow. In either case we are confronted with the problem of reconstructing the complete, continuous velocity field from observations at discrete points in space, namely the measuring sites or the grid points of the numerical model. The sampling theorem tells us that from a set of discrete values, only those features of the field with scales larger than the discretization interval can be reproduced in their entirety (Papoulis, 1965). Therefore, we decompose the wind velocity in the form

$$\mathbf{u}(x, y, z, t) = \bar{\mathbf{u}}(x, y, z, t) + \mathbf{u}'(x, y, z, t) \quad (2.12)$$

where $\bar{\mathbf{u}}$ represents the large, explicitly resolvable portion of the flow and \mathbf{u}' represents all of the remaining (unresolvable) components.

Because the velocity \mathbf{u} contains the random component \mathbf{u}' , the concentration c is a stochastic function since, by virtue of Eq. (2.2), c is a function of \mathbf{u}' . The mean value of c , as expressed in Eq. (2.5), is an *ensemble* mean formed by averaging c over the entire ensemble of identical experiments. Temporal and spatial mean values, by contrast, are obtained by averaging values from a single member of the ensemble over a period or area, respectively. The ensemble mean, which we have denoted by the angle brackets $\langle \rangle$, is the easiest to deal with mathematically. Unfortunately, ensemble means are not measurable quantities, although under the conditions of the ergodic theorem they can be related to observable temporal or spatial averages. In Eq. (2.7) the mean concentration $\langle c \rangle$ represents a true ensemble mean, whereas if we decompose c as

$$c(x, y, z, t) = \bar{c}(x, y, z, t) + c'(x, y, z, t) \quad (2.13)$$

to correspond with the velocity field decomposition (2.12), then \bar{c} is the mean value that corresponds to the particular velocity field decomposition (2.12). If $\bar{\mathbf{u}}$ is obtained, theoretically at least, from an ensemble average of \mathbf{u} , then \bar{c} can be viewed as the ensemble average $\langle c \rangle$. Even though $\bar{\mathbf{u}}$ is, of course, not obtained from an ensemble-averaging procedure, we will take this viewpoint since we want to compare Eq. (2.7) with the equation for \bar{c} that results from Eqs. (2.2), (2.12), and (2.13). Henceforth, therefore, we will use the overbar to denote the mean value.

If we substitute Eqs. (2.12) and (2.13) into Eq. (2.2) and perform the averaging operation indicated by the overbar, using the equation of continuity for an incompressible fluid,

$$\nabla \cdot \mathbf{u} = 0 \quad (2.14)$$

and $\overline{\mathbf{u}'} = \overline{c'} = 0$, we obtain

$$\partial \bar{c} / \partial t + \bar{\mathbf{u}} \cdot \nabla \bar{c} + \nabla \cdot \overline{\mathbf{u}'c'} = S \quad (2.15)$$

Equation (2.15) governs the mean concentration when the decompositions (2.12) and (2.13) are used. If the variables $\overline{\mathbf{u}'c'}$ are known functions of space and time, then Eq. (2.15) can, in principle, be solved to yield \bar{c} . Unfortunately, the $\overline{\mathbf{u}'c'}$ cannot be measured at all points in an atmospheric flow and, in addition, cannot be exactly predicted because of the classic closure problem of turbulent flow. A great deal of research effort has been directed at attempts to resolve this problem. The most well-known method of approximating the fluctuating transport term $\overline{\mathbf{u}'c'}$ is the so-called *mixing length, gradient transport, or K-theory hypothesis*. With this approach, the transport is based on an analogy to molecular diffusion in which the flux is assumed to be proportional to the mean gradients, that is,

$$\overline{\mathbf{u}'c'} = -\mathbf{K} \cdot \nabla \bar{c} \quad (2.16)$$

where the so-called eddy diffusivity \mathbf{K} is the following second-order tensor:

$$\mathbf{K} = \begin{bmatrix} K_{xx} & K_{xy} & K_{xz} \\ K_{yx} & K_{yy} & K_{yz} \\ K_{zx} & K_{zy} & K_{zz} \end{bmatrix} \quad (2.17)$$

Upon using (2.16) in Eq. (2.15), we obtain

$$\partial \bar{c} / \partial t + \bar{\mathbf{u}} \cdot \nabla \bar{c} = \nabla \cdot \{\mathbf{K} \cdot \nabla \bar{c}\} + S \quad (2.18)$$

to so-called *atmospheric diffusion equation*. Ordinarily only the diagonal elements of \mathbf{K} are retained, so that Eq. (2.18) becomes⁵

$$\begin{aligned} \frac{\partial \bar{c}}{\partial t} + \bar{u} \frac{\partial \bar{c}}{\partial x} + \bar{v} \frac{\partial \bar{c}}{\partial y} + \bar{w} \frac{\partial \bar{c}}{\partial z} \\ = \frac{\partial}{\partial x} \left(K_{xx} \frac{\partial \bar{c}}{\partial x} \right) + \frac{\partial}{\partial y} \left(K_{yy} \frac{\partial \bar{c}}{\partial y} \right) + \frac{\partial}{\partial z} \left(K_{zz} \frac{\partial \bar{c}}{\partial z} \right) + S \end{aligned} \quad (2.19)$$

We delay a discussion of the nature and determination of the elements of \mathbf{K} until later.

Considering the almost universal use of Eq. (2.16) as a closure approximation, it is important to outline some of its limitations. Monin and Yaglom (1971), Corrsin (1974), and Seinfeld (1975) have identified some conditions which are necessary for the valid use of a gradient transport hypothesis. In short, a basic requirement is that the transport mechanism length scale must be much smaller than the distance over which the mean transported field gradient changes appreciably. Similar conditions apply to the temporal scales. A more fundamental difficulty occurs when the flows are buoyancy driven. In this situation, particularly for free convection, the fluxes $\overline{\mathbf{u}'c'}$ are no longer described by the local gradient.

In an attempt to circumvent some of these problems, considerable effort has been expended to develop so-called second moment turbulent closure models in which the governing equations are closed by including terms parameterizing various turbulent correlations (see, for example, Lewellen *et al.*, 1974; Wyngaard and Cote, 1974; Lumley and Khajeh-Nouri, 1974; Mellor and Yamada, 1974; Yamada and Mellor, 1975; Zeman and Lumley, 1976, 1979; Zeman and Tennekes, 1977; Freeman, 1977; Yamada, 1977; Manton, 1979; Binkowski, 1979). While second-order closure models are conceptually very appealing, their use in atmospheric

⁵ For a discussion of the off-diagonal terms of \mathbf{K} , see Corrsin (1974).

diffusion calculations often requires very burdensome computations because of the additional equations that must be solved beyond those for the mean quantities. In spite of the increased rigor of second-order closure models, there remains a need for a computationally tractable approach that produces results consistent with the known behavior of pollutants in the planetary boundary layer. The approach adopted in this article is to focus on the use of the eddy diffusion concept and to develop the components of \mathbf{K} using modern atmospheric boundary layer theory.

We have now derived two fundamentally different expressions for the mean concentration of an inert tracer in a turbulent flow: Eqs. (2.7) and (2.19). To compute the mean concentration \bar{c} from Eq. (2.7) requires only that $p(x, y, z, t|x', y', z', t')$, the transition probability density, be specified, whereas the mean velocities and eddy diffusivities must be prescribed to obtain \bar{c} from Eq. (2.19). In the next section we see how forms of \bar{c} are obtained from Eqs. (2.7) and (2.19).

III. Mean Concentration from an Instantaneous Source in Stationary, Homogeneous Turbulence

A. LAGRANGIAN APPROACH

The Lagrangian approach to turbulent diffusion is embodied in Eq. (2.7),

$$\begin{aligned} \bar{c}(x, y, z, t) = & \int_{-\infty}^{\infty} \int_{-\infty}^{\infty} \int_{-\infty}^{\infty} \int_0^t p(x, y, z, t|x', y', z', t') \\ & \times S(x', y', z', t') dt' dx' dy' dz' \end{aligned} \quad (3.1)$$

The key problem in using Eq. (3.1) is the specification of p . We ask whether we can derive an expression for p . The velocity components u , v , and w , although random, are related through conservation of mass and momentum for the flow, that is, they are governed by the stochastic Navier-Stokes and continuity equations. In general, as we have noted, an exact solution for u , v , and w is unobtainable. We can, however, consider an idealized situation in which the statistical properties of u , v , and w are specified *a priori*. Then, in so doing, we wish to see if we can obtain an exact solution of Eq. (2.4) from which p can be obtained through Eq. (2.6).

We seek therefore to evaluate p through its relationship as the expected value of the stochastic Green's function G . To do so requires that we make appropriate assumptions that allows us to solve Eq. (2.2). Our basic assumption is that the turbulence is stationary and homogeneous, and

therefore that the statistical properties of u , v , and w are independent of time and position. The stationarity assumption implies that if the mean velocities are changing, they do so on a temporal scale that is long compared to that associated with the concentration dynamics.

In the terminology of stochastic processes, a process $u(t)$ is stationary in the *strict sense* if the marginal distributions of $u(t_1)$, $u(t_2)$, ... are identical, the joint distribution of $u(t_1)$ and $u(t_2)$ depends only on $t_2 - t_1$, and the joint distribution of $u(t_1)$, $u(t_2)$, $u(t_3)$ depends only on $t_3 - t_2$, $t_2 - t_1$, etc. The process $u(t)$ is stationary in the *wide sense* if $E\{u(t)\}$ is constant and $E\{u(t_1)u(t_2)\}$ depends only on $t_2 - t_1$. Now, for a wide sense Markovian process, the distribution of $u(t)$ given $u(t_1)$ does not depend on $u(t_2)$. Thus, the partial correlation coefficient of $u(t)$ and $u(t_2)$ given $u(t_1)$ is zero (Papoulis, 1965). For a Gaussian process this correlation coefficient is given by (Cramer, 1946, p. 306)

$$\rho^* = \frac{\rho[u(t), u(t_2)] - \rho[u(t), u(t_1)]\rho[u(t_2), u(t_1)]}{\{1 - \rho^2[u(t), u(t_1)]\}^{1/2}\{1 - \rho^2[u(t_2), u(t_1)]\}^{1/2}}$$

The numerator for a stationary process is $\rho(t - t_2) - \rho(t - t_1)\rho(t_1 - t_2)$, which is zero if and only if $\rho(\alpha_1 + \alpha_2) = \rho(\alpha_1)\rho(\alpha_2)$, that is, if and only if ρ is an exponential function. For a stationary process $\rho(\tau) = \rho(-\tau)$ and thus $\rho(t_1 - t_2) = \exp(-\beta|t_1 - t_2|)$. In all cases of physical interest $\beta > 0$, so that $\rho < \infty$ for $|t_1 - t_2| \rightarrow \infty$.

The mean velocity components are expressed as \bar{u} , \bar{v} , and \bar{w} . We assume that the velocity components are stationary Gaussian random processes, so that, based on the preceding discussion, the autocovariances of u , v , and w can be written as (Papoulis, 1965, p. 397)

$$\begin{aligned} E\{[u(t_1) - \bar{u}][u(t_2) - \bar{u}]\} &= \sigma_u^2 \exp(-\beta|t_1 - t_2|) \\ E\{[v(t_1) - \bar{v}][v(t_2) - \bar{v}]\} &= \sigma_v^2 \exp(-\beta|t_1 - t_2|) \\ E\{[w(t_1) - \bar{w}][w(t_2) - \bar{w}]\} &= \sigma_w^2 \exp(-\beta|t_1 - t_2|) \end{aligned} \quad (3.2)$$

Let us now consider the solution of Eq. (2.2) for a time-varying point source located at the origin, that is, $S(x, y, z, t) = S(t)\delta(x)\delta(y)\delta(z)$. The solution is

$$c(x, y, z, t) = \int_0^t S(\tau)\delta[x - B_x(t, \tau)]\delta[y - B_y(t, \tau)]\delta[z - B_z(t, \tau)] d\tau \quad (3.3)$$

where

$$B_x(t, \tau) = \int_\tau^t u(\theta) d\theta, \quad B_y(t, \tau) = \int_\tau^t v(\theta) d\theta, \quad B_z(t, \tau) = \int_\tau^t w(\theta) d\theta \quad (3.4)$$

The stochastic Green's function G is identified from Eq. (3.3) as

$$G(x, y, z, t|0, 0, 0, t') = \delta[x - B_x(t, t')] \\ \times \delta[y - B_y(t, t')]\delta[z - B_z(t, t')] \quad (3.5)$$

The mean of c is given by Eq. (2.5)

$$E\{c(x, y, z, t)\} = \int_0^t E\{\delta[x - B_x(t, \tau)]\delta[y - B_y(t, \tau)] \\ \times \delta[z - B_z(t, \tau)]S(\tau) d\tau \quad (3.6)$$

We define the joint probability density function (pdf) of B_x , B_y , and B_z as $f(b_x, b_y, b_z; t, \tau)$. Then Eq. (3.6) can be expressed as

$$E\{c(x, y, z, t)\} = \int_0^t S(\tau) \int_{-\infty}^{\infty} \int_{-\infty}^{\infty} \int_{-\infty}^{\infty} \\ \times \delta[x - b_x(t, \tau)]\delta[y - b_y(t, \tau)]\delta[z - b_z(t, \tau)] \\ \times f(b_x, b_y, b_z; t, \tau) db_x db_y db_z d\tau \\ = \int_0^t S(\tau)f(x, y, z; t, \tau) d\tau \quad (3.7)$$

The mean square concentration is given by Eq. (2.10), which can be rewritten as

$$E\{c(x, y, z, t)^2\} = \int_0^t \int_0^t E\{\delta[x - b_x(t, t')]\delta[y - b_y(t, t')]\delta[z - b_z(t, t')] \\ \times \delta[x - b_x(t, t'')]\delta[y - b_y(t, t'')]\delta[z - b_z(t, t'')] \\ \times S(t')S(t'') dt' dt'' \quad (3.8)$$

Let us define the joint pdf $g(b_x, b_y, b_z, b'_x, b'_y, b'_z; t, t', t'')$ such that $g db_x db_y db_z db'_x db'_y db'_z$ is the probability that $b_x \leq B_x(t, t') \leq b_x + db_x, \dots, b'_z < B_z(t, t'') \leq b'_z + db'_z$. Then, Eq. (3.8) can be written as

$$E\{c(x, y, z, t)^2\} = \int_0^t \int_0^t g(x, y, z, x, y, z; t, t', t'') \\ \times S(t')S(t'') dt' dt'' \quad (3.9)$$

Since u , v , and w are Gaussian random processes, it can be shown that B_x , B_y , and B_z are also Gaussian processes. If b_x , b_y , and b_z are independent,

$$f(b_x, b_y, b_z; t, \tau) = f_x(b_x; t, \tau)f_y(b_y; t, \tau)f_z(b_z; t, \tau)$$

where for f_x , for example,

$$f_x(b_x; t, \tau) = \frac{1}{(2\pi\sigma_x^2)^{1/2}} \exp\left[-\frac{(b_x - \bar{B}_x)^2}{2\sigma_x^2}\right] \quad (3.10)$$

where \bar{B}_x and σ_x are the mean and standard deviation of $B_x(t, \tau)$.

From the definition (3.4), we see that

$$\bar{B}_x = E\{B_x(t, \tau)\} = E\left\{\int_{\tau}^t u(\theta) d\theta\right\} = \bar{u}(t - \tau) \quad (3.11)$$

and similarly that $\bar{B}_y = \bar{v}(t - \tau)$ and $\bar{B}_z = \bar{w}(t - \tau)$.

The variance $\sigma_x^2(t, \tau)$ of $B_x(t, \tau)$ can be computed from its definition

$$\sigma_x^2(t, \tau) = E\{[B_x(t, \tau) - \bar{B}_x]^2\} = E\{B_x(t, \tau)^2\} - \bar{B}_x^2 \quad (3.12)$$

Consider the first term on the right-hand side of Eq. (3.12):

$$\begin{aligned} E\{B_x(t, \tau)^2\} &= E\left\{\int_{\tau}^t u(\theta) d\theta \int_{\tau}^t u(\theta) d\theta\right\} \\ &= E\left\{\int_{\tau}^t \int_{\tau}^t u(\theta)u(\lambda) d\theta d\lambda\right\} = \int_{\tau}^t \int_{\tau}^t E\{u(\theta)u(\lambda)\} d\theta d\lambda \end{aligned} \quad (3.13)$$

Using Eqs. (3.2), (3.11), (3.12), and (3.13), we obtain

$$\sigma_x^2(t, \tau) = \sigma_x^2(t - \tau) = (2\sigma_u^2/\beta^2)[\beta(t - \tau) + e^{-\beta(t-\tau)} - 1] \quad (3.14)$$

The mean value of $c(x, y, z, t)$ is given by Eq. (3.7) in conjunction with Eqs. (3.10), (3.11), and (3.14). For a pulse input of strength Q at the origin at $t = 0$, $S(t) = Q\delta(t)$, and the mean concentration is given by

$$\begin{aligned} \bar{c}(x, y, z, t) &= \frac{Q}{(2\pi)^{3/2}\sigma_x(t)\sigma_y(t)\sigma_z(t)} \\ &\times \exp\left[-\frac{(x - \bar{u}t)^2}{2\sigma_x^2(t)} - \frac{(y - \bar{v}t)^2}{2\sigma_y^2(t)} - \frac{(z - \bar{w}t)^2}{2\sigma_z^2(t)}\right] \end{aligned} \quad (3.15)$$

where σ_x , σ_y , and σ_z are given by Eq. (3.14) and its analogs for σ_y and σ_z .

Summarizing, we have demonstrated that the mean concentration of a tracer released in a velocity field where the three components are Gaussian random processes has a spatial distribution that is Gaussian with variances that increase with time according to Eq. (3.14). This is an important result. The mean concentration distribution is completely specified from the mean velocities \bar{u} , \bar{v} , and \bar{w} , the variances of the velocities σ_u^2 , σ_v^2 , and σ_w^2 , and the characteristic decay time β^{-1} .

Let us examine the limits of Eq. (3.14) for large and small t for $\tau = 0$. For $t \gg \beta^{-1}$, Eq. (3.14) reduces to

$$\sigma_x^2 = 2\sigma_u^2 t/\beta \quad (3.16)$$

For $t \ll \beta^{-1}$, $\exp(-\beta t) \cong 1 - \beta t + (\beta t)^2/2$ and

$$\sigma_x^2 = \sigma_u^2 t^2 \quad (3.17)$$

Thus, we find that

$$\sigma_x^2 \sim \begin{cases} t^2 & \text{for small } t \\ t & \text{for large } t \end{cases}$$

We point out that the variances of B_x , B_y , and B_z are also the variances of the concentration distribution in the three coordinate directions. This result is physically plausible since B_x represents the random distance that a fluid particle travels in the x direction between times τ and t , and this distance is precisely that which a tracer molecule travels. Consequently, the variance of B_x is equivalent to the x -direction variance of the concentration distribution.

B. EULERIAN APPROACH

The Eulerian approach to turbulent diffusion was shown to lead to the atmospheric diffusion equation (2.19):

$$\begin{aligned} \frac{\partial \bar{c}}{\partial t} + \bar{u} \frac{\partial \bar{c}}{\partial x} + \bar{v} \frac{\partial \bar{c}}{\partial y} + \bar{w} \frac{\partial \bar{c}}{\partial z} \\ = \frac{\partial}{\partial x} \left(K_{xx} \frac{\partial \bar{c}}{\partial x} \right) + \frac{\partial}{\partial y} \left(K_{yy} \frac{\partial \bar{c}}{\partial y} \right) + \frac{\partial}{\partial z} \left(K_{zz} \frac{\partial \bar{c}}{\partial z} \right) + S \end{aligned} \quad (2.19)$$

As noted in Section II, the eddy diffusivities K_{xx} , K_{yy} , and K_{zz} embody the information concerning turbulent diffusion. To the extent that the solution of (2.19) can be represented as

$$\begin{aligned} \bar{c}(x, y, z, t) = \iiint \int_0^t \bar{G}(x, y, z, t|x', y', z', t') \\ \times S(x', y', z', t') dt' dx' dy' dz' \end{aligned} \quad (3.18)$$

the Eulerian and Lagrangian approaches can be compared directly.

Let us consider, as we did in the previous section, an instantaneous point source of strength Q at the origin in an infinite fluid with a velocity \bar{u} in the x direction. The mean concentration in the case of constant K_{xx} , K_{yy} , and K_{zz} is governed by

$$\frac{\partial \bar{c}}{\partial t} + \bar{u} \frac{\partial \bar{c}}{\partial x} = K_{xx} \frac{\partial^2 \bar{c}}{\partial x^2} + K_{yy} \frac{\partial^2 \bar{c}}{\partial y^2} + K_{zz} \frac{\partial^2 \bar{c}}{\partial z^2} \quad (3.19)$$

$$\bar{c}(x, y, z, 0) = Q\delta(x)\delta(y)\delta(z) \quad (3.20)$$

$$\bar{c}(x, y, z, t) = 0, \quad x, y, z \rightarrow \pm\infty \quad (3.21)$$

Let

$$\bar{c}(x, y, z, t) = c_1(x, t)c_2(y, t)c_3(z, t)$$

with $c_1(x, 0) = Q^{1/3}\delta(x)$, $c_2(y, 0) = Q^{1/3}\delta(y)$, and $c_3(z, 0) = Q^{1/3}\delta(z)$. Then we have

$$\frac{\partial c_1}{\partial t} + \bar{u} \frac{\partial c_1}{\partial x} = K_{xx} \frac{\partial^2 c_1}{\partial x^2}, \quad \frac{\partial c_2}{\partial t} = K_{yy} \frac{\partial^2 c_2}{\partial y^2}, \quad \frac{\partial c_3}{\partial t} = K_{zz} \frac{\partial^2 c_3}{\partial z^2} \quad (3.22)$$

Each of these equations may be solved by the Fourier transform. We illustrate with the equation for c_1 . The Fourier transform of $c_1(x, t)$ is

$$C(\alpha, t) = F\{c_1(x, t)\} = (2\pi)^{-1/2} \int_{-\infty}^{\infty} c_1(x, t) e^{-i\alpha x} dx$$

and thus transforming, we obtain

$$\partial C / \partial t + i\alpha \bar{u} C = -\alpha^2 K_{xx} C, \quad C(\alpha, 0) = Q^{1/3} (2\pi)^{-1/2} \quad (3.23)$$

The solution of Eqs. (3.23) is

$$C(\alpha, t) = Q^{1/3} (2\pi)^{-1/2} \exp[-(\alpha^2 K_{xx} + i\alpha \bar{u})t]$$

The inverse transform is

$$c_1(x, t) = (2\pi)^{-1/2} \int_{-\infty}^{\infty} C(\alpha, t) e^{i\alpha x} d\alpha$$

Thus,

$$c_1(x, t) = \frac{Q^{1/3}}{2\pi} \int_{-\infty}^{\infty} \exp\{-[\alpha^2 K_{xx} t - i\alpha(x - \bar{u}t)]\} d\alpha$$

Completing the square in the exponent,

$$\begin{aligned} & \alpha^2 K_{xx} t - i\alpha(x - \bar{u}t) - \frac{(x - \bar{u}t)^2}{4K_{xx}t} + \frac{(x - \bar{u}t)^2}{4K_{xx}t} \\ &= \left[\alpha(K_{xx}t)^{1/2} - \frac{i(x - \bar{u}t)}{2(K_{xx}t)^{1/2}} \right]^2 - \frac{(x - \bar{u}t)^2}{4K_{xx}t} \end{aligned}$$

Let $\eta = \alpha(K_{xx}t)^{1/2} - i(x - \bar{u}t)/2(K_{xx}t)^{1/2}$ and $d\eta = (K_{xx}t)^{1/2} d\alpha$. Then

$$c_1(x, t) = \frac{Q^{1/3}}{2\pi(K_{xx}t)^{1/2}} \exp\left[-\frac{(x - \bar{u}t)^2}{4K_{xx}t}\right] \int_{-\infty}^{\infty} e^{-\eta^2} d\eta$$

The integral equals $\sqrt{\pi}$, so

$$c_1(x, t) = \frac{Q^{1/3}}{2(\pi K_{xx}t)^{1/2}} \exp\left[-\frac{(x - \bar{u}t)^2}{4K_{xx}t}\right] \quad (3.24)$$

By the same method

$$c_2(y, t) = \frac{Q^{1/3}}{2(\pi K_{yy}t)^{1/2}} e^{-y^2/4K_{yy}t} \quad (3.25)$$

$$c_3(z, t) = \frac{Q^{1/3}}{2(\pi K_{zz}t)^{1/2}} e^{-z^2/4K_{zz}t} \quad (3.26)$$

and thus

$$\begin{aligned} \bar{c}(x, y, z, t) &= \frac{Q}{8(\pi t)^{3/2}(K_{xx}K_{yy}K_{zz})^{1/2}} \\ &\times \exp\left[-\frac{(x - \bar{u}t)^2}{4K_{xx}t} - \frac{y^2}{4K_{yy}t} - \frac{z^2}{4K_{zz}t}\right] \end{aligned} \quad (3.27)$$

We note the similarity of Eqs. (3.27) and (3.15). In particular, if we define $\sigma_x^2 = 2K_{xx}t$, $\sigma_y^2 = 2K_{yy}t$, and $\sigma_z^2 = 2K_{zz}t$, the two expressions are identical when $\bar{v} = \bar{w} = 0$. Thus, we see that the mean concentration from an instantaneous point source in an infinite fluid with stationary, homogeneous turbulence has a Gaussian form, with the variances of the concentration distribution related to the variances of the wind velocity fluctuations or to constant eddy diffusivities.

IV. Mean Concentration from Continuous Sources

Solutions were obtained in Section III for the mean concentration resulting from an instantaneous release of a quantity Q of material at the origin in an infinite fluid with stationary, homogeneous turbulence and a mean velocity \bar{u} in the x direction. We now wish to consider the case of a continuously emitting source under the same conditions. The source strength is specified as q (g sec⁻¹).

A. LAGRANGIAN APPROACH

A continuous source is viewed conceptually as one that began emitting at $t = 0$ and continues as $t \rightarrow \infty$. The mean concentration achieves a

steady state, independent of time, and $S(x, y, z, t) = q\delta(x)\delta(y)\delta(z)$. Thus, Eq. (3.1) can be written as

$$\bar{c}(x, y, z, t) = \int_0^t p(x, y, z, t|0, 0, 0, t')q dt' \quad (4.1)$$

The steady-state concentration is given by

$$\bar{c}(x, y, z) = \lim_{t \rightarrow \infty} \bar{c}(x, y, z, t) = \lim_{t \rightarrow \infty} \int_0^t p(x, y, z, t|0, 0, 0, t')q dt'$$

The transition probability density $p(x, y, z, t|0, 0, 0, t')$ is interpreted as the concentration at (x, y, z) at time t resulting from a unit source at the origin at time t' . From Eq. (3.15),

$$\begin{aligned} p(x, y, z, t|0, 0, 0, t') &= (2\pi)^{-3/2}[\sigma_x(t-t')\sigma_y(t-t')\sigma_z(t-t')]^{-1} \\ &\times \exp\left[-\frac{(x-\bar{u}(t-t'))^2}{2\sigma_x(t-t')^2} - \frac{y^2}{2\sigma_y(t-t')^2} \right. \\ &\quad \left. - \frac{z^2}{2\sigma_z(t-t')^2}\right] \end{aligned} \quad (4.2)$$

which we note can be expressed as $p(x, y, z, t-t'|0, 0, 0, 0)$. Thus

$$\begin{aligned} \bar{c}(x, y, z) &= \lim_{t \rightarrow \infty} \int_0^t p(x, y, z, t-t'|0, 0, 0, 0)q dt' \\ &= \lim_{t \rightarrow \infty} \int_0^t p(x, y, z, \tau|0, 0, 0, 0)q d\tau \end{aligned}$$

Therefore the steady-state concentration is obtained by integrating the non-steady-state concentration over all time from 0 to ∞ .

We note that the term $\exp\{-(x-\bar{u}t)^2/2\sigma_x^2\}$ is peaked about the value of the travel time $t = x/\bar{u}$ and falls off exponentially for longer or shorter values of t . Consequently, the major contribution of this term to Eq. (4.2) comes from a range of values of t given roughly by $(x - \sigma_x)/\bar{u} \leq t \leq (x + \sigma_x)/\bar{u}$. This expression is not really symmetric about x/\bar{u} because of the distortion caused by $\sigma_x(t)$, i.e., the older puffs are larger than the younger ones. By rewriting the exponential argument as $(x/\bar{u} - t)^2/2[\sigma_x(t)/\bar{u}]^2$ we see that the mean wind speed \bar{u} scales the rate of fall off of the integrand from its peak value. The smaller \bar{u} is, the larger will be the range of t over which the integrand in Eq. (4.2) will contribute significantly.

Combining Eqs. (4.1) and (4.2), the mean concentration from the continuous source is expressed as

$$\bar{c}(x, y, z) = \int_0^\infty q[(2\pi)^{3/2}\sigma_x\sigma_y\sigma_z]^{-1} \times \exp\left[-\frac{(x - \bar{u}t)^2}{2\sigma_x^2} - \frac{y^2}{2\sigma_y^2} - \frac{z^2}{2\sigma_z^2}\right] dt \quad (4.3)$$

$$1. \quad \sigma_x(t) = \sigma_y(t) = \sigma_z(t) = \sigma(t)$$

We now want to evaluate the integral in Eq. (4.3). To do so, let us assume that

$$\sigma_x(t) = \sigma_y(t) = \sigma_z(t) = \sigma(t) \quad (4.4)$$

A Taylor series expansion of the puff kernel about the time $t = x/\bar{u}$ is

$$\exp\left[-\frac{(x - \bar{u}t)^2 + y^2 + z^2}{2\sigma^2(t)}\right] = e^{-\eta} \left\{ 1 - \left(t - \frac{x}{\bar{u}}\right) 2\alpha\eta \right\} + \cdots \quad (4.5)$$

where

$$\eta = \frac{y^2 + z^2}{2\sigma^2(x/\bar{u})} \quad (4.6)$$

$$\alpha = \left\{ \frac{1}{\sigma(t)} \frac{d\sigma(t)}{dt} \right\}_{t=x/\bar{u}}$$

We now assume, consistent with the Taylor series expansion, that the major contribution to the integral comes from the range

$$x/\bar{u} - \delta \leq t \leq x/\bar{u} + \delta$$

where $\delta < x/\bar{u}$ (and $|t - x/\bar{u}| < \delta$). We expect δ to be proportional to $\sigma(t)/\bar{u}$ based on the form of the expression.

The parameter δ must be sufficiently large so that a substantial portion of the entire integral is contained within the integration limits $x/\bar{u} - \delta$, $x/\bar{u} + \delta$. However, since the integrand is peaked about the value $t = x/\bar{u}$ and falls off exponentially for $t \gtrless x/\bar{u}$, we reasonably expect δ to be a small quantity.

Substituting Eq. (4.5) into Eq. (4.3) yields

$$\bar{c}(x, y, z) \cong \int_{x/\bar{u}-\delta}^{x/\bar{u}+\delta} \frac{q}{(2\pi)^{3/2}\sigma^3(t)} e^{-\eta} \left[1 - \left(t - \frac{x}{\bar{u}}\right) 2\alpha\eta + \cdots \right] dt \quad (4.7)$$

If we further assume that $\sigma^2(t)$ does not change significantly in the interval $x/\bar{u} - \delta \leq t \leq x/\bar{u} + \delta$, and hence $\sigma^2(t) \approx \sigma^2(x/\bar{u})$ within the integration limits, we conclude that only the first term in the expansion will contribute to lowest order in δ , since to order δ ,

$$\int_{x/\bar{u}-\delta}^{x/\bar{u}+\delta} \left(t - \frac{x}{\bar{u}} \right)^n dt = 0 \quad \text{for } n \geq 1 \quad (4.8)$$

Consequently, to order δ , we get from Eq. (4.7),

$$\bar{c}(x, y, z) \cong \frac{q e^{-\eta}}{\sqrt{2}(\pi)^{3/2} \sigma^3(x/\bar{u})} \delta \quad (4.9)$$

We now have an expression for $\bar{c}(x, y, z)$ that depends on the parameter δ , which itself depends on time. The quantity $\bar{u}\delta$ expresses the distance for which a puff emitted at $t = 0$, and whose center is located at $x = \bar{u}t$, has appreciable concentrations. Physically, Eq. (4.9) expresses the concentration emanating from the point source to be a plume composed of many puffs whose concentration distributions are sharply peaked about the puff centroids at all travel distances. We have not specified the parameter δ , although we expect that it should be proportional to $\sigma(x/\bar{u})/\bar{u}$. The assumptions made in deriving Eq. (4.8) require that $\delta \ll x/\bar{u}$. If the proportionality constant relating δ and $\sigma(x/\bar{u})/\bar{u}$ is of order one, as we expect it to be, then the condition of validity of Eq. (4.9) can be stated as

$$\sigma(x/\bar{u})/x \ll 1 \quad (4.10)$$

Physically, this condition states that the spread of the individual puffs is small compared to the downwind distance. An alternative way of expressing this condition is that the rate of spreading of a puff in the direction of the mean flow is small compared to the rate of advection of the puff by the mean flow. This assumption is termed the *slender-plume approximation*.

The above analysis does not tell us the constant of proportionality relating δ and σ/\bar{u} . However, if we assume $\delta = a\sigma/\bar{u}$, substitute this expression for δ into Eq. (4.9), and impose the condition of conservation of mass (i.e., that the total flow of material past the plane at x is q), we obtain $a = (\pi/2)^{1/2}$. The resulting equation for $\bar{c}(x, y, z)$ is

$$\bar{c}(x, y, z) = \frac{q}{2\pi\bar{u}\sigma^2(x/\bar{u})} \exp\left[-\frac{y^2}{2\sigma^2(x/\bar{u})} - \frac{z^2}{2\sigma^2(x/\bar{u})}\right] \quad (4.11)$$

Summarizing, we have evaluated the general expression (4.3) in the special case in which the standard deviations of the puff distribution are the same in the three coordinate directions and in which the standard deviation is much smaller than the distance from the source at any x , the so-called slender-plume approximation.

$$2. \quad \sigma_x^2 = \gamma_x t, \quad \sigma_y^2 = \gamma_y t, \quad \sigma_z^2 = \gamma_z t$$

Let us return to Eq. (4.3) and consider the case in which $\sigma_x \neq \sigma_y \neq \sigma_z$. To perform the integration, it is necessary to specify the temporal depen-

dences of σ_x , σ_y , and σ_z . A particular form of dependence was developed in Eq. (3.16), from which we write

$$\sigma_x^2 = \gamma_x t, \quad \sigma_y^2 = \gamma_y t, \quad \sigma_z^2 = \gamma_z t \quad (4.12)$$

Thus, it is desired to evaluate

$$\begin{aligned} \bar{c}(x, y, z) &= \int_0^\infty \frac{q}{(2\pi)^{3/2}(\gamma_x \gamma_y \gamma_z)^{1/2} t^{3/2}} \\ &\times \exp\left[-\frac{(x - \bar{u}t)^2}{2\gamma_x t} - \frac{y^2}{2\gamma_y t} - \frac{z^2}{2\gamma_z t}\right] dt \end{aligned} \quad (4.13)$$

This integral can be expressed as

$$\begin{aligned} \bar{c}(x, y, z) &= \frac{q}{(2\pi)^{3/2}(\gamma_x \gamma_y \gamma_z)^{1/2}} \int_0^\infty t^{-3/2} \\ &\times \exp\left[-\frac{(r^2 - 2\bar{u}xt + \bar{u}^2 t^2)}{2\gamma_x t}\right] dt \end{aligned} \quad (4.14)$$

where $r^2 = x^2 + (\gamma_x/\gamma_y)y^2 + (\gamma_x/\gamma_z)z^2$. Thus,

$$\begin{aligned} \bar{c}(x, y, z) &= \frac{q}{(2\pi)^{3/2}(\gamma_x \gamma_y \gamma_z)^{1/2}} e^{\bar{u}x/\gamma_x} \int_0^\infty t^{-3/2} \\ &\times \exp\left[-\left(\frac{r^2}{2\gamma_x t} + \frac{\bar{u}^2 t^2}{2\gamma_x}\right)\right] dt \end{aligned} \quad (4.15)$$

Let $\eta = t^{-1/2}$ and

$$\begin{aligned} \bar{c}(x, y, z) &= \frac{2q}{(2\pi)^{3/2}(\gamma_x \gamma_y \gamma_z)^{1/2}} e^{\bar{u}x/\gamma_x} \\ &\times \int_0^\infty \exp\left[-\left(\frac{r^2 \eta^2}{2\gamma_x} + \frac{\bar{u}^2}{2\gamma_x \eta^2}\right)\right] d\eta \end{aligned} \quad (4.16)$$

The integral is equal to

$$\int_0^\infty e^{-(a\eta^2 + b/\eta^2)} d\eta = \frac{1}{2}(\pi/a)^{1/2} e^{-2(ab)^{1/2}}$$

so finally

$$\bar{c}(x, y, z) = \frac{q}{2\pi(\gamma_y \gamma_z)^{1/2} r} \exp\left[-\frac{\bar{u}}{\gamma_x}(r - x)\right] \quad (4.17)$$

is the expression for the mean concentration from a continuous point source of strength q at the origin in an infinite fluid with the variances given by Eq. (4.12).

Equation (4.17) can be simplified somewhat for most situations of practical interest by the slender-plume approximation. In dealing with Eq. (4.17), this approximation implies that advection dominates plume dispersion so that only the concentrations close to the plume centerline are of importance. In the case of Eq. (4.17) we are interested in values of x , y , and z that satisfy

$$\frac{(\gamma_x/\gamma_y)y^2 + (\gamma_x/\gamma_z)z^2}{x^2} \ll 1$$

which can be viewed as the result of two assumptions,

$$(i) \quad \frac{y^2 + z^2}{x^2} \ll 1; \quad (ii) \quad \frac{\gamma_x}{\gamma_y} = O(1), \quad \frac{\gamma_x}{\gamma_z} = O(1)$$

Assumption (ii) implies that the variances of the wind speeds are of the same order of magnitude. Since

$$r = x \left[1 + \frac{(\gamma_x/\gamma_y)y^2 + (\gamma_x/\gamma_z)z^2}{x^2} \right]^{1/2} \quad (4.18)$$

using $(1 + \zeta)^p = 1 + \zeta p + \dots$, Eq. (4.18) can be approximated by⁶

$$r \cong x \left[1 + \frac{(\gamma_x/\gamma_y)y^2 + (\gamma_x/\gamma_z)z^2}{2x^2} \right] \quad (4.19)$$

In Eq. (4.17) we approximate r by x and $r - x$ by the above expression. Thus, Eq. (4.17) becomes

$$\bar{c}(x, y, z) = \frac{q}{2\pi(\gamma_y\gamma_z)^{1/2}x} \exp \left\{ -\frac{\bar{u}}{\gamma_x} \left[\frac{(\gamma_x/\gamma_y)y^2 + (\gamma_x/\gamma_z)z^2}{2x} \right] \right\} \quad (4.20)$$

If we relate time and distance from the source x by $t = x/\bar{u}$, then we can use Eq. (4.12) to give

$$\sigma_y^2 = \gamma_y x / \bar{u}, \quad \sigma_z^2 = \gamma_z x / \bar{u} \quad (4.21)$$

⁶ The expression

$$(1 + \zeta)^p = 1 + \binom{p}{1} \zeta + \binom{p}{2} \zeta^2 + \dots$$

is valid for all p if $-1 < \zeta < 1$. Thus,

$$(1 + \zeta)^{1/2} = 1 + \frac{1}{2}\zeta + \frac{1}{8}\zeta^2 + \dots$$

for $-1 < \zeta < 1$. Note that

$$\binom{p}{v} = \frac{p!}{v!(p-v)!}$$

where for noninteger p , $p! = \Gamma(p+1)$.

Then Eq. (4.21) becomes the anisotropic version of Eq. (4.11):

$$\bar{c}(x, y, z) = \frac{q}{2\pi\bar{u}\sigma_y\sigma_z} \exp\left[-\left(\frac{y^2}{2\sigma_y^2} + \frac{z^2}{2\sigma_z^2}\right)\right] \quad (4.22)$$

Equation (4.22) is the expression for the mean concentration from a continuous point source of strength q at the origin in an infinite fluid when the standard deviations of plume spread are different in the different coordinate directions and when the slender-plume approximation is invoked.

B. EULERIAN APPROACH

The problem of determining the concentration distribution resulting from a continuous source of strength q at the origin in an infinite fluid with a velocity \bar{u} in the x direction can be formulated by the Eulerian approach as⁷

$$\bar{u} \frac{\partial \bar{c}}{\partial x} = K \left(\frac{\partial^2 \bar{c}}{\partial x^2} + \frac{\partial^2 \bar{c}}{\partial y^2} + \frac{\partial^2 \bar{c}}{\partial z^2} \right) + q\delta(x)\delta(y)\delta(z) \quad (4.23)$$

$$\bar{c}(x, y, z) = 0, \quad x, y, z \rightarrow \pm\infty \quad (4.24)$$

To solve Eq. (4.23), we begin with the transformation

$$f(x, y, z) = \bar{c}(x, y, z)e^{-kx} \quad (4.25)$$

where $k = \bar{u}/2K$, and Eq. (4.23) becomes

$$\nabla^2 f - k^2 f = -(q/K)e^{-kx}\delta(x)\delta(y)\delta(z), \quad (4.26)$$

$$f(x, y, z) = 0, \quad x, y, z \rightarrow \pm\infty$$

First we will solve $\nabla_r^2 f - k^2 f = 0$, where $r^2 = x^2 + y^2 + z^2$. To do so, let $f(r) = g(r)/r$ and

$$\nabla_r^2 f = \frac{1}{r^2} \frac{d}{dr} \left(r^2 \frac{df}{dr} \right) = \frac{1}{r} \frac{d^2 g}{dr^2}$$

so the equation to be solved is $d^2 g/dr^2 - k^2 g = 0$. The solution is $g(r) = A_1 e^{kr} + A_2 e^{-kr}$. Then $A_1 = 0$ satisfies the condition that g is finite as $r \rightarrow \infty$, and $f(r) = (A/r)e^{-kr}$. To determine A , we will evaluate

$$\int_V (\nabla_r^2 f - k^2 f) dV = - \int_V \frac{q}{K} e^{-kx} \delta(x)\delta(y)\delta(z) dV \quad (4.27)$$

⁷ We illustrate the solution procedure for the case of $K_{xx} = K_{yy} = K_{zz} = K$. The solution for the general case is presented subsequently.

on the sphere with unit radius. The right-hand side of Eq. (4.27) is simply $-q/K$. The left-hand side is, using Green's theorem,

$$\int_V (\nabla_r^2 f - k^2 f) dV = \int_S \frac{\partial f}{\partial n} dS - k^2 \int_V f dV$$

On a sphere of unit radius,

$$\begin{aligned} \int_S \frac{\partial f}{\partial n} dS &= \int_0^{2\pi} \int_{-\pi}^{\pi} \cos \theta \left(\frac{\partial f}{\partial r} \right)_{r=1} d\theta d\phi = -4\pi A e^{-k}(k+1) \\ - \int_V f dV &= \int_0^1 4\pi r^2 f dr = 4\pi A [e^{-k}(k+1) - 1] \end{aligned}$$

Thus, Eq. (4.27) becomes $4\pi A = q/K$. Finally,

$$\bar{c}(x, y, z) = \frac{q}{4\pi K r} \exp\left[-\frac{\bar{u}(r-x)}{2K}\right] \quad (4.28)$$

where $r^2 = x^2 + y^2 + z^2$, or

$$r = x \left(1 + \frac{y^2 + z^2}{x^2} \right)^{1/2} \quad (4.29)$$

If we invoke the slender-plume approximation, we are interested only in the solution close to the plume centerline. Thus, as in Eq. (4.20), Eq. (4.29) can be approximated by

$$r \cong x \left(1 + \frac{y^2 + z^2}{2x^2} \right) \quad (4.30)$$

If in Eq. (4.28) r is approximated by x and $r-x$ by $(y^2 + z^2)/2x$, Eq. (4.28) becomes

$$\bar{c}(x, y, z) = \frac{q}{4\pi K x} \exp\left[-\left(\frac{\bar{u}}{4Kx}\right)(y^2 + z^2)\right] \quad (4.31)$$

We will now show that Eq. (4.31) may be obtained by solving the atmospheric diffusion equation in which diffusion in the direction of the mean flow is neglected relative to advection:

$$\begin{aligned} \bar{u} \frac{\partial \bar{c}}{\partial x} &= K \left(\frac{\partial^2 \bar{c}}{\partial y^2} + \frac{\partial^2 \bar{c}}{\partial z^2} \right) + q \delta(x) \delta(y) \delta(z) \\ \bar{c}(0, y, z) &= 0, \quad \bar{c}(x, y, z) = 0, \quad y, z \rightarrow \pm\infty \end{aligned} \quad (4.32)$$

In fact, the source may now be included in the $x = 0$ boundary condition by

$$\bar{u} \frac{\partial \bar{c}}{\partial x} = K \left(\frac{\partial^2 \bar{c}}{\partial y^2} + \frac{\partial^2 \bar{c}}{\partial z^2} \right)$$

$$\bar{c}(0, y, z) = (q/\bar{u})\delta(y)\delta(z), \quad \bar{c}(x, y, z) = 0, \quad y, z \rightarrow \pm\infty \quad (4.33)$$

where the $x = 0$ boundary condition arises by equating material fluxes across the plane at $x = 0$. We will present the solution of Eq. (4.33).

The solution can be carried out by Fourier transform, first with respect to the y direction, $C(x, \alpha, z) = F_y\{\bar{c}(x, y, z)\}$, and then with respect to the z direction, $C'(x, \alpha, \beta) = F_z\{C(x, \zeta, z)\}$, in which case Eq. (4.33) becomes

$$\bar{u} \frac{\partial C'}{\partial x} = -K(\alpha^2 + \beta^2)C'(x, \alpha, \beta) \quad (4.34)$$

The $x = 0$ boundary condition, when transformed doubly, is

$$C'(0, \alpha, \beta) = q/2\pi\bar{u} \quad (4.35)$$

The solution of Eq. (4.34) subject to Eq. (4.35) is

$$C'(x, \alpha, \beta) = \frac{q}{2\pi\bar{u}} \exp\left[-\frac{Kx}{\bar{u}}(\alpha^2 + \beta^2)\right] \quad (4.36)$$

We must now invert Eq. (4.36) twice to return to $\bar{c}(x, y, z)$. First,

$$C(x, \alpha, z) = \frac{1}{(2\pi)^{1/2}} \int_{-\infty}^{\infty} C'(x, \alpha, \beta) e^{i\beta z} d\beta$$

Thus,

$$C(x, \alpha, z) = \frac{q}{(2\pi)^{3/2}\bar{u}} e^{-\alpha^2 Kx/\bar{u}} \int_{-\infty}^{\infty} \exp\left[i\beta z - \frac{Kx\beta^2}{\bar{u}}\right] d\beta \quad (4.37)$$

It is now necessary to express the exponential in the integrand as

$$-\left(\frac{Kx\beta^2}{\bar{u}} - i\beta z\right) = -\left[\left(\frac{Kx}{\bar{u}}\right)^{1/2} \beta - \frac{iz}{2} \left(\frac{\bar{u}}{Kx}\right)^{1/2}\right]^2 - \frac{z^2 \bar{u}}{4Kx}$$

and let $\eta = (Kx/\bar{u})^{1/2}\beta - (iz/2)(\bar{u}/Kx)^{1/2}$. Then Eq. (4.37) becomes

$$C(x, \alpha, z) = \frac{q}{(2\pi)^{3/2}\bar{u}} \left(\frac{\bar{u}}{Kx}\right)^{1/2} \exp\left[-\frac{\alpha^2 Kx}{\bar{u}} - \frac{z^2 \bar{u}}{4Kx}\right] \int_{-\infty}^{\infty} e^{-\eta^2} d\eta$$

Proceeding through identical steps to invert $C(x, \alpha, z)$ to $\bar{c}(x, y, z)$, we obtain

$$\bar{c}(x, y, z) = \frac{q}{4\pi Kx} \exp\left[-\frac{\bar{u}}{4Kx}(y^2 + z^2)\right] \quad (4.38)$$

Finally, we can proceed through similar steps in solving the more general form

$$\bar{u} \frac{\partial \bar{c}}{\partial x} = K_{yy} \frac{\partial^2 \bar{c}}{\partial y^2} + K_{zz} \frac{\partial^2 \bar{c}}{\partial z^2}$$

$$\bar{c}(0, y, z) = (q/\bar{u})\delta(y)\delta(z), \quad \bar{c}(x, y, z) = 0, \quad y, z \rightarrow \pm\infty \quad (4.39)$$

to obtain

$$\bar{c}(x, y, z) = \frac{q}{4\pi(K_{yy}K_{zz})^{1/2}x} \exp\left[-\frac{\bar{u}}{4x}\left(\frac{y^2}{K_{yy}} + \frac{z^2}{K_{zz}}\right)\right] \quad (4.40)$$

C. SUMMARY OF CONTINUOUS POINT SOURCE SOLUTIONS

Table I presents a summary of the solutions obtained in this section. Of primary interest at this point is comparison of the forms of the Lagrangian and Eulerian expressions, in particular the relationships between the eddy diffusivities and the plume dispersion variances. For the slender-plume cases, for example, the Lagrangian and Eulerian expressions are identical if

$$\sigma_y^2 = 2K_{yy}x/\bar{u}, \quad \sigma_z^2 = 2K_{zz}x/\bar{u} \quad (4.41)$$

which can be compared to Eq. (4.21).

In most applications of the Lagrangian formulas, the dependences of σ_y^2 and σ_z^2 on x are determined empirically rather than as indicated in Eqs. (4.41). Thus, the main purpose of the formulas in Table I is to provide a comparison between the two approaches to atmospheric diffusion theory.

V. Point Source Diffusion Formulas Based on a Gaussian Distribution

The presumption of a Gaussian distribution for the mean concentration from a point source, although demonstrated only in the case of stationary, homogeneous turbulence, has been made widely and, in fact, is the basis for many of the atmospheric diffusion formulas in common use. Based on the developments of Section IV, we present in this section the Gaussian point source diffusion formulas that have been used for practical calculations.

TABLE I
MEAN CONCENTRATION $\bar{c}(x, y, z)$ FROM A CONTINUOUS POINT SOURCE IN AN INFINITE FLUID IN STATIONARY,
HOMOGENEOUS TURBULENCE

Approach	Full solution	Slender-plume approximation
Lagrangian $\sigma_x^2 = \gamma_x t$ $\sigma_y^2 = \gamma_y t$ $\sigma_z^2 = \gamma_z t$	$\frac{q}{2\pi(\gamma_y \gamma_z)^{1/2} r} \exp\left[-\frac{\bar{u}}{\gamma_x}(r-x)\right]$ $r^2 = x^2 + (\gamma_x/\gamma_y)y^2 + (\gamma_x/\gamma_z)z^2$	$\frac{q}{2\pi\bar{u}\sigma_y\sigma_z} \exp\left[-\left(\frac{y^2}{2\sigma_y^2} + \frac{z^2}{2\sigma_z^2}\right)\right]$
Eulerian $K_{xx} \neq K_{yy} \neq K_{zz}$	$\frac{q}{4\pi} (K_{yy}K_{zz}x^2 + K_{xx}K_{zz}y^2 + K_{xx}K_{yy}z^2)^{-1/2}$ $\times \exp\left\{-\frac{\bar{u}}{2K_{xx}}\left[\left(\frac{x^2}{K_{xx}} + \frac{y^2}{K_{yy}} + \frac{z^2}{K_{zz}}\right)^{1/2} - x\right]\right\}$	$\frac{q}{4\pi(K_{yy}K_{zz})^{1/2}x} \exp\left[-\frac{\bar{u}}{4x}\left(\frac{y^2}{K_{yy}} + \frac{z^2}{K_{zz}}\right)\right]$

A. LAGRANGIAN APPROACH

The Gaussian concept can be extended beyond that already developed in Section IV. The general Gaussian probability density function for the position of a fluid particle released from a source located at (x', y', z') at time t' can be expressed as (Lamb, 1980)

$$p(x, y, z, t|x', y', z', t') = [(2\pi)^3|\mathbf{P}|]^{-1/2} \exp[-\frac{1}{2}\boldsymbol{\zeta}^T\mathbf{P}^{-1}\boldsymbol{\zeta}] \quad (5.1)$$

where $\boldsymbol{\zeta}^T$ is the transpose of the column vector with the following components:

$$\begin{aligned} \zeta_x &= x - x' - \bar{u}(t - t'), & \zeta_y &= y - y' - \bar{v}(t - t') \\ \zeta_z &= z - z' - \bar{w}(t - t') \end{aligned} \quad (5.2)$$

and \mathbf{P}^{-1} and $|\mathbf{P}|$ are the inverse and determinant, respectively, of the matrix

$$\mathbf{P} = \begin{bmatrix} \langle \zeta_x^2 \rangle & \langle \zeta_x \zeta_y \rangle & \langle \zeta_x \zeta_z \rangle \\ \langle \zeta_y \zeta_x \rangle & \langle \zeta_y^2 \rangle & \langle \zeta_y \zeta_z \rangle \\ \langle \zeta_z \zeta_x \rangle & \langle \zeta_z \zeta_y \rangle & \langle \zeta_z^2 \rangle \end{bmatrix} \quad (5.3)$$

where the covariance $\langle \zeta_x^2 \rangle$, $\langle \zeta_x \zeta_y \rangle$, etc., are

$$\begin{aligned} \langle \zeta_x^2 \rangle &= \langle (x - x')^2 \rangle - (\bar{u}(t - t'))^2 \\ \langle \zeta_x \zeta_y \rangle &= \langle (x - x')(y - y') \rangle - \bar{u}\bar{v}(t - t')^2 \end{aligned} \quad (5.4)$$

Since measurements of $\langle u'v' \rangle$, $\langle u'w' \rangle$, etc., usually indicate that the magnitudes of these covariances are much smaller than the mean square velocity fluctuations $\langle u'^2 \rangle$, $\langle v'^2 \rangle$, etc., it is generally assumed that the off-diagonal elements of \mathbf{P} are negligible. Also, we use the notation, $\sigma_x^2 = \langle \zeta_x^2 \rangle$, $\sigma_y^2 = \langle \zeta_y^2 \rangle$, $\sigma_z^2 = \langle \zeta_z^2 \rangle$.

It is customary to assume that the mean wind is directed along the x axis, i.e., $\bar{v} = \bar{w} = 0$. Then, Eq. (5.1) becomes

$$\begin{aligned} p(x, y, z, t|x', y', z', t') &= [(2\pi)^3\sigma_x^2\sigma_y^2\sigma_z^2]^{-1/2} \\ &\times \exp\left[-\frac{(x - x' - \bar{u}(t - t'))^2}{2\sigma_x^2} - \frac{(y - y')^2}{2\sigma_y^2} \right. \\ &\quad \left. - \frac{(z - z')^2}{2\sigma_z^2}\right] \end{aligned} \quad (5.5)$$

Up to this point we have assumed a fluid occupying an infinite domain. For atmospheric applications a boundary at $z = 0$, the earth, is present.

One can modify Eq. (5.5) to allow for different concentration distributions in the z direction by separating out the form of the distribution in the z direction:

$$\begin{aligned}
 p(x, y, z, t|x', y', z', t') &= p_z(z, t|z', t') \\
 &\times [4\pi\sigma_x^2\sigma_y^2]^{-1/2} \\
 &\times \exp \left[-\frac{(x - x' - \bar{u}(t - t'))^2}{2\sigma_x^2} - \frac{(y - y')^2}{2\sigma_y^2} \right]
 \end{aligned} \quad (5.6)$$

The form of p_z will depend on the extent of the vertical domain and the type of interaction between the surface and the species. Two possibilities are generally considered when specifying the extent of the vertical domain in the atmosphere:

- (1) unbounded domain, $0 \leq z \leq \infty$;
- (2) bounded domain, $0 \leq z \leq H$.

Case (2) corresponds to the existence of a layer occupying $z > H$ that acts to inhibit diffusion of material. Three possible situations exist when specifying the type of interaction between the surface and the material:

- (1) total reflection;
- (2) total absorption;
- (3) partial absorption;

Consider first an unbounded domain and a totally reflecting surface. To obtain an expression for p_z , we assume that the presence of the boundary at $z = 0$ can be accounted for by adding the concentration resulting from an imaginary source at $z = -z'$ to that from the source at $z = z'$ in the region $z \geq 0$. Then p_z assumes the form

$$p_z(z, t|z', t') = \frac{1}{(2\pi)^{1/2}\sigma_z} \left(\exp \left[-\frac{(z - z')^2}{2\sigma_z^2} \right] + \exp \left[-\frac{(z + z')^2}{2\sigma_z^2} \right] \right) \quad (5.7)$$

If the earth is a perfect absorber, the concentration of material at the surface is zero. The form of the vertical distribution can be obtained by the method of an image source, with the change that we now subtract the distribution from the source at $-z'$ from that for the source at $+z'$. The resulting vertical distribution is

$$p_z(z, t|z', t') = \frac{1}{(2\pi)^{1/2}\sigma_z} \left(\exp \left[-\frac{(z - z')^2}{2\sigma_z^2} \right] - \exp \left[-\frac{(z + z')^2}{2\sigma_z^2} \right] \right) \quad (5.8)$$

Either Eq. (5.7) or (5.8) can be used in Eq. (5.6) to give the complete distribution in the cases of totally reflecting and totally absorbing surfaces, respectively. The case of a partially absorbing surface cannot be treated by the same image source approach since some material particles are reflected and some are absorbed. The Eulerian approach offers a convenient way to determine the form of the vertical distribution over the range of situations.

We now turn to the case of a continuous source. The mean concentration from a continuous point source of strength q at height h above the (totally reflecting) earth is given by (it is conventional to let h denote the source height, and we do so henceforth)

$$\bar{c}(x, y, z) = \lim_{t \rightarrow \infty} \int_0^t \frac{q}{(2\pi)^{3/2} \sigma_x \sigma_y \sigma_z} \exp \left[-\frac{(x - \bar{u}\tau)^2}{2\sigma_x^2} - \frac{y^2}{2\sigma_y^2} \right] \times \left[\exp \left(-\frac{(z - h)^2}{2\sigma_z^2} \right) + \exp \left(-\frac{(z + h)^2}{2\sigma_z^2} \right) \right] d\tau \quad (5.9)$$

As usual, we will be interested in the slender-plume case, so we evaluate the integral in the limit as $\sigma_x \rightarrow 0$. We can use the following relation:

$$\lim_{\sigma \rightarrow 0} \frac{1}{(2\pi)^{1/2} \sigma} \exp \left[-\frac{(x - x')^2}{2\sigma^2} \right] = \delta(x - x') \quad (5.10)$$

to take the limit of the x term as $\sigma_x \rightarrow 0$. Using this relationship and letting $\xi = \bar{u}t$, we get from Eq. (5.9)

$$\bar{c}(x, y, z) = \lim_{\xi \rightarrow \infty} \int_0^{\xi/\bar{u}} \frac{q}{2\pi \bar{u} \sigma_y \sigma_z} \exp \left(-\frac{y^2}{2\sigma_y^2} \right) \times \left(\exp \left[-\frac{(z - h)^2}{2\sigma_z^2} \right] + \exp \left[-\frac{(z + h)^2}{2\sigma_z^2} \right] \right) \delta(x - \xi) d\xi \quad (5.11)$$

where σ_y and σ_z are now functions of ξ/\bar{u} . The final result is

$$\bar{c}(x, y, z) = \frac{q}{2\pi \bar{u} \sigma_y \sigma_z} \exp \left(-\frac{y^2}{2\sigma_y^2} \right) \times \left(\exp \left[-\frac{(z - h)^2}{2\sigma_z^2} \right] + \exp \left[-\frac{(z + h)^2}{2\sigma_z^2} \right] \right) \quad (5.12)$$

the so-called *Gaussian plume equation*.

This result may also be obtained by starting with Eq. (4.11), assuming a source at $z = h$ and a fictitious source at $z = -h$, and adding the two expressions in the region $z \geq 0$. If we assume a totally absorbing earth, the corresponding form of the Gaussian plume equation is

$$\begin{aligned}\bar{c}(x, y, z) = & \frac{q}{2\pi\bar{u}\sigma_y\sigma_z} \exp\left(-\frac{y^2}{2\sigma_y^2}\right) \\ & \times \left(\exp\left[-\frac{(z-h)^2}{2\sigma_z^2}\right] - \exp\left[-\frac{(z+h)^2}{2\sigma_z^2}\right]\right) \quad (5.13)\end{aligned}$$

Now we turn to the Eulerian approach to obtain the same results as we have just obtained by the Lagrangian approach.

B. EULERIAN APPROACH

The object of this section is to derive the Gaussian equations of the previous section as solutions to the atmospheric diffusion equation. Such a relationship has already been demonstrated in Section IV,B for the case of no boundaries. We extend that consideration now to boundaries. We recall that constant eddy diffusivities were assumed in Section IV,B.

1. *Instantaneous Source*

Assuming a uniform wind speed \bar{u} in the x direction, we begin with the unsteady atmospheric diffusion equation with constant eddy diffusivities:

$$\frac{\partial \bar{c}}{\partial t} + \bar{u} \frac{\partial \bar{c}}{\partial x} = K_{xx} \frac{\partial^2 \bar{c}}{\partial x^2} + K_{yy} \frac{\partial^2 \bar{c}}{\partial y^2} + K_{zz} \frac{\partial^2 \bar{c}}{\partial z^2} + S(x, y, z, t) \quad (5.14)$$

with initial condition

$$\bar{c}(x, y, z, 0) = 0 \quad (5.15)$$

and x and y boundary conditions

$$\bar{c}(x, y, z, t) = 0, \quad x, y \rightarrow \pm\infty \quad (5.16)$$

The z boundary conditions specify both the extent of the region and the physical interaction of the material with the boundaries. It will be convenient in solving Eq. (5.14) to assume that an impermeable barrier to diffusion exists at a height $z = H$. Then the case of an unbounded region $z \geq 0$ is obtained by letting $H \rightarrow \infty$. The surface ($z = 0$) boundary condition can be represented in general as

$$K_{zz} \partial \bar{c} / \partial z = v_d \bar{c}, \quad z = 0 \quad (5.17)$$

where v_d is a parameter that is proportional to the degree of absorptivity of the surface. For total reflection, $v_d = 0$, and for total absorption, $v_d = \infty$. The specification of the problem is completed with the $z = H$ boundary condition:

$$\partial \bar{c} / \partial z = 0, \quad z = H \quad (5.18)$$

The solution of Eq. (5.14) can be expressed in terms of the Green's function $\bar{G}(x, y, z, t|x', y', z', t')$ as

$$\begin{aligned} \bar{c}(x, y, z, t) = & \int_0^H \int_{-\infty}^{\infty} \int_{-\infty}^{\infty} \int_0^t \bar{G}(x, y, z, t|x', y', z', t') \\ & \times S(x', y', z', t') dt' dx' dy' dz' \end{aligned} \quad (5.19)$$

where \bar{G} satisfies

$$\begin{aligned} \frac{\partial \bar{G}}{\partial t} + \bar{u} \frac{\partial \bar{G}}{\partial x} &= K_{xx} \frac{\partial^2 \bar{G}}{\partial x^2} + K_{yy} \frac{\partial^2 \bar{G}}{\partial y^2} + K_{zz} \frac{\partial^2 \bar{G}}{\partial z^2} \\ \bar{G}(x, y, z, 0|x', y', z', 0) &= \delta(x - x')\delta(y - y')\delta(z - z') \\ \bar{G} &= 0, \quad x, y \rightarrow \pm\infty \\ \frac{\partial \bar{G}}{\partial z} &= \begin{cases} \beta \bar{G} & \text{for } z = 0 \\ 0 & \text{for } z = H \end{cases} \end{aligned} \quad (5.20)$$

where $\beta = v_d/K_{zz}$. First we remove the convection term by the coordinate transformation $\xi = x - \bar{u}(t - t')$, which converts Eq. (5.20) to

$$\frac{\partial \bar{G}}{\partial t} = K_{xx} \frac{\partial^2 \bar{G}}{\partial \xi^2} + K_{yy} \frac{\partial^2 \bar{G}}{\partial y^2} + K_{zz} \frac{\partial^2 \bar{G}}{\partial z^2}$$

To obtain \bar{G} , we let

$$\bar{G}(\xi, y, z, t|x', y', z', t') = A(\xi, y, t|x', y', t')B(z, t|z', t')$$

where

$$\begin{aligned} \frac{\partial A}{\partial t} &= K_{xx} \frac{\partial^2 A}{\partial \xi^2} + K_{yy} \frac{\partial^2 A}{\partial y^2} \\ A(\xi, y, 0|x', y', 0) &= \delta(\xi - x')\delta(y - y') \\ A(\xi, y, t|x', y', t') &= 0, \quad \xi, y \rightarrow \pm\infty \end{aligned} \quad (5.21)$$

$$\begin{aligned} \frac{\partial B}{\partial t} &= K_{zz} \frac{\partial^2 B}{\partial z^2} \\ B(z, 0|z', 0) &= \delta(z - z') \end{aligned} \quad (5.22)$$

$$\frac{\partial B}{\partial z} = \begin{cases} \beta B & \text{for } z = 0 \\ 0 & \text{for } z = H \end{cases}$$

We begin with the solution of Eqs. (5.21). Using separation of variables, $A(\xi, y, t|x', y', t') = P(\xi, t|x', t')Q(y, t|y', t')$. The solutions are symmetric,

$$P(\xi, t|x', t') = \frac{a}{[K_{xx}(t - t')]^{1/2}} \exp \left[-\frac{(\xi - x')^2}{4K_{xx}(t - t')} \right]$$

$$Q(y, t|y', t') = \frac{b}{[K_{yy}(t - t')]^{1/2}} \exp \left[-\frac{(y - y')^2}{4K_{yy}(t - t')} \right]$$

Thus,

$$A(\xi, y, t|x', y', t') = \frac{a'}{(K_{xx}K_{yy})^{1/2}(t - t')} \times \exp \left[-\frac{(\xi - x')^2}{4K_{xx}(t - t')} - \frac{(y - y')^2}{4K_{yy}(t - t')} \right]$$

We determine a' from the initial condition

$$A(\xi, y, 0|x', y', 0) = \delta(\xi - x')\delta(y - y')$$

or

$$\frac{a'}{(K_{xx}K_{yy})^{1/2}(t - t')} \int_{-\infty}^{\infty} \int_{-\infty}^{\infty} \exp \left[-\frac{(\xi - x')^2}{4K_{xx}(t - t')} \right] \exp \left[-\frac{(y - y')^2}{4K_{yy}(t - t')} \right] d\xi dy$$

$$= \int_{-\infty}^{\infty} \int_{-\infty}^{\infty} \delta(\xi - x')\delta(y - y') d\xi dy$$

which reduces to $a' = 1/4\pi$. Thus,

$$A(\xi, y, t|x', y', t') = \frac{1}{4\pi(K_{xx}K_{yy})^{1/2}(t - t')} \times \exp \left[-\frac{(\xi - x')^2}{4K_{xx}(t - t')} - \frac{(y - y')^2}{4K_{yy}(t - t')} \right] \quad (5.23)$$

Now we proceed to solve Eq. (5.22) to obtain

$$B(z, t|z', t') = \frac{2}{H} \sum_{n=1}^{\infty} \frac{(\lambda_n^2 + \beta^2) \cos[\lambda_n(H - z')] \cos[\lambda_n(H - z)]}{(\lambda_n^2 + \beta^2) + \beta}$$

$$\times \exp[-\lambda_n^2 K_{zz}(t - t')] \quad (5.24)$$

where the λ_n are the roots of

$$\lambda_n \tan \lambda_n H = \beta$$

In the case of a perfectly reflecting surface, $\beta = 0$ and

$$B(z, t|z', t') = \frac{2}{H} \sum_{n=1}^{\infty} \cos[\lambda_n(H - z')] \cos[\lambda_n(H - z)] \exp[-\lambda_n^2 K_{zz}(t - t')]$$

where $\sin \lambda_n H = 0$. This result can be simplified somewhat to

$$B(z, t|z', t') = \frac{2}{H} \sum_{n=0}^{\infty} \cos\left(\frac{n\pi z}{H}\right) \cos\left(\frac{n\pi z'}{H}\right) \exp\left[-\left(\frac{n\pi}{H}\right)^2 K_{zz}(t - t')\right] \quad (5.25)$$

The desired solution for $\bar{G}(x, y, z, t|x', y', z', t')$ is obtained by combining the expressions for $A(\xi, y, t|x', y', t')$ and $B(z, t|z', t')$. Physically \bar{G} represents the mean concentration at (x, y, z) at time t resulting from a unit source at (x', y', z') at time t' . For example, in the case of a totally reflecting earth, we have

$$\begin{aligned} \bar{G}(\xi, y, z, t|x', y', z', t') &= \frac{1}{2\pi H (K_{xx} K_{yy})^{1/2} (t - t')} \sum_{n=0}^{\infty} \cos\left(\frac{n\pi z}{H}\right) \cos\left(\frac{n\pi z'}{H}\right) \\ &\times \exp\left[-\left(\frac{n\pi}{H}\right)^2 K_{zz}(t - t')\right] \\ &\times \exp\left[-\frac{(\xi - x')^2}{4K_{xx}(t - t')} - \frac{(y - y')^2}{4K_{yy}(t - t')}\right] \quad (5.26) \end{aligned}$$

As usual, we are interested in neglecting diffusion in the x direction as compared with convection, i.e., the slender-plume approximation. We could return to the original problem neglecting the term $\partial^2 \bar{c} / \partial x^2$ in Eq. (5.14) and repeat the solution. We can also work with Eq. (5.26) and let $K_{xx} \rightarrow 0$. To do so, return to Eq. (5.23) and let $\sigma_x^2 = 2K_{xx}(t - t')$. Using Eq. (5.10) to take the limit of the x term as $\sigma_x \rightarrow 0$,

$$\begin{aligned} \lim_{\sigma_x \rightarrow 0} A(x, y, t|x', y', t') &= \frac{1}{2[\pi K_{yy}(t - t')]^{1/2}} \\ &\times \exp\left[-\frac{(y - y')^2}{4K_{yy}(t - t')}\right] \delta(x - x' - \bar{u}(t - t')) \end{aligned}$$

Thus, the slender-plume form of Eq. (5.26) is

$$\begin{aligned} \bar{G}(x, y, z, t|x', y', z', t') &= \sum_{n=0}^{\infty} \left\{ \frac{2}{H} \cos\left(\frac{n\pi z}{H}\right) \cos\left(\frac{n\pi z'}{H}\right) \right. \\ &\times \exp\left[-\left(\frac{n\pi}{H}\right)^2 K_{zz}(t - t')\right] \Big\} \\ &\times \frac{1}{2[\pi K_{yy}(t - t')]^{1/2}} \exp\left[-\frac{(y - y')^2}{4K_{yy}(t - t')}\right] \\ &\times \delta(x - x' - \bar{u}(t - t')) \quad (5.27) \end{aligned}$$

2. Continuous Source

Now we consider a continuous point source of strength q at $(0, 0, h)$. The continuous source solution is obtained from the unsteady solution from

$$\begin{aligned}\bar{c}(x, y, z) = \lim_{t \rightarrow \infty} \int_0^H \int_{-\infty}^{\infty} \int_{-\infty}^{\infty} \int_0^t \bar{G}(x, y, z, t|x', y', z', t')q \\ \times \delta(x')\delta(y')\delta(z' - h) dt' dx' dy' dz'\end{aligned}$$

The solution is illustrated for the case of a totally reflecting earth. Using Eq. (5.27) and carrying out the integration, we obtain

$$\begin{aligned}\bar{c}(x, y, z) = \frac{q}{(\pi K_{yy})^{1/2} H} \sum_{n=0}^{\infty} \cos\left(\frac{n\pi z}{H}\right) \cos\left(\frac{n\pi h}{H}\right) \\ \times \int_0^{\infty} \frac{1}{(t - t')^{1/2}} \exp\left[-\frac{y^2}{4K_{yy}(t - t')} - \left(\frac{n\pi}{H}\right)^2 K_{zz}(t - t')\right] \\ \times \delta(x - \bar{u}(t - t')) dt'\end{aligned}$$

Evaluating the integral,

$$\begin{aligned}\bar{c}(x, y, z) = \frac{q}{(\pi K_{yy})^{1/2} H \bar{u}} \sum_{n=0}^{\infty} \cos\left(\frac{n\pi z}{H}\right) \cos\left(\frac{n\pi h}{H}\right) \\ \times \left\{ \left(\frac{x}{\bar{u}}\right)^{-1/2} \exp\left[-\frac{y^2}{4K_{yy}x/\bar{u}} - \left(\frac{n\pi}{H}\right)^2 K_{zz} \frac{x}{\bar{u}}\right] \right\} \quad (5.28)\end{aligned}$$

This is the expression for the steady-state concentration resulting from a continuous point source located at $(0, 0, h)$ between impermeable, nonabsorbing boundaries separated by a distance H when diffusion in the direction of the mean flow is neglected.

Finally, we wish to obtain the result when $H \rightarrow \infty$, i.e., only one bounding surface at a distance h from the source. Let

$$\sigma_y^2 = 2K_{yy}x/\bar{u} \quad \sigma_z^2 = 2K_{zz}x/\bar{u}$$

and Eq. (5.28) can be expressed as

$$\begin{aligned}\bar{c}(x, y, z) = \frac{2q}{(2\pi)^{1/2} \bar{u} \sigma_y H} \sum_{n=0}^{\infty} \cos\left(\frac{n\pi z}{H}\right) \\ \times \cos\left(\frac{n\pi h}{H}\right) \exp\left[-\frac{y^2}{2\sigma_y^2} - \left(\frac{n\pi}{H}\right)^2 \frac{\sigma_z^2}{2}\right]\end{aligned}$$

Now let $H \rightarrow \infty$. Let $S = 1/H$, and

$$\frac{1}{H} \sum_{n=0}^{\infty} \cos\left(\frac{n\pi z}{H}\right) \cos\left(\frac{n\pi h}{H}\right) \exp\left[-\left(\frac{n\pi}{H}\right)^2 \frac{\sigma_z^2}{2}\right] = \sum_{n=0}^{\infty} f(H, \Delta S) \Delta S$$

As $\Delta S \rightarrow 0$, the summation approaches $\int_0^{\infty} f(S) dS$ and

$$\begin{aligned} \bar{c}(x, y, z) &= \frac{2q}{(2\pi)^{1/2} \bar{u} \sigma_y} \exp\left[-\frac{y^2}{2\sigma_y^2}\right] \int_0^{\infty} \cos(\pi S z) \\ &\quad \times \cos(\pi S h) \exp\left[-\frac{(\pi \sigma_x S)^2}{2}\right] dS \end{aligned}$$

Now,

$$\begin{aligned} \cos(\pi z S) \cos(\pi h S) &= \frac{1}{2} [\cos \pi S(z + h) + \cos \pi S(z - h)] \\ \bar{c}(x, y, z) &= \frac{q}{(2\pi)^{1/2} \bar{u} \sigma_y} \exp\left[-\frac{y^2}{2\sigma_y^2}\right] \\ &\quad \times \left\{ \int_0^{\infty} \cos[\pi(z + h)S] e^{-(\pi \sigma_x S)^2/2} dS \right. \\ &\quad \left. + \int_0^{\infty} \cos[\pi(z - h)S] e^{-(\pi \sigma_x S)^2/2} dS \right\} \end{aligned}$$

The integrals can be evaluated with the aid of tables to produce the final result,⁸

$$\begin{aligned} \bar{c}(x, y, z) &= \frac{q}{2\pi \bar{u} \sigma_y \sigma_z} \exp\left[-\frac{y^2}{2\sigma_y^2}\right] \\ &\quad \times \left\{ \exp\left[-\frac{(z - h)^2}{2\sigma_z^2}\right] + \exp\left[-\frac{(z + h)^2}{2\sigma_z^2}\right] \right\} \quad (5.29) \end{aligned}$$

the Gaussian plume equation.

The various point source formulas we have derived in Section V are summarized in Table II.

C. LINE AND AREA SOURCE SOLUTIONS

Consider Fig. 2 showing a line source of length L_l , the coordinates of the midpoint of which are (x_l, y_l) . The line source, of strength $q(t)$, is

⁸ We note that

$$\int_0^{\infty} e^{-\alpha x^2} \cos \beta x \, dx = \frac{1}{2} \left(\frac{\pi}{\alpha}\right)^{1/2} \exp\left(-\frac{\beta^2}{4\alpha}\right)$$

TABLE II

POINT SOURCE GAUSSIAN DIFFUSION FORMULAS

Mean concentration	Assumptions
<i>Gaussian puff formula</i>	
$\bar{c}(x, y, z, t) = \frac{Q}{(2\pi)^{3/2}\sigma_x\sigma_y\sigma_z} \exp \left[-\frac{(x-x'-\bar{u}(t-t'))^2}{2\sigma_x^2} - \frac{(y-y')^2}{2\sigma_y^2} \right]$ $\times \left[\exp \left(-\frac{(z-z')^2}{2\sigma_z^2} \right) + \exp \left(-\frac{(z+z')^2}{2\sigma_z^2} \right) \right]$	Totally reflecting earth at $z = 0$ $\bar{\mathbf{u}} = (\bar{u}, 0, 0)$ $S = Q\delta(x-x')\delta(y-y')\delta(z-z')\delta(t-t')$ $0 \leq z \leq \infty$
$\bar{c}(x, y, z, t) = \frac{Q}{(2\pi)^{3/2}\sigma_x\sigma_y\sigma_z} \exp \left[-\frac{(x-x'-\bar{u}(t-t'))^2}{2\sigma_x^2} - \frac{(y-y')^2}{2\sigma_y^2} \right]$ $\times \left[\exp \left(-\frac{(z-z')^2}{2\sigma_z^2} \right) - \exp \left(-\frac{(z+z')^2}{2\sigma_z^2} \right) \right]$	Totally absorbing earth at $z = 0$ $\bar{\mathbf{u}} = (\bar{u}, 0, 0)$ $S = Q\delta(x-x')\delta(y-y')\delta(z-z')\delta(t-t')$ $0 \leq z \leq \infty$
$\bar{c}(x, y, z, t) = \frac{Q}{4\pi(K_{xx}K_{yy})^{1/2}(t-t')} \exp \left[-\frac{(x-x'-\bar{u}(t-t'))^2}{4K_{xx}(t-t')} - \frac{(y-y')^2}{4K_{yy}(t-t')} \right]$ $\times \frac{2}{H} \sum_{n=0}^{\infty} \cos \lambda_n z \cos \lambda_n z' \exp[-\lambda_n^2 K_{xx}(t-t')]$ $\lambda_n = \frac{n\pi}{H}$ $\sigma_x^2 = 2K_{xx}(t-t')$ $\sigma_y^2 = 2K_{yy}(t-t')$ $\sigma_z^2 = 2K_{zz}(t-t')$	Totally reflecting earth at $z = 0$ $\bar{\mathbf{u}} = (\bar{u}, 0, 0)$ $S = Q\delta(x-x')\delta(y-y')\delta(z-z')\delta(t-t')$ $0 \leq z \leq H$

$$\begin{aligned}\tilde{c}(x, y, z, t) &= \frac{Q}{4\pi(K_{xx}K_{yy})^{1/2}(t-t')} \exp \left[-\frac{(x-x'-\bar{u}(t-t'))^2}{4K_{xx}(t-t')} - \frac{(y-y')^2}{4K_{yy}(t-t')} \right] \\ &\times \frac{2}{H} \sum_{n=0}^{\infty} \frac{(\lambda_n^2 + \beta^2) \cos[\lambda_n(H-z')] \cos[\lambda_n(H-z)]}{(\lambda_n^2 + \beta^2) + \beta} \\ &\times \exp[-\lambda_n^2 K_{xx}(t-t')] \\ \lambda_n \tan \lambda_n H &= \beta \\ \beta &= v_d/K_{zz} \\ \sigma_x^2 &= 2K_{xx}(t-t') \\ \sigma_y^2 &= 2K_{yy}(t-t') \\ \sigma_z^2 &= 2K_{zz}(t-t')\end{aligned}$$

Gaussian plume formula

$$\tilde{c}(x, y, z) = \frac{q}{2\pi\bar{u}\sigma_y\sigma_z} \exp \left(-\frac{y^2}{2\sigma_y^2} \right) \left[\exp \left(-\frac{(z-h)^2}{2\sigma_z^2} \right) + \exp \left(-\frac{(z+h)^2}{2\sigma_z^2} \right) \right]$$

$$\tilde{c}(x, y, z) = \frac{q}{2\pi\bar{u}\sigma_y\sigma_z} \exp \left(-\frac{y^2}{2\sigma_y^2} \right) \left[\exp \left(-\frac{(z-h)^2}{2\sigma_z^2} \right) - \exp \left(-\frac{(z+h)^2}{2\sigma_z^2} \right) \right]$$

$$\begin{aligned}\tilde{c}(x, y, z) &= \frac{q}{(2\pi)^{1/2}\bar{u}\sigma_y H} \sum_{n=0}^{\infty} \cos \left(\frac{n\pi z}{H} \right) \cos \left(\frac{n\pi h}{H} \right) \\ &\times \exp \left[-\left(\frac{y^2}{2\sigma_y^2} \right) - \left(\frac{n\pi}{H} \right)^2 \frac{\sigma_z^2}{2} \right]\end{aligned}$$

$$\bar{\mathbf{u}} = (u, 0, 0)$$

$$S = Q\delta(x-x')\delta(y-y')\delta(z-z')\delta(t-t')$$

$$0 \leq z \leq H$$

Totally reflecting earth at $z = 0$

$$\bar{\mathbf{u}} = (\bar{u}, 0, 0)$$

$$S = q\delta(x)\delta(y)\delta(z-h)$$

Slender-plume approximation

$$0 \leq z \leq \infty$$

Totally absorbing earth at $z = 0$

$$\bar{\mathbf{u}} = (\bar{u}, 0, 0)$$

$$S = q(x)\delta(y)\delta(z-h)$$

Slender-plume approximation

$$0 \leq z \leq \infty$$

Totally reflecting earth at $z = 0$

$$\bar{\mathbf{u}} = (\bar{u}, 0, 0)$$

$$S = q\delta(x)\delta(y)\delta(z-h)$$

$$0 \leq z \leq H$$

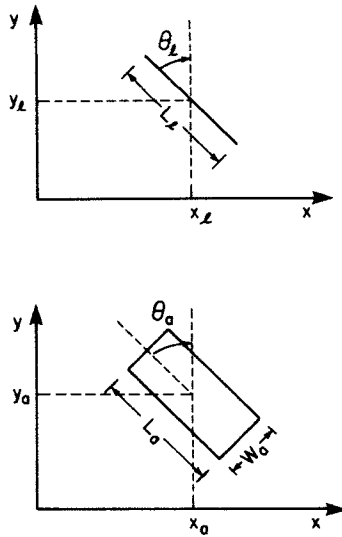


FIG. 2. Line and area sources.

inclined at an angle θ_l to the y axis. Assuming that the wind velocity components are \bar{u} and \bar{v} and that $K_H = K_{xx} = K_{yy}$, the previous solutions may be used to give the mean concentration at time t after the source began emitting at time zero. The result is

$$\begin{aligned} \bar{c}(x, y, z, t) = & \int_0^t \frac{q(\tau) p_z(z, \tau | h, 0) |\sin \theta_l|}{4(\pi K_H \tau)^{1/2}} \\ & \times \exp \left\{ - \frac{[(x - x_l - \bar{x}) \cos \theta_l + (y - y_l - \bar{y}) \sin \theta_l]^2}{4 K_H \tau} \right\} \\ & \times \left\{ \operatorname{erf} \left[\frac{(y - y_l - \bar{y}) \cos \theta_l - (x - x_l - \bar{x}) \sin \theta_l + L_l/2}{2(K_H \tau)^{1/2}} \right] \right. \\ & \left. - \operatorname{erf} \left[\frac{(y - y_l - \bar{y}) \cos \theta_l - (x - x_l - \bar{x}) \sin \theta_l - L_l/2}{2(K_H \tau)^{1/2}} \right] \right\} d\tau \end{aligned} \quad (5.30)$$

where $\bar{x} = \bar{u}t$ and $\bar{y} = \bar{v}t$.

As before, p_z is determined from the vertical boundary conditions. If the source is at height h and the only barrier to diffusion is the ground,

$$p_z(z, t | h, 0) = \frac{1}{2(\pi K_{zz} t)^{1/2}} \left\{ \exp \left[- \frac{(z - h)^2}{4 K_{zz} t} \right] + \exp \left[- \frac{(z + h)^2}{4 K_{zz} t} \right] \right\} \quad (5.31)$$

If a barrier also exists at $z = H$, an alternative form to Eq. (5.28) is

$$p_z(z, t|h, 0) = \frac{1}{2(\pi K_{zz}t)^{1/2}} \sum_{n=-\infty}^{\infty} \left\{ \exp \left[-\frac{(z - h + 2nH)^2}{4K_{zz}t} \right] + \exp \left[-\frac{(z + h + 2nH)^2}{4K_{zz}t} \right] \right\} \quad (5.32)$$

Now we consider the area source shown in Fig. 2. The mean concentration corresponding to Eq. (5.30) is

$$\begin{aligned} \bar{c}(x, y, z, t) = & \int_0^t \frac{q(\tau)p_z(z, \tau|h, 0)}{4} \\ & \times \left\{ \operatorname{erf} \left[\frac{R - W_a/2}{2(K_H\tau)^{1/2}} \right] - \operatorname{erf} \left[\frac{R + W_a/2}{2(K_H\tau)^{1/2}} \right] \right\} \\ & \times \left\{ \operatorname{erf} \left[\frac{T - L_a/2}{2(K_H\tau)^{1/2}} \right] - \operatorname{erf} \left[\frac{T + L_a/2}{2(K_H\tau)^{1/2}} \right] \right\} d\tau \quad (5.33) \end{aligned}$$

where

$$\begin{aligned} R &= (x - x_a - \bar{x}) \cos \theta_a + (y - y_a - \bar{y}) \sin \theta_a \\ T &= (y - y_a - \bar{y}) \cos \theta_a - (x - x_a - \bar{x}) \sin \theta_a \end{aligned} \quad (5.34)$$

D. FLUCTUATING PLUME MODEL

The cornerstone of the Gaussian expressions for the mean concentration from a point source are the standard deviations of plume spread, σ_y and σ_z . Although we have not yet discussed how these quantities vary with downwind distance, some insight into their behavior may be gained by comparing the instantaneous and time-averaged plume. As we have seen, a plume may be thought of conceptually as consisting of an infinite series of overlapping puffs, each released an infinitesimal time interval after the preceding one. Each puff, as it is transported with the mean wind, meanders and expands diffusively in the crosswind, vertical, and downwind directions. If diffusive transport in the downwind direction is small compared to advective transport, then each puff need only be thought of as diffusively spreading in the vertical and crosswind directions as it meanders downwind.

The x axis, aligned with the direction of the mean wind, is assumed to represent the centerline for the mean plume. At any instant, the center of a particular disk is conceived of as having a random displacement (D_y, D_z) from the fixed position of the x axis. The coordinates (D_y, D_z) vary not

only as a function of travel time for each disk but also for successive puffs at the same travel times. We note that the ensemble average of many puffs viewed at the same travel times, $t - t_0$, is analogous to averaging the real plume at a fixed downwind position, $x = \bar{u}(t - t_0)$, for a significant finite averaging time δT .

If it is now assumed that the crosswind and vertical concentration distributions in each disk are Gaussian, i.e.,

$$c(x, y, z) = \frac{Q}{2\pi\bar{u}(\bar{Y}^2\bar{Z}^2)^{1/2}} \exp \left[-\frac{(y - D_y)^2}{2\bar{Y}^2} - \frac{(z - D_z)^2}{2\bar{Z}^2} \right] \quad (5.35)$$

where \bar{Y}^2 and \bar{Z}^2 are the variances of the material distribution in the crosswind and vertical directions, respectively, at $x = \bar{u}(t - t_0)$ and are functions of x , and if it is also assumed that the probability density functions of the disk center displacements D_y and D_z are Gaussian,

$$\begin{aligned} g_y(D_y) &= [2\pi\bar{D}_y^2]^{-1/2} \exp[-y^2/2\bar{D}_y^2] \\ g_z(D_z) &= [2\pi\bar{D}_z^2]^{-1/2} \exp[-z^2/2\bar{D}_z^2] \end{aligned} \quad (5.36)$$

where $\bar{D}_y = \bar{D}_z = 0$, then an expression for the mean concentration $\bar{c}(x, y, z)$ can be obtained by taking the expected value of Eq. (5.35) (Gifford, 1959). The result is the so-called fluctuating plume model:

$$\begin{aligned} \bar{c}(x, y, z) &= \frac{q}{2\pi\bar{u}[(\bar{Y}^2 + \bar{D}_y^2)(\bar{Z}^2 + \bar{D}_z^2)]^{1/2}} \\ &\times \exp \left[-\frac{y^2}{2(\bar{Y}^2 + \bar{D}_y^2)} - \frac{z^2}{2(\bar{Z}^2 + \bar{D}_z^2)} \right] \end{aligned} \quad (5.37)$$

The dispersive contributions due to plume spreading (given by \bar{Y}^2 and \bar{Z}^2) are statistically independent of the contributions due to plume meandering (given by \bar{D}_y^2 and \bar{D}_z^2). The fluctuating plume model is depicted in Fig. 3.

Gifford (1960) has also shown, for the case of one-dimensional spreading, that the sum of the mean square dispersion due to spreading of the plume elements and the dispersion of the center of the plume as a result of the overall plume fluctuations is equal to the total average dispersion of the plume:

$$\sigma_y^2 = \bar{Y}^2 + \bar{D}_y^2, \quad \sigma_z^2 = \bar{Z}^2 + \bar{D}_z^2 \quad (5.38)$$

where \bar{Y}^2 is the variance of the instantaneous concentration of the fluctuating plume in the crosswind direction, centered about the crosswind displacement of fluctuating plume, D_y , from the axis of the mean plume; \bar{Z}^2 is the variance of the instantaneous concentration of the fluctuating plume in the vertical direction, centered about the vertical displacement

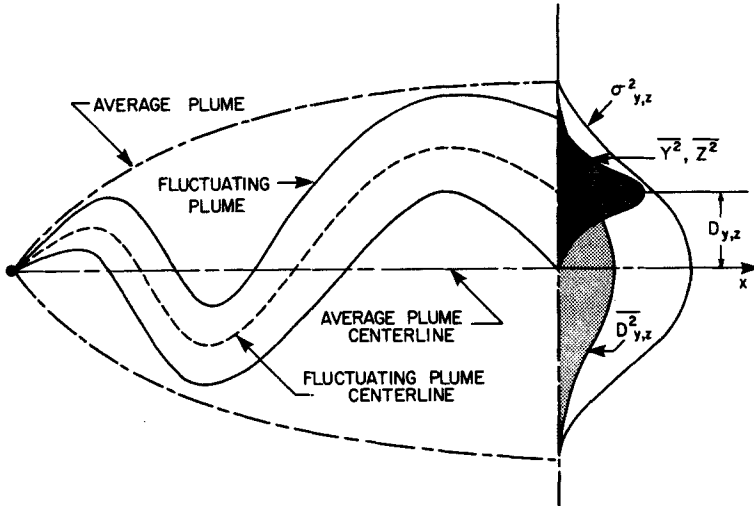


FIG. 3. Definitions of quantities associated with average and fluctuating plumes.

of the fluctuating plume, D_z , from the axis of the mean plume; $\overline{D_y^2}$ is the variance in the crosswind direction of the frequency distribution of the fluctuating plume centerline displacement from the mean plume axis, i.e., the variance of the frequency distribution of D_y ; and $\overline{D_z^2}$ is the variance (vertical direction) of the frequency distribution of D_z .

In Eq. (5.9), the reflection condition at the ground is accomplished by taking the solution for an actual source position $(0, 0, h)$ and adding to this the solution for a fictitious image source at the position $(0, 0, -h)$. Consequently, the exponential term in z in Eq. (5.9) is merely replaced by one exponential term in $(z - h)$ and another exponential term in $(z + h)$. This technique directly accomplishes reflection only because the Gaussian material distribution of the steady-state plume is symmetric with respect to the mean plume line.

For the fluctuating plume model, the simple addition of the solutions for sources at altitudes h and $-h$ will not accomplish reflection because the asymmetries due to plume meandering must also be reflected in the fictitious image source at $-h$. The correct reflection for the fluctuating plume model is

$$c(x, y, z) = \frac{q}{2\pi(\overline{Y^2}\overline{Z^2})^{1/2}} \exp \left\{ -\frac{(y - D_y)^2}{2\overline{Y^2}} \right\} \\ \times \left\{ \exp \left[-\frac{(z - h - D_z)^2}{2\overline{Z^2}} \right] + \exp \left[-\frac{(z + h + D_z)^2}{2\overline{Z^2}} \right] \right\} \quad (5.39)$$

where c is the instantaneous concentration. The expected value of Eq. (5.39) provides the concentration of the time-averaged plume,

$$\bar{c}(x, y, z) = \frac{q}{2\pi(\bar{Y}^2 + \bar{D}_y^2)^{1/2}(\bar{Z}^2 + \bar{D}_z^2)^{1/2}\bar{u}} \exp\left\{-\frac{y^2}{2(\bar{Y}^2 + \bar{D}_y^2)}\right\} \\ \times \left\{\exp\left[-\frac{(z-h)^2}{2(\bar{Z}^2 + \bar{D}_z^2)}\right] + \exp\left[-\frac{(z+h)^2}{2(\bar{Z}^2 + \bar{D}_z^2)}\right]\right\} \quad (5.40)$$

VI. Validity of the Atmospheric Diffusion Equation

To arrive at the atmospheric diffusion equation (3.17), a number of constraints must be imposed (Seinfeld, 1975). The deviation between reality and these constraints will thus represent a measure of the inaccuracies associated with the atmospheric diffusion equation. Among these constraints, the following two are most pertinent:

(1) The time scale for describing the temporal variations of the pollutant species, T , is large when compared with the time scale characterizing the turbulent processes in the atmosphere (i.e., the Lagrangian time scale, T_L).⁹ Thus, $T \gg T_L$.

(2) The length scale for describing the spatial variation of the pollutant species, L , is large when compared with the turbulent mean free path, l , a distance traveled by a particle in time T_L . Assuming the root-mean-square (rms) turbulent velocity of the particle is \bar{u} , this condition can be expressed as $L \gg l = \bar{u}T_L$.

According to measurements made in the atmosphere, the Lagrangian time scale is of the order of 100 sec (Csanady, 1973). Using a characteristic particle velocity of 5 m sec⁻¹, the above conditions are $T \gg 100$ sec and $L \gg 500$ m. Since one primary concern is to examine diffusion from point sources such as industrial stacks, which are generally characterized by small T and L , it is apparent that either one (but particularly the second one) or both of the above constraints cannot be satisfied, at least locally, in the vicinity of the point-like source. Therefore, in these situations, it is important to assess the error incurred by the use of the atmospheric diffusion equation.

This problem has been addressed by Corrsin (1974) for several simple hypothetical cases. Many qualitative and, in some instances, semiquanti-

⁹ The Lagrangian integral time scale T_L can be considered as a measure of the time during which a fluid particle persists, in the mean, in a motion in a given direction. In Section VIII we will discuss T_L quantitatively. Where unambiguous, T_L will be denoted simply by T .

tative estimates have been obtained. By first writing a general equation describing the transport process, a simplified form of the atmospheric diffusion equation, a one-dimensional counterpart of Eq. (3.17) can be derived if one assumes that the transporting mechanism is fairly local in space and time, that the transporting mechanism is homogeneous and stationary, that the transporting mechanism is symmetric in space, and that the transporting mechanism is characterized by negligible higher derivatives. The validity of these assumptions is essentially dependent upon the so-called homogeneity condition and stationarity condition of the mean field. Based on a simple kinetic theory (a random walk model), it was shown (Corrsin, 1974) that these two conditions can be expressed as follows

$$(\bar{c}_{zzz}/\bar{c}_z)(l^2/24) \ll 1 \quad (\text{homogeneity condition})$$

$$(\bar{c}_z/\bar{c}_z)T_L \ll 1 \quad (\text{stationarity condition})$$

where the subscripts z and t indicate partial derivatives of the mean concentration \bar{c} . Thus, the left-hand sides (denoted below as E_1 and E_2 , respectively) may be used as measures of the possible error associated with the use of the atmospheric diffusion equation. Using turbulent boundary layer data collected by Blackwelder and Kovaszny (1972), Corrsin (1974) estimated the Lagrangian integral time scale T_L and the turbulent mean free path l to be

$$T_L = \begin{cases} 4.2\delta/\bar{u} & \text{at } z/\delta = 0.20 \\ 6.8\delta/\bar{u} & \text{at } z/\delta = 0.45 \end{cases}$$

$$l = \begin{cases} 0.23\delta & \text{at } z/\delta = 0.20 \\ 0.31\delta & \text{at } z/\delta = 0.45 \end{cases}$$

where δ is a boundary layer thickness defined by $\bar{u}(x, \delta) = 0.99\bar{u}_\infty$, where \bar{u}_∞ is the free stream velocity. He was therefore able to establish that the criteria analogous to the left-hand sides of the above conditions are

$$E_1 = \begin{cases} 12\% & \text{at } z/\delta = 0.20 \\ 4\% & \text{at } z/\delta = 0.45 \end{cases}$$

$$E_2 = \begin{cases} 0.5\% & \text{at } z/\delta = 0.20 \\ 0.9\% & \text{at } z/\delta = 0.45 \end{cases}$$

Thus, for the case of a turbulent boundary layer, although the stationarity condition is fairly well satisfied, the homogeneity condition is probably satisfied only for $z/\delta \geq 0.2$.

This analysis can also be extended to the dispersion of point source emissions in the atmosphere if we assume that the mean concentration gradient is expressed by $\bar{c}_z \sim \alpha/z$, where α is a constant that is proportional to the emission rate. It then can be shown that

$$E_1 \equiv \frac{\bar{c}_{zzz}}{\bar{c}_z} \frac{l^2}{24} = \frac{1}{12} \left(\frac{l}{z} \right)^2$$

Thus, using the estimated turbulent mean free path in the atmosphere of 500 m, the above criterion gives $E_1 \leq 10\%$ if $z \geq 0.913l \sim 450$ m.

The approach described above is by no means complete or exclusive. For example, Lamb *et al.* (1975) have proposed an alternative route to assess the adequacy of the atmospheric diffusion equation. Their approach is based on the Lagrangian description of the statistical properties of nonreacting particles released in a turbulent atmosphere. By employing the boundary layer model of Deardorff (1970), the transition probability density $p(x, y, z, t|x', y', z', t')$ is determined from the statistics of particles released into the computed flow field. Once p has been obtained, Eq. (3.1) can then be used to derive an estimate of the mean concentration field. Finally, the validity of the atmospheric diffusion equation is assessed by determining the profile of vertical diffusivity that produced the best fit of the predicted mean concentration field.

It was found by Lamb *et al.* (1975) that the errors are nearly randomly distributed in space except for the neutral case where rather large errors occur near the source. That the errors are larger in this region is consistent with the conclusion drawn from theoretical considerations that the gradient transport hypothesis should not hold when the length scale of the mean concentration distribution is comparable to or smaller than the Lagrangian length scale of turbulence, as we have shown previously by adopting Corrsin's approach. For the most part, however, it appears that the use of the atmospheric diffusion equation is reasonable. Errors in the calculated concentrations are not larger than about 10% at points farther than about $6u_* / f$ (where u_* denotes the friction velocity and f the Coriolis parameter¹⁰) from the source in the neutral case and at nearly all points at ground level in the unstable case. These conclusions, again, are qualitatively consistent with those obtained earlier, following Corrsin's analysis.

In summary, we conclude that the application of the atmospheric diffusion equation to point sources will introduce an error of the order of 10% into predictions at points reasonably well removed (on the order of 1 km) from the source.

¹⁰ See Section VII for definitions of these quantities.

VII. Meteorological Parameters Characterizing the Atmospheric Boundary Layer

Material released at or near the earth's surface is dispersed in the planetary boundary layer. The portion of the planetary boundary layer closest to the surface is called the *surface layer*, and that above the surface layer is called the *Ekman layer*. The Ekman layer extends to a height of from 300 to 500 m depending on the type of terrain, with the greater thickness corresponding to the more disturbed terrain. In the Ekman layer, the wind direction tends to turn clockwise with increasing height in the Northern Hemisphere (counterclockwise in the Southern Hemisphere). The wind speed in the Ekman layer generally increases rapidly with height; however, the rate lessens as the free atmosphere is approached. The exact distribution of the wind speed depends on many parameters, particularly the vertical distribution of the horizontal pressure gradient as well as the atmospheric stability. The layer immediately adjacent to the surface, typically up to 100 m from the ground, is called the surface layer. Within this layer, the vertical turbulent fluxes of momentum and heat are assumed constant with respect to height, and indeed they define the extent of this region.

In this section primary attention is directed at the turbulent processes that occur in the mixed layer as a result of the interaction between shear- and buoyancy-driven flows. The flux Richardson number R_f gives a measure of the relative importance of the buoyancy terms in the equations of motion, $(g/T)\overline{w'\theta'}$, as compared to the shear production terms, $\overline{u'w'} \partial \bar{u} / \partial z$, i.e.,

$$R_f = \frac{(g/T)\overline{w'\theta'}}{\overline{u'w'} \partial \bar{u} / \partial z} \quad (7.1)$$

where $\overline{w'\theta'}$ is a measure of the kinematic sensible heat flux, $\overline{u'w'}$ is the x component of vertical momentum flux, and T and θ are the absolute and potential temperature, respectively.¹¹ When R_f is large, the flow is dominated by buoyancy effects. The flux Richardson number is a function of the distance from the ground and is thus a measure of the local stability of the turbulent flow.

A major deterrent to the use of Eq. (7.1) as a measure of atmospheric

¹¹ The potential temperature θ is that to which dry air originally in the state (T, p) would come if brought adiabatically to p_0 . Adiabatic temperature profiles expressed in terms of θ are vertical on a plot of z vs θ , facilitating comparisons of actual temperature profiles to the adiabatic lapse rate.

stability is the need for simultaneous determinations of both the heat and momentum fluxes. Another approach is to define a quantity similar to Eq. (7.1) called the gradient Richardson number R_i ,

$$R_i = \frac{g}{T} \frac{\partial \theta}{\partial z} \left(\frac{\partial \bar{u}}{\partial z} \right)^{-2} \quad (7.2)$$

The relationship between R_f and R_i is

$$R_f = (K_h/K_m) R_i \quad (7.3)$$

where K_m and K_h are the eddy diffusion coefficients for momentum and heat, respectively.

Another stability parameter often used in micrometeorology is the Monin–Obukhov length

$$L = - \frac{u_*^3 c_p \rho T}{k Q_0 g} \quad (7.4)$$

where c_p is the specific heat of air at constant pressure, ρ the air density, k the von Karman constant (0.4), g the acceleration of gravity, Q_0 the vertical heat flux, and u_* the friction velocity (see Section VII,C). Physically, the Monin–Obukhov length is the approximate height above the surface at which the production of turbulence by buoyancy effects becomes comparable to that by shear effects. The Monin–Obukhov length L , like R_f , provides a measure of the stability of the surface layer: stable for $L > 0$, neutral for $L = \infty$, and unstable for $L < 0$. The interpretation of L in terms of atmospheric stability is given in Table III.

Atmospheric stability is frequently characterized in terms of the Pasquill A–F stability classes (Pasquill, 1961). The A–F categories refer to atmospheric conditions as follows: A—very unstable, B—moderately un-

TABLE III
INTERPRETATION OF THE MONIN–OBUKHOV LENGTH L WITH RESPECT TO
ATMOSPHERIC STABILITY

L		Stability condition
Small negative	$-100 \text{ m} < L < 0$	Very unstable
Large negative	$-10^5 \text{ m} \leq L \leq -100 \text{ m}$	Unstable
Very large (positive or negative)	$ L > 10^5 \text{ m}$	Neutral
Large positive	$10 \text{ m} \leq L \leq 10^5 \text{ m}$	Stable
Small positive	$0 < L < 10 \text{ m}$	Very stable

stable, C—slightly unstable, D—neutral, E—moderately stable, and F—very stable.

A. ESTIMATION OF THE MONIN-OBUKHOV LENGTH

The Monin-Obukhov length L is not a parameter that is routinely measured. Golder (1972), however, established a relation between the stability classes of Pasquill, the roughness height z_0 (see Section VII,B), and L . The results of his investigation are shown in Fig. 4. Alternatively, the local wind speed and cloud cover measurements are used to estimate the Pasquill stability class (Table IV). In addition, Golder developed a nomogram for relating the gradient Richardson number R_i to the more easily determined bulk Richardson number R_b :

$$R_b = \frac{g}{T} \frac{\partial \theta}{\partial z} \left[\frac{z}{\bar{u}} \right]^2 \quad (7.5)$$

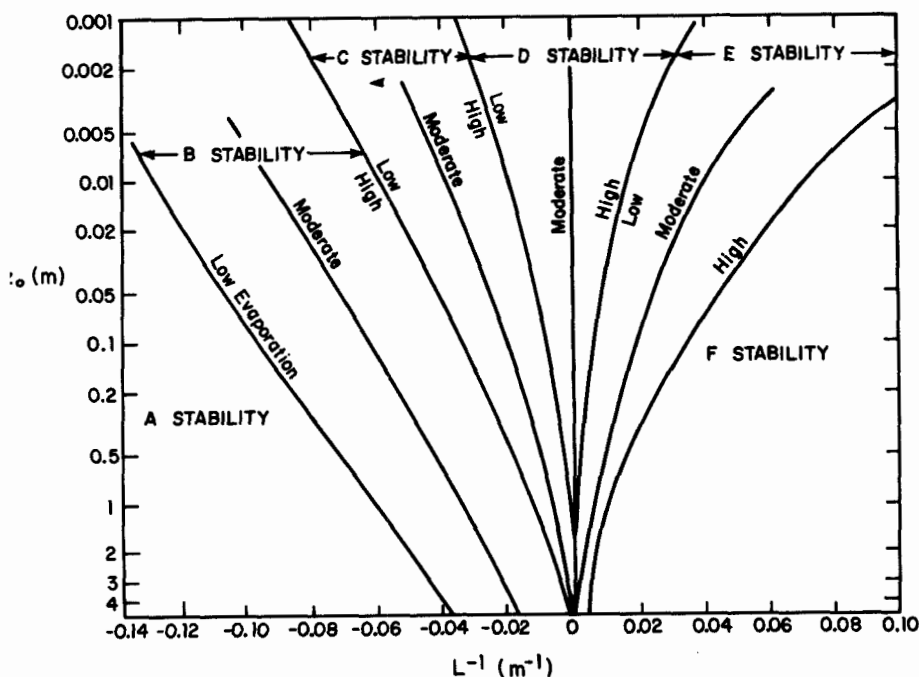


FIG. 4. Relationship between Monin-Obukhov length L and roughness height z_0 for various Pasquill stability classes. From Myrup and Ranzieri (1976).

TABLE IV
ESTIMATION OF PASQUILL STABILITY CLASSES^a

Surface wind speed at 10 m (m sec ⁻¹)	Solar radiation ^b			Night-time Cloud cover fraction	
	Strong	Moderate	Slight	≥ $\frac{4}{8}$	≤ $\frac{4}{8}$
<2	A	A-B	B		
2-3	A-B	B	C	E	F
3-5	B	B-C	C	D	E
5-6	C	C-D	D	D	D
>6	C	D	D	D	D

Incoming radiation ^b (category)	Solar insolation	
	langley min ⁻¹	W m ⁻²
Strong	$I > 1.0$	$I > 700$
Moderate	$0.5 \leq I \leq 1.0$	$350 \leq I \leq 700$
Slight	$I < 0.5$	$I < 350$

^a From Turner (1969).

In order to simplify calculation of $1/L$, Golder's (1972) stability classes can be approximated by a single straight line of $1/L$ against surface roughness. The parameters for the straight-line approximations to the stability classes are shown in Table V.

The Monin-Obukhov length L can also be estimated from conventional meteorological data by first evaluating the parameter a (Fulle, 1975):

$$a = \left[\left(10 + \frac{\partial T}{\partial z} \right)^{-2} + 0.0025 \frac{\partial u}{\partial z} \right]^{-1/2} \quad (7.6)$$

where the vertical temperature gradient $\partial T/\partial z$ is in units of degrees Celsius per 100 m, and the vertical wind speed gradient $\partial u/\partial z$ is in units of reciprocal seconds. The Pasquill stability class corresponding to a given value of a is determined as shown in Table VI. Then, L is determined within each class as a function of roughness length z_0 from Fig. 4.

B. ESTIMATION OF SURFACE ROUGHNESS

The effects of small-scale surface irregularities on the boundary layer transfer processes are usually incorporated only through the surface roughness parameter z_0 . The range of variation of z_0 over different land

TABLE V
COEFFICIENTS FOR STRAIGHT-LINE APPROXIMATION TO
GOLDER'S PLOT AS A FUNCTION OF STABILITY CLASSES

$$1/L = a + b \log_{10} z_0$$

Stability condition	Pasquill stability class	Coefficients	
		<i>a</i>	<i>b</i>
Extremely unstable	A	-0.096	0.029
Moderately unstable	B	-0.037	0.029
Slightly unstable	C	-0.002	0.018
Neutral	D	0	0
Slightly stable	E	0.004	-0.018
Moderately stable	F	0.035	-0.036

types is quite large, and the measurements required to estimate the effective roughness are quite complex. As an alternative, Plate (1971) proposed a simple formula that relates z_0 to the mean canopy height h_c :

$$z_0 = 0.15h_c \quad (7.7)$$

Depending on the conditions, the "constant" 0.15 varied from $\frac{1}{7}$ to $\frac{1}{30}$. Figure 5 presents surface roughness values for a variety of land use categories compiled primarily from the reviews of Myrup and Ranzieri (1976) and Hodgkin (1980) and presented by McRae *et al.* (1982). The precision implied by some entries on the figure is deceptive because there is considerable scatter in many of the underlying experimental data.

When a region includes a large body of water, the roughness cannot be characterized by simply associating h_c with the wave height. Unlike the land, the effective roughness of the water surface is a dynamic variable whose magnitude is influenced by factors such as the wave state and wind stress. There is a variety of models of the air-sea interaction and

TABLE VI
RELATIONSHIP OF PASQUILL STABILITY CATEGORIES TO
RANGES OF THE PARAMETER a^a

<i>a</i>	Stability category	<i>a</i>	Stability category
$a \leq 7.0$	A	$8.75 < a \leq 9.5$	D
$7.0 < a \leq 8.0$	B	$9.5 < a \leq 11.25$	E
$8.0 < a \leq 8.75$	C	$11.25 < a \leq 13.5$	F

^a From Fulle (1975).

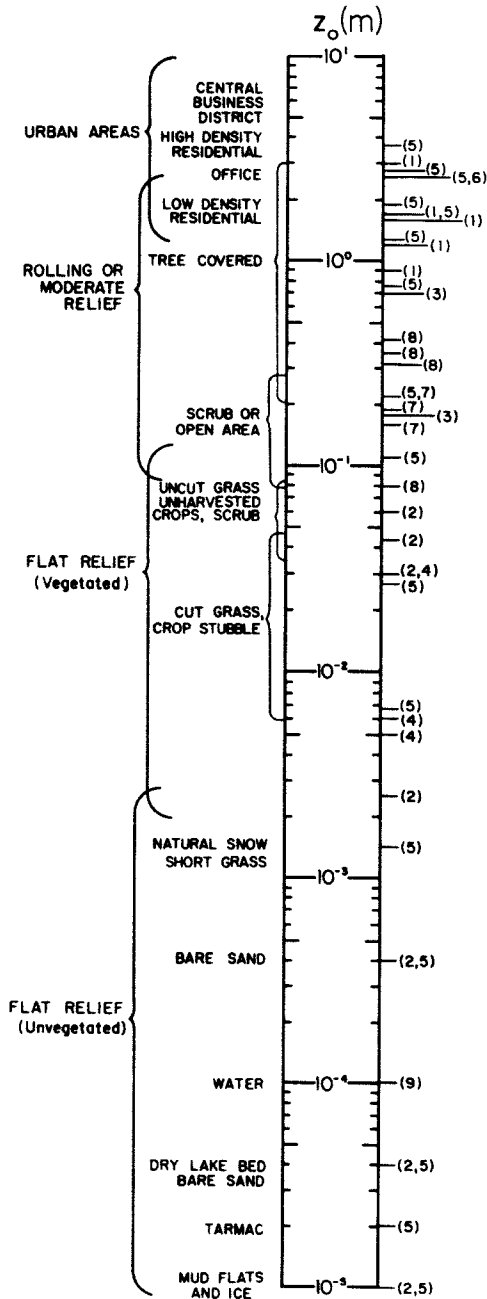


FIG. 5. Surface type and aerodynamic roughness: (1) Counihan (1975); (2) Deacon (1949); (3) Fichtl and McVehil (1970); (4) Golder (1972); (5) Myrup and Ranzieri (1976); (6) Slade (1969); (7) Touma (1977); (8) Weber *et al.* (1975); (9) see text. From McRae *et al.* (1982).

its influence on z_0 . The studies by Gent (1977), Hsu (1974), and Kitaigorodskii (1970) illustrate some of the complexities. Arya (1977) has recently reviewed some of the simpler parameterizations that are applicable to the present study. For example, Wipperman (1972) has suggested the following formula for smooth as well as rough conditions:

$$z_0 = 0.1\nu/u_* + bu_*^2/g \quad (7.8)$$

where ν is the kinematic viscosity of air and b is a constant (≈ 0.02). The formula implies a considerably increasing trend in z_0 ; the results of Stewart (1974) and calculations by Gent (1977) imply a more or less constant value of $z_0 \approx 0.01$ – 0.02 cm for 10-m wind speeds in the range 6–12 m sec^{-1} .

C. DETERMINATION OF THE FRICTION VELOCITY u_*

Close to the ground, in the constant flux layer, u_* is a measure of the turbulent transfer of momentum. The friction velocity is defined by

$$u_*^2 = \tau_0/\rho = -\overline{u'w'} \quad (7.9)$$

where τ_0 is the shear stress per unit area of the boundary and ρ is the density of the fluid. Monin–Okukhov similarity theory predicts that the mean wind speed gradient is representable as

$$\partial\bar{u}/\partial z = (u_*/kz)\phi_m(z/L) \quad (7.10)$$

where $\phi_m(z/L)$ is a universal function (Monin and Yaglom, 1971). The friction velocity can be obtained by integrating Eq. (7.10) between z_0 and a reference height z_r at which a measurement of \bar{u} is available:

$$u_* = k\bar{u}(z_r) \left[\int_{z_0}^{z_r} \phi_m \left(\frac{z}{L} \right) \frac{dz}{z} \right]^{-1} \quad (7.11)$$

where it has been assumed that $\bar{u}(z_0) = 0$.

Generally accepted forms of the universal function ϕ_m are those of Businger *et al.* (1971):

$$\phi_m \left(\frac{z}{L} \right) = \begin{cases} 1 + 4.7z/L & \text{for } z/L > 0 \text{ (stable)} \\ 1 & \text{for } z/L = 0 \text{ (neutral)} \\ [1 - 15z/L]^{-1/4} & \text{for } z/L < 0 \text{ (unstable)} \end{cases} \quad (7.12)$$

These forms of ϕ_m can be used in Eq. (7.11) to obtain the following expressions for u_* :

$$\frac{\bar{u}_*}{k\bar{u}(z_r)} = \begin{cases} \left[\ln\left(\frac{z_r}{z_0}\right) + \frac{4.7}{L}(z_r - z_0) \right]^{-1} & \text{for } z/L > 0 \\ \left[\ln\left(\frac{z_r}{z_0}\right) \right]^{-1} & \text{for } z/L = 0 \\ \left\{ \ln\left(\frac{z_r}{z_0}\right) + \ln \left[\frac{(\zeta_0^2 + 1)(\zeta_0 + 1)^2}{(\zeta_r^2 + 1)(\zeta_r + 1)^2} \right] \right. \\ \quad \left. + 2[\tan^{-1}\zeta_r - \tan^{-1}\zeta_0] \right\}^{-1} & \text{for } z/L < 0 \end{cases} \quad (7.13)$$

$$\zeta_r = [1 - 15z_r/L]^{1/4}, \quad \zeta_0 = [1 - 15z_0/L]^{1/4}$$

where the $z/L < 0$ form in Eqs. (7.13) is not the exact integral of Eq. (7.11) but has values very close to the exact integral while not suffering from numerical divergence in the neutral limit (Benoit, 1977).

D. THE CONVECTIVE BOUNDARY LAYER

When the turbulence in the atmospheric boundary layer is maintained largely by buoyant production, the boundary layer is said to be in a convective state. The source of buoyancy is the upward heat flux originating from the ground heated by solar radiation. Convective turbulence is relatively vigorous and causes rapid vertical mixing in the atmospheric boundary layer.

The height of the atmospheric or planetary boundary layer under neutral conditions can be estimated from (Blackadar and Tennekes, 1968)

$$z_p = au_*f \quad (\text{neutral}) \quad (7.14)$$

where f is the Coriolis parameter and a is a constant (≈ 0.35) (Zilitinkevich, 1972).¹² Under nonneutral conditions the corresponding estimates are (Zilitinkevich, 1972)

$$z_p = \begin{cases} \alpha(u_*f)(u_*fL)^{-1/2} & (\text{stable}) \\ \alpha(u_*f)(-u_*fL)^{1/2} & (\text{unstable}) \end{cases} \quad (7.15)$$

where the stable value is not allowed to exceed that calculated from Eq. (7.14) and the unstable value is not allowed to be less than that calculated from Eq. (7.14).

The determination of z_p under unstable conditions is usually not critical

¹² The Coriolis parameter f is defined by $f = 2\omega \cos \phi$, where ω is the earth's rotation rate and ϕ is the latitude.

to performing atmospheric diffusion calculations because a temperature inversion layer, which limits the extent of vertical mixing, is generally present at some height z_i well below z_p . The value of the height z_i of the base of an elevated inversion layer can be determined from a temperature sounding as the height at which the potential temperature equals the potential temperature at the surface. In short, z_i is the height at which a line of slope $-0.0098^\circ\text{C m}^{-1}$ (the so-called dry adiabat) extended up from the observed surface temperature intersects the measured temperature profile. The height z_i then serves as the upper vertical boundary location to define the layer $(0, z_i)$ within which diffusion occurs.

From the definition of the Monin–Obukhov length, shear production of turbulence is confined to a layer of height of the order of $|L|$. Under convective conditions, then, we expect

$$-L/z_i \ll 1 \quad (7.16)$$

Equation (7.16) can be written as

$$-L/z_i = (u_*/w_*)^{1/3} \ll 1 \quad (7.17)$$

where w_* is the *convective velocity scale* given by

$$w_* = \left(\frac{g}{T_0} Q_0 z_i \right)^{1/3} \quad (7.18)$$

Velocity and temperature gradients are confined to the surface layer defined by $z < |L|$. Above $|L|$ the wind velocity and potential temperature are virtually uniform with height. Venkatram (1978) has presented a method to estimate the value of the convective velocity scale w_* . On the basis of this method, he showed that convective conditions in the planetary boundary layer are a common occurrence (Venkatram, 1980). In particular, the planetary boundary layer is convective during the daytime hours for a substantial fraction of each year (~ 7 months). For example, for a wind speed of 5 m sec^{-1} , a kinematic heat flux Q_0 as small as $0.1^\circ\text{C sec}^{-1}$ can drive the planetary boundary layer into a convective state.

VIII. Dispersion Parameters in Gaussian Models

In Section V we derived several Gaussian-based models for estimating the mean concentration resulting from point source releases of material. We have seen that the conditions under which the equation is valid are highly idealized and therefore that it should not be expected to be applicable to very many actual ambient situations. Because of its simplicity,

nevertheless, the Gaussian plume equation has been applied widely (Environmental Protection Agency, 1980). The justification for these applications is that the dispersion parameters σ_y and σ_z (σ_x , σ_y , and σ_z in the case of an instantaneous release) used have been derived from concentrations measured in actual atmospheric diffusion experiments under conditions approximating those of the application. This section is devoted to a summary of several results available for estimating Gaussian dispersion coefficients.

A. SPATIAL AND TEMPORAL AVERAGING

It is useful to begin our discussion with a consideration of spatial and temporal averaging, with particular reference to the dispersion of emissions from a continuous point source. A key problem in specifying plume dispersion is distinguishing between mean and turbulent motions. The demarcation line is indeed arbitrary and depends on the averaging time involved. Roughly speaking, the demarcation line lies between eddies much larger in dimension than the instantaneous plume width and all eddies below the scale of the instantaneous plume width.

The very large eddies contribute to changes in the instantaneous wind vector. The very smallest eddies cause slight dispersive spreading of the plume, but eddies about the same size as the local plume width are the most effective in producing turbulent plume dispersion. Eddies larger than the instantaneous plume width but smaller than the characteristic horizontal scale of the region of interest (typically, the downwind distance from the source) produce the meandering character of the instantaneous plume. In summary, if l is the characteristic eddy dimension, x is the characteristic horizontal scale of the region, and D is the average instantaneous plume width, then the role of eddies in plume dispersion is given by the following:

- (1) $l \ll D$, slight plume dispersion and internal plume mixing;
- (2) $l \sim D$, most effective in plume dispersion;
- (3) $D < l \leq x$, produces plume meandering;
- (4) $l > x$, produces changes in the wind vector.

If a plume is photographed or measured by a device having an averaging time of the order of a fraction of a second, the appearance will have a sinuous form. The sinuosities appear to increase in amplitude and characteristic wavelength as one observes at greater distances from the source. Generally, eddies of all scales can be expected to be present in the atmosphere but not necessarily to an equal degree. Near the source, the diffu-

sive spreading of the plume is produced by the small turbulent eddies comparable in scale to the initial plume width. As the plume is advected downwind, the instantaneous plume spreads horizontally and vertically and also tends to meander within more or less definite limits. The amplitude of the crosswind and vertical meandering increases as the plume is advected downwind, as does the apparent effective wavelength of the sinuosities. The increasing crosswind and vertical spreading in the downwind direction constantly brings into play larger-scale eddies that become the most effective in spreading the instantaneous plume. Based on the above observations, one would expect the effective wavelength of the sinuosities to increase in the downstream direction, since this "effective" wavelength must also be characteristic of the dominant scale of the eddies producing the meandering effect.

The description of the plume physics given above intimately associates the spatial scale of eddies governing the phenomena of plume spread and meander with the downwind distance from the source. However, the description also implies certain temporal scales that, together with these spatial scales, dictate the state of the plume actually measured or observed. First, the downwind distance from the source, x , can be associated with a time, $\Delta\tau$, based on the fact that transport in that direction is mostly due to advection, $x \sim \bar{u} \Delta\tau$. Similarly, at any given downwind distance x , there is some associated spatial range of eddies. Measurements or observations of the plume made at position x would have to be repeated over some time interval, δt , in order to view approximately the same values of the state more than once, i.e., in order to just average out the meandering effects. The time δt must be associated with the time interval required to advect the governing range of eddies past the observation point. Since the scale of eddies l is not a single well-defined value, the time scale of δt is also not well defined. However, in some sense, we would expect $\delta t = [l/\bar{u}]_{\max}$. Since l is proportional to x , δt increases downstream from the source. In terms of meandering, we know that l is bounded by x , so that, for example, if $\bar{u} \sim 5 \text{ m sec}^{-1}$:

$$\delta t \sim 20 \text{ sec}, \quad x \sim 100 \text{ m}$$

$$\delta t \sim 3 \text{ min}, \quad x \sim 1 \text{ km}$$

$$\delta t \sim \frac{1}{2} \text{ hr}, \quad x \sim 10 \text{ km}$$

$$\delta t \sim 5 \text{ hr}, \quad x \sim 100 \text{ km}$$

The form of the instantaneous cross-sectional distribution will be a function of the initial conditions and, again, the averaging time associated with the "instantaneous" observation. Close to the source, the measure-

ment time must be fairly short in order to differentiate between the instantaneous plume and the plume averaged over the short period meandering motions. Consequently, observations of the instantaneous plume for small distances x can be expected to show a rather irregular cross-sectional material distribution. However, for large distances x , the irregularities due to initial conditions can be expected to be sharply reduced. Also, longer measurement times can be made of the instantaneous plume without averaging out the meandering motion. For long measurement times, the small scale turbulent eddies can be expected to smooth the material distribution in the "instantaneous" plume, so that its form may be similar to the cross-sectional distribution obtained by averaging over the meandering motions. A truly instantaneous view could be expected to portray an irregular cross-sectional material distribution at any distance x .

The question now arises as to how the average plume will be manifested when viewed or measured with an instrument that has a fixed averaging time, $\delta T = \delta T' = \text{constant}$. Clearly, $\delta T'$ can correspond to the characteristic time scale of the dominant eddies that produce meandering near only one downstream position x' , $\delta T' = \delta t(x')$. For all positions $0 \leq x \leq x'$, $\delta T'$ will be longer than the characteristic time scale $\delta t(x)$ of the eddies that produce meandering and for all positions $x' < x \leq x_0$, $\delta T'$ will be shorter than the characteristic time scale $\delta t(x)$. When $x \gg x'$, then $\delta t \gg \delta T'$ and one can expect to view what is essentially the "instantaneous" meandering plume with a possibly non-Gaussian cross-sectional concentration distribution having a central peak offset from the axis of the mean wind. For $x \ll x'$, then $\delta t \ll \delta T'$ and the averaging time of the instrument will include the effect of eddies larger than the dominant class of eddies responsible for meandering; the motion of these eddies would normally be ascribed to the mean wind by an observer fixed at that location.

Based on the manner of derivation of the Gaussian equations in Section III, we see that the dispersion parameters σ_y and σ_z are originally defined for an instantaneous release and are functions of travel time from release. Since the puff equations depend on the travel time of individual puffs or releases, the dispersion coefficients depend on this time, i.e., these coefficients describe the growth of each puff about its own center. This is basically a Lagrangian formulation.

In determining how the dispersion coefficients depend on travel time one may employ atmospheric diffusion theory or the results of experiments. Because of the difficulty of performing puff experiments, however, the coefficients are usually inferred not from instantaneous releases but from continuous releases. Thus, the dispersion coefficients derived from such experiments are essentially a measure of the size of the plume envelope formed by sampling a real meandering plume emitted from a

continuous point source for, say, 1 hr. Consequently, to the extent that the puff equation represents the plume envelope, one is treating the envelope as though it were composed of a continuous train of effective spherical puffs ($\sigma_x = \sigma_y$) whose growth is specified by the desired dispersion coefficients. This decomposition of the plume envelope into a continuous train of effective puffs is not the same as building up a plume envelope from an ensemble of isolated true puffs the growth of which is specified by true Lagrangian coefficients. This distinction arises because the effects of mutual interactions of overlapping puffs are taken into account in an average way in the effective puff picture but not in the true individual puff picture. Because the experimentally determined σ_y and σ_z values that are generally used are based on plume experiments, it seems reasonable that this distinction will not be of concern in the application of formulas.

In the puff situation the overlapping train of effective puffs that contribute to the mean concentration at a receptor location at a particular time have a range of travel times associated with them and therefore have undergone a range in degree of growth. For the steady-state equation, there is, strictly speaking, only one time that can be defined, the time x/\bar{u} . Consequently, the dispersion coefficients, if expressed in terms of travel time, are evaluated at the times x/\bar{u} corresponding to the source-receptor pair of interest.

B. DETERMINATION OF σ_y AND σ_z

The basic Gaussian plume dispersion parameters are σ_y and σ_z . The essential theoretical result concerning the dependence of these parameters on travel time is for stationary, homogeneous turbulence (Taylor, 1921). Consider marked particles that are released from the origin in a stationary, homogeneous turbulent flow with a mean flow in the x direction. The y component, ζ_y , of the position of a fluid particle satisfies the equation

$$d\zeta_y/dt = v'(t) \quad (8.1)$$

where $v'(t)$ is the Lagrangian velocity of the particle at time t , evidently the velocity component in the y direction at the position of the marked fluid particle at time t . Since we have assumed no mean flow in the y direction, $v'(t)$ is just the fluctuating component $v'(\zeta_y(t), t)$. Equation (8.1) may be integrated from $t = 0$, the assumed time of release of the particle, to time t , to give

$$\zeta_y(t) = \int_0^t v'(\tau) d\tau \quad (8.2)$$

We are interested in computing the ensemble mean square deviation of all particles, $\langle \zeta_y^2 \rangle$. This quantity is, in fact, one of the desired elements of **P**. If we multiply Eq. (8.1) by (8.2), integrate, and then take the ensemble mean of the resulting equation, we obtain

$$\langle \zeta_y^2(t) \rangle = 2 \int_0^t \int_0^{t'} \langle v^j(\tau) v^j(t') \rangle d\tau dt' \quad (8.3)$$

The value of the joint moment, $\langle v^j(\tau) v^j(t') \rangle$, indicates the degree of correlation between the y components of the velocities of a fluid particle at times τ and t' . This joint moment is usually expressed in terms of the Lagrangian velocity autocorrelation:

$$R(t', \tau) = \frac{\langle v^j(\tau) v^j(t') \rangle}{\langle v^2 \rangle} \quad (8.4)$$

where the mean square $\langle v^2 \rangle$ is independent of time and location due to the assumption of stationary, homogeneous turbulence. In fact, in stationary, homogeneous turbulence, $R(t', \tau) = R(t' - \tau)$. Using Eq. (8.4) in Eq. (8.3), we have

$$\langle \zeta_y^2(t) \rangle = 2\langle v^2 \rangle \int_0^t \int_0^{t'} R(t' - \tau) d\tau dt' \quad (8.5)$$

Another quantity of interest is the Lagrangian integral time scale,

$$T = \int_0^\infty R(\eta) d\eta \quad (8.6)$$

the value of which is indicative of the length of temporal correlation between the Lagrangian velocities.

The limiting behavior of $\langle \zeta_y^2 \rangle$ at small times ($t \rightarrow 0$) is obtained by noting that $R(\eta) = 1$ as $\eta \rightarrow 0$. For long times ($t \rightarrow \infty$) the definition of T can be employed. The results are

$$\langle \zeta_y^2(t) \rangle = \begin{cases} \langle v^2 \rangle t^2 & \text{for } t \ll T \\ 2\langle v^2 \rangle T t & \text{for } t \gg T \end{cases} \quad (8.7)$$

It has been pointed out over the years that the simple exponential function of the form $e^{-t/T}$, where t is travel time from the source, appears to approximate the Lagrangian velocity autocorrelation function $R(t)$ rather well (Neumann, 1978; Tennekes, 1979). If $R(t) = \exp(-t/T)$, then the mean square particle displacement is given by (Taylor, 1921)

$$\begin{aligned}
 \langle \zeta_y^2(t) \rangle &= 2\langle v^2 \rangle \int_0^t (t - t') R(t') dt' \\
 &= 2\langle v^2 \rangle \int_0^t (t - t') e^{-t'/T} dt' \\
 &= 2\langle v^2 \rangle T^2 [t/T - (1 - e^{-t/T})]
 \end{aligned} \tag{8.8}$$

This result is seen to be identical to Eq. (3.14) if $\beta = T^{-1}$. If the exponential function in Eq. (8.8) is expanded in a Taylor series near $t = 0$,

$$\langle \zeta_y^2(t) \rangle = \langle v^2 \rangle t^2 - \frac{1}{3} \langle v^2 \rangle t^3/T + \dots \tag{8.9}$$

The first term of Eq. (8.9), identical to that given in Eqs. (8.7), describes turbulent diffusion very close to the source. Particle paths remain straight lines as long as the Lagrangian velocity remains equal to that at the time of departure from the source (Tennekes, 1979). The second term in Eq. (8.9) shows that the dispersion rate slows down relative to the initial stage of turbulent diffusion. This term reflects the fact that Lagrangian velocities gradually lose their correlation as the time interval increases.

The results just obtained for $\langle \zeta_y^2 \rangle$ are, however, rarely used in applications because $\langle v^2 \rangle$ and T are generally not known. The Gaussian dispersion parameters σ_y^2 and σ_z^2 are, in a sense, generalizations of $\langle \zeta_y^2 \rangle$ and $\langle \zeta_z^2 \rangle$. The particle displacement variances σ_y^2 and σ_z^2 are not calculated by Eq. (8.8). Rather, they are treated as empirical dispersion coefficients the functional forms of which are determined by matching the Gaussian solution to data. In that way, the empirically determined σ_y and σ_z actually compensate for deviations from stationary, homogeneous conditions which are inherent in the assumed Gaussian distribution.

There exist a number of correlations for the dispersion parameters σ_y and σ_z as a function of downwind distance x and atmospheric stability. These correlations have been reviewed extensively and repeatedly, and the reader is referred to Gifford (1976), Weber (1976), American Meteorological Society Workshop (1977), Doran *et al.* (1978), Irwin (1979), and Sedefian and Bennett (1980) for comprehensive summaries of the available formulas. In particular, these references provide one with the relations necessary to select σ_y and σ_z for a specific application. We do not endeavor to survey these relations here.

Of the two standard deviations σ_y and σ_z , more is known about σ_y . First, most of the experiments from which σ_y and σ_z values are inferred involve ground-level measurements. Such measurements provide an adequate indication of σ_y , whereas vertical concentration distributions are needed to determine σ_z . Also, the Gaussian expression for vertical con-

centration distribution is known not to be obeyed for ground-level releases (see Section IX,D), so the fitting of a measured vertical distribution to a Gaussian form is considerably more difficult than that for the horizontal distribution where lateral symmetry and an approximate Gaussian form are good assumptions.

Some of the correlations for σ_y have the convenient form

$$\sigma_y(x) = \sigma_y^0 x^a \quad (8.10)$$

where the constants σ_y^0 and a depend on the atmospheric stability and the averaging time. The vertical standard deviation can likewise be expressed in the form¹³

$$\sigma_z(x) = \sigma_z^0 x^b \quad (8.11)$$

where σ_z^0 is a function of atmospheric stability and averaging time. In contrast to Eq. (8.10), in some sets of correlations, b is a function both of atmospheric stability and of downwind distance x . It has been found that in such cases $b(x)$ may be approximated by

$$b(x) = b_0 + b' \exp(-\lambda x) \quad (8.12)$$

where b_0 , b' , and λ are all functions of atmospheric stability. $b_0 > 0$ for all stability conditions, but conditions for b' are as follows: unstable for $b' > 0$, neutral for $b' \approx 0$, and stable for $b' < 0$. For small x , $b(x) \rightarrow b_0 + b'$, and for large x , $b(x) \rightarrow b_0$. Table VII summarizes four correlations for σ_y and σ_z that can be expressed in the form of Eqs. (8.10)–(8.12). In presenting these forms, we are not necessarily recommending their use. The reader is urged to consult the references cited above for guidance in selecting a set of σ_y and σ_z correlations for a particular application.

C. DISPERSION COEFFICIENTS IN CONVECTIVE CONDITIONS

The case of convective conditions is a special one in determining atmospheric dispersion (Section VII,D). Since under convective conditions the most energetic eddies in the mixed layer scale with z_i , the time scale relevant to dispersion is z_i/w_* . This time scale is therefore roughly the time needed after release for material to become well mixed through the

¹³ Because of the accuracy of the exponential form of the Lagrangian velocity correlation function $R(t)$ and the resulting simplicity of the expression (8.8) for $\langle z_i^2 \rangle$, Neumann (1978) has questioned the use of the power-law forms for σ_y and σ_z . Although estimates of $\langle v^2 \rangle$ and T are seldom available, Neumann argues that the parameters σ_y^0 and a or σ_z^0 and b must also be estimated, and, in fact, the relationship of these parameters to physical quantities is not known. He shows that excellent approximation is obtained when Eq. (8.8) is fit to a set of commonly used dispersion parameters.

TABLE VII
COEFFICIENTS IN GAUSSIAN PLUME DISPERSION PARAMETER CORRELATIONS^a

Source	Averaging time (min)	Coefficient	Stability class					
			A	B	C	D	E	F
$\sigma_y(x) = \sigma_y^0 x^a$ and $\sigma_z(x) = \sigma_z^0 x^b$								
Pasquill-Gifford (Turner, 1969; Gifford, 1961)	10	σ_y^0	0.443	0.324	0.216	0.141	0.105	0.071
American Society of Mechanical Engineers (1973)	60	a	0.894	0.894	0.894	0.894	0.894	0.894
		σ_y^0	0.40	0.36		0.32		0.31
		a	0.91	0.86		0.78		0.71
		σ_z^0	0.40	0.33		0.22		0.06
		b	0.91	0.86		0.78		0.71
Klug (1969)	10	σ_y^0	0.469	0.306	0.230	0.219	0.237	0.273
		a	0.903	0.885	0.855	0.764	0.691	0.594
		σ_z^0	0.017	0.072	0.076	0.140	0.217	0.262
		b	1.380	1.021	0.879	0.727	0.610	0.500
		$\sigma_z(x) = \sigma_z^0 x^{b_0 + b' \exp(-\lambda x)}$						
Pasquill-Gifford (Turner, 1969; Gifford, 1961; Diamante <i>et al.</i> , 1976)	10	σ_z^0	0.000186	0.0560	0.107	0.385	0.428	0.432
		b_0	2.13	1.10	0.918	0.638	0.570	0.511
		b'	0.749	0.105	0.00164	-0.159	-0.162	-0.194
		$\lambda \times 10^3$	8.73	8.74	6.55	5.11	4.30	3.58

^a x in meters.

depth of the mixed layer. The dimensionless travel distance $X = xw_*/\bar{u}z_i$ can then be defined.

As we have noted in Section VII,D, the wind is essentially uniform in $|L| < z < z_i$. In the same region the standard deviation of the horizontal velocity fluctuations $\sigma_v \sim w_*$ (Kaimal *et al.*, 1976). Thus, it can be assumed that the lateral standard deviation σ_y can be described by

$$\sigma_y/z_i = g(X) \quad (8.13)$$

The definition of X incorporates the fact that the Lagrangian integral time scale is of the order of z_i/w_* . The statistical theory of turbulent diffusion outlined in the beginning of Section VIII,B can be used to estimate the functional dependence of g as

$$g(X) \sim \begin{cases} X & \text{for small } X \\ X^{1/2} & \text{for large } X \end{cases} \quad (8.14)$$

Vertical dispersion cannot be described in such simple terms (Kaimal *et al.*, 1976). First, σ_w varies throughout the planetary boundary layer. In the region, $|L| < z < 0.1z_i$, $\sigma_w \sim z^{1/3}$, and σ_w scales with w_* only above $0.1z_i$. For $z_i = 1500$ m and an effective stack height of 400 m, the dispersing plume is controlled by an inhomogeneous region that is almost half the effective stack height.

Venkatram (1980) has summarized the aspects of dispersion in the convective boundary layer:

The longevity and coherence of the thermal plumes in the PBL can give rise to unusual effects. Pollutants emitted into a downdraft may continue to travel downward until they impact on the ground. Similarly pollutants caught in an updraft can be carried up all the way to the top of the mixed layer. As the downdraft velocities are smaller and less turbulent the plume is more coherent when it travels downwards. This causes the locus of maximum concentration to descend from the source. Numerical modeling shows (Lamb, 1979) that for source heights greater than $0.25z_i$ this rate of descent is about $0.5w_*$. It is also found that the centerline rises upwards some distance downwind of the point of impingement.

The estimation of ground-level concentrations close to an elevated source under convective conditions is difficult. Concentrations can be predicted with considerably more accuracy after the emissions have become nearly well mixed. The work of Willis and Deardorff (1976) suggests that mixing throughout the boundary layer is nearly complete at $X = 3$. Beyond this distance the mean ground-level concentration can be estimated as

$$\bar{c} \sim q/\bar{u}z_i^2 g(X) \quad (8.15)$$

which, on the basis of the range of X dependences of $g(X)$, leads to the functional dependence,

$$\bar{c} \sim X^{-\alpha}, \quad \frac{1}{2} < \alpha < 1 \quad (8.16)$$

In water tank studies Willis and Deardorff (1978) found $\alpha = 0.82$.

The study of Lamb (1979) has provided some understanding of the concentration distribution close to the source ($X < 3$). He has shown that for release heights $z_s > 0.25z_i$, the maximum concentration at the point of impingement x_i is given by

$$\bar{c}_{\max} \sim q/\bar{u}z_s z_i \quad (8.17)$$

This result implies that the effect of the mixed layer height z_i is felt by the plume by the time it impinges at x_i . Assuming a downdraft velocity of $0.5w_*$, $x_i = 2\bar{u}z_s/w_*$. Thus, for $z_s/z_i = 0.25$, the point of impingement corresponds to $X = 0.5$, implying that z_i affects the concentration even before $X = 1$.

D. DETERMINATION OF $\overline{D_y^2}$ AND $\overline{D_z^2}$

The state of theoretical and observational knowledge of the fluctuating plume parameters, including the horizontal and vertical variances $\overline{D_y^2}$ and $\overline{D_z^2}$ (Diamante *et al.*, 1976) of the distribution of the instantaneous plume centerline displacement with respect to the mean plume axis, is limited. We note the relations that were developed in Section V,D:

$$\sigma_y^2 = \overline{D_y^2} + \overline{Y^2}, \quad \sigma_z^2 = \overline{D_z^2} + \overline{Z^2} \quad (8.18)$$

relating the parameters of the mean and fluctuating plume models.

Hilst (1957) measured the variances of the instantaneous and mean plumes for very stable conditions for $x < 1$ km and found that $\overline{D_y^2}$ could be represented by

$$\overline{D_y^2} = \overline{D_{y0}^2} x^{2d} \quad (8.19)$$

where $\overline{D_{y0}^2}$ is a constant. In addition, he found that $\overline{D_y^2}$ contributed one half or more of the total variance σ_y^2 and that these instances divided about equally between the situations $\overline{D_y^2} \approx \overline{Y^2}$ and $\overline{D_y^2} \gg \overline{Y^2}$. Thus, this implies that $\frac{1}{2}(\sigma_y^0)^2 \leq \overline{D_{y0}^2} < (\sigma_y^0)^2$, and that a reasonable estimate of $\overline{D_{y0}^2}$ is $\frac{1}{2}(\sigma_y^0)^2$. From Eq. (8.10) and Table VII, we see that $b \sim d \sim 1.0$.

Since the width of the instantaneous plume can never equal zero for $x > 0$, we know that $\overline{D_{y0}^2} < (\sigma_y^0)^2$ for all $x > 0$. However, it is clear from the fact that

$$\overline{D_y^2} \rightarrow \overline{D_{y\infty}^2} \quad \text{and} \quad \overline{D_z^2} \rightarrow \overline{D_{z\infty}^2} \quad \text{as} \quad x \rightarrow \infty \quad (8.20)$$

and Eq. (8.10) that $\overline{Y^2}$ must eventually predominate as $x \rightarrow \infty$, so that if Eq. (8.19) were to hold for all x , then $d = d(x) \rightarrow 0$ for $x \rightarrow \infty$. Since the fluctuations characterized by D_y are of amplitude determined by the range of turbulent eddies whose scale is proportional to the distance from the source up to some limiting scale, we would further expect $\overline{D_y^2}$ to be a monotone increasing function of x .

Little is known about the actual limiting value $\overline{D_{y\infty}^2}$ or the downwind distance x_∞ at which this value is reached. Let $x = x_p$ be the hypothetical distance at which $\overline{D_y^2} = \overline{D_{y\infty}^2}$ from Eq. (8.19), i.e.,

$$\overline{D_{y\infty}^2} = \overline{D_{y0}^2} x_p^{2d} \quad (8.21)$$

Assume that Eq. (8.19) is actually valid out to a distance $x \leq \frac{1}{2}x_p$. Furthermore, let the actual limit $\overline{D_{y\infty}^2}$ be approximately achieved at a distance $x = 2x_p$. A relation for $\overline{D_y^2}$ that provides a smooth transition in the range $\frac{1}{2}x_p \leq x \leq 2x_p$ is (Diamante *et al.*, 1976)

$$\overline{D_y^2} = \overline{D_{y0}^2} [x_p \tanh(x/x_p)]^{2d} \quad (8.22)$$

By analogy with $\overline{D_y^2}$, we can assume

$$\overline{D_z^2} = \overline{D_{z0}^2} x^{2e} \quad (8.23)$$

for $x < x_p/2$. If $\overline{D_z^2} \rightarrow \overline{D_{z\infty}^2}$ as $x \rightarrow \infty$, then we can define the distance

$$x'_p = [\overline{D_{z\infty}^2} / \overline{D_{z0}^2}]^{1/2e} \quad (8.24)$$

and the interpolation relation,

$$\overline{D_z^2} = \overline{D_{z0}^2} [x'_p \tanh(x/x'_p)]^{2e} \quad (8.25)$$

For the exponent e , by analogy to Eq. (8.12), it can be assumed that

$$e(x) = e_0 + e' \exp(-\Lambda x) \quad (8.26)$$

where, for lack of better information, it can be assumed that $e_0 \cong b_0$, $e' \cong b'$, and $\Lambda \cong \lambda$, i.e., $\overline{D_z^2}$ follows approximately the same power law as σ_z^2 for $x \leq x'_p/2$. For very stable conditions, however, $\overline{D_z^2} \cong \overline{D_{z\infty}^2} \cong \overline{D_{z0}^2}$ are very small. Then, $e' \cong e_0$, $e_0 \cong b_0$, $\Lambda \cong 0$.

E. DETERMINATION OF $\overline{Y^2}$ AND $\overline{Z^2}$

As $x \rightarrow \infty$, Batchelor (1950) has shown that the variance of the instantaneous relative concentration distribution $\overline{Y^2}$ must become independent of two-particle statistics. As a consequence, $\overline{D_y^2} \rightarrow \overline{D_{y\infty}^2}$ and $\overline{Y^2} \sim \sigma_y^2$. Consequently, for all x , the power law

$$\overline{Y^2} = \overline{Y_0^2} x^{2\eta} \quad (8.27)$$

can be expected to provide a reasonable approximation. As noted previously, Hilst's observations indicated that meandering effects either dominated relative diffusion effects or contributed about equally, so that $\eta \sim d \sim a$ and $0 < \overline{Y}^2 \leq \frac{1}{2}\sigma_y^2$.

Theoretical considerations and observations for neutral stability indicate for small x that $\overline{Y}^2 \sim \frac{1}{2}\sigma_y^2$, where σ_y^2 is determined for averaging times on the order of tens of minutes (Högström, 1964). Consequently, \overline{Y}_0^2 can be estimated as $\frac{1}{2}(\sigma_y^0)^2$. If Eq. (8.8) holds strictly, then \overline{Y}_0^2 must actually be a weak function of x , i.e.,

$$\overline{Y}_0^2 = \frac{1}{2}(\sigma_y^0)^2 \left\{ 2x^{2(a-\eta)} - \frac{2\overline{D}_y^2}{(\sigma_y^0)^2} \left[x_p \tanh\left(\frac{x}{x_p}\right) \right]^{2d} x^{-2\eta} \right\} \quad (8.28)$$

The quantity in brackets is $\cong 1$ for $x \leq x_p/2$.

With respect to \overline{Z}^2 , observations for neutral stability and small x indicate that $\overline{Z}^2 \sim \frac{1}{2}\sigma_z^2$. Hilst (1957) made observations of σ_z^2 under very stable conditions, so that vertical meandering was almost completely suppressed and $\sigma_z^2 \sim \overline{Z}^2$. The observations were limited in extent but supported the relation

$$\overline{Z}^2 = \overline{Z}_0^2 x^{2e'} \quad (8.29)$$

and leveled out so that $\sigma_z^2 \sim \overline{Z}^2 \rightarrow \text{constant}$ for $x > 300$ m.

Since the very little theoretical or observational information that is available concerning \overline{Y}^2 and \overline{Z}^2 is not in conflict with Eqs. (8.18) and with the functional forms proposed for the pairs (σ_y^2, σ_z^2) and $(\overline{D}_y^2, \overline{D}_z^2)$, we can assume \overline{Y}^2 and \overline{Z}^2 to be determined by Eqs. (8.18), namely

$$\overline{Y}^2 = \sigma_y^2 - \overline{D}_y^2, \quad \overline{Z}^2 = \sigma_z^2 - \overline{D}_z^2 \quad (8.30)$$

F. AVERAGING TIME CONSIDERATIONS

At various points in Section VIII we have referred to the concept of averaging time. As we have used it, the term "averaging time" refers to the time period over which measurements are made, and was denoted by δt in Section VIII,A.

Ordinarily one deals with averaging times less than about 5 hr. Experience suggests that the concept of a mean wind (magnitude \bar{u} and direction) is reasonably valid over an interval of 2–3 hr, but breaks down rapidly after 5 hr. The value of 5 hr also coincides with the appropriate averaging times for which the mean plume model will be valid at downwind distances of approximately 100 km.

As noted in Section VIII,A for a given downwind position x from a point source, there is an averaging time $\delta t \sim x/\bar{u}$ that will be just appropri-

ate for the measurement to apply to the mean plume representation. This order of δt is the value required to view approximately the same values of the concentration more than once, i.e., in order to properly average out the meandering effect. The mean plume model still applies for averaging times δT much larger than this δt . However, if $\delta T \gg \delta t$, dispersion effects of larger-scale eddies enter. If, on the other hand, $\delta T \ll \delta t$, the correct local representation is the fluctuating plume model.

The available values of $\sigma_y(x)$ and $\sigma_z(x)$ are based on averaging times ranging from 10 min to 1 hr depending on the particular correlation chosen. For example, the widely used Pasquill–Gifford correlations, as reported in Turner (1969), are based on a 10-min averaging time. Based on the above discussion, we see that σ values determined on a 10-min time scale apply only to distances relatively close to the source, since $\delta t \sim x/\bar{u}$ implies that for any reasonable wind speed, an averaging time of about 10 min at a 100-km downwind distance would still apply to the fluctuating plume. Most of the original data were in fact taken at distances < 1 km from the source. Turner (1969) has indicated reasonable accuracy of the Pasquill–Gifford σ -curves for distances ranging from a few hundred meters to 10 km or more depending on stability conditions. For an averaging time of 10 min and wind speeds in the range $1\text{--}10\text{ m sec}^{-1}$, $\delta t \sim x/\bar{u}$ implies values of x ranging from 600 m to 6 km.

At downwind distance x the characteristic time scale $\delta\tau$ of the eddies governing the crosswind fluctuations is bounded by

$$2\sqrt{2}\sigma_y^0 x^a/\bar{u} < \delta\tau < x/\bar{u} \quad (8.31)$$

The condition for an averaging time δT to apply to the fluctuating plume is $\delta T \leq 2\sqrt{2}\sigma_y^0 x^a/\bar{u}$. For the measurement to apply to the mean plume, the condition is $\delta T > x/\bar{u}$.

The question now arises as to how to relate dispersion parameters σ_y and σ_z measured over two different averaging times. It has been suggested that peak ground-level concentrations measured over two averaging times, δt and δT , can be related by (Herman, 1980)

$$c(\delta T)/c(\delta t) = (\delta t/\delta T)^s \quad (8.32)$$

Conservation of mass suggests a relation between the product of the peak values of mean plume concentrations and the corresponding dispersion parameters (σ_y , σ_z) for all averaging times

$$c_{\max}(\delta T)\sigma_y(x; \delta T)\sigma_z(x; \delta T) = c_{\max}(\delta t)\sigma_y(x; \delta t)\sigma_z(x; \delta t) \quad (8.33)$$

Equations (8.32) and (8.33) give

$$\sigma_y(x; \delta T)\sigma_z(x; \delta T) = \sigma_y(x; \delta t)\sigma_z(x; \delta t)(\delta T/\delta t)^s \quad (8.34)$$

Assuming the same dependence on averaging time for both σ_y and σ_z ,

$$\frac{\sigma_y(x; \delta T)}{\sigma_y(x; \delta t)} = \frac{\sigma_z(x; \delta T)}{\sigma_z(x; \delta t)} = \left(\frac{\delta T}{\delta t}\right)^{s/2} \quad (8.35)$$

Herman (1980) has surveyed values of s in Eq. (8.35) for data on SO_2 . He found that a value of $s = 0.5$ best fit the data analyzed, with an uncertainty in s of ± 0.2 .

IX. Parameters in the Atmospheric Diffusion Equation

The atmospheric diffusion equation

$$\begin{aligned} \frac{\partial \bar{c}}{\partial t} + \bar{u} \frac{\partial \bar{c}}{\partial x} + \bar{v} \frac{\partial \bar{c}}{\partial y} + \bar{w} \frac{\partial \bar{c}}{\partial z} \\ = \frac{\partial}{\partial x} \left(K_{xx} \frac{\partial \bar{c}}{\partial x} \right) + \frac{\partial}{\partial y} \left(K_{yy} \frac{\partial \bar{c}}{\partial y} \right) + \frac{\partial}{\partial z} \left(K_{zz} \frac{\partial \bar{c}}{\partial z} \right) + S \end{aligned} \quad (2.19)$$

embodies information on the flow field and the nature of turbulent mixing through the mean velocities and the eddy diffusivities. While the Gaussian equations of Section V have been widely used for atmospheric diffusion estimates, the underlying presumption of stationary, homogeneous turbulence and a uniform velocity field imposes restrictions on the situations in which the equations may be employed with a degree of confidence. To deal with situations where inhomogeneities exist, such as shear flows, resource is often made to Eq. (2.19). There exist a number of solutions of Eq. (2.19) under various assumptions concerning the spatial dependences of the mean velocities and eddy diffusivities. The key problem is to choose the functional forms of these coefficients in a manner consistent with observations and available theories of turbulent diffusion.

A. MEAN WIND SPEED

The mean wind speed is often represented as a power-law function of height which may be expressed as

$$\bar{u}/\bar{u}_r = (z/z_r)^p \quad (9.1)$$

The exponent p is then to be determined on the basis of atmospheric conditions. By differentiating Eq. (9.1) with respect to z , p is found from

$$p = (z/\bar{u})(\partial \bar{u}/\partial z) \quad (9.2)$$

Monin–Obukhov similarity theory, as expressed by (7.10), can be used in (9.2) to give

$$p = (u_* / k\bar{u})\phi_m(z/L) \quad (9.3)$$

which can be expressed as

$$p = \frac{\phi_m(z/L)}{F(z/L, z_0/L)} \quad (9.4)$$

A functional representation of the approximate form of the universal function F has been obtained by Huang and Nickerson as (Huang, 1979)

$$F\left(\frac{z}{L}, \frac{z_0}{L}\right) = \ln \left[\frac{(\zeta - 1)(\zeta_0 + 1)}{(\zeta + 1)(\zeta_0 - 1)} \right] + 2[\tan^{-1} \zeta - \tan^{-1} \zeta_0] \quad (9.5)$$

where $\zeta = \phi_m(z/L)^{-1}$ and $\zeta_0 = \phi_m(z_0/L)^{-1}$. Huang (1979) has presented values of the power law index p computed from Eqs. (9.4), (7.12), and (9.5), and these values are reproduced in Fig. 6.

B. VERTICAL EDDY DIFFUSION COEFFICIENTS

Monin–Obukhov similarity theory can be used to prescribe the form of K_{zz} in the surface layer. K_{zz} can be expressed as

$$K_{zz} = \frac{ku_* z}{\phi(z/L)} \quad (9.6)$$

where $\phi(z/L)$ is a universal function of z/L for material transport. The universal function $\phi_m(z/L)$, for momentum transport, as determined by Businger *et al.* (1971), has been given by Eq. (7.12). The function $\phi(z/L)$ can be expressed as

$$\phi\left(\frac{z}{L}\right) = \begin{cases} 1 + 4.7z/L & \text{for } z/L > 0 \\ 1 & \text{for } z/L = 0 \\ [1 - 15z/L]^{-1/2} & \text{for } z/L < 0 \end{cases} \quad (9.7)$$

where for stable and neutral conditions $\phi(z/L) = \phi_m(z/L)$, whereas for unstable conditions $\phi(z/L) = \phi_m^2(z/L)$ by analogy to heat transport (Galbally, 1971; Crane *et al.*, 1977).

1. Unstable Conditions

If we define K_{zz}^m as the eddy diffusivity for momentum, the vertical eddy diffusion coefficient under unstable conditions can be expressed as

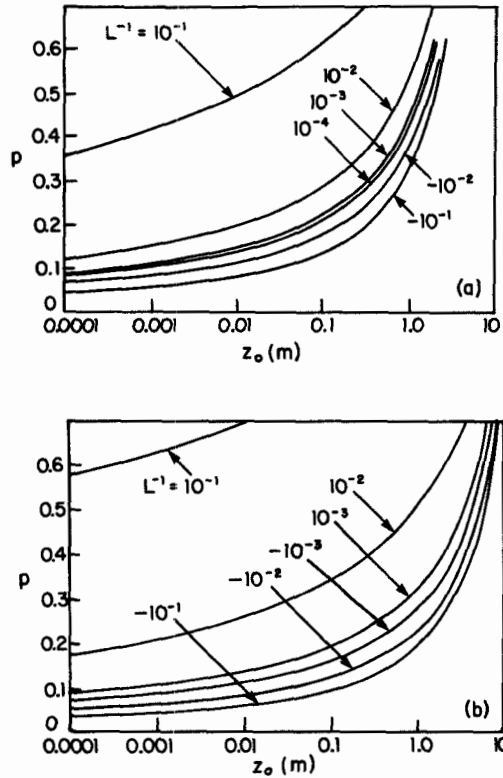


FIG. 6. Variation of the power law index p with surface roughness and Monin-Obukhov length L : (a) $z = 10$ m; (b) $z = 30$ m. From Huang (1979).

$$K_{zz} = \frac{K_{zz}^m}{\phi_m(z/L)} \quad (9.8)$$

We note that the assumption that $K_{zz} \approx K_{zz}^m$ can lead to an underestimate of K_{zz} by a factor of three.

Carl *et al.* (1973) suggested an expression for K_{zz}^m that closely fits a second-order closure model calculation of Zeman and Lumley (1976):

$$K_{zz}^m = 2.5w_*z_i(kz/z_i)^{4/3} \quad (9.9)$$

Combining Eqs. (9.8) and (9.9) gives an expression for K_{zz} in the surface layer under unstable conditions:

$$K_{zz} = 2.5w_*z_i(kz/z_i)^{4/3}[1 - 15z/L]^{1/4} \quad (9.10)$$

Now we consider specification of K_{zz} in the Ekman layer. We begin with convective (unstable) conditions. Lamb *et al.* (1975) derived empiri-

cal expressions for K_{zz} using the numerical turbulence model of Deardorff (1970). Lamb and Duran (1977) improved the numerical procedures of the earlier paper and extended the stability range from $z/L < -4.5$ to $z/L < -1100$. When scaled with w_* , the convective velocity, and z_i , the diffusivity profiles are sufficiently similar in shape to suggest that a single profile of the form $\bar{K}_{zz} = K_{zz}/w_*z_i = \psi(z/z_i)$ might be applicable. Convective scaling is appropriate because L is small compared with z_i . The function ψ can be assumed to be universal under the following conditions: (i) the turbulence structure within the mixed layer is self-similar and in equilibrium with the current boundary conditions and (ii) the normalized eddy diffusivity \bar{K}_{zz} is independent of the nature of the pollutant source distribution (Crane *et al.*, 1977). In practice, the equilibrium condition is usually satisfied since it requires that the mixed layer depth varies slowly, i.e., that $\partial z_i/\partial t \ll w_*$. Willis and Deardorff (1976) indicate that self-similarity occurs after $w_*x/\bar{u}z_i$ exceeds 2.5, where x is the distance covered after the material has been released. Condition (ii) is not, in general, satisfied in convectively driven flows. If the eddy diffusivity were truly a local property of the turbulent flow, then K_{zz} would be independent of the height of source emissions. Lamb and Duran (1977) determined that the form of the K_{zz} profile is quite dependent on the source height. With the proviso that the result be applied when emissions are released or at near ground level and so a single profile is applicable, the form of K_{zz} recommended for unstable conditions is (see Fig. 7)

$$\frac{K_{zz}}{w_*z_i} = \begin{cases} 2.5(kz/z_i)^{4/3}[1 - 15(z/L)]^{1/4}, & 0 \leq z/z_i < 0.05 \\ 0.021 + 0.408(z/z_i) + 1.351(z/z_i)^2 \\ \quad - 4.096(z/z_i)^3 + 2.560(z/z_i)^4, & 0.05 \leq z/z_i \leq 0.6 \\ 0.2 \exp[6 - 10(z/z_i)], & 0.6 < z/z_i \leq 1.1 \\ 0.0013, & z/z_i > 1.1 \end{cases} \quad (9.11)$$

The maximum value of the diffusivity occurs when $z/z_i \approx 0.5$ and has a magnitude $\approx 0.21w_*z_i$. For typical meteorological conditions this corresponds to a diffusivity of $O(100 \text{ m}^2 \text{ sec}^{-1})$ and a characteristic diffusion time defined by z_i^2/K_{zz} of $O(5z_i/w_*)$. Yamada (1977), for example, has observed diffusivities of $O(100 \text{ m}^2 \text{ sec}^{-1})$ when simulating the Wangara day 34 field experiment. Above the surface layer the observational evidence is inadequate to verify more than an order of magnitude estimate of the diffusivity. Clearly there is a need for more field data to establish the shape of the profile in the upper portions of the mixed layer.

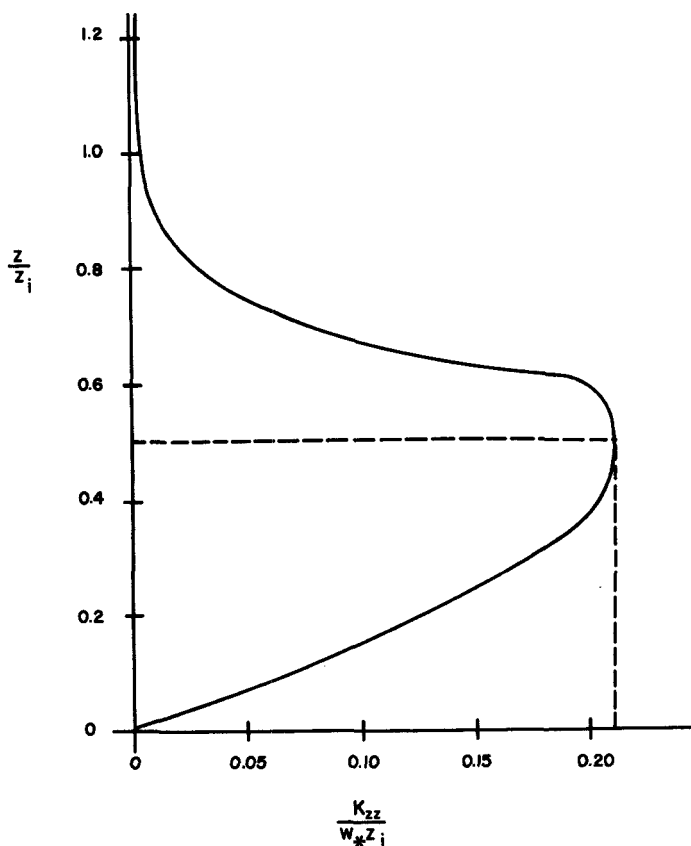


FIG. 7. Vertical turbulent diffusivity profile corresponding to Eq. (9.11). From Lamb and Duran (1977).

A number of other models for unstable conditions have been used, notably the formulations of O'Brien (1970) and of Myrup and Ranzieri (1976). O'Brien's model defines a cubic polynomial variation of K_{zz} above the surface layer. Boundary conditions are established by matching a similarity solution at the top of the surface layer and fixing profile gradients at $z = |L|$ and z_i . The expression for the diffusivity is

$$\begin{aligned}
 K_{zz} = K_{zz}(z_i) + \left[\frac{z_i - z}{z_i - |L|} \right]^2 & \left[K_{zz}(|L|) - K_{zz}(z_i) + (z - |L|) \left\{ \frac{\partial K_{zz}}{\partial z} \right\}_{z=|L|} \right. \\
 & \left. + 2 \left(\frac{K_{zz}(|L|) - K_{zz}(z_i)}{z_i - |L|} \right) \right] \quad (9.12)
 \end{aligned}$$

where the height of the top of the surface layer is given by $z = |L|$. The similarity solution can be used to evaluate $K_{zz}(|L|)$, the gradient $\partial K_{zz}/\partial z$, and the maximum diffusivity in the mixed layer:

$$K_{zz}(|L|) = 5.0w_*z_i(k|L|/z_i)^{4/3} = 2u_*|L| \quad (9.13)$$

$$\left. \frac{\partial K_{zz}}{\partial z} \right|_{z=|L|} = 8.23kw_* \left(\frac{k|L|}{z_i} \right)^{1/3} = 3.3u_* \quad (9.14)$$

Assuming $z_i \gg |L|$, the maximum diffusivity occurs at $z/z_i \approx 0.3$ and is given by

$$K_{zz}(\text{max}) \approx \frac{4}{27} \left[K_{zz}(|L|) + z_i \left. \frac{\partial K_{zz}}{\partial z} \right|_{z=|L|} \right] = 0.5u_*z_i \quad (9.15)$$

Myrup and Ranzieri (1976) developed an approach based on similarity theory and a set of empirical formulas. For unstable conditions ($z/L < -5$) their profile is specified by

$$K_{zz} = ku_*z[1 - 15z/L]^{1/4}q \quad (9.16)$$

where

$$q = \begin{cases} 1 & \text{for } z/z_i < 0.1 \\ 1.1 - z/z_i & \text{for } 0.1 \leq z/z_i \leq 1.1 \end{cases} \quad (9.17)$$

For the above conditions, the maximum diffusivity occurs at $z/z_i \approx 0.5$ with a value $K_{zz}(\text{max}) \approx 0.4u_*z_i$. Figure 8 presents a comparison of the three different diffusivity expressions for a set of typical meteorological conditions. The maximum diffusivity for all models is quite large, which in turn implies that vertical mixing is quite rapid under unstable conditions.

2. Neutral Conditions

Under neutral conditions the atmospheric lapse rate is adiabatic. Close to the ground the vertical eddy diffusivity profile can be based on Monin-Obukhov similarity theory, in which case $\phi_m = 1$ and $K_{zz} = ku_*z$. With this formulation, K_{zz} increases without limit—clearly a physically unrealistic situation. Myrup and Ranzieri (1976) proposed a set of empirical “roll off” functions for altitudes above the surface layer:

$$K_{zz} = \begin{cases} ku_*z & \text{for } z/z_i < 0.1 \\ ku_*z(1.1 - z/z_i) & \text{for } 0.1 \leq z/z_i \leq 1.1 \\ 0 & \text{for } z/z_i > 1.1 \end{cases} \quad (9.18)$$

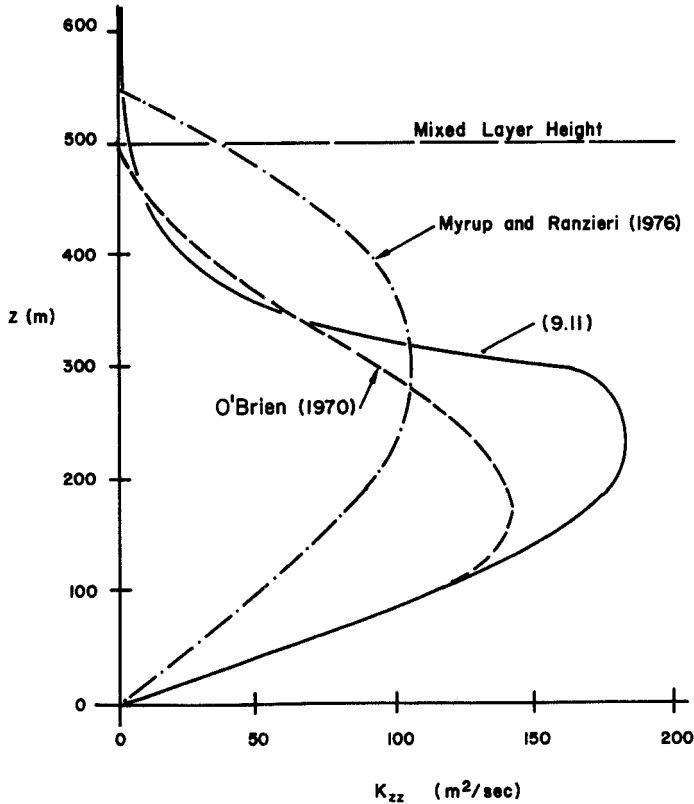


FIG. 8. Comparison of diffusivity profiles for unstable conditions ($L = -30$ m; $u_z = 0.5$ m sec⁻¹; $z_i = 500$ m).

Shir (1973) developed the following relationship from a study of a one-dimensional version of a turbulent transport model for extrapolation above the surface layer:

$$K_{zz} = ku_* z \exp[-8fz/u_*] \quad (9.19)$$

Under neutral conditions, $L = \infty$ and so the Monin–Obkuhov length is not an appropriate choice for the vertical length scale. An alternative is to define the scale in terms of the Ekman layer height u_*/f . Another formulation was proposed by Businger and Arya (1974) for neutral and stable conditions:

$$K_{zz} = \frac{ku_* z}{1 + \alpha \phi_m(z/L)} \exp \left[-|V_g| \frac{zf}{u_*^2} \right] \quad (9.20)$$

where V_g is the geostrophic wind component orthogonal to the surface wind and α a constant. Note that if $V_g \approx 8u_*$, as has been predicted by the turbulence models of Wyngaard (1973) and of Deardorff (1970), then both Eqs. (9.19) and (9.20) are very similar. Lamb *et al.* (1975) calculated the eddy diffusivity of virtual particles by employing the same techniques described in the previous section. Their polynomial form for the neutral case is given by

$$K_{zz} = \frac{u_*^2}{f} \left[7.396 \times 10^{-4} + 6.082 \times 10^{-2} \left(\frac{zf}{u_*} \right) + 2.532 \left(\frac{zf}{u_*} \right)^2 - 12.72 \left(\frac{zf}{u_*} \right)^3 + 15.17 \left(\frac{zf}{u_*} \right)^4 \right] \quad \text{for } 0 \leq \frac{zf}{u_*} \leq 0.45 \quad (9.21)$$

$$K_{zz} \approx 0 \quad \text{for } \frac{zf}{u_*} > 0.45$$

The predictions of the various expressions for K_{zz} in the neutral case are shown in Fig. 9, where the scale height has been replaced with

$$H = \begin{cases} 0.5u_*/f & \text{by Shir (1973)} \\ z_i & \text{by Myrup and Ranzieri (1976)} \\ u_*/f & \text{by Lamb *et al.* (1975)} \end{cases} \quad (9.22)$$

From an examination of the profiles it is clear that there are substantial differences in the magnitudes of K_{zz} predicted by the various models. The diffusivity estimates at the top of the boundary layer predicted by the similarity solution are excessively large. The profiles of Shir (1973) and Lamb *et al.* (1975) are in quite close agreement up to a height of $z/H \approx 0.3$. Above this elevation the polynomial profile is considerably smaller.

3. Stable Conditions

In the surface layer, similarity theory can be used to give an expression for eddy diffusivity under stable conditions:

$$K_{zz} = \frac{ku_*z}{0.74 + 4.7z/L} \quad (9.23)$$

Again, as in the previous cases, the above results are not applicable for $z/L > 1$. Under stable conditions, mixing above the surface layer can be expected to be quite different from local free convection where the eddies scale with the depth of the mixed layer z_i . When $z > L$, the appropriate scale for the eddies is L because buoyancy inhibits vertical excursions of

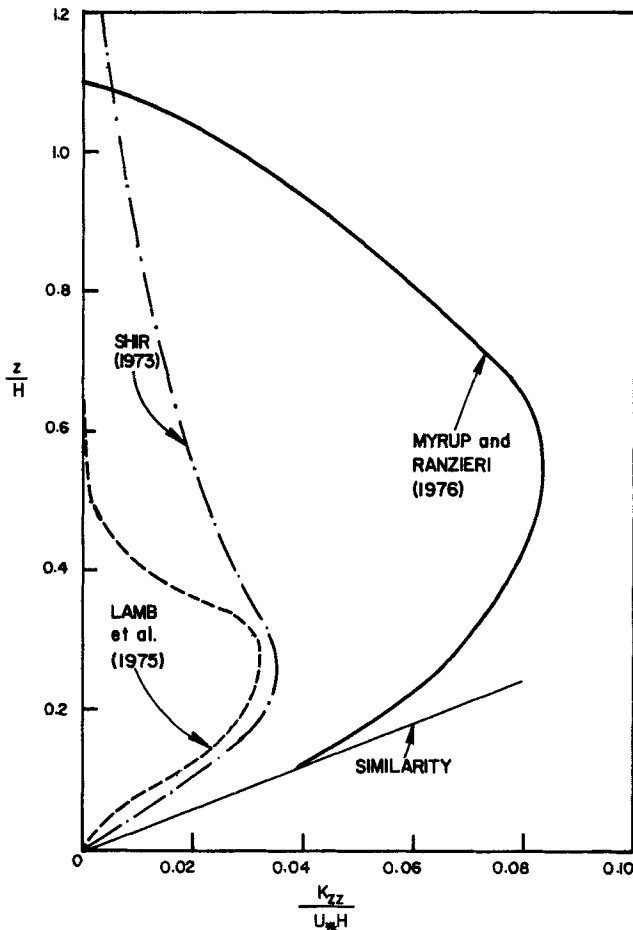


FIG. 9. Comparison of various models for vertical diffusivity profile under neutral conditions: $H = z_i$ (—), $0.5u_*f$ (---), u_*f (— · —), and z_i (····).

air parcels over larger distances. This fact emphasizes that under stable conditions there is a minimum of turbulent exchange in the vertical direction. Businger and Arya (1974) proposed a modification of Eq. (9.23) to extend the model above $z = L$:

$$K_{zz} = \frac{ku_*z}{0.74 + 4.7z/L} \exp \left[- \left| \frac{V_g}{u_*} \right| \frac{fz}{u_*} \right] \quad (9.24)$$

The maximum value of the diffusivity for this model is given by

$$K_{zz}(\max) \approx 0.03(u_*^2/f)(fL/u_*)^{0.9} \quad (9.25)$$

For typical meteorological conditions the maximum diffusivity can be expected to be in the range $0.5\text{--}5\text{ m}^2\text{ sec}^{-1}$. The magnitude is considerably smaller than the equivalent values encountered under strongly unstable conditions. A limitation of the above formulation is the need for knowledge of the geostrophic wind velocity V_g . If the assumption $V_g \approx 8u_*$, discussed in the previous section, is employed, then Eq. (9.25) can be written in the form

$$K_{zz} = \frac{ku_*z}{0.74 + 4.7z/L} \exp \left[-\frac{8fz}{u_*} \right] \quad (9.26)$$

This model is quite similar to the Myrup and Ranzieri (1976) form in neutral conditions except that the exponential decay is replaced by the functions defined by Eq. (9.16). An alternative approach is to modify the O'Brien formula, noting that the expression (9.12) enables a unique polynomial profile to be established by matching the applied boundary conditions. From Eq. (9.23), the slope at $z = L$ is given by

$$(\partial K_{zz}/\partial z)|_{z=L} = 0.025ku_* \quad (9.27)$$

Substituting this result into Eq. (9.12) and defining the scale height to be H , the vertical diffusivity variation is

$$\begin{aligned} K_{zz} = K_{zz}(H) + \left[\frac{H-z}{H-L} \right]^2 & \left[K_{zz}(L) - K_{zz}(H) \right. \\ & \left. + (z-L) \left\{ \frac{\partial K_{zz}}{\partial z} \right|_{z=L} + 2 \left(\frac{K_{zz}(L) - K_{zz}(H)}{H-L} \right) \right] \end{aligned} \quad (9.28)$$

where $K_{zz}(L) = 0.025ku_*L$. If $K_{zz}(H)$ is set equal to $K_{zz}(L)$, then Eq. (9.28) can be simplified further to

$$K_{zz} = 0.025ku_*L \left[1 + 0.025 \left(\frac{z}{L} - 1 \right) \left(\frac{H-z}{H-L} \right)^2 \right] \quad (9.29)$$

The form and magnitude of the scale height H clearly depends on the meteorological conditions. Wyngaard (1975) concluded that turbulence is confined to a layer of thickness H given approximately by

$$H = 0.22(u_*/f)(fL/u_*)^{1/2} \quad (9.30)$$

This result is the same form as the power law predicted by Zilitinkevich (1972) and, apart from a different constant, 0.74, is identical to the Businger and Arya (1974) model. The diffusivity profiles for the above models are very similar to the forms shown in Fig. 9.

C. HORIZONTAL EDDY DIFFUSION COEFFICIENT

The statistical theory of turbulent diffusion (Section VIII,B) predicts that the mean square displacement of a fluid particle in, say, the y direction manifests the following behavior:

$$\sigma_y^2(t) = \begin{cases} \langle v'^2 \rangle t^2 & \text{for } t \ll T_L \\ 2K_{yy}t & \text{for } t \gg T_L \end{cases} \quad (9.31)$$

where T_L is the Lagrangian integral time scale of the turbulence. As a result, the crosswind eddy diffusion coefficient K_{yy} is related to the variance of plume spread by

$$K_{yy} = \frac{1}{2}(d\sigma_y^2/dt) = \frac{1}{2}\bar{u}(d\sigma_y^2/dx) \quad (9.32)$$

for $t \gg T_L$.

Measurements of T_L in the atmosphere are extremely difficult to perform and it is difficult to establish when $t \gg T_L$ holds for urban scale flows. Csanady (1973) indicates that a typical eddy which is generated by shear flow near the ground has a Lagrangian time scale of the order of 100 sec. Lamb and Neiburger (1971), in a series of measurements in the Los Angeles Basin, estimated the Eulerian time scale T_E to be ~ 50 sec. In a discussion of some field experiments, Lumley and Panofsky (1964) suggested that $T_L < 4T_E$. If the averaging interval is selected to be equal to the travel time, then an approximate value for K_{yy} can be deduced from the measurements of Willis and Deardorff (1976). Their data indicate that for unstable conditions ($L > 0$) and a travel time $t = 3z_i/w_*$

$$\sigma_y^2/z_i^2 \approx 0.64 \quad (9.33)$$

Employing the previous travel time estimate and combining this result with Eq. (9.33) gives

$$K_{yy} = \frac{1}{6}(\sigma_y^2/z_i^2)w_*z_i \approx 0.1w_*z_i \quad (9.34)$$

This latter result can be expressed in terms of the friction velocity u_* and the Monin-Obukhov length L as

$$K_{yy} \approx 0.1z_i^{3/4}(-kL)^{-1/3}u_* \quad (9.35)$$

For a range of typical meteorological conditions this formulation results in diffusivities of $O(50-100 \text{ m}^2 \text{ sec}^{-1})$. Some typical results (given in Table VIII) are in quite close agreement with field measurements and the formulas recommended by Briggs (1974) for city conditions. In the above model, K_{yy} varies as a function of the surface conditions at different spatial locations but is assumed to be invariant with height.

TABLE VIII

TYPICAL HORIZONTAL EDDY DIFFUSIVITIES AND CROSS WIND STANDARD DEVIATIONS

Stability class	z_0 (m)	L (m)	\bar{u} (m sec ⁻¹)	u^* (m sec ⁻¹)	z_i (m)	w^* (m sec ⁻¹)	K_H (m ² sec ⁻¹)	σ_y (m)	Travel time (sec)
A	0.5	-14	2	0.42	300	2.44	73	231	368
B	1.08	-29	2	0.43	500	1.58	79	387	949
C	1.75	-250	4	0.83	500	1.48	74	387	1013

In most cases of practical calculations, it is usually assumed that $K_{xx} = K_{yy}$.

D. SOLUTIONS OF THE STEADY-STATE ATMOSPHERIC DIFFUSION EQUATION

The Gaussian expressions are not expected to be valid descriptions of turbulent diffusion close to the surface because of spatial inhomogeneities in the mean wind and the turbulence. To deal with diffusion in layers near the surface, recourse is generally had to the atmospheric diffusion equation, in which, as we have noted, the key problem is proper specification of the spatial dependence of the mean velocity and eddy diffusivities. Under steady-state conditions, turbulent diffusion in the direction of the mean wind is usually neglected (the slender-plume approximation), and if the wind direction coincides with the x axis, then $K_{xx} = 0$. Thus, it is necessary to specify only the lateral (K_{yy}) and vertical (K_{zz}) coefficients. It is generally assumed that horizontal homogeneity exists so that \bar{u} , K_{yy} , and K_{zz} are independent of y . Hence, Eq. (2.19) becomes

$$\bar{u} \frac{\partial \bar{c}}{\partial x} = \frac{\partial}{\partial y} \left(K_{yy} \frac{\partial \bar{c}}{\partial y} \right) + \frac{\partial}{\partial z} \left(K_{zz} \frac{\partial \bar{c}}{\partial z} \right) \quad (9.36)$$

Sections IX,A-C have been devoted to expressions for $\bar{u}(z)$, $K_{zz}(z)$, and K_{yy} based on atmospheric boundary layer theory. Because of the rather complicated dependence of \bar{u} and K_{zz} on z , Eq. (9.36) must generally be solved numerically (see, for example, Nieuwstadt and van Ulden, 1978; van Ulden, 1978). However, if they can be found, analytical solutions are advantageous for studying the behavior of the predicted mean concentration.

A solution of Eq. (9.36) has been obtained by Huang (1979) in the case when the mean wind speed and vertical eddy diffusivity can be represented by the power-law expressions:

$$\bar{u}(z) = az^p \quad (9.37)$$

$$K_{zz}(z) = bz^n \quad (9.38)$$

and when the horizontal eddy diffusivity is related to σ_y^2 by Eq. (9.32).

For a point source of strength q at height h above the ground, the solution of Eq. (9.36), subject to Eqs. (9.32), (9.37), and (9.38), is

$$\begin{aligned} \bar{c}(x, y, z) = & \frac{q}{(2\pi)^{1/2}\sigma_y} \exp \left[-\frac{y^2}{2\sigma_y^2} \right] \frac{(zh)^{(1-n)/2}}{b\alpha x} \\ & \times \exp \left[-\frac{a(z^\alpha + h^\alpha)}{b\alpha^2 x} \right] I_{-\nu} \left[\frac{2a(zh)^{\alpha/2}}{b\alpha^2 x} \right] \end{aligned} \quad (9.39)$$

where $\alpha = 2 + p - n$, $\nu = (1 - n)/\alpha$, and $I_{-\nu}$ is the modified Bessel function of the first kind of order $-\nu$.

Equation (9.39) can be used to obtain some special cases of interest. If it is assumed that $p = n = 0$, then Eq. (9.39) reduces to

$$\begin{aligned} \bar{c}(x, y, z) = & \frac{q}{(2\pi)^{1/2}\sigma_y} \exp \left[-\frac{y^2}{2\sigma_y^2} \right] \frac{(zh)^{1/2}}{\sigma_z^2 \bar{u}} \\ & \times \exp \left[-\frac{z^2 + h^2}{2\sigma_z^2} \right] I_{-1/2} \left(\frac{zh}{\sigma_z^2} \right) \end{aligned} \quad (9.40)$$

where

$$\sigma_y^2 = 2K_{yy}x/\bar{u}, \quad \sigma_z^2 = 2K_{zz}x/\bar{u} \quad (9.41)$$

Using the asymptotic form

$$I_{-1/2}(x) = (2/\pi x)^{1/2} \cosh x \quad \text{as } x \rightarrow \infty \quad (9.42)$$

Eq. (9.40) reduces to the Gaussian plume equation. Note that the asymptotic condition in Eq. (9.42) corresponds to $zh \gg \sigma_z^2$.

The case of a point source at or near the ground can also be examined. We can take the limit of Eq. (9.39) as $h \rightarrow 0$ using the asymptotic form of $I_\nu(x)$ as $x \rightarrow 0$:

$$I_\nu(x) = \frac{x^\nu}{2^\nu \Gamma(1 + \nu)} \quad \text{as } x \rightarrow 0 \quad (9.43)$$

to obtain

$$\begin{aligned} \bar{c}(x, y, z) = & \frac{q}{(2\pi)^{1/2}\sigma_y x^{(1+p)/\alpha}} \frac{\alpha}{a^\nu (b\alpha^2)^{(1+p)/\alpha} \Gamma((1+p)/\alpha)} \\ & \times \exp \left[-\frac{y^2}{2\sigma_y^2} \right] \exp \left[-\frac{a(z^\alpha + h^\alpha)}{b\alpha^2 x} \right] \end{aligned} \quad (9.44)$$

Finally, in the case of an infinite, cross wind line source, Eq. (9.39) can be integrated over y from $-\infty$ to $+\infty$ to give

$$\bar{c}(x, z) = \frac{q(zh)^{(1-n)/2}}{b\alpha x} \exp \left[-\frac{a(z^\alpha + h^\alpha)}{b\alpha^2 x} \right] I_{-\nu} \left[\frac{2a(zh)^{\alpha/2}}{b\alpha^2 x} \right] \quad (9.45)$$

Again, letting $h \rightarrow 0$, we obtain

$$\bar{c}(x, z) = \frac{q\alpha}{a^\nu(b\alpha^2)^{(1+p)/\alpha}\Gamma((1+p)/\alpha)x^{(1+p)/\alpha}} \exp \left[-\frac{a(z^\alpha + h^\alpha)}{b\alpha^2 x} \right] \quad (9.46)$$

X. Monte Carlo Simulation of Turbulent Diffusion

The fundamental Lagrangian quantity in turbulent diffusion theory is the probability density function $p(x, y, z, t|x', y', z', t')$. Unless a functional form of p , e.g., Gaussian, is assumed, p must be evaluated experimentally (Willis and Deardorff, 1978, 1980) or numerically (Lamb *et al.* 1975; Lamb, 1978). The numerical evaluation of p carried out in the two references cited involved tracking fluid particles in a flow field generated by a numerical solution of the turbulent Navier-Stokes equations. An alternative approach to the numerical evaluation of p that is receiving considerable attention is that of tracking fluid particles in a flow field generated by a Monte Carlo algorithm that produces velocity fluctuations with the same statistics as the turbulent flow simulated (Reid, 1979; Lamb, 1981; Runca *et al.*, 1981). In this section we will examine the basic elements of the Monte Carlo simulation of turbulent diffusion. We restrict our attention to homogeneous turbulence.

A. ELEMENTS OF MONTE CARLO SIMULATION OF TURBULENT DIFFUSION

The basis of all the experimental and numerical approaches to evaluating p is the following approximation:

$$p(x, y, z, t|x', y', z', t') = \frac{P(x, y, z, t|x', y', z', t')}{\Delta x \Delta y \Delta z} \quad (10.1)$$

where $P(x, y, z, t|x', y', z', t')$ is the probability that a particle released at (x', y', z') at time t' will be in $[x \pm \Delta x/2, y \pm \Delta y/2, z \pm \Delta z/2]$ at time t . For brevity, we will henceforth consider only the single spatial variable x and assume $t' = 0$. $P(x, t|x', 0)$ can be estimated by

$$P(x, t|x', 0) = \lim_{k \rightarrow \infty} \frac{1}{k} \sum_{j=1}^k \phi_j(x, t|x', 0) \quad (10.2)$$

where

$$\phi_j(x, t|x', 0) = \begin{cases} 1 & \text{if particle } j \text{ is in } (x \pm \Delta x/2) \text{ at } t \\ 0 & \text{otherwise} \end{cases} \quad (10.3)$$

To compute $\phi_j(x, t|x', 0)$, particle trajectories must be obtained. In the numerical approaches, these particle trajectories are generated by following fluid particles in the numerical flow field. In the Monte Carlo method, an algorithm is formulated to produce the particle velocity and position as a function of time. Perhaps the simplest such algorithm is the following:

$$\begin{aligned} n = 0, \quad u_j^l(\Delta t, x') &= u_j^e(x') \\ n \geq 1, \quad u_j^l((n+1)\Delta t, x') &= \alpha u_j^l(n\Delta t, x') + \rho_j((n+1)\Delta t) \\ x_j((n+1)\Delta t, x') &= x_j(n\Delta t, x') + u_j^l((n+1)\Delta t, x') \Delta t \end{aligned} \quad (10.4)$$

where $u_j^l((n+1)\Delta t, x')$ is the velocity of the j th particle (released at x') after $(n+1)$ intervals of time Δt . This velocity is used to advance the particle from location $x_j(n\Delta t, x')$ to $x_j((n+1)\Delta t, x')$. At the first time step, the particle velocity coincides with that at the source location x' . (The suffices l and e refer to Lagrangian and Eulerian quantities, respectively.) The coefficient α reflects the degree of persistence of the particle's velocity from time step to time step and obeys $0 < \alpha < 1$, and $\rho_j((n+1)\Delta t)$ is a random contribution to the velocity of the j th particle that must be generated by a Monte Carlo method. To generate ρ_j , we need to know the probability density of ρ , p_ρ .

In homogeneous, stationary turbulence, the probability density of u^l , p_u^l , must coincide at all times with that of the velocity recorded at any fixed point, p_u^e . The probability densities of $u^l((n+1)\Delta t, x')$ and $u^l(n\Delta t, x')$ are thus identical. Under homogeneous, stationary conditions, p_u^e is known to be Gaussian (see Section III). We indicate the distribution p_u^e as

$$p_u^e = N(\langle u \rangle, \langle u^2 \rangle) \quad (10.5)$$

where $N(\langle u \rangle, \langle u^2 \rangle)$ denotes a normal distribution with mean $\langle u \rangle$ and mean square $\langle u^2 \rangle$.

Based on Eq. (10.5), we can determine the distribution of the random component ρ , p_ρ . Since

$$\rho_j((n+1)\Delta t) = u_j^l((n+1)\Delta t, x') - \alpha u_j^l(n\Delta t, x') \quad (10.6)$$

the expected value of ρ is found from Eq. (10.6),

$$\langle \rho \rangle = (1 - \alpha) \langle u \rangle \quad (10.7)$$

The mean square value of ρ is found from

$$\rho_j^2((n+1)\Delta t) = [u_j^l((n+1)\Delta t, x') - \alpha u_j^l(n\Delta t, x')]^2 \quad (10.8)$$

Henceforth we will not indicate the explicit dependence of u^l on the source location x' , and we will drop the suffix l because of the assumption of stationary, homogeneous turbulence. Taking the expected value of Eq. (10.8),

$$\langle \rho^2 \rangle = \langle u^2((n+1)\Delta t) \rangle - 2\alpha \langle u((n+1)\Delta t)u(n\Delta t) \rangle + \alpha^2 \langle u(n\Delta t)^2 \rangle \quad (10.9)$$

The second term on the right-hand side of Eq. (10.9) can be expressed as

$$\begin{aligned} 2\alpha \langle u(n\Delta t)[\alpha u(n\Delta t) + \rho((n+1)\Delta t)] \rangle \\ = 2\alpha^2 \langle u(n\Delta t)^2 \rangle + 2\alpha \langle u(n\Delta t)\rho((n+1)\Delta t) \rangle \end{aligned} \quad (10.10)$$

It is generally assumed that $\rho(m\Delta t)$ is uncorrelated with $u(n\Delta t)$ for $m > n$, i.e.,

$$\langle \rho(m\Delta t)u(n\Delta t) \rangle = 0, \quad m > n \quad (10.11)$$

Thus, Eqs. (10.9)–(10.11) yield

$$\langle \rho^2 \rangle = (1 - \alpha^2) \langle u^2 \rangle \quad (10.12)$$

The random component of the particle velocity in stationary, homogeneous turbulence is normally distributed with mean, $(1 - \alpha)\langle u \rangle$, and mean square, $(1 - \alpha^2)\langle u^2 \rangle$,

$$p_p = N[(1 - \alpha)\langle u \rangle, (1 - \alpha^2)\langle u^2 \rangle] \quad (10.13)$$

It is of interest to compute the Lagrangian velocity autocorrelation resulting from trajectories generated by Eq. (10.4):

$$R(t, \tau) = \langle u^l(t)u^l(\tau) \rangle / \langle u^2 \rangle \quad (10.14)$$

Let $t = m\Delta t$ and $\tau = n\Delta t$. Then

$$\begin{aligned} \langle u^l(t)u^l(\tau) \rangle &= \langle [\alpha u((m-1)\Delta t) + \rho(m\Delta t)]u(n\Delta t) \rangle \\ &= \langle \{ \alpha [\alpha u((m-2)\Delta t) + \rho((m-1)\Delta t)] + \rho(m\Delta t) \} u(n\Delta t) \rangle \\ &= \alpha^{m-n} \langle u^2 \rangle + \sum_{k=n+1}^m \alpha^{m-k} \langle \rho(k\Delta t)u(n\Delta t) \rangle \end{aligned} \quad (10.15)$$

Using Eq. (10.11), we obtain

$$R((m-n)\Delta t) = \alpha^{m-n} \quad (10.16)$$

or, equivalently,

$$R(t, \tau) = R(t - \tau) = \alpha^{(t-\tau)/\Delta t} \quad (10.17)$$

Next, it is of interest to compute the Lagrangian integral time scale of the process [recall Eq. (8.6)]:

$$T = \int_0^\infty R(\eta) d\eta \quad (10.18)$$

Using Eq. (10.17), we obtain

$$T = \Delta t / \ln(1/\alpha) \quad (10.19)$$

We note that as $\alpha \rightarrow 0$, $T \rightarrow 0$ and as $\alpha \rightarrow 1$, $T \rightarrow \infty$.

Finally, it is of interest to compute the mean square particle displacements resulting from the algorithm (10.4). From Eq. (8.3) we write

$$\begin{aligned} \langle x^2(t) \rangle &= 2 \int_0^t \int_0^{t'} \langle u(\tau) u(t') \rangle d\tau dt' \\ &= 2 \langle u^2 \rangle \int_0^t \int_0^{t'} R(t' - \tau) d\tau dt' \end{aligned} \quad (10.20)$$

Using Eq. (10.17) in Eq. (10.20), we obtain, with $t = n \Delta t$,

$$\langle x^2(n \Delta t) \rangle = \frac{2 \langle u^2 \rangle \Delta t^2}{(\ln \alpha)^2} [\alpha^n - 1 - n \ln \alpha] \quad (10.21)$$

or, equivalently, using Eq. (10.19),

$$\langle x^2(n \Delta t) \rangle = 2 \langle u^2 \rangle T^2 [n \Delta t / T - (1 - e^{-n \Delta t / T})] \quad (10.22)$$

which agrees with Taylor's classical result.

B. APPLICATION OF THE MONTE CARLO METHOD TO A CONTINUOUS, ELEVATED LINE SOURCE

To illustrate the application of the Monte Carlo method, we consider the problem of simulating the dispersion of material emitted from a continuous line source located between the ground and an inversion layer. A similar case has been considered by Runca *et al.* (1981). We assume that the mean wind \bar{u} is constant and that the slender-plume approximation holds. The line source is located at a height h between the ground ($z = 0$) and an inversion layer ($z = z_i$). If the ground is perfectly reflecting, the analytical expression for the mean concentration is found by integrating the last entry of Table II over y from $-\infty$ to $+\infty$. The result can be expressed as

$$\begin{aligned} \bar{c}(x, z) = \frac{q_l}{(2\pi)^{1/2} \sigma_z \bar{u}} \sum_{n=-\infty}^{\infty} \left\{ \exp \left[-\frac{(z - h + 2nz_i)^2}{2\sigma_z^2} \right] \right. \\ \left. + \exp \left[-\frac{(z + h + 2nz_i)^2}{2\sigma_z^2} \right] \right\} \end{aligned} \quad (10.23)$$

where σ_z^2 is given by Eq. (10.22) with $\langle u^2 \rangle$ replaced by $\langle w^2 \rangle$:

$$\sigma_z^2 = 2\langle w^2 \rangle T^2 [n \Delta t/T - (1 - e^{-n \Delta t/T})] \quad (10.24)$$

It is convenient to express the analytical solution in dimensionless form by defining $W = w/w_*$, $X = xw_*/\bar{u}z_i$, $Z = z/z_i$, $\tau = z_i t/w_*$, and $C = \bar{c}\bar{u}z_i/q_l$, where w_* is the convective velocity scale. The result is

$$\begin{aligned} C(X, 0) = (2\pi)^{-1/2} \left(\frac{z_i}{\sigma_z} \right) \sum_{n=-\infty}^{\infty} \left\{ \exp \left[-\frac{(2n - (h/z_i))^2}{2(\sigma_z/z_i)^2} \right] \right. \\ \left. + \exp \left[-\frac{(2n + (h/z_i))^2}{2(\sigma_z/z_i)^2} \right] \right\} \end{aligned} \quad (10.25)$$

where

$$\left(\frac{\sigma_z}{z_i} \right)^2 = 2 \left(\frac{Tw_*}{z_i} \right)^2 \left[\left(\frac{z_i}{Tw_*} \right) X - \left(1 - \exp \left(-\frac{z_i X}{Tw_*} \right) \right) \right] \quad (10.26)$$

Figure 10 shows $C(X, 0)$ as a function of X from Eqs. (10.25) and (10.26) for $h/z_i = 0.25$, $\langle w^2 \rangle = w_*^2$ and $Tw_*/z_i = 0.2$, the conditions chosen by Runca *et al.* (1981).

The Monte Carlo approach can now be used for the same problem. The algorithm for the z velocity component and position in dimensionless form can be written as

$$W_j((n+1) \Delta\tau) = \alpha W_j(n \Delta\tau) + \Omega_j((n+1) \Delta\tau) \quad (10.27)$$

$$Z_j((n+1) \Delta\tau) = Z_j(n \Delta\tau) + W_j((n+1) \Delta\tau) \Delta\tau \quad (10.28)$$

where $W = w/w_*$, $\Delta\tau = w_* \Delta t/z_i$, and $\Omega = \rho/w_*$. The probability density function of Ω is $p_\Omega = N(0, 1 - \alpha^2)$. For the simulation, $\Delta z/z_i = 0.1$ and $\Delta x/\bar{u} \Delta t = 1$. The value of α used was given by $\alpha = \exp(-\Delta t/T)$, with $\Delta t/T = 0.5$.

To implement the method, it is necessary to decide how to handle the case when a particle encounters either vertical boundary. Following Fig. 11, if a particle is predicted to cross the boundary, its position can be reflected. At the next step, $n+1$ to $n+2$, the velocity at step $n+1$ can be taken as the reflected value (line a in Fig. 11), as the previous value unreflected (line b), or as zero with only the random component (case c). In Fig. 12, dimensionless surface concentrations are shown corresponding to each of these three options. As expected, the lowest concentrations

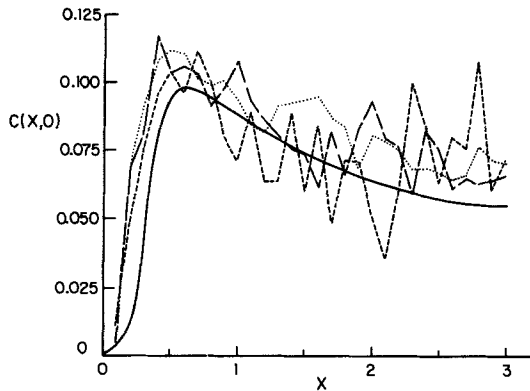


FIG. 10. Dimensionless ground-level concentration resulting from an elevated line source located at a height $(h/z_0) = 0.25$. Analytical solution (—) and three Monte Carlo solutions corresponding to 250 (---), 1000 (— — —), and 2000 (.....) particles.

are achieved with reflection of the velocities and the highest with the velocities unaltered from the previous step. Case c falls intermediate between the other two.

Figure 10 shows the effect of the number of particles used in the Monte Carlo calculation. The calculations were carried out with 250, 1000, and 2000 particles using randomized velocities, case c of Fig. 12. Although as the number of particles is increased from 250 to 1000, a noticeable reduction in fluctuations occurs, from 1000 to 2000 particles the change is not as pronounced.

This section has illustrated a relatively simple application of the Monte Carlo technique for simulating atmospheric diffusion. With the availability of large-scale computing capacities, Monte Carlo methods can be envi-

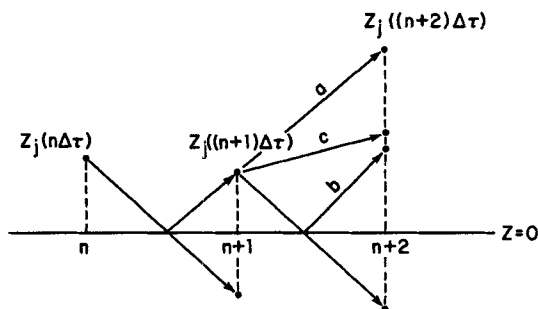


FIG. 11. Three ways of treating particles that intersect a boundary in a Monte Carlo calculation. In case a the velocity is reflected at step $n + 2$. In case b the velocity is unaltered at step $n + 2$. In case c the velocity at step $n + 2$ is assumed to have a random component only.

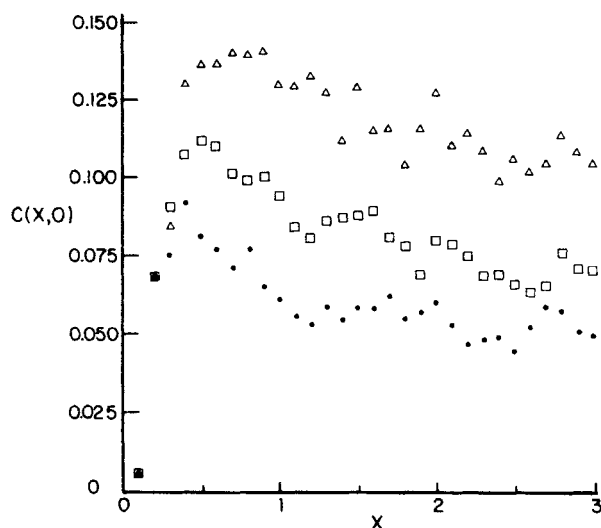


FIG. 12. Dimensionless ground-level concentration resulting from an elevated line source located at a height $(h/z_i) = 0.25$. Monte Carlo solution corresponding to the three-boundary treatments of Fig. 11: (●) case a, velocities reflected; (△) case b, velocities unaltered; (□) case c, velocities randomized.

sioned to become more and more important in the arsenal of techniques in atmospheric diffusion theory. The key problem in such methods is to select properly the statistical properties of the random fluctuations in accord with the turbulent properties of the atmosphere.

XI. Summary

We have presented a relatively self-contained development of the fundamentals of atmospheric diffusion theory. The emphasis has been on elucidating the origin and applicability of the basic expressions commonly used in atmospheric diffusion calculations. This article is intended for the practicing scientist who desires a tutorial introduction to atmospheric diffusion theory or for the advanced undergraduate or graduate student who is entering atmospheric diffusion research.

ACKNOWLEDGMENT

Appreciation is extended to Panos Georgopoulos for his careful reading of the manuscript and his several contributions to it, to Greg McRae for providing much of the material in Section IX, and to Susan Hunts for carrying out the calculations in Section X.

References

- Adomian, G. (1963). Linear stochastic operators. *Rev. Mod. Phys.* **35**, 185–207.
- American Meteorological Society Workshop on Stability Classification Schemes and Sigma Curves—Summary of Recommendations (1977). *Bull. Am. Meteorol. Soc.* **58**, 1305–1309.
- American Society of Mechanical Engineers (1973). “Recommended Guide for the Prediction of the Dispersion of Airborne Effluents,” 2nd ed. ASME, New York.
- Arya, S. P. S. (1977). Suggested revision to certain boundary layer parameterization schemes used in atmospheric circulation models. *Mon. Weather Rev.* **105**, 215–227.
- Batchelor, G. K. (1950). Application of similarity theory of turbulence to atmospheric diffusion. *Q. J. R. Meteorol. Soc.* **76**, 133–146.
- Benoit, R. (1977). On the integral of the surface layer profile-gradient functions. *J. Appl. Meteorol.* **16**, 859–860.
- Binkowski, F. S. (1979). A simple semi-empirical theory for turbulence in the atmospheric surface layer. *Atmos. Environ.* **13**, 247–253.
- Bird, R. B., Stewart, W. E., and Lightfoot, E. N. (1960). “Transport Phenomena.” Wiley, New York.
- Blackadar, A. K., and Tennekes, H. (1968). Asymptotic similarity in neutral barotropic planetary boundary layers. *J. Atmos. Sci.* **25**, 1015–1020.
- Blackwelder, R. F., and Kovasznay, L. S. G. (1972). Time scales and correlations in a turbulent boundary layer. *Phys. Fluids* **15**, 1545–1554.
- Briggs, G. A. (1974). Diffusion estimation for small emissions. In “Environmental Research Laboratories, Air Resources Atmosphere Turbulence and Diffusion Laboratory 1973 Annual Report,” USAEC Rep. ATDL-106. Natl. Oceanic Atmos. Adm., Washington, D.C.
- Businger, J. A., and Arya, S. P. S. (1974). Height of the mixed layer in the stably stratified planetary boundary layer. *Adv. Geophys.* **18A**, 73–92.
- Businger, J. A., Wyngaard, J. C., Izumi, Y., and Bradley, E. F. (1971). Flux-profile relationship in the atmospheric surface layer. *J. Atmos. Sci.* **28**, 181–189.
- Carl, D. M., Tarbell, T. C., and Panofsky, H. A. (1973). Profiles of wind and temperature from towers over homogeneous terrain. *J. Atmos. Sci.* **30**, 788–794.
- Corrsin, S. (1974). Limitations of gradient transport models in random walks and in turbulence. *Adv. Geophys.* **18A**, 25–59.
- Counihan, J. (1975). Adiabatic atmospheric boundary layers: A review and analysis of data from the period 1880–1972. *Atmos. Environ.* **9**, 871–905.
- Cramer, H. (1946). “Mathematical Methods of Statistics.” Princeton Univ. Press, Princeton, New Jersey.
- Crane, G., Panofsky, H., and Zeman, O. (1977). A model for dispersion from area sources in convective turbulence. *Atmos. Environ.* **11**, 893–900.
- Csanady, G. T. (1973). “Turbulent Diffusion in the Environment.” Reidel Publ., Dordrecht, Netherlands.
- Deacon, E. L. (1949). Vertical diffusion in the lowest layers of the atmosphere. *Q. J. R. Meteorol. Soc.* **75**, 89–103.
- Deardorff, J. W. (1970). A three-dimensional numerical investigation of the idealized planetary boundary layer. *Geophys. Fluid Dyn.* **1**, 377–410.
- Diamante, J. M., Englar, T. S., Jr., and Jazwinski, A. H. (1976). “Final Report. Phase 1. Urban Air Quality Estimation Study,” Business and Technological Systems, Inc., Seabrook, Maryland.
- Doran, J. C., Horst, T. W., and Nickola, P. W. (1978). Experimental observations of the

- dependence of lateral and vertical dispersion characteristics on source height. *Atmos. Environ.* **12**, 2259–2263.
- Environmental Protection Agency (1980). "OAQPS Guideline Series, Guidelines on Air Quality Models." EPA, Research Triangle Park, North Carolina.
- Fichtl, G. D., and McVehil, G. E. (1970). Longitudinal and lateral spectra of turbulence in the atmospheric boundary layer at the Kennedy Space Center. *J. Appl. Meteorol.* **9**, 51–63.
- Freeman, B. E. (1977). Tensor diffusivity of a trace constituent in a stratified boundary layer. *J. Atmos. Sci.* **34**, 124–136.
- Fulle, D. J. (1975). Lapse rate-wind shear classification of turbulent diffusion. M. S. Thesis, Dept. of Meteorology, University of Utah, Salt Lake City.
- Galbally, I. E. (1971). Ozone profiles and ozone fluxes in the atmospheric surface layer. *Q. J. R. Meteorol. Soc.* **97**, 18–29.
- Gent, P. R. (1977). A numerical model of the air flow above water waves. Part II. *J. Fluid Mech.* **82**, 349–369.
- Gifford, F. A. (1959). Statistical properties of a fluctuating plume dispersion model. *Adv. Geophys.* **6**, 117–138.
- Gifford, F. A. (1960). Peak to average concentration ratios according to a fluctuating plume dispersion model. *Int. J. Air Pollut.* **3**, 253–260.
- Gifford, F. A. (1961). Use of routine meteorological observation for estimating atmospheric dispersion. *Nucl. Saf.* **2**, 47–51.
- Gifford, F. A. (1968). An outline of theories of diffusion in the lower layers of the atmosphere. In "Meteorology and Atomic Energy" (D. Slade, ed.), USAEC TID-24190, Chapter 3. U.S. At. Energy Comm., Oak Ridge, Tennessee.
- Gifford, F. A. (1976). Turbulent diffusion-typing schemes: A review. *Nucl. Saf.* **17**, 68–86.
- Golder, D. (1972). Relations among stability parameters in the surface layer. *Boundary Layer Meteorol.* **3**, 47–58.
- Herman, M. N. (1980). Estimating long-term ground level concentration of SO₂ from short-term peak data. *J. Air. Pollut. Control Assoc.* **30**, 676–678.
- Hilst, G. R. (1957). Observations of the diffusion and transport of stack effluents in stable atmospheres. Ph.D. Thesis, University of Chicago, Chicago, Illinois.
- Hodgin, C. R. (1980). Logarithmic wind profile parameters applied to air quality assessment studies. *Proc. J. Conf. Appl. Air Pollut. Meteorol.*, 2nd, pp. 770–775.
- Högström, U. (1964). An experimental study on atmospheric diffusion. *Tellus* **16**, 205–251.
- Hsu, S. A. (1974). A dynamic roughness equation and its application to wind stress determination at air-sea interface. *J. Phys. Oceanogr.* **4**, 116–120.
- Huang, C. H. (1979). Theory of dispersion in turbulent shear flow. *Atmos. Environ.* **13**, 453–463.
- Irwin, J. S. (1979). "Scheme for Estimating Dispersion Parameters as a Function of Release Height," EPA-600/4-79-062. U.S. Environ. Prot. Agency, Washington, D.C.
- Kaimal, J. C., Wyngaard, J. C., Haugen, D. A., Cote, O. R., Izumi, Y., Caughey, S. J., and Readings, C. J. (1976). Turbulence structure in the convective boundary layer. *J. Atmos. Sci.* **33**, 2152–2169.
- Kitaigorodskii, S. A. (1970). "The Physics of Air-sea Interaction (Translated from Russian by Israel Program for Scientific Translation), TT72-50062. Isr. Program Sci. Transl., Jerusalem.
- Klug, W. (1969). A method for determining diffusion conditions from synoptic observations. *Staub—Reinhalt. Luft* **29**, (4) 14–20.
- Lamb, R. G. (1978). A numerical simulation of dispersion from an elevated point source in the convective planetary boundary layer. *Atmos. Environ.* **12**, 1297–1304.
- Lamb, R. G. (1979). The effects of release height on material dispersion in the convective

- planetary boundary layer. *Proc. Symp. Turbul. Diffus. Air Pollut.*, 4th, 1979 pp. 27–33.
- Lamb, R. G. (1980). Mathematical principles of turbulent diffusion modeling. *Dev. Atmos. Sci.* **11**, 173–210.
- Lamb, R. G. (1981). A scheme for simulating particle pair motions in turbulent fluid. *J. Comput. Phys.* **39**, 329–346.
- Lamb, R. G., and Duran, D. R. (1977). Eddy diffusivities derived from a numerical model of the convective boundary layer. *Nuov. Cimento* [1] **1C**, 1–17.
- Lamb, R. G., and Neiburger, M. (1971). An interim version of a generalized air pollution model. *Atmos. Environ.* **5**, 239–264.
- Lamb, R. G., Chen, W. H., and Seinfeld, J. H. (1975). Numerico-empirical analyses of atmospheric diffusion theories. *J. Atmos. Sci.* **32**, 1794–1807.
- Lewellen, W. S., Teske, M., and Donaldson, C. duP. (1974). Turbulence model of diurnal variation in the planetary boundary layer. In "Proceedings of the 1974 Heat Transfer and Fluid Mechanics Institute" (L. R. Davis and E. R. Wilson, eds.), pp. 301–319. Stanford Univ. Press, Stanford, California.
- Lumley, J. L., and Khajeh-Nouri, B. (1974). Computational modeling of turbulent transport. *Adv. Geophys.* **18A**, 169–192.
- Lumley, J. L., and Panofsky, H. A. (1964). "The Structure of Atmospheric Turbulence." Wiley (Interscience), New York.
- McRae, G. J., Goodin, W. R., and Seinfeld, J. H. (1982). Development of a second-generation mathematical model for urban air pollution. I. Model formulation. *Atmos. Environ.* **16**, 679–696.
- Manton, M. J. (1979). On the dispersion of particles in the atmosphere. *Boundary Layer Meteorol.* **17**, 145–165.
- Mellor, G. L., and Yamada, T. (1974). A hierarchy of turbulence closure models for planetary boundary layers. *J. Atmos. Sci.* **31**, 1791–1806.
- Monin, A. S., and Yaglom, A. M. (1971). "Statistical Fluid Mechanics: Mechanics of Turbulence." MIT Press, Cambridge, Massachusetts.
- Morse, P. M., and Feshbach, H. (1953). "Methods of Theoretical Physics." McGraw-Hill, New York.
- Myrup, L. O., and Ranzieri, A. J. (1976). "A Consistent Scheme for Estimating Diffusivities to be Used in Air Quality Models," Rep. CA-DOT-TL-7169-3-76-32. California Department of Transportation, Sacramento.
- Neumann, J. (1978). Some observations on the simple exponential function as a Lagrangian velocity correlation function in turbulent diffusion. *Atmos. Environ.* **12**, 1965–1968.
- Nieuwstadt, F. T. M., and van Ulden, A. P. (1978). A numerical study on the vertical dispersion of passive contaminants from a continuous source in the atmospheric surface layer. *Atmos. Environ.* **12**, 2119–2124.
- O'Brien, J. (1970). On the vertical structure of the eddy exchange coefficient in the planetary boundary layer. *J. Atmos. Sci.* **27**, 1213–1215.
- Özisik, M. N. (1980). "Heat Conduction." Wiley, New York.
- Papoulis, A. (1965). "Probability, Random Variables and Stochastic Processes." McGraw-Hill, New York.
- Pasquill, F. (1961). The estimation of the dispersion of windborne material. *Meteorol. Mag.* **90**, 33–49.
- Pasquill, F. (1974). "Atmospheric Diffusion," 2nd ed. Wiley, New York.
- Plate, E. J. (1971). "Aerodynamic Characteristics of Atmospheric Boundary Layers," AEC Crit. Rev. Ser. NTIS TID-25465. U.S. At. Energy Comm., Washington, D. C.

- Reid, J. D. (1979). Markov chain simulations of vertical dispersion in the neutral surface layer for surface and elevated releases. *Boundary Layer Meteorol.* **16**, 3–22.
- Runca, E., Bonino, G., and Posch, M. (1981). Lagrangian modeling of air pollutants dispersion from a point source. *12th Int. Tech. Meet. Air Pollut. Model. Its Appl., Menlo Park.*
- Saffman, P. G. (1960). On the effect of molecular diffusivity in turbulent diffusion. *J. Fluid Mech.* **8**, 273–283.
- Sedefian, L., and Bennett, E. (1980). A comparison of turbulence classification schemes. *Atmos. Environ.* **14**, 741–750.
- Seinfeld, J. H. (1975). "Air Pollution—Physical and Chemical Fundamentals." McGraw-Hill, New York.
- Shir, C. C. (1973). A preliminary numerical study of atmospheric turbulent flows in the idealized planetary boundary layer. *J. Atmos. Sci.* **30**, 1327–1339.
- Slade, D. H. (1969). Wind measurements on a tall tower in rough and inhomogeneous terrain. *J. Appl. Meteorol.* **8**, 293–297.
- Stewart, R. W. (1974). The air-sea mass momentum exchange. *Boundary Layer Meteorol.* **6**, 151–167.
- Taylor, G. I. (1921). Diffusion by continuous movements. *Proc. London Math. Soc.* **2**, 196–211.
- Tennekes, H. (1979). The exponential Lagrangian correlation function and turbulent diffusion in the inertial subrange. *Atmos. Environ.* **13**, 1565–1567.
- Touma, J. S. (1977). Dependence of the wind profile power law on stability for various locations. *J. Air Pollut. Control Assoc.* **27**, 863–866.
- Turner, D. B. (1969). "Workbook of Atmospheric Diffusion Estimates," USEPA 999-AP-26. U.S. Environ. Prot. Agency, Washington, D.C.
- van Ulden, A. P. (1978). Simple estimates for vertical diffusion for sources near the ground. *Atmos. Environ.* **12**, 2125–2129.
- Venkatram, A. (1978). Estimating the convective velocity scale for diffusion applications. *Boundary Layer Meteorol.* **15**, 447–452.
- Venkatram, A. (1980). The relationship between the convective boundary layer and dispersion from tall stacks. *Atmos. Environ.* **14**, 763–767.
- Weber, A. H. (1976). "Atmospheric Dispersion Parameters in Gaussian Plume Modeling," EPA-600/4-76-030A. U.S. Environ. Prot. Agency, Washington, D.C.
- Weber, A. H., Irwin, J. S., Kahler, J. P., and Peterson, W. B. (1975). "Atmospheric Turbulence in the Lowest 300 Meters." EPA-600/4-75-004. U.S. Environ. Prot. Agency, Washington, D.C.
- Willis, G. E., and Deardorff, J. W. (1976). A laboratory model of diffusion into the convective boundary layer. *Q. J. R. Meteorol. Soc.* **102**, 427–447.
- Willis, G. E., and Deardorff, J. W. (1978). A laboratory study of dispersion from an elevated source within a modeled convective planetary boundary layer. *Atmos. Environ.* **12**, 1305–1311.
- Willis, G. E., and Deardorff, J. W. (1980). A laboratory study of dispersion from a source in the middle of the convectively mixed layer. *Atmos. Environ.* **15**, 109–117.
- Wipperman, F. (1972). A note on parameterization of large scale wind stress at the sea-surface. *Beitr. Phys. Atmos.* **45**, 260–266.
- Wyngaard, J. C. (1973). On surface-layer turbulence. In "Workshop on Micrometeorology" (D. A. Haugen, ed.), pp. 101–149. Am. Meteorol. Soc., Boston, Massachusetts.
- Wyngaard, J. C. (1975). Modeling the planetary boundary layer-extension to the stable case. *Boundary Layer Meteorol.* **9**, 441–460.
- Wyngaard, J. C., and Cote, O. R. (1974). The evolution of a convective planetary boundary layer—a higher order closure model study. *Boundary Layer Meteorol.* **7**, 289–308.

- Yamada, T. (1977). A numerical experiment on pollutant dispersion in a horizontally-homogeneous atmospheric boundary layer. *Atmos. Environ.* **11**, 1014–1024.
- Yamada, T., and Mellor, G. L. (1975). A simulation of the Wangara atmospheric boundary layer data. *J. Atmos. Sci.* **32**, 2309–2329.
- Zeman, O., and Lumley, J. L. (1976). Modeling buoyancy driven mixed layers. *J. Atmos. Sci.* **33**, 1974–1988.
- Zeman, O., and Lumley, J. L. (1979). Buoyancy effects in entraining turbulent boundary layers: A second-order closure study. In “Turbulent Shear Flows I” (F. Durst, B. E. Launder, F. W. Schmidt, and J. H. Whitelaw, eds.), pp. 295–305. Springer-Verlag, Berlin, and New York.
- Zeman, O., and Tennekes, H. (1977). Parameterization of the turbulent energy budget at the top of the daytime atmospheric boundary layer. *J. Atmos. Sci.* **34**, 111–123.
- Zilitinkevich, S. S. (1972). On the determination of the height of the Ekman boundary layer. *Boundary Layer Meteorol.* **3**, 141–145.

This Page Intentionally Left Blank

INDEX

A

Acrylonitrile-butadiene-styrene manufacture, 62-63
 Aerojet-General Corporation molten metals study, 166-167
 Air pollution
 conservation of mass, 211
 mathematical model components, 211
 Air quality model, 211-212
 Alcoa test program, 162-166
 initiating event, 165
 molten aluminum variation, 162-163
 pour variations, 163
 site details, 163
 water variations, 163-164
 water vessel, 164-165
 Aluminum alloys, variation, and rapid phase transitions, 162-163
 Aluminum plants, explosions, 110
 API 6A6 subcommittee, LNG spill tests, 116
 Argonne National Laboratory
 molten aluminum studies, 167-169
 molten salt studies, 155
 Arrhenius relationship, k , 8-9
 Atmospheric boundary layer
 convective, 260-261
 height estimate, 260
 meteorological parameters, *see* Meteorological parameters
 Atmospheric diffusion equation, 217, 222, 231-232, 275
 boundary conditions, 238-239
 constraints, 250
 errors, 252
 Lagrangian integral time scale, 251
 parameters, 275-288
 eddy diffusion coefficients, *see* Eddy diffusion coefficients

 mean wind speed, 275-276
 universal function F , 276
 point source emission dispersion, 252
 solution, 286-288
 turbulent mean free path, 251
 validity, 250-252
 Atmospheric diffusion theory, 209-299, *see also* Point source diffusion formulas

B

Battelle molten aluminum study, 169-170
 Black liquor recovery boiler explosion list, 150-154
 Bubble column, 199-200
 Bubble growth dynamics, 87-99, 189-193
 bubble pressure, 190
 chemical criteria, 190
 constant population, 93-97
 critical bubble size, 190, 196-197
 destruction rate, 93
 devolatilization efficiency, 94-95
 diffusion-control model, 94-95
 disappearance, 89, 92
 energy equation, 191
 and extraction efficiency, 92, 94-97
 formation rate, 93
 function of composition, 202
 gas pressure, 89
 hydrodynamic control, 96-97
 Newman-Simon model, 97-98
 nucleation rate, 89
 number per unit volume, 89
 physical and mathematical model, 88-98
 radius and extraction efficiency, 94-97
 superheated propane, 192-193
 vapor blanketing, 197-198

- velocity, 191
 - water in silicone oil, 194
- Buffalo kiln afterburning control, 54, 56
- Bureau of Mines LNG spill tests, 117–119
- BURRO test series, 130–133
- n*-Butane spill tests, 121–122

C

- Carbon, molar disappearance rate, 16
- Catalyst
 - change in diffusivity and kiln performance, 24–26
 - inlet temperature and burn-off distance, 27–28
 - linear velocity, 17
 - response to increased temperature of, 35, 37–38
 - throughput, 51, 54
- Catalyst beads
 - and burning rates, 6–7
 - interface, 7–8
- CO
 - conversion
 - catalytic activity, 53, 55
 - kinetics, 45–47
 - rate, 46
 - rate of change, 50
- CO/CO₂ ratio, 45–46
 - function of temperature, 46
- Coatings, organic, on water vessels, and aluminum rapid phase transitions, 164
- Coke burning, 1–59, *see also* Fast coke burning; Slow coke burning
 - accumulation term, 31, 33
 - afterburning, 50–51
 - amount of carbon burning, 48
 - burning rate constant, 9–10
 - carbon remaining versus burning time, 8
 - catalyst beads, whole versus pulverized, 6–7
 - catalyst throughput, 51, 54
 - chemical reaction, 46
 - comparison of control schemes with step coke change, 40, 44
 - dynamic response model, *see* Dynamic response model
 - explicit model, *see* Explicit model
 - fish eye, 7
 - history, 2–3

- interface with catalyst bead, 7–8
- nomenclature, 57–59
- rate, 5
 - noncatalyzing oxide bases, 9, 11
- shell progression, 47
- silica–alumina catalyst, 8
- single-particle kinetics, 3–13
 - burning rate, 5–7
 - diffusional limited burning, 9–13
 - intrinsic kinetics, 3–9
 - oxygen utilization rate, 5–6
- slide rule, 12
- temperature dependency of *k*, 8–9
- transitional and observed rates, Arrhenius plot, 13–14
- Combustion Engineering, smelt-water explosion investigations, 146–147
- Conoco tests, 120
- Conservation of mass, air pollutants, 211
- Constock Liquid Methane Corporation, LNG spill tests, 116
- Continuity equation, incompressible fluid, 216
- COYOTE test series, 133–134

D

- Diffusion-control model, 94–95, 98
- Diffusion coefficient, 65–66
 - poly(vinylacetate) and toluene system, 66
- Dispersion parameters
 - averaging time considerations, 273–275
 - convective conditions, 268, 270–271
 - correlations, 267–269
 - dependence on travel time, 264–265
 - determination, 265–268
 - eddies
 - characteristic time scale, 274
 - role, 262
 - fluctuating, 271–272
 - in Gaussian models, 261–275
 - spatial and temporal averaging, 262–265
 - groundlevel concentrations, 270–271, 274
 - instantaneous cross-sectional distribution, 263–264
 - instantaneous relative concentration distribution variance, 272–273
 - joint moment, 266
 - lateral standard deviation, 270

mean plume concentrations, 274
 mean square particle displacement, 266–267
 plume envelope decomposition, 264–265
 puff equations, 264
 and stability class, 269
 vertical standard deviation, 268
 Dissolver-tank explosions, 144–145
 Drag flow shape factors, 72
 Dynamic response model, 31, 33–42
 accumulation terms, 31, 34
 amount of fast coke, 35
 closed-loop schemes, 40, 42–43
 increased catalytic temperature response, 35, 37–38
 prediction to plant performance comparison, 40–41
 simulation kiln conditions, 36

E

Eddy diffusion coefficients
 horizontal, 285–286
 vertical, 276–284
 above mixed layer, 283
 extrapolation above surface layer, 281
 maximum value, 278, 283
 neutral conditions, 280–282
 profile, 278–279, 281, 283
 roll-off functions, 280
 scale height, 284
 stable conditions, 282–284
 unstable conditions, 276–280
 Eddy diffusivity, 217, 238
 Ekman layer defined, 253
 Energy, activation, thermoform catalytic cracking kiln, 50, 53
 Energy equation, bubbles, 191
 Escalation model, 195–198
 basic concepts, 198
 Ezzo spill tests, 120–121
 Ethane–propane–*n*-butane system spill tests, 122–123
 RPT regions on 298-K water, 128
 Ethane spill tests, 121–123
 binary mixtures, 121, 123, 129
 Ethylbenzene–polystyrene system, 83
 Ethylene–poly(ethylene) system, 85–86
 Ethylene spill tests, binary mixture, 121, 123

Eulerian approach, turbulent diffusion, 214, 222–224
 mean concentration, continuous source, 230–233
 point source diffusion formulas, 238–245
 Explicit model
 CO₂/CO ratio, 45–46
 conversion kinetics, 42–43, 45–57
 diffusion kinetics, 47–57
 extension for fast and slow, 26–31
 initial temperature and residual carbon, 26–27
 steady-state solution, 30
 Explosive boiling, *see* Rapid phase transitions
 Extraction efficiency, 92
 Extruder, *see also* Mass transfer rate
 single-screw
 flow patterns, 68–69
 partially filled screw channel, 68
 schematic view, 67–68
 twin-screw
 intermeshing counter rotating, schematic, 79–81
 nonintermeshing counter rotating, schematic, 78–79
 partially filled channel, 81–82
 presence of bubbles, 88, 90–91
 schematic, 78–79

F

Fast coke burning, 4
 effect on slow coke, 31–33
 kiln equations, 15–16
 Fluctuating plume parameters, *see* Dispersion parameters, fluctuating
 Fluctuating transport, 216–217
 Fourier transform, concentration, 223
 Free contact model, 195
 Freon, *see* R-22
 Friction velocity, 259–260
 Fuel-coolant interactions, *see* Rapid phase transitions

G

Gaussian models, dispersion parameters, *see* Dispersion parameters

Gaussian plume equation, 237–238, 243, 287
 Gaussian plume formula, 245
 Golder's plot, coefficients as function of stability classes, 257
 Green's function, 213, 241
 atmospheric diffusion equation, 239
 slender-plume form, 241
 stochastic, 220

H

Heat of combustion, slow coke, 29
 Heptane–poly(dimethyl siloxane) system, 88, 90–91
n-Hexane, LNG spills on, 120
 Hexane–polyethylene system, 84
 Hexane–polystyrene system, 84

I, J, K

Isobutane spill tests, 121–122
 Isobutylene spill tests, 121–122
 Jacob number, 191
 K-theory hypothesis, 216–217

L

Lagrangian approach, turbulent diffusion, 214, 218–222
 mean concentration
 continuous source, 224–230
 Gaussian distribution, 235–238
 instantaneous source, 218–222
 Lagrangian integral time scale, 251, 266, 291
 Lagrangian velocity autocorrelation, 266, 290–291
 Latex, continuous conversion, 62–63
 Lawrence Livermore National Laboratory/
 Naval Weapons Center, *see* LLNL/
 NWC
 Liquefied natural gas, rapid phase transitions, 113–141
 background, 116–117
 delayed, 115
 large-scale circumstances, 115
 overpressures, 115–116, 136–141
 spill tests, 108–109
 Bureau of Mines, 117–119

Conoco, 120
 Esso, 120–121
 LNG composition, 133–136
 Memphis Light, Gas and Water Division, 116–117
 M.I.T., 120–128
 on organic liquids, 120
 Shell Pipeline Corporation, 128–130
 Transco, 117
 University of Maryland, 119–120
 on water, overpressures, 137–139
 Wisconsin Gas Co., 116
 summary, 113–116
 superheated-liquid model, 108
 superheat-limit temperature, 114
 Liquefied natural gas–*n*-hexane explosions, 120
 Liquid refrigerant explosions, 186–189, *see also* R-22
 properties, 187
 thermal boundary-layer development, 195–197
 Lithium, and probability of rapid phase transitions, 166–167
 LLNL/NWC, spill tests, 130–136
 BURRO test series, 131–133
 COYOTE test series, 133–134
 LNG spill facility, 130–131

M

Massachusetts Institute of Technology
 early spill tests, 120
 LNG Research Center, 121–128
 Mass transfer rate, 67–87, 93–94
 enhanced, 87–99
 fictitious coefficients, 98–99
 liquid mass flow rate, 98
 molar flux, 92, 98
 momentum equations, 93
 single-screw extruder, 68–78
 assumptions, 70
 axial dispersion, 73
 boundary and initial conditions, 70
 drag flow shape factor, 72
 experimental studies, 74–78, 83–87
 exposure time, 69
 molar flux, 71
 penetration theory, 70

- and screw speed, 72–73
 - styrene–polystyrene system, *see* Styrene–polystyrene system
 - theory, 69–74, 81–83
 - total molar rate, 69
 - volatile component concentration, 73
 - twin-screw extruder, 78–87
 - average value, 86
 - compared to single-screw, 82
 - exposure time, 82
 - polystyrene system, 83
 - Matagorda Bay, Texas, LNG RPT, 127–128
 - Memphis Light, Gas and Water Division, LNG spill tests, 116–117
 - Meteorological parameters, 253–261
 - bulk Richardson number, 255
 - convective boundary layer, 260–261
 - convective velocity scale, 261
 - flux Richardson number, 253
 - friction velocity, 259–260
 - gradient Richardson number, 254
 - mean wind speed gradient, 259
 - Monin–Obukhov length, *see* Monin–Obukhov length
 - parameter a , 256–257
 - Pasquill–Gifford stability classes, *see* Pasquill–Gifford stability classes
 - surface roughness estimation, 256–259
 - universal function ϕ_m , 259
 - Methane–ethane–propane system, RPT regions on 298-K water, 127
 - Methanol, thermal conductivity, 125–126
 - Methanol–poly(propylene) system, 76–77
 - Methyl methacrylate–poly(methyl methacrylate) system, 85
 - Molar flux, 92, 98
 - mass transfer, 69, 71
 - Molten aluminum–water explosions, 159–182
 - Alcoa test program, 162–166
 - background, 161–162
 - Battelle study, 169–170
 - criteria for, 178–179
 - external trigger shock, 181
 - industrial accidents, 171, 177–178
 - descriptions, 172–176
 - modified superheated theory, 179–180
 - salt-gradient theory, 180–181
 - spectra, 170
 - summary, 159–161
 - test schemes, 159–160
 - transitional boiling model, 181–182
 - trigger shock, 168–170
 - Molten copper–water explosions, industrial accidents, 171, 177–178
 - Molten metal–water explosions, 110–111
 - Molten salt studies, 155
 - pressure–temperature–composition diagram, 157–158
 - Molten saltwater explosions, 109–110
 - pressure effects, 193–194
 - Molten steel–water explosions, industrial accidents, 171, 177–178
 - Momentum transfer, 93–94
 - Monin–Obukhov length, 254
 - estimation, 255–256
 - and roughness height, 255
 - and stability condition, 254
 - Monin–Obukhov similarity theory, 259, 276
 - Monte Carlo simulation, turbulent diffusion, 288–294
 - continuous, elevated line source application, 291–294
 - dimensionless ground-level concentration, 292–294
 - elements, 288–291
 - Lagrangian integral time scale, 291
 - Lagrangian velocity autocorrelation, 290–291
 - mean square particle displacements, 291
 - particle velocity, 290
 - probability density function, 288–289
 - ways of treating particles, 292–293
- N**
- Na_2CO_3 , solubility in water, 156–157
 - Naval Weapons Center, *see* Lawrence Livermore National Laboratory/Naval Weapons Center spill tests
 - Newman–Simon model, 97–98
 - predictions, 99
 - Nucleation
 - heterogeneous, 199
 - homogeneous, 88, 199
 - temperature, *see* Superheat-limit temperature
 - rate, 89, 201

O

Overpressure

- distance graph, 137, 140
- liquid propane, 119
- LNG spills, 115–116, 137–140
- Shell Pipeline spill tests, 136–137

Oxygen

- accumulation term, 34
- concentration, clean burned region, 9–10
- diffusion rate, 47
- flow rate, through bead surface, 10–11
- as function of distance down the kiln, 29–30
- molar consumption rate, 16
- rate of change, 49
- utilization rate, 5–6, 48
- versus temperature, 6

P

Pasquill–Gifford stability classes, 254–255

- estimation, 255–256
- and parameter a , 257
- and plume dispersion parameters, 269

Peclet number, 73–74, 83

Penetration theory, 98

- assumptions, 70
- boundary and initial conditions, 70

Plume model, fluctuating, 247–250

- crosswind and vertical concentration distributions, 258
- definitions, 249
- plume average dispersion, 248
- reflection, 249

Plume physics

- description, 262–263
- dispersion, *see* Dispersion parameters
- envelope, decomposition, 265
- instantaneous cross-sectional distribution, 263–264
- spread deviations, 247

Point source diffusion formulas

- atmospheric diffusion equation, 222–224, 231–232
- concentration
 - Fourier transform, 223
 - Lagrangian approach, 218–222
 - steady-state, 225
- correlation coefficient, 219

Eulerian approach, 222–224, 238–245

- continuous source, 242–243
- instantaneous source, 238–241
- separation of variables, 240

fluctuating plume model, *see* Plume model, fluctuating

fundamental equations, 212–218

- atmospheric diffusion equation, 217
- concentration autocorrelation, 215
- concentration cross-correlation, 214–215
- concentration decomposition, 216
- concentration distribution, 215
- continuity, 216
- eddy diffusivity, 217
- Eulerian description, 212, 214
- fluctuating transport, 216–217
- Green's function, 213
- inert tracer concentration, 213–214
- Lagrangian approach, 218–222
- Lagrangian description, 214
- species conservation, 212–213
- transition probability density, 214
- wind velocity, 215

Gaussian diffusion formulas, 244–245

Gaussian distribution, 233, 235–250

- covariance, 235
- Lagrangian approach, 235–238
- probability density function, 235–236
- unbounded domain, 236–237

Green's function, stochastic, 220

individual puff spread, 227

line and area source solutions, 243, 246–247

mean concentration, 222

- continuous sources, 224–234
- equal velocity variances, 226–227
- Eulerian approach, 230–233
- instantaneous source, 218–224
- unequal velocity variances, 227–228

mean square concentration, 220

Monte Carlo simulation, *see* Monte Carlo simulation, turbulent diffusion

probability density function, 220

puff kernel, Taylor series, 226

slender-plume approximation, 227, 229, 231

transition probability density, 225

velocity, variance, 221–222

velocity components, autocovariances, 219

Polybutenefreon system, 84
 Polymers, stripping operations, *see* Vapor-liquid stripping operations
 Polymer-vapor equilibrium relations, 65-66
 Poly(vinyl acetate)-toluene system, 66
 Power law index, and surface roughness, 275-277
 Probability density function, 220
 Gaussian, 235-236
 Monte Carlo simulation, 288-289
 Propane spill tests, 121-122
 overpressure, 119
 superheated, bubble growth, 192-193
 superheat-limit temperature, 114
 Propylene spill tests, 121-122
 Puff
 kernel, Taylor series expansion, 226-227
 spread, 227

R

R-22
 critical bubble size, 196-197
 thermal boundary-layer development, 195-197
 thermal explosions, 193
 water contact experiments, 188-189
 Rapid phase transitions, 105-208
 absolute pressure effects, 189-198
 bubble growth dynamics, 189-193
 binary mixtures, 121, 123, 129
 criteria, 107-108
 defined, 112
 escalation model, 195-198
 interfacial temperature ranges, 125-126
 laboratory scale, 124
 large-scale, coherent, 109
 liquefied gases on water, 129
 LNG-water, *see* Liquefied natural gas, rapid phase transitions
 metal, *see* Molten aluminum-water explosions; Reactive metal-water explosions
 nomenclature, 203
 possibility, rules for, 114
 regions, methane-ethane-propane system, 127
 small-scale, and interfacial temperature, 125
 superheated-liquid model, 108
 trigger shock, 109, 112

Reactive metal-water explosions, 182-186
 background, 182-183
 discussion, 185
 titanium melting-furnace explosions, 183-185
 tungsten casting explosion, 185
 Richardson number
 bulk, 255
 flux, 253
 gradient, 254

S

Salt-gradient theory, 142-143, 180-181
 Shell Pipeline Corporation spill tests, 128-130, 136-137
 Silica-alumina catalyst, 8
 mass balances, 15
 transitional and observed burning rates, 13-14
 Slender-plume approximation, 227, 229, 231, 233, 241
 Gaussian plume equation, 237
 Slow coke burning, 4-5
 effect of fast coke, 31-33
 intrinsic rate of burning, 9
 kiln equation, 13-26
 countercurrent zone, 18
 explicit solution, 13-19
 kiln performance and explicit solution, 21, 23-26
 one-dimensional, 16-18
 parameters, 20
 test and use of explicit solution, 19-23
 oxygen accumulation term, 34
 Smelt
 defined, 141
 desensitizers, 158-159
 kraft, 141
 analysis, 145
 explosions, 144-145
 soda, 141
 analysis, 145
 explosions, 144
 Smelt-saltwater explosions, 109-110
 Smelt-water explosions, 141-149
 black liquor recovery boiler explosion list, 150-154
 boiler, statistical survey, 148-149
 description, 149, 155

- dissolving tank explosions, 144–145
 - laboratory investigations, 142, 146–148
 - modified superheat theory, 156–158
 - salt-gradient theory, 142–143
 - summary, 141–143
 - superheat model, 155–156
 - Stationary process, defined, 219
 - Styrene–polystyrene system, 77
 - experimental results comparison, 78
 - stripping operations, 75–76
 - Superheated-liquid model, 108
 - modified, 160–161
 - Superheated liquids, 198–203
 - defined, 198
 - encapsulation, 199
 - existence, 198–199
 - explosion strength, and system pressure, 111–112
 - rate of formation, vapor embryos, 201
 - Superheated-liquid theory
 - modified, 110, 179–180
 - smelt–water explosions, 156–158
 - smelt–water explosions, 155–156
 - Superheat-limit temperature, 114, 124, 199–200
 - function of composition, 201–202
 - function of temperature, 200–201
 - NaCl solutions, 157–158
- T**
- Taylor series, puff kernel, 226
 - Temperature
 - cold liquid profiles, 195
 - as function of distance down the kiln, 29
 - interfacial, 124–125, 129–130
 - and LNG composition, 135
 - RPT range for hydrocarbon spills, 125–126
 - plenum, effect of cooling air, 54, 56
 - rate of change, 49–51
 - superheat-limit, *see* Superheat-limit temperature
 - Thermal explosions, *see* Rapid phase transitions
 - Thermoform catalytic cracking kiln, *see also*
 - Coke burning
 - activation energies, 50, 53
 - afterburning control, 53, 56
 - air lift version, 3–4
 - catalyst inlet temperature and burn-off distance, 27–28
 - catalyst linear velocity, 17
 - catalysts, 3
 - closed-loop schemes, 40, 42–43
 - CO conversion catalytic activity, 53, 55
 - development, 2–3
 - flow patterns, 3, 5
 - mass balances, silica–alumina catalyst, 15
 - operation
 - coke remaining versus distance from top, 21–23
 - conditions, 23, 52
 - parameters investigated, 51, 53
 - performance, 24
 - and air-inlet locations, 25–26
 - parameters, 18–19
 - change in catalyst diffusivity, 25–26
 - use of explicit solution, 21, 23–26
 - plenum temperature and cooling air addition, 54, 56
 - plume burner, 27
 - response to coke increase, 36, 39–40
 - temperature in top zone, 21–22
 - Titanium melting-furnace explosions, 183–185
 - Transco, LNG spill tests, 117
 - Transfer unit
 - length, 99–102
 - experimental values, 101
 - number, 99–100
 - Transition probability density, 214, 225, 246–247, 252
 - Transitional boiling model, 181–182
 - Tungsten casting explosion, 185
 - Turbulent closure models, second moment, 217–218
- U, V**
- University of Maryland spill tests, 119–120
 - Vapor explosions, *see* Rapid phase transitions
 - Vapor–liquid stripping operations, 61–104
 - analysis and design problem, 64–67
 - diffusion coefficients, 65–66
 - mass transfer rates, *see* Mass transfer rate
 - nomenclature, 102–103
 - nonlinear constitutive equations, 64–65
 - polymer–vapor equilibrium relations, 65–66

Velocity
 autocorrelation, 266
 autocovariances, 219
 variance, 221–222
 equal, 226–227
Velocity scale, convective, 261

W

Wind speed
 gradient, 259
 mean, 275–276

Wind velocity, 215
Wisconsin Gas Co., LNG spill tests, 116
Wood pulp preparation, 143–144
Wiped-film processors, mass transfer rates,
 see Mass transfer rate

X, Z

Xylene–polypropylene system, 76–77
Zeolite catalysts, thermofor catalytic crack-
 ing, 43
 with chromia, 51, 53

This Page Intentionally Left Blank

CONTENTS OF PREVIOUS VOLUMES

Volume 1

Boiling of Liquids

J. W. Westwater

Non-Newtonian Technology:
Fluid Mechanics, Mixing, and
Heat Transfer

A. B. Metzner

Theory of Diffusion

R. Byron Bird

Turbulence in Thermal and Material Transport

J. B. Oppell and B. H. Sage

Mechanically Aided Liquid Extraction

Robert E. Treybal

The Automatic Computer in the Control and
Planning of Manufacturing Operations

Robert W. Schrage

Ionizing Radiation Applied to Chemical Processes
and to Food and Drug Processing

Ernest J. Henley and Nathaniel F. Barr

AUTHOR INDEX—SUBJECT INDEX

Volume 2

Boiling of Liquids

J. W. Westwater

Automatic Process Control

Ernest F. Johnson

Treatment and Disposal of Wastes in Nuclear
Chemical Technology

Bernard Manowitz

High Vacuum Technology

George A. Sofer and Harold C. Weingartner

Separation by Adsorption Methods

Theodore Vermeulen

Mixing of Solids

Sherman S. Weidenbaum

AUTHOR INDEX—SUBJECT INDEX

Volume 3

Crystallization from Solution

*C. S. Grove, Jr., Robert V. Jelinek, and
Herbert M. Schoen*

High Temperature Technology

F. Alan Ferguson and Russell C. Phillips

Mixing and Agitation

Daniel Hyman

Design of Packed Catalytic Reactors

John Beek

Optimization Methods

Douglass J. Wilde

AUTHOR INDEX—SUBJECT INDEX

Volume 4

Mass-Transfer and Interfacial Phenomena

J. T. Davies

Drop Phenomena Affecting Liquid Extraction

R. C. Kintner

Patterns of Flow in Chemical Process Vessels

Octave Levenspiel and Kenneth B. Bischoff

Properties of Cocurrent Gas-Liquid Flow

Donald S. Scott

A General Program for Computing Multistage
Vapor-Liquid Processes

D. N. Hanson and G. F. Somerville

AUTHOR INDEX—SUBJECT INDEX

Volume 5

Flame Processes—Theoretical and Experimental

J. F. Wehner

Bifunctional Catalysts

J. H. Sinfelt

Heat Conduction or Diffusion with Change of Phase

S. G. Bankoff

The Flow of Liquids in Thin Films

George D. Fulford

Segregation in Liquid-Liquid Dispersions and Its Effect on Chemical Reactions

K. Rietema

AUTHOR INDEX—SUBJECT INDEX

Volume 6

Diffusion-Controlled Bubble Growth

S. G. Bankoff

Evaporative Convection

John C. Berg, Andreas Acrivos, and Michel Boudart

Dynamics of Microbial Cell Populations

H. M. Tsuchiya, A. G. Fredrickson, and R. Aris

Direct Contact Heat Transfer between

Immiscible Liquids

Samuel Sideman

Hydrodynamic Resistance of Particles at Small

Reynolds Numbers

Howard Brenner

AUTHOR INDEX—SUBJECT INDEX

Volume 7

Ignition and Combustion of Solid Rocket

Propellants

Robert S. Brown, Ralph Anderson, and Larry J. Shannon

Gas-Liquid-Particle Operations in Chemical

Reaction Engineering

Knud Østergaard

Thermodynamics of Fluid-Phase Equilibria at

High Pressures

J. M. Prausnitz

The Burn-Out Phenomenon in Forced-Convection

Boiling

Robert V. Macbeth

Gas-Liquid Dispersions

William Resnick and Benjamin Gal-Or

AUTHOR INDEX—SUBJECT INDEX

Volume 8

Electrostatic Phenomena with Particulates

C. E. Lapple

Mathematical Modeling of Chemical Reactions

J. R. Kittrell

Decomposition Procedures for the Solving of Large-Scale Systems

W. P. Ledet and D. M. Himmelblau

The Formation of Bubbles and Drops

R. Kumar and N. R. Kuloor

AUTHOR INDEX—SUBJECT INDEX

Volume 9

Hydrometallurgy

Renato G. Bautista

Dynamics of Spouted Beds

Kishan B. Mathur and Norman Epstein

Recent Advances in the Computation of

Turbulent Flows

W. C. Reynolds

Drying of Solid Particles and Sheets

R. E. Peck and D. T. Wasan

AUTHOR INDEX—SUBJECT INDEX

Volume 10

Heat Transfer in Tubular Fluid-Fluid Systems

G. E. O'Connor and T. W. F. Russell

Balling and Granulation

P. C. Kapur

Pipeline Network Design and Synthesis

Richard S. H. Mah and Mordechai Shacham

Mass-Transfer Measurements by the

Limiting-Current Technique

J. Robert Selman and Charles W. Tobias

AUTHOR INDEX—SUBJECT INDEX

Volume 11

Mass-Transfer Rates in Gas-Liquid Absorbers and Reactors

Jean-Claude Charpentier

The Indian Chemical Industry—Its Development and Needs

Dee H. Barker and C. R. Mitra

The Analysis of Interphase Reactions and Mass Transfer in Liquid-Liquid Dispersions

Lawrence L. Tavlarides and

Michael Stamatoudis

Transport Phenomena and Reaction in Fluidized Catalyst Beds

Terukatsu Miyauchi, Shintaro Furusaki,

Shigeharu Morooka, and Yoneichi Ikeda

INDEX